THE INFLUENCE OF SOIL CRYOSTRUCTURE ON THE CREEP AND LONG TERM STRENGTH PROPERTIES OF FROZEN SOILS

A

THESIS

Presented to the Faculty

of the University of Alaska Fairbanks

in Partial Fulfillment of the Requirements

for the Degree of

DOCTOR OF PHILOSOPHY

By

Matthew Thomas Bray, M.S.

Fairbanks, Alaska

December 2008

The Influence of Soil Cryostructure on the Creep and Long Term Strength Properties of Frozen Soils

by

Matthew Thomas Bray

RECOMMENDED:

Advisory Committee Chair

Chair, Department of Civil & Environmental Engineering

APPROVED:

Dean, College of Engineering and Mines

Dean of the Graduate School

Dec 12, 2008

Date

Abstract

The time dependent mechanical properties of ice-rich frozen soils were studied in relation to their cryostructure. The CRREL permafrost tunnel was the primary source of the studied ice-rich soils. Mapping of the permafrost geology of the main adit of the CRREL permafrost tunnel was performed and reinterpreted in the context of a cryofacial approach. The cryofacial approach in based on the concept that cryostructure is dependent on how a soil was deposited and subsequently frozen. Three main soil cryostructures were determined to represent the main aspects of the permafrost geology. Soils with micro-lenticular cryostructure represent the original ice-rich syngenetic permafrost formed during the Pleistocene. Reworked sediment due to fluvial-thermal erosion resulted in soils with massive cryostructure and soils with reticulate-chaotic cryostructure. Ice bodies within the tunnel include syngenetic wedge ice and secondary thermokarst cave ice deposits.

A testing program for determining the time dependent mechanical properties, including the creep and long term strength characteristics of permafrost in relation to soil cryostructure, was performed. Undisturbed frozen soils include silty soil containing micro-lenticular, reticulate-chaotic, and massive cryostructure. Remolded silt from the tunnel was used to create artificial samples with massive cryostructure for comparison to the undisturbed frozen soils. In addition to frozen silt, undisturbed ice facies were tested. These included syngenetic wedge ice, Matanuska basal glacial ice, and Matanuska glacial ice. Testing methods include uniaxial constant stress creep (CSC) tests and uniaxial relaxation tests. It was shown that soil cryostructure and ice facies influences the creep and long term strength properties of frozen soils. It was shown that remolded soils provide non-conservative creep and long term strength estimates when extrapolated to undisturbed frozen soils. Minimum strain rate flow laws show that at low stresses, undisturbed soils creep at a faster rate than remolded soils. At high stresses, frozen soils creep at a faster rate than ice. It was also shown that the unfrozen water content influences the mechanical properties of frozen soils and that the unfrozen water content is influenced by soil cryostructure. Through cryostructure, the permafrost geology is related to the time dependent mechanical properties of frozen soils.

Table of Contents

Page

List of Figures

Page

Page

Page

Page

Page

Page

List of Tables

Page

Acknowledgments

I want to thank Dr. Doug Goering, Dean, College of Engineering and Mines, University of Alaska Fairbanks for being a member of my committee. I want to thank Dr. Mikhail Kanevskiy, Assistant Research Professor at the University of Alaska Fairbanks for serving as a committee member and his all around knowledge on permafrost and soil cryostructure.

Special thanks is extended to Alaska EPSCoR who made this work possible through their funding support. Without their support, this project would never have occurred. Alaska EPSCoR supports many students and faculty and their support is appreciated.

I want to extend special thanks to Dr. Scott L. Huang, Professor of Geological Engineering, University of Alaska Fairbanks, for serving as a committee member and taking the time to constructively aid in discussions in regards to this research project.

Special thanks is extended to Dr. Yuri Shur, Professor of Civil Engineering, University of Alaska Fairbanks, for serving as my committee chair. Dr. Shur also spent considerable amount of time reviewing numerous drafts of this thesis and took time for countless discussions on aspects of the research project. Dr. Shur was also instrumental in finding funding for necessary equipment and supplies required during the course of the research. Dr. Shur's love of permafrost is contagious and wears off on those around him, thank you.

And finally, I would like to thank my family for their support. Also a special thanks to those four legged friends which allow for the important times when diversion is needed.

Preface

Portions of this research were previously published and presented in several conferences. The peer reviewed publications include:

Bray, M.T. 2008. Effects of soil cryostructure on the long-term strength of ice-rich permafrost near melting temperatures. Proceeding of the Ninth International Conference on Permafrost, University of Alaska Fairbanks, Alaska, June 29-July 3, 2008: 183-188.

Bray, M.T., French, H.M. & Shur, Y. 2006. Further Cryostratigraphic Observations in the CRREL Permafrost Tunnel, Fox, Alaska. Permafrost and Periglacial Processes, 17: 233-243.

Shur, Y., French, H.M, Bray, M.T. & Anderson, D.A. 2004. Syngenetic permafrost growth: cryostratigraphic observation from the CRREL tunnel near Fairbanks, Alaska. Permafrost and Periglacial Processes 15(4): 339-347.

Chapter 1: Introduction

This work was undertaken with the hope to bridge a small part of the gap that exists between permafrost geology and permafrost engineering. The field of permafrost geology is well established in North America. The field of permafrost engineering is also well established in North America. However, the two fields rarely cross disciplines despite the fact that the most value comes from combination of the two.

The overall goal of this work was to connect the permafrost geology of the soils tested with their creep properties which is illustrated in Figure 1.1. This was primarily approached through the application of a cryo-facial model. The cryo-facial approach makes the assumption that a soil's cryostructure is dependent on how a soil was deposited and then subsequently frozen. Cryostructure is the pattern of ice inclusion found within a soil. Therefore, cryostructure is directly related to the permafrost geology of a deposit. So the fundamental approach of this work consists of correlating cryostructure to the time dependent mechanical properties of the soils in question and to study soil with original cryostructure and ice content instead of remolded soils. The geology of the soils is presented first, followed by the mechanical properties.

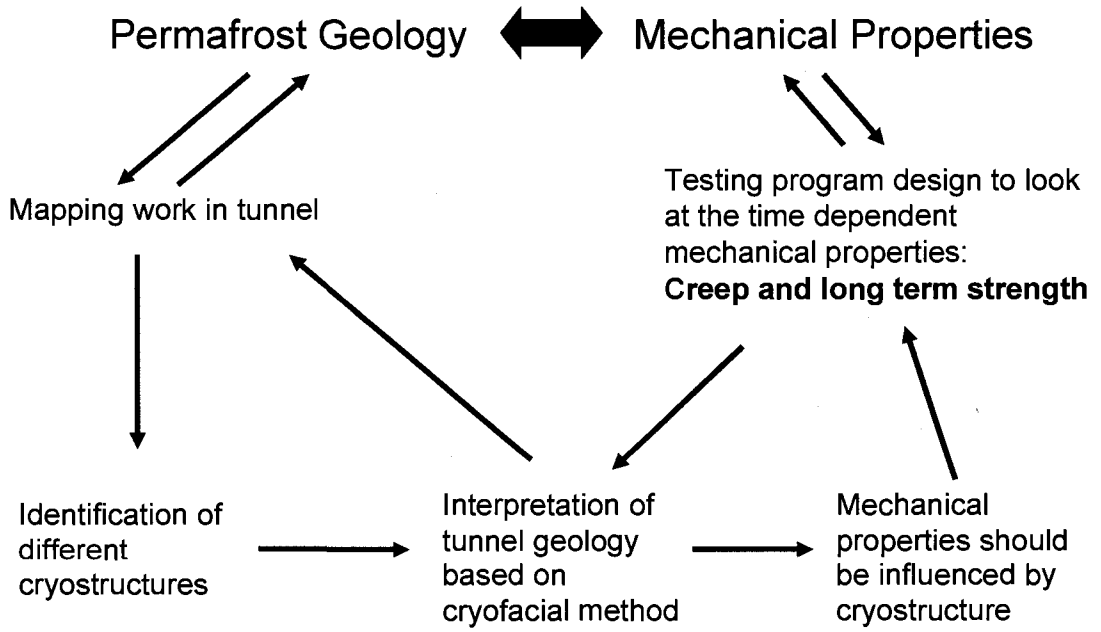

Figure 1.1. Conceptual schematic illustrating the overall approach of the research program.

The work of this thesis will be presented in the following format. Chapter 2 presents a review of relevant literature. Chapter 3 discusses the permafrost geology of the CRREL permafrost tunnel. Chapter 4 presents the soil, soil cryostructure, and ice facies used in the testing program. Chapter 5 provides an overview of the testing equipment and methods. In chapter 6, the deformation patterns observed for the various soil cryostructures and ice facies will be discussed. Chapter 7 presents the results and discussion of the testing program. Chapter 8 presents a summary of conclusions of the work.

Chapter 2 presents a review of relevant literature. The focus of the literature review is to 1) review work which discusses soil cryostructure and the influence of cryostructure on mechanical properties and 2) review relevant creep data for ice and ice-rich permafrost soils. The first area primarily discusses work that has been conducted in Russia where more work has been conducted in regards to soil cryostructure and mechanical properties. The second area looks at simple minimum strain rate flow laws for ice, Fairbanks silt, and undisturbed ice-rich silt. These flows laws will then be compared to those derived in this study in Chapter 7.

Chapter 3 presents the geology of the CRREL permafrost tunnel. The CRREL permafrost tunnel, Fox, Alaska, was chosen as the primary permafrost deposit for this work. The CRREL permafrost tunnel is composed of a Pleistocene syngenetic permafrost body commonly known as "Yedoma" or "Ice-complex." The original syngenetic permafrost is characterized by silts with high ice contents and large syngenetic ice wedges. The original permafrost is modified by reworked and subsequently refrozen deposits. The CRREL tunnel contains a reasonably large data set in regards to the mechanical properties under both undisturbed and remolded soil conditions. The tunnel also supplies a range of soil cryostructures which contain a similar sediment type, mineralogy, and grain size distribution.

Chapter 4 presents a detailed description of the soils, soil cryostructures, and ice facies that were used in the testing program. The first section includes a description of the samples which include macro images, ESEM (environmental scanning electron microscope) micro scale images, and CT scan images. The second half of the chapter looks at the physical properties of the soil and volumetric unfrozen water contents. Volumetric unfrozen water contents are related to soil cryostructure.

In chapter 5, the testing equipment and methods are described. Two main types of tests were used. The first is constant stress creep (CSC) tests which consist of applying a constant stress

and observing the deformation with time. The second type is relaxation tests which consist of loading the sample to a prescribed load and observing the stress and deformation with time as the sample relaxes due to creep deformation. For each test type, a description of the loading equipment, observation equipment, and temperature control are described. The testing methods applied for each test type are also described.

Chapter 6 discusses deformation patterns for the various soil cryostructues and ice facies. This chapter attempts to bring into focus some of the basic physical processes that occur which result in the deformation patterns seen. The discussions are grouped into separate soil cryostructures and ice facies. In addition, strain vs. time curves are presented in this section.

Chapter 7 presents the results and discussion for the creep and strength data derived from the CSC and relaxation tests. The chapter is grouped into two main areas. The first main area presents minimum strain rate flow laws as determined from CSC tests. The data is then compared to the flow laws outlined in Chapter 2. The second main area presents long term strength interpretations as determined from CSC and relaxation data. The results are compared to literature for Fairbanks silt and ice-rich permafrost soils. During the course of the chapter, special emphasis is made to discuss how the results from CSC and relaxation tests compare.

Chapter 8 concludes the work and summarizes important findings. To summarize the flow of chapters, Chapter 2 reviews relevant literature, the permafrost geology of the soils is described in Chapters 3 and 4, and the time dependent mechanical property testing program is discussed in Chapters 5, 6, and 7. The hope is that the permafrost geology is linked to the mechanical behavior.

Chapter 2: Literature Review

The amount of information in the field of permafrost, frozen ground mechanics, and ice mechanics is very large. The amount of literature for ice is especially large. The purpose of this review is not to present a complete and current review of all information, especially for frozen ground and ice mechanics. No attempt is made to present information discussing the creep and strength behavior of coarse grained materials, despite the potential similarities to the mechanics of fine grained frozen soils. The purpose is to present reviews of information that is most prevalent to this thesis. Sections 2.1 and 2.2 will introduce work that has been done, which relates cryostructure (pattern of ice inclusion in a soil) to strength and deformation characteristics. Section 2.3 introduces general information in regards to data interpretation necessary for determination of flow laws. Section 2.4 introduces flow laws for polycrystalline ice. Section 2.5 discusses the flow laws for undisturbed permafrost. Finally, Section 2.6 briefly summarizes all relevant research that has been conducted in relationship to the creep or strength characteristics of Fairbanks Silt. Included are laboratory tests on remolded and undisturbed samples, as well as field studies conducted in the CRREL permafrost tunnel. One of the primary goals of this study is to compare the testing results from remolded and undisturbed soils. It is a basic premise that remolded soils are not representative of undisturbed soils. In this work, Fairbanks silt refers to eolian and reworked silt from the CRREL permafrost tunnel located in Fox, Alaska.

2.1 Background on Cryostructure

Cryogenic structure or cryostructure is the pattern of ice inclusion found within a frozen soil. Cryostructure depends both on the depositional genesis and the cryogenic genesis (i.e. how the soil was frozen). For example, the cryostructure of silt, which was frozen under a closed system, depends on the freezing conditions. Rapid freezing generally creates a soil with massive cryostructure with ice in pore spaces. Slow freezing at -1°C will allow for moisture redistribution to occur. The nature of the moisture redistribution depends on the physiochemical characteristics of the silty sediments and the direction of freezing. This moisture redistribution results in the formation of segregated ice patterns. Chapter 3 presents information on the influence of soil deposition and freezing on soil cryostructure for the CRREL permafrost tunnel. The important aspect of cryostructure is that certain permafrost deposits contain reasonably predictable cryostructure. The type of cryostructure controls the physical characteristics of a soil including ice content, unfrozen water content, mechanical discontinuities, thermal conductivity, thaw settlement, and strength.

The presence of a distinct ice structure essentially introduces discontinuities into the soil. The presence of ice also introduces anisotropic properties based on the ice crystal structure and the relative arrangement of the ice crystals. The direction of the applied stress relative to the ice structure influences the resulting behavior. In a rock mass, the genesis of the rock, its stress and deformation history, the joint density and orientations, and degree of weathering all affect how the rock mass will behave and deform. The general idea is that cryostructure is a fundamental part of the frozen ground system. In permafrost, silt may not necessarily be just frozen silt. Frozen clay may not be just frozen clay. Frozen sand may not be just frozen sand. All permafrost is not created equal and should not be treated as such.

2.2 Effects of Cryostructure on Deformation Behavior

It is commonly acknowledged that soil cryostructure should play a role in the deformation behavior of frozen soils. Roggensack (1977) states, "This emphasizes the need to recognize discrete forms of ground ice and to treat them as geological discontinuities which may exert a significant influence on overall geotechnical behavior." Sayles and Carbee (1981) acknowledge that "texture" should play a role. Savigny and Morgenstern (1986a) acknowledge that "creep properties determined from reconstituted frozen soils cannot be applied indiscriminately to natural permafrost soils because the cryogenic textures are different." The heterogeneous and anisotropic effect of ice inclusion (ie. soil cryostructure) makes analysis of the deformation behavior difficult. Ice inclusions not only act as potential discontinuity planes, but the deformation behavior of the ice crystal is very dependent on the direction of applied stress to the basal planes (planes of easy glide). Combining with the natural variations of undisturbed soils, large variations in deformation responses of the frozen soils are common. Because of the reasons mentioned above, remolded soils are commonly used since the soil uniformity can be controlled more accurately and thus the degree of uncertainty is reduced.

Very little information is available in the English literature which discusses the effects of soil cryostructure on the strength and creep properties of frozen soils. This includes both artificially created cryostructure in remolded soils and cryostructure of natural permafrost. Pekarskaya (1965) is perhaps the most detailed source. One of the main foci of her work was to look at the effect of cryostructure on frozen soil deformation behavior. In addition, translated monographs from Vialov (1959) and Vyalov et al. (1980) include a discussion on the effects of soil cryostructure. Vialov (1959) presents data derived from the pressing of cylindrical punches into undisturbed permafrost soils. Vyalov et al. (1980) present data on artificially created types of soil cryostructure. Very little North American literature attempts to specifically address the role of

cryostructure on the deformation behavior of frozen soils. Savigny and Morgenstern (1986a) provide a detailed description of the failure nature of clay permafrost that contains well developed ice lenses (3-25 mm thick) with varying orientations. Included below is a summary of the primary literature sources regarding the role of cryostructure on strength and deformation behavior of frozen soils.

Pekarskaya (1965, pg 60-63) summarizes the extent of Russian data on the effect of soil cryostructure up to the 1960's and is described briefly below. Soil cryostructure has been shown to have a large influence on the behavior and strength properties of a thawed soil as a consequence of the original frozen soil morphology. Studies in the 1950's by Brodskaya (referenced in Pekarskaya, 1965) using uniaxial compression showed that soils with massive cryostructure showed less deformation than stratified or cellular structure. Compressibility is dependent on the area of contact between ice and mineral bands for a given moisture content. It was found that the larger the contact area, the larger the compressibility. Pekarskaya (1965) also mentions that many authors have indicated that cryostructure should have an influence on the mechanical behavior of frozen soils since structural anisotropies likely exist. However, they did further address the role of cryostructure. Tystovich (referenced in Pekarskaya (1965)) showed that plastic deformation in stratified sand depends on the thickness of the ice layers (for hour long tests). Observation by Gol'dshtlin (referenced in Pekarskaya 1965) showed that the contact of soil with ice layers is more easily broken when a force is applied parallel to the contact. Alternatively, the contact of soil with ice layers is more difficult to break when a force is applied perpendicular to ice layers. This suggests that the contact between soil and ice layers may be a weak component of the frozen soil-ice system. Data by Vialov (1959) showed that the amount of deformation for a footing is influenced by the vicinity of ice layers to the base of the footing.

2.2.1 Influence of Cryostructure on Rapid Loading

Pekarskaya (1965) defines "texture" as the relative arrangement and size of the components of the system, which include ice inclusions and mineral particles and aggregates. Therefore, "texture" is equivalent to soil cryostructure. Pekarskaya (1965) performed rapid loading shear tests on remolded soils with varying cryostructure. The soils, cryostructure, and testing results are outlined below. The soil cryostructure used in the testing program include massive cryostructure, stratified cryostructure, and cellular cryostructure. The different cryostructures were created from remolded Beskudnikovkaya clay. Soils with massive cryostructure contain no segregated ice, only ice formed in the pores. Soil with massive cryostructure was created by freezing the prepared samples at temperatures of -70°C to -76°C. Stratified cryostructure consists

of ice inclusions that are arranged in parallel layers. Stratified cryostructure is commonly referred to as layered cryostructure. Cellular cryostructure forms a continuous to discontinuous network of ice inclusions. Cellular cryostructure is commonly referred to as reticulate cryostructure. Soils with cellular cryostructure were formed by unidirectional freezing of the sample at a temperature of -10°C to -15°C to form fine cellular cryostructure. To form large cellular cryostructure (i.e. larger ice inclusions), freezing temperatures of -3°C to -5°C were used. Both stratified and cellular cryostructure were grouped into additional subdivisions. Gravimetric water contents of soils with massive and cellular cryostructures remained constant between 29 to 34%. Therefore, the moisture content remained the same for different textures. Ice was also included in the testing program and can be considered a fourth texture. The tests were conducted on remolded samples at temperatures ranging from -0.5°C to -2.0°C.

Under rapid shear, ice showed the highest strength and exceeded the strength of clay with massive cryostructure by 51-54%, and clay with cellular cryostructure by 30-40%. The strength of clay with cellular cryostructure exceeded the strength of clay with massive cryostructure by 27-34%. In addition, the cohesion and friction angle for clay with cellular cryostructure was greater than for clay with massive cryostructure. Clay with large cellular cryostructure also exhibited greater strength over clay with fine cellular cryostructure.

Pekarskaya (1965) proposed an explanation for the effects of soil cryostructure and its influence on rapid shear strength. It is assumed that the contact between ice and soil particles is the weakest component of the soil-ice system. Ice is considered the strongest component under rapid shear conditions. In soils with massive cryostructure, it is assumed that shear planes can pass along the weaker bonds which occur at the contact between the pore ice and soil particles, thus bypassing ice grains. The ice in soils with cellular cryostructure creates an ice skeleton or support structure around the mineral aggregates. When a rapid load is transmitted to the soil, the load is transferred through the ice skeleton. When the ice skeleton is thicker, the strength increases. This trend is shown when comparing clay with large cellular cryostructure with clay with fine cellular cryostructure. Under rapid shear conditions for the data presented, the relative strength relationships to soil cryostructure are $\tau_{ice} > \tau_{large\ cellular} > \tau_{fine\ cellular} > \tau_{massive}$. This would suggest that the more developed and interconnected the ice lens system, the greater the rapid shear strength.

Rapid shear tests were also conducted by Pekarskaya (1965) using undisturbed soils to look at the effect of soil cryostructure. The cryostructures tested included clayey soils with massive

cryostructure and clayey soils with stratified cryostructure. The clayey soils with stratified cryostructure contained ice lenses ranging from 20 to 100 mm in thickness and were separated by soil layers. When the applied force was perpendicular to ice lenses in clay with stratified cryostructure, the results were similar to the remolded soils where the icier soils tended to show higher strengths. In general, $\tau_{ice} > \tau_{stratified} > \tau_{massive}$. However, it was found that when the applied force was parallel to the ice lenses, the clayey soil with stratified cryostructure showed the lowest strength. Therefore, the strength relationship would be $\tau_{ice} > \tau_{massive} > \tau_{stratified}$. This supports the assumption that the contact between soil particles and ice is the weakest component of the frozen soil under rapid shear conditions. It was acknowledged that the experiments were conducted at temperatures close to melting conditions (i.e. -0.4 to -2.0°C), thus significant unfrozen water was likely present. Caution, therefore, should be used when assuming the soil particle-ice bond is the weakest component. As temperatures become colder and the amount of unfrozen water decreases, this trend may not remain valid. Pekarskaya (1965) showed that soil cryostructure and the direction of applied force in relationship to the orientation of the ice lenses are important. General observations suggest that increased ice content in the shear zone results in higher shear strengths. When a shear stress is applied parallel to ice lenses, the shear strength tends to be reduced.

2.2.2 Influence of Cryostructure on Long Term Loading

Experiments were also run by Pekarskaya (1965) looking at the effects of soil cryostructure on the strength under a long term application of load. Tests were conducted on undisturbed clayey soils from the Igarka region. Cryostructures include soils with massive and stratified cryostructure. Ground ice taken from the same permafrost deposits was also tested. Samples were tested under shear and compression.

As with the rapid shear tests, clay with massive cryostructure showed lower strength than clay with stratified cryostructure. Vialov et al. (1962) state the opposite, in which soils with massive texture show the highest strengths. Under a given stress (i.e constant stress tests), clay with massive cryostructure failed much quicker than clay with stratified cryostructure when brought to failure. In addition, clay with massive cryostructure failed under lower loads. Under step loading, with tests running from 2 to 3 months, the same general relationship for shear strength was found in which strength of $\sigma_{ground\ ice} > \sigma_{stratified} > \sigma_{massive}$. These experiments were performed at temperatures from -0.4°C to -3°C.

Figure 2.1 shows steady state creep patterns for tests conducted by Pekarksaya (1965). The term steady state was used by Pekarskaya (1965). In this case, steady state indicates that the deformation rate or strain rate remains constant. The stress subscripts on the x-axis have physical meanings. The stress, σ_k, correlates to the long term strength limit. Below this stress value, the rate of deformation is essentially zero. The stress, σ_r, is the transition into disrupted flow (i.e. linear dependency between flow and stress no longer maintained). The subscripts 1, 2, and 3 refer to the specific curves that the stress values correspond to. Ice is assumed to have a σ_k value of zero (i.e. no long term strength). Soils with massive cryostructure have a higher σ_k stress (or larger long term strength) value than ground ice or soils with stratified cryostructure. Alternatively, soils with massive cryostructure have lower σ_r stress values than ground ice or soils with stratified cryostructure. This indicates that soils with massive cryostructure proceed to disrupted flow at a lower stress value.

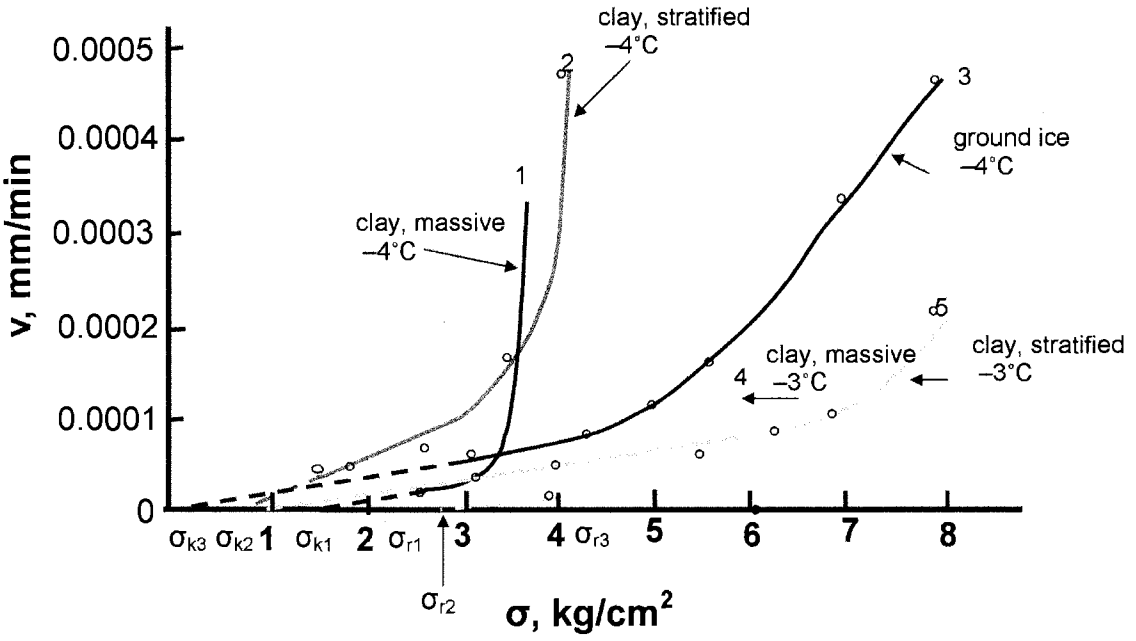

Figure 2.1: Creep rate vs. stress for clay with different soil cryostructures and temperature. (Figure taken from Pekarskaya, 1965, Figure 31). *See text for definition of σ_k and σ_r. Note: 1 kg/cm^2 is equal to 98 kPa.

The creep patterns for clay with massive and stratified cryostructure and ground ice are shown in Figure 2.1. The nature of the creep curves depends on the different soil cryostructures. For clay with massive cryostructure, the initial creep rates are low until a certain stress level is achieved, after which the creep rates increase rapidly. Pekarskaya (1965) uses the term "flow with avalanche collapse." This suggests that once a threshold is reached, failure occurs rapidly with disruption of the soil's structure. Clay with stratified cryostructure shows a gradual transition in creep rates with an increase in stress. Ground ice shows an even more gradual transition in creep rates with an increase in stress as compared to clay with massive or stratified cryostructure. Generally, the amount of ice increases from clay with massive cryostructure, to clay with stratified cryostructure, to ground ice. The nature of the creep curves, therefore, suggests that ice has the ability to "heal" after the structure is disrupted. The ability of clay with massive cryostructure to heal is low; therefore, it fails quickly once a threshold stress level is reached. Alternatively, ground ice has the ability to "heal or restore bonds" after the bonds are disrupted. Clay with stratified cryostructure falls in between.

The creep curves in Figure 2.1 generally have points of intersection with each other for a given temperature. The points of intersection usually occur at low creep velocities and stresses whose values depend on temperature and soil conditions. Comparing the creep curves at -4°C from Figure 2.1, the following observations are made. For stresses less than the intersection of ground ice and clay with stratified cryostructure, ground ice shows higher creep rates. For stress greater than the intersection, clay with stratified cryostructure show higher creep rates. In turn, for stresses less than the intersection of clay with stratified cryostructure and clay with massive cryostructure, clay with stratified cryostructure exhibits higher creep rates than clay with massive cryostructure. For stress greater than the intersection, clay with massive cryostructure show higher creep rates. Based on the above observations, a general trend is seen where an increase in ice content results in a decrease in the flow resistance of frozen soil at stress values less than the point of intersection. Above this stress, increased ice content results in higher resistance to flow (creep). Using this concept, Pekarskaya (1965) made the assumption that the relaxation curve (or long term strength curve) will have a point of intersection as well. All these observations support the idea that ice relaxes at a much slower rate than frozen soil. Pekarskaya's (1965) experiments were not able to show this intersecting of relaxation curves directly despite experiments lasting 2 to 3 months. However, the concept has validity.

In summary, Pekarskaya's (1965) work shows that the creep behavior (long acting stress) and rapid shear behavior are affected by the "texture" or soil cryostructure. Clay with massive

cryostructure showed the lowest strengths. Ground ice showed the highest strengths. Clay with stratified cryostructure was intermediate between the two. The creep "flow patterns" show smoother, more gradual changes in creep rates with increasing ice content. Clay with massive cryostructure fails quickly once a threshold strength or stress is reached. At low stresses, an increase in the ice content results in increased creep rates. At higher stresses, an increase in the ice content results in lower creep rates. This relates to the slower rate of relaxation of ice and its ability to restore broken bonds more effectively. The stress values at which this occurs depends on temperature and soil conditions.

Vialov (1959) studied the influence of ice inclusions on the bearing capacity of frozen soils by applying loads to frozen soil blocks through the use of cylindrical punches. The soil was undisturbed varved clay with stratified (layered) cryostructure. It was found that when ice lenses are close to the base of the punch, soil deformation and the rate of deformation increase under the action of a long term load. Soil without ice lenses showed lower deformation rates for stresses greater than 392 kPa. For stresses less than 392 kPa, the rate of deformation was similar between soil with and without ice lenses. As the punch was loaded, a densified kernel developed under the punch. As the stress increased, the densified kernel penetrated into and in most cases, through the ice lens. As the thickness of the ice lens increased, so did the deformation. Once the ice lens was completely penetrated, the rate and amount of deformation decreased. The influence of ice lenses decreased as the distance of the ice lenses from the base of the punch increased. The soil layer between the punch and the ice lens acts as a buffer. The result is plastic deformation (bending) of the ice lens rather than penetration of the ice lens. This results in much lower values of total deformation and deformation rates. It was also found that the presence of thin isolated ice lenses, even in large amounts, resulted in smaller deformations than the deformation which occurs with presence of one larger ice lens. Isolated ice lenses also showed less deformation than continuous horizontal ice lenses. It should be noted that these experiments were performed in undisturbed dense varved clay with ice lenses. The varved clay consists of alternating mineral layers of clay and silt with a high degree of consolidation of the mineral layers. So the question that should be asked is would the same effect be seen with an unconsolidated, ice-rich soil?

Uniaxial compressive experiments where performed on artificially prepared soils with volumetric ice contents between 40 and 80% by Vyalov et al. (1980). Two soil cryostructures were recreated. The first is "basal texture" which is characterized by uniformly distributed ice and mineral aggregates. This correlates to massive cryostructure. The second is "stratified texture"

which is characterized by alternating layers of soil and ice layers of varying thicknesses. This correlates to stratified or layered cryostructure. Supes, silty soils that contain sand and clay were used. Strength values were found for soils with different ice contents, temperatures, and cryostructure (i.e. massive vs. stratified). The two creep strength values used are called attenuated creep strength, R_a, and linear creep strength, R_L. R_a is the stress value below which deformation attenuates or does not enter a secondary or tertiary creep mode (i.e. similar to σ_k in Fig. 2.1). Deformation rates tend towards zero and total deformation tends towards a constant value. R_L is the stress value below which strain rate is linearly proportional to stress (i.e. n equal to 1 in Eq. 2.1). If the stress is above R_L, the strain rate is no longer linearly proportional to stress thus the n value is greater than one in Equation 2.1 (i.e similar to in σ_r Fig. 2.1).

$$\dot{\gamma} = \chi(\tau - \tau_s)^n \qquad \text{Eq. 2.1}$$

Where $\dot{\gamma}$ is the shear strain rate, χ is a constant related to the viscosity of the specimen with units of $(1/P^n \cdot T)$, where P has units of pressure and T has units of temperature, τ is the shear stress applied to the specimen, and τ_s is the shear stress below which the shear strain rate is zero or negligibly small so that it can be essentially ignored.

For silty soils (supes) with massive cryostructure, R_a and R_L increase with decreasing temperature and decrease with increasing ice content. For silty soils with stratified cryostructure, volumetric ice contents of 60%, and ice bands less than 8 mm, attenuated deformation exists. In soils with ice bands greater than 8 mm, no attenuated deformation exists (i.e. $R_a = 0$). The R_a and R_L values for silty soils with massive cryostructure are similar to silty soils with stratified cryostructure containing ice bands less than the 8 mm in thickness. With ice band thicknesses greater than 8 mm, R_a values tend towards zero and R_L values are lower than for silty soils with massive cryostructure for given ice content. Data is presented relating strain rate and stress to ice band thickness. It was determined that for ice bands less than 4 to 8 mm thick, damped creep is possible. Above an ice band thickness of 20 mm, the creep rate increases slowly and approaches a constant value at about an ice band thickness of 50 mm. With ice band thicknesses between 8 and 20 mm, the rate increases quickly. The χ value in Equation 2.1 for n equal to one decreases with decreasing temperature and increases with ice band thickness. This indicates that the soil more readily deforms with warmer temperatures and increasing ice band thickness.

The information above presents the available Russian literature that was translated to English, which describe the creep and strength properties of frozen soils as related to varying soil

cryostructure. Below is a summary of the findings. The work by Pekarskaya (1965) is the most detailed in relation to various soil cryostructures. The works by Vialov (1959) and Vyalov et al. (1980) tend to support the findings by Pekarskaya (1965). Figure 2.1 summarizes some of the most important concepts. At high stresses, the flow rate or creep rate of ice tends be lower than for frozen soils. For low stresses it was shown that soil cryostructures with higher ice contents tended to creep at higher rates than soil cryostructures containing less ice. Soils with massive cryostructure tend to have higher long term strengths or attenuated creep strengths. Increased ice contents in the soil result in lower attenuated creep strengths. In addition, increased ice contents result in a more prolonged transition of flow rates with increasing stresses. It was also found that the orientation of ice lenses in relation to the applied stress has an important influence on the resulting deformation behavior. The data by Vialov (1959) shows that ice lenses next to the base of a punch tend to increase deformation and deformation rates. With ice lenses close to the base of a punch, a dense soil wedge beneath the punch penetrates though the ice lenses. The lack of ice lenses increases the penetration resistance of the dense soil wedge. However, the soil component of the varved clay used in the study was very dense, leading to the development of a dense soil wedge beneath the punch. An unconsolidated soil may not show the same effects as readily due to changes in the nature of the soil wedge beneath the punch. It is also shown that for an applied pressure, water/moisture migration occurs to regions of lower stress.

Savigny and Morgenstern (1986a) discuss the apparent effect of cryostructure on the resulting creep and failure behavior of ice-rich glaciolacustrine clay. The soil typically contained reticulate or stratified ice inclusions from sub millimeter to 30 mm in thickness. The frozen bulk densities typically ranged from 1.78 g/cm^3 to 2.06 g/cm^3. Cores from the same boreholes (McRoberts, 1988) yielded gravimetric water contents ranging from 20-30%. The densely compacted varved clays reported earlier (Vialov, 1959), also glaciolacustrine in origin, had typical bulk densities of 1.80 g/cm^3. This would suggest that the mineral components of the soils used by Savigny and Morgenstern (1986a) are similar to the varved clays used by Vialov (1959) and are potentially well compacted. However, the authors did not discuss the degree of sediment compaction. Test temperatures ranged from -1.0°C to -1.4°C. The soils were tested at high confining pressures of 400 kPa. Deviatoric stresses (σ_1-σ_3) ranged from 35 to 196 kPa. The soils were described as containing reticulate cryostructure with prominent ice lenses (8-25mm thick) oriented from 0° to 40° from the long core axis (i.e. from the major principal stress axis). This corresponds closely to the planes of maximum shear that develop during compression. Failure along the ice lenses was the primary mode of displacement. Secondary movement occurred along the smaller ice lenses. The more interconnected or well developed the ice lenses along the planes of shear, the more

likely quick failure and high strain rates were observed. Soils with reticulate cryostructure which contained small ice lenses (described as secondary) up to 3 mm thick, tended to show slower creep rates and a longer time to failure. The mode of deformation also occurred along ice lenses. A sample with stratified cryostructure, consisting of ice lenses up to 4 mm thick with the ice lenses oriented approximately horizontal (i.e. perpendicular to long axis of core), underwent large amount of strains in the first 200 hrs, but generally showed lower creep rates than soil samples with diagonally oriented ice lenses. The sample showed the formation of vertical ice lenses due to migration and redistribution of moisture into tensile cracks resulting from shear displacement along ice lenses. The final sample contained an irregular reticulate network of ice lenses with ice reaching 35% by volume. Savigny and Morgenstern (1986a) describe the sample as containing segregated ground ice. The specimen exhibited a near constant creep rate from almost the beginning of the test and failed within 40 hours. As with the other cryostructures, it was observed that much of the displacement in the sample occurred along ice lenses even though a well defined failure plane did not emerge. It was noticed that for samples that underwent longer periods of deformation (tests with durations greater than 2 months), crystals of pure ice formed on the outside of the samples. The crystals tended to form on the upper and lower ends of the sample. This supports that moisture had migrated from within the sample to the outside free surface as well as into tension cracks that had formed. The formation of ice crystals on the outside free surface was also observed by Vialov (1959).

Savigny and Morgenstern (1986a) report on three samples that were tested without confining pressures. Failure of these samples did not occur even though the deviatoric stresses were of the same range as for samples that were tested with confining pressures. Savigny and Morgenstern (1986a) believe that failure of samples in their laboratory tests was caused by excess pore pressure in the unfrozen water due to the higher confining pressures (400 kPa). As a result, confining pressure actually helped increase the susceptibility of the sample failing along the ice lenses. Roggensack (1977) for similar silty clay noticed a decrease in the strain rate when the confining pressure was reduced from 550 kPa to 0 kPa. The glaciolacustrine varved clay reported in Vialov (1959), at a temperature of -1.4°C had a total unfrozen water content of 59%. By rough association, it can be assumed that a significant amount of unfrozen water is likely found in these soils (the unfrozen water contents not given). Therefore, the explanation of increasing pore pressures seems plausible. The high unfrozen water contents also support the observation that moisture had migrated to regions of low stress (cracks and free surfaces). The observation that movement develops primarily along the ice lens-soil contacts supports the observation made by Pekarskaya (1965).

To summarize the observations, it was found that ice lenses and the orientation of the ice lenses have a large influence on the deformation behavior of these glaciolacustrine soils. Soils with well developed ice lenses oriented in the direction of maximum shear, tended to fail quickly along the ice lenses with little displacement in other parts of the specimen. Samples with thinner, less interconnected ice lenses tended to show slower strain rates. In addition, tension cracks commonly formed due to shear displacement, resulting in the formation of additional ice lenses in the tension cracks. Slope displacements measured from borehole inclinometers installed in the same boreholes from which the above samples were taken from are reported by Savigny and Morgenstern (1986b). It was found that regions between large ice lenses showed greater displacement. A question that should be asked is if a less dense soil was used would the same effect be seen?

2.3 Background for Creep Determination

The purpose of this section is to present a brief outline on the general characteristics of creep for understanding of the flow laws that will be discussed in the following sections. Creep is the time dependent plastic deformation of a material. The creep of frozen soils is stress, strain rate, and temperature dependent. The two most common creep tests are constant stress creep (CSC) and constant strain rate (CSR) tests. In a CSC test, a stress is applied to a sample and held constant. The pattern of strain vs. time is then recorded. Figure 2.2 shows the most general creep characteristic for a CSC test. The three accepted stages of a creep curves include primary, secondary, and tertiary. When a load is applied to a soil, the sample may develop an initial elastic or instantaneous strain designated by ε_o. The creep process then proceeds into a primary creep stage. Primary creep is characterized by a decreasing strain rate vs. time. As seen in Figure 2.2 (c), soils may not proceed past the primary creep stage. This is generally seen for ice poor soils where frictional affects significantly influence the deformation process. The second stage is called the secondary creep stage which is characterized by a region where the strain rate remains mostly constant (Fig. 2.2 (b)). For ice and ice-rich soils, the secondary creep stage may dominate. The third stage is the tertiary creep stage in which the strain rate increases with time. Tertiary creep eventually leads to failure of the sample. For high constant stresses, the creep curves can proceed directly from primary into tertiary creep. For low stresses, secondary or tertiary creep stages may not be seen.

In the following sections, flow laws relating the minimum strain rate vs. stress are presented for ice, undisturbed permafrost soils, and remolded frozen soils. The use of minimum strain rate vs. stress is widely adopted for determination of a constant rate flow law for ice and frozen soils

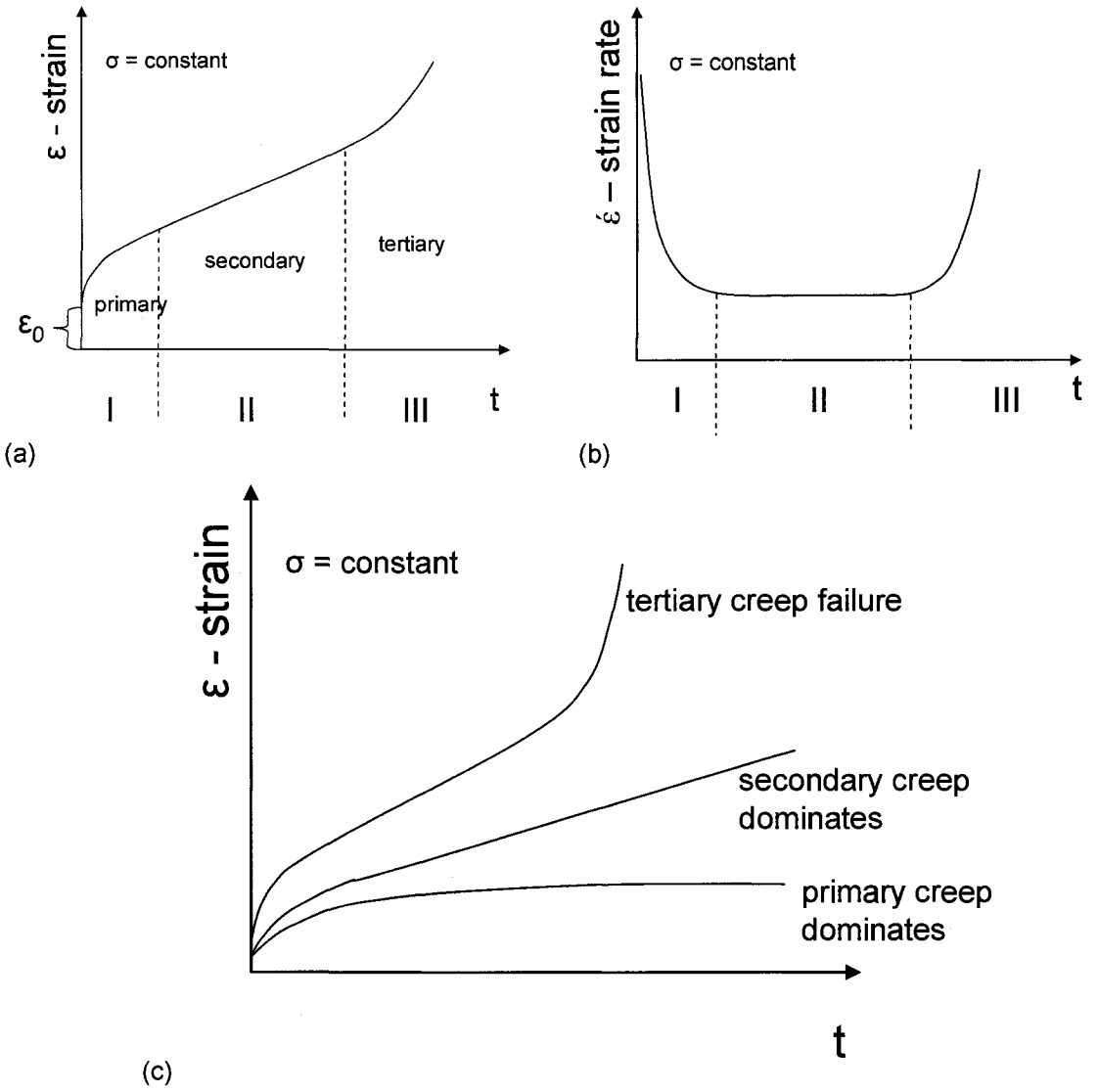

Figure 2.2. Creep curves for constant stress creep (CSC) tests. (a) shows the three phases of a creep curve, (b) shows the three phases on strain rate vs. time plot, and (c) shows the main types of creep responses for CSC tests.

(Arenson and Springman, 2005a,b; Glen, 1955; Andersland and Ladanyi, 1994; McRoberts, 1988; Nixon and Lem, 1984; Nixon and McRoberts, 1976; Savigny and Morgenstern, 1986a; Sego and Morgenstern, 1983). In a primary creep condition, the material undergoes strain hardening and eventually cessation of plastic deformation if the internal physical processes do not lead to a flow condition. For a secondary creep condition to occur, the deformation processes within the material must be favorable for relief of the internal stresses and thus flow of the material. Therefore, physically, the minimum strain rate represents the condition where the

plastic flow of material is in balance with the processes which relieve the internal stresses. The minimum strain rate condition is commonly referred to as the secondary creep condition or a steady-state condition. In this work, minimum strain rates will be used. Figure 2.3 illustrates how the minimum strain rate and stress values are determined for insertion into analysis of the flow laws. Figure 2.3 (a) shows the test data for a CSC test on a strain rate vs. time plot. Assuming that a sample enters into the secondary and tertiary creep modes, a plot of a strain rate vs. time should yield a point or zone that corresponds to the minimum strain rate value. This is designated as $\dot{\varepsilon}_{min}$ on the plot. Therefore, for the flow law, $\dot{\varepsilon}_{min}$ corresponds to the constant stress condition for which the test was conducted. Andersland and Ladanyi (1994) state that "creep strength consists of finding a relationship among the creep strength, time to failure, secondary or minimum creep rate, failure strain, and temperature." Therefore, the long term strength can be related to stress, time to minimum strain rate (t_{min} in Figure 2.3 (a)), and minimum strain rate. The other common testing method is a constant strain rate (CSR) test. In this case a constant strain rate is applied to the sample in lieu of a constant stress. Figure 2.3 (b) shows typical responses of a CSR test on a stress vs. strain plot. For a constant strain rate, typically a peak stress value can be determined from the curve. This correlates to σ_{max} in Figure 2.3 (b). In this case, σ_{max} corresponds to the desired stress for the strain rate condition of the test. For ice and frozen soils, it has been shown that ratio of $\sigma/\dot{\varepsilon}_{min}$ from a CSC test is approximately equal to $\sigma_{max}/\dot{\varepsilon}$ from a CSR test (Ladanyi, 1981; Hooke et al., 1980; Sego and Morgenstern, 1983; Arenson and Springman, 2005a,b). From these values, strain rate vs. stress flow law relationships are determined.

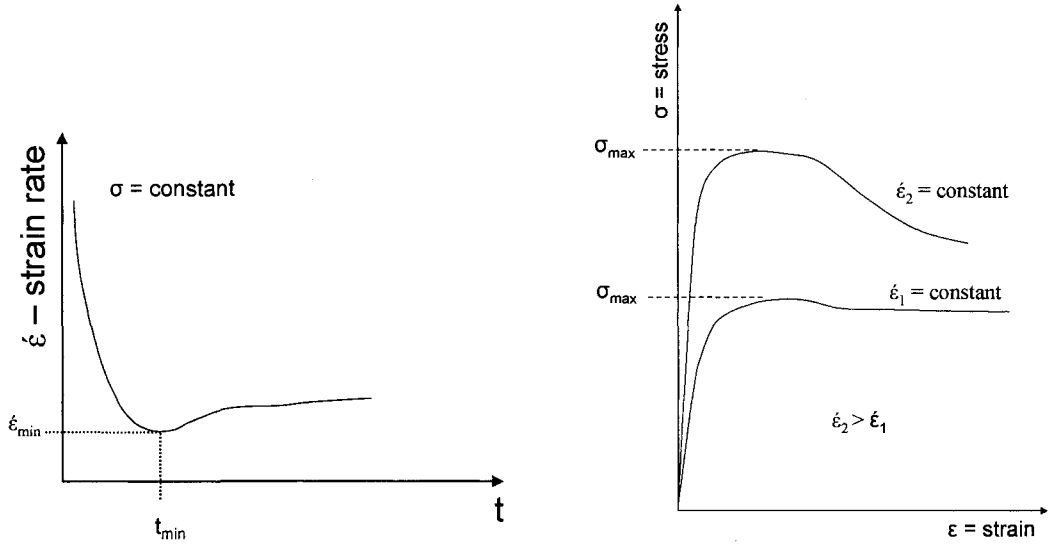

Figure 2.3. Determination of minimum strain rate for flow law with (a) showing results from CSC tests and (b) showing results from CSR test.

2.4 Creep of Ice

The most common flow law for ice relating the minimum strain rate vs. stress was proposed by Glen (1955) and is shown in Equation 2.2.

$$\dot{\varepsilon} = A\sigma^n \qquad \text{Eq. 2.2}$$

Where $\dot{\varepsilon}$ is the strain rate, A is a constant with units of time^{-1}stress^{-n}, and σ is the applied stress. Variations of the power law exist, but the form in Equation 2.2 is still the most common.

Sego and Morgenstern (1983) conducted tests on artificially prepared, polycrystalline ice at low stresses and temperatures from -0.7°C to -1.5°C. Using composite data from uniaxial constant stress and uniaxial constant strain rate tests, they defined that n=3.14 over a stress range of 100-1200 kPa. The relationship for ice is expressed in Equation 2.3.

$$\dot{\varepsilon} = 3.564x10^{-11}\sigma^{3.14} \qquad \text{Eq.2.3}$$

Where A=hr^{-1}kPa^{-n} and σ is stress in kPa. A and n are referenced to Equation 2.2. By normalizing data from Glen (1955), Barnes et al. (1971), and Steinemann (1958) along with their experimental data (Sego and Morgenstern, 1983) to a GSR of 0.03 (grain size ratio=$D_{\text{ice crystal diameter}}/D_{\text{sample diameter}}$), Sego and Morgenstern (1983) came up with a relationship for ice at -2.0°C as shown by Equation 2.4. Equations 2.5 and 2.6 show the pre and post peak failure conditions with failure strain taken as 1%.

$$\dot{\varepsilon} = 2.9630x10^{-10}\sigma^{3.00} \qquad \text{Eq. 2.4}$$

$$\dot{\varepsilon} = 3.6352x10^{-9}\sigma^{2.47}, \text{ pre peak (0-1\% strain)} \qquad \text{Eq. 2.5}$$

$$\dot{\varepsilon} = 1.5353x10^{-10}\sigma^{3.18}, \text{ post peak (10\% strain)} \qquad \text{Eq. 2.6}$$

Where A=hr^{-1}kPa^{-n} and σ is stress in kPa. It was determined that the flow law for ice between 0 and 1% strain is different than for higher strains, where a second flow law exists. This relates to post peak changes in ice crystal structure, reorientations, and recrystallization. However, n=3 is generally assumed for ice.

A review of creep data for ice by Morgenstern et al. (1980) show the creep of ice could be described by a flow law of the Glen type (1955) and is shown by Equation 2.7. The flow law is modified to von Mises equivalent stress and strain rate (Johnston and Ladanyi, 1972).

$$\dot{\varepsilon}_e = A\sigma_e^{\ n} \qquad \text{Eq 2.7}$$

Where A=time^{-1}stress^{-n}, $\dot{\varepsilon}_e$ is the von Mises equivalent strain rate, and σ_e is the von Mises equivalent stress. The parameters in Equation 2.7 as a function of temperature for ice are shown in Table 2.1.

Table 2.1: Flow law coefficients in Eq. 2.7 for ice (Morgenstern et al., 1980).

Temperature (°C)	n	A (hr^{-1} kPa^{-n})
-1	3.0	$5.1370x10^{-12}$
-2	3.0	$2.2831x10^{-12}$
-5	3.0	$1.1416x10^{-13}$
-10	3.0	$6.3927x10^{-13}$

Nixon and McRoberts (1976) reviewed available creep data for ice and defined a bilinear flow law presented in Equation 2.8.

$$\dot{\varepsilon}_z = A_1\sigma_z^{\ n_1} + A_2\sigma_z^{\ n_2} \qquad \text{Eq. 2.8}$$

Where A=time^{-1}stress^{-n}, $\dot{\varepsilon}_z$ is the uniaxial strain rate, and σ_z is uniaxial stress. Table 2.2 presents the various coefficients for Equation 2.8.

Table 2.2. Flow law coefficients A_1,A_2,n_1,n_2 for Eq. 2.8.

Temperature (°C)	A_1 (hr^{-1} kPa^{-n1})	n_1	A_2 (hr^{-1} kPa^{-n2})	n_2
0	$1.6553x10^{-7}$	1.34	$1.3739x10^{-11}$	4
-2	$8.2763x10^{-9}$	1.72	$2.0525x10^{-12}$	4
-5	$1.9863x10^{-9}$	1.92	$5.7934x10^{-13}$	4
-11	$3.3105x10^{-10}$	2.12	$6.6210x10^{-14}$	4

As with all empirical data, variations exist from test program to test program. The flow law coefficients described earlier are best fit power law approximations of the minimum strain rates vs. stress. Portions of the data presented may be influenced by primary creep, which would result in high estimates of the creep rates. Generally, n equal to 3 was used for ice with the A coefficient (relates to viscosity) influenced by changes in temperature. Based on the data presented in Table 2.2 the creep exponent n changes below approximately 100 kPa. Mellor and Testa (1969) presented data for tests at 43 kPa and -2.06°C where the creep exponent was n equal to 1.8. Above 100 kPa, the creep exponent n appears to increase. Goldsby and Kohlstedt (2001) describe variations in the creep exponent in response to different creep mechanisms. Dislocation creep is characterized by a stress exponent of 4. Grain boundary sliding (GBS) is

characterized by a stress exponent of 1.8. Slip along the basal planes is characterized by a stress exponent of 2.4. Very low stress and strain rate conditions are characterized by diffusion creep with a stress exponent of 1. The stress range typical of most testing programs (0.1 MPa to 1 MPa) is thought to represent a transition zone from dislocation creep to creep caused by grain boundary sliding.

2.5 Literature on Undisturbed Permafrost

Little data is available on the creep properties of ice-rich undisturbed permafrost soils. The data available will be presented below, excluding data for Fairbanks silt, which will be the focus of a following section (the data presented in section 2.2 will not be discussed here). McRoberts et al. (1978) report results of uniaxial compression tests for ice-rich silt sampled from the Canadian Arctic Gas Study Limited Test Site at Norman Wells, NWT, Canada. This study is of special interest, as it is the only one that reports data for undisturbed silts with high gravimetric water contents, typically in the range from 70% to 130%. The samples were taken by horizontally coring into silt with finely stratified cryostructure. This resulted in soil samples containing vertically alternating ice-soil layers (i.e. ice lenses parallel to long axis of core). Test temperatures ranged from -1°C to -3°C and stress conditions ranged from 70 to 300 kPa. In the results, there is no comment on the effects of cryostructure. It was concluded by McRoberts et al. (1978) that in most of the tests steady state creep rates (i.e. minimum strain rates) were reached. Based on assumed secondary strain rates, it was concluded that at low stresses, the ice-rich clayey silt creeps at a slower rate than ice. At higher stresses, creep rates for the frozen clayey silt are similar or faster than for ice. This agrees well with the data from Pekarskaya (1965), Figure 2.1. A bilinear flow law is defined which is predicted to be an upper bound relationship (i.e. all measured creep rates for soils are lower than those predicted by the relationship) and is expressed by Equation 2.9 and 2.10.

$$\dot{\varepsilon} = \frac{A\sigma^n}{(1-T)^m} \qquad \text{Eq. 2.9}$$

$$\dot{\varepsilon} = \frac{1.6x10^{-7}\sigma^{3.0}}{(1-T)^{1.8}} + \frac{1.5x10^{-14}\sigma^{6.0}}{(1-T)^{1.8}} \qquad \text{Eq. 2.10}$$

The strain rate, $\dot{\varepsilon}$, has units of years^{-1}, deviatoric stress, σ, has units of kPa, and temperature, T, has units of °C. The first term in Equation 2.10 dominates for stresses up to 100-140 kPa. The second term dominates for stresses above 300-400 kPa.

McRoberts (1988) presents a larger data set for secondary creep interpretations of ice-rich permafrost for temperatures from -0.8°C to -4.0°C. The soils were sampled in the Mackenzie River Valley between Fort Simpson and Norman Wells, NWT, Canada. The soils consists of a B-series silt reported in McRoberts et al. (1978), an E-series which have gravimetric water contents ranging from 26-254%, a G-series originating from the same boreholes as Savigny and Morgenstern (1986a), and a P-series soils which are fibrous woody peat with gravimeteric water contents of 181-1988%. The B-series samples contain finely banded, stratified of alternating ice-soil layers (ice lenses 5-20 mm thick). The E-series samples contained ice lenses up to 80 mm thick oriented at various angles to the long axis of the cores. The P-series have readily visible ice. As a result of the larger data set, Equation 2.10 was slightly modified to Equation 2.11.

$$\dot{\varepsilon} = \frac{4.0x10^{-7}\sigma^{3.0}}{(1-T)^{2.0}} + \frac{2.16x10^{-14}\sigma^{6.0}}{(1-T)^{2.0}} \qquad \text{Eq. 2.11}$$

The stress exponent n equal to 6 in the second term is largely influenced by samples that failed or entered the tertiary creep stage. Savigny and Morgenstern (1986a) argue against the use of samples in which failure has occurred since the creep conditions no longer represent secondary creep. The temperature exponent m (refer to Eq. 2.9) was determined to be equal to 2 by Nixon (1978). Equation 2.11 is a best fit upper bound (i.e. largest strain rates for a given stress) for all of the data at a reference temperature of -1.0°C. Equations 2.10 and 2.11 were further reduced for stress levels below 400 kPa (Equations 2.12 and 2.13).

$$\dot{\varepsilon} = \frac{6.1x10^{-8}\sigma^{3.0}}{(1-T)^{1.0}}, \text{ for T<-2.0}^{\circ}C \qquad \text{Eq 2.12}$$

$$\dot{\varepsilon} = \frac{4.0x10^{-7}\sigma^{3.0}}{(1-T)^{2.0}}, \text{ for -0.8}^{\circ}C < \text{T<-1.5}^{\circ}C \qquad \text{Eq. 2.13}$$

Equations 2.12 and 2.13 suggest that at stresses commonly seen in slopes and foundations, a value of n equal to 3 appears reasonable. The data shows considerable scatter, with creep rates for any given stress level varying by as much as two orders of magnitude. In the discussion, it was acknowledged that "it is possible that ice structure and the favorable orientations of ice lenses to planes of higher shear stress may play a role" (McRoberts, 1988). Soil index properties and grain size analysis yielded no singular trends. Descriptions of the deformation patterns (physical) were not included. So the role of cryostructure is difficult to conjecture from the results.

2.6 Literature on Fairbanks Silt

The soils used in the testing program of this study are composed primarily of Fairbanks silt from the CRREL permafrost tunnel, Fox, Alaska. Therefore, the testing data available for Fairbanks silt was of special interest as it provides important comparative data. A large amount of data for remolded Fairbanks silt is available in the published literature. Data for remolded Fairbanks silt is presented in section 2.6.1. Most of the data for undisturbed Fairbanks silt is derived from in-situ testing techniques conducted in the CRREL permafrost tunnel. Data for undisturbed Fairbanks silt is presented in section 2.6.2.

2.6.1 Creep of Remolded Fairbanks Silt

Two main sources of laboratory results on the strength of remolded Fairbanks silt are from studies by Yuanlin and Carbee (1983; 1987a; 1987b) and Sayles and Carbee (1981). The silt used in these studies was obtained from the CRREL permafrost tunnel. A summary of the results from these research programs will be summarized below as they are important comparisons for the results presented in this thesis.

Yuanlin and Carbee (1983; 1987a) present the results of uniaxial compressive data for remolded Fairbanks silt. Three dry densities of 1.08 g/cm^3, 1.20 g/cm^3, and 1.40 g/cm^3 were used and are referred to as low, medium, and high densities, respectively. The average gravimetric water contents were 50%, 43%, and 31% for low, medium, and high densities. The bulk unit densities were 1.62 g/cm^3, 1.72 g/cm^3, and 1.83 g/cm^3 for low, medium, and high densities.

The bulk of the data presented by Yuanlin and Carbee (1987a) is for medium density silt with test temperatures ranging from -0.5°C to -10°C. Creep failure is defined for a constant stress as the minimum strain rate on a log $\dot{\varepsilon}$ vs. log t plot (see Figure 2.3). The minimum strain rate was then related to stress. Logarithmic plots of minimum strain rate vs. stress show a change in slope at a strain rate of approximately 1x10^{-6} s^{-1} (0.0036 hr^{-1}) for all temperature ranges. This is described as a critical creep rate. Creep rates above this value are considered short-term creep and below, long-term creep. The minimum creep rates as function of stress are expressed by Equations 2.14, 2.15, and 2.16 in a power law relationship similar to Glen (1955).

$$\dot{\varepsilon}_m = \dot{\varepsilon}_c \left(\frac{\sigma}{\sigma_c} \right)^n \qquad \text{Eq 2.14}$$

$$n = 5.59 \left(\frac{T}{T_0} \right)^{0.223} \text{, for } \dot{\varepsilon}_c > 1\text{x}10^{-6}\ \text{s}^{-1} \qquad \text{Eq. 2.15}$$

$$n = 27.36\left(\frac{T}{T_0}\right)^{0.223}, \text{ for } \dot{\varepsilon}_c < 1\text{x}10^{-6}\ \text{s}^{-1} \qquad \text{Eq. 2.16}$$

Note: equations valid for medium density silt.

Where, $\dot{\varepsilon}_m$ is minimum creep rate (s^{-1}), $\dot{\varepsilon}_c$ is the critical creep rate (change of slope) equal to $1x10^{-6}$ s^{-1}, σ is applied stress (kg/cm^2), σ_c is stress at which $\dot{\varepsilon}_c$ occurs (kg/cm^2), n is stress creep exponent, T is temperature in °C, T_0 is a reference temperature taken as -1°C. The n values below the critical strain rate are much larger than above. The n values were found to be significantly higher than 3, which is accepted for ice (and subsequently ice-rich soils).

It was observed for medium and high density silts that the minimum strain rates rapidly decrease for stresses which result in minimum strain rates less than $1x10^{-6}$ s^{-1}. This is seen by Equations 2.15 and 2.16 and the resulting changes in the power exponent n. Therefore, the minimum strain rate is increasingly sensitive to changing stress condition for strain rates less than $1x10^{-6}$ s^{-1} and by association the minimum strain rate is sensitive to changes in stress for low stress states. The classification of a stress as low is somewhat arbitrary and depends on temperature, but for -2°C this effect is seen for stresses below 784 kPa for medium density silts. Alternatively, for low density silt, it was observed that the minimum strain rates did not exhibit a sudden drop at low stresses and thus exhibited no change in the stress exponent, n. It was found that at -2°C, a straight line fits the data on log $\dot{\varepsilon}_m$ vs. log σ plot. The flow law for low density silt is shown in Equation 2.17.

$$\dot{\varepsilon}_m = c_1\left(\frac{\sigma}{\sigma_1}\right)^n, \qquad \text{Eq. 2.17}$$

Note: equation valid for low density silt.

Where $\dot{\varepsilon}_m$ is minimum creep rate (s^{-1}), c_1 is minimum creep rate when $\sigma=\sigma_1$, σ is applied stress (kg/cm^2), σ_1= 1 kg/cm^2. For the low density silt tested c_1= $1.68x10^{-13}$ s^{-1} ($6.048x10^{-10}$ hr^{-1}) and n=6.90 for a temperature of -2°C.

Short-term creep and long-term creep are described by two different mechanisms. Short term creep was described by Yuanlin and Carbee (1987a) and termed glide creep. It occurs when a threshold stress level is exceeded, the frozen bond between particles is broken and the particles and fractured ice crystals slide against each other. Therefore, frictional resistance dominates the

creep process. Once this threshold is overcome, failure eventually occurs. The second mechanism is described for long-term creep in which the creep of ice crystal occurs. The term used for this mechanism by Yuanlin and Carbee (1987a) is dislocation creep. It is assumed that for samples with low densities and increased ice contents, the ice matrix controls the creep behavior. It is speculated that this is the reason that low density silts do not experience such an abrupt drop in minimum strain rate once the critical strain rate or critical stress is reached. Based on this mechanistic explanation, the critical stress (σ_c) is the threshold at which the bonding forces between particles and ice is overcome. Recall that the critical stress (σ_c) corresponds to the change in slope of the log $\dot{\varepsilon}_m$ vs. log σ plot at a strain rate of $1x10^{-6}$ s^{-1}.

Yuanlin and Carbee (1987a) supply an expression for the long term strength for medium density silt, which is shown in Equation 2.18.

$$\sigma_{lt} = 3.49\left(\frac{T}{T_o}\right)^{0.87} \qquad \text{Eq. 2.18}$$

Where σ_{lt} is the long term strength for 100 years in kg/cm^2, T is the temperature in °C, and T_o is -1°C. The long term strength was compared by Yuanlin and Carbee (1987a) to literature sources for undisturbed frozen soils. It was shown that the long term strength is significantly less for the ice-rich undisturbed silt than for the remolded silts.

It was found that the failure strain was a function of the dry density of the silt. Failure strain is defined as the strain correlating to the point from which the minimum strain rate was determined. The low density silt had lower failure strains than the high density silts. Low density silt tended to fail at 1% strain for all minimum strain rates. Medium density silts failed on average at 8 to 9% strain and high density silts failed on average between 17 to 18% strain. Polycrystalline ice tends to fail at 1% strain (Mellor and Cole, 1982).

A companion paper to Yuanlin and Carbee (1987a), presents the results of remolded Fairbanks silt under uniaxial tension (Yuanlin and Carbee, 1987b). Under constant strain rate conditions, the peak strengths for uniaxial tension compared favorably to uniaxial compression for strain rates up to $1x10^{-2}$ s^{-1}, upon which they diverge significantly. For low strain rate conditions, the failure strain for low, medium, and high densities occurred at approximately 1% strain. This suggests that under low strain rates, the ice matrix begins to control the behavior. For higher strain rates, the more ice in the soil (i.e. higher water content, lower density), the more brittle the behavior. For example, at -2°C, brittle behavior was seen at a strain rate of $1x10^{-2}$ s^{-1} for medium

density silts and at a strain rate of $5x10^{-4}$ s^{-1} for low density silts. Alternatively, peak tensile strength increases with increasing ice contents.

Rein (1985) used data by Yuanlin and Carbee (1983, 1987a) to compare CSR (constant strain rate) tests and CSC (constant stress creep) tests. They found that at high stresses, good correspondence is seen between CSR and CSC. At low stresses, CSR tests over predict minimum strain rates as determined from CSC test.

Sayles and Carbee (1981) present data on remolded, saturated Fairbanks silt. Dry densities ranged from 0.993 g/cm^3 to 1.490 g/cm^3 with water contents from 28 to 58%. A strain rate of $5x10^{-3}$ s^{-1} was used in all tests at a test temperature of -1.67°C. This would correspond to the region of glide creep in Yualin and Carbee (1987a). The main purpose of the work was to look at the effects of ice content and dry unit weight on the strength of frozen soils. However, from a practical view point or from a long term creep perspective, these experiments can be considered rapid. The corresponding high strength values are directly related to the high strain rate. The specimens failed in plastic mode with formation of cracks, but no brittle failure. The important findings are that at low strains, less than 1%, higher water contents yielded significantly higher axial compressive strengths. This relates directly to the ice behavior. At 20% strain levels, the residual strength is not dependent on dry density or water content and essentially becomes constant.

The cited literature described above is the summary of work performed on remolded Fairbanks silt sampled from the CRREL permafrost tunnel. The data by Yaunlin and Carbee (1987a) is the most applicable in that more realistic stress and strain rates were used.

2.6.2 Creep of Undisturbed Fairbanks Silt

The only reported laboratory test on undisturbed ice-rich silt taken from the CRREL tunnel is reported by Thompson and Sayles (1972). The tests were conducted at temperatures of -1.67°C. The soil had average water contents of 94% and average dry densities of 0.705 g/cm^3. A flow law was defined and is expressed in Equation 2.19.

$$\dot{\varepsilon} = 3x10^{-10}\sigma^4 \qquad \text{Eq. 2.19}$$

Where $\dot{\varepsilon}$ is the strain rate (hr^{-1}), the A coefficient is $3x10^{-10}$ hr^{-1} psi^{-4}, and σ is the applied stress in psi (lb/in^2). The reported strain-time curves show rapid entry into secondary creep (small primary creep stage) which was maintained for strains exceeding 20% (Figure 2.4). This was

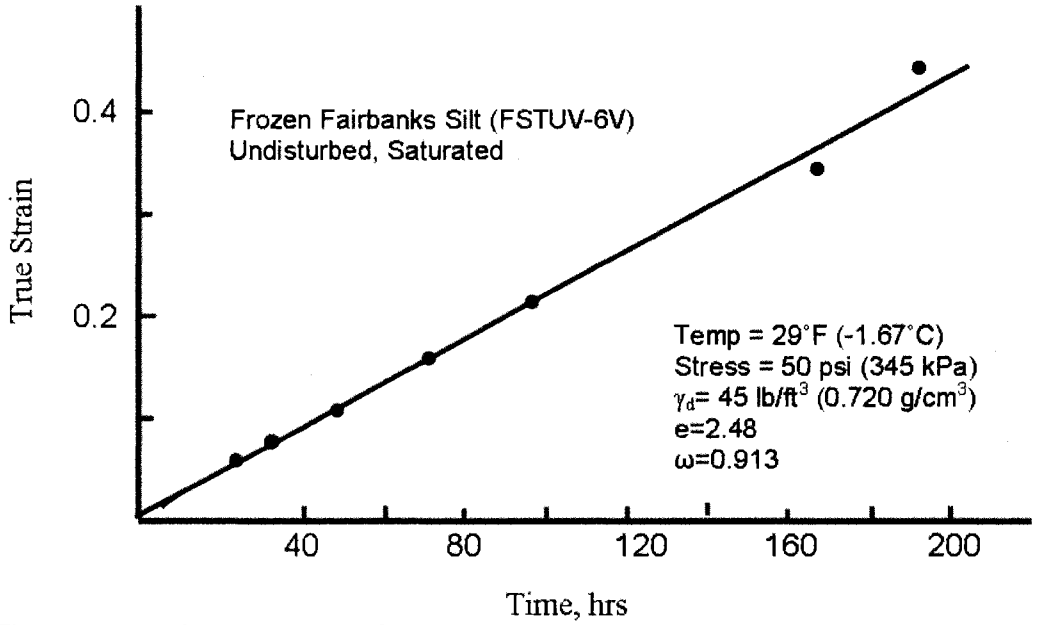

Figure 2.4. Typical creep curve for undisturbed Fairbanks silt showing dominant secondary creep behavior. (Figure Taken from Thompson and Sayles, 1972, Figure 7).

attributed to the ice-rich nature of Fairbanks Silt. The tests were run at stress levels ranging from approximately 35 psi (241 kPa) to 300 psi (2067 kPa). The stress exponent, n equal to 4 defined by Nixon and McRoberts (1976) for higher stresses in ice is in agreement with Equation 2.19.

Several field studies have been performed in the tunnel and are an important source of creep data for undisturbed Fairbanks silt. Thompson and Sayles (1972) collected data on closure rates of the CRREL permafrost tunnel. Ladanyi et al (1991) performed pressuremeter relaxation tests in the tunnel walls. Ladanyi and Huneault (1989) performed cone penetrometer tests in the CRREL permafrost tunnel. These important works will be discussed in detail below.

Thompson and Sayles (1972) report measured data on the creep (closure) rates from the CRREL tunnel. They used the tunnel closure data and numerical analysis in an attempt to determine the flow law for the creep rates measured in the tunnel. The closure rate measurements were conducted in the winze (adit off of main tunnel) at stations 1+83 and 2+02 which are located in a gravel room at the end of the winze. Due to slabbing of overlying gravel, the overlying silt was exposed. The floor consists of gravel and decomposed bedrock. Sand and gravel compose the walls. The closure rates were observed for a period of 1 year. Numerical modeling was used to back calculate the fundamental flow equation, which describes the measured closure rates (creep rates). A few important results were obtained. Attempts to model the closure rates with primary

creep relationships (i.e. creep rates decrease with time) did not compare favorably to the field measurements. The best fit to the measured data was obtained by setting the long term strength to zero and neglecting primary creep effects. In other words, the creep was modeled using secondary creep relationships. Laboratory testing on undisturbed silt from the tunnel also showed that secondary creep dominates (see Figure 2.4). It was determined that creep rates in the CRREL tunnel remain constant despite changes in time and accumulated strain. Based on the numerical modeling, the flow law that best modeled tunnel closure rates in the silt is shown in Equation 2.20.

$$\dot{\varepsilon} = 9.80x10^{-10}\sigma^4 \qquad \text{Eq. 2.20}$$

Where $\dot{\varepsilon}$ is the strain rate (hr^{-1}), the A coefficient is $9.80x10^{-10}$ hr^{-1} psi^{-4}, and σ is the applied stress in psi (lb/in^2). The resulting flow law in Equation 2.20 agrees fairly well with the flow law derived from the laboratory results (Eq. 2.19). In this instance the laboratory tests model the in-situ soils accurately. Based on the agreement between field and laboratory results, the observation that secondary creep dominates is accurate.

Huang et al. (1986) and Huang and Speck (1989) analyzed tunnel closure rates in relation to temperature, tunnel width, and overburden pressure. It was found that exponential relationships exist for the various factors. Using convergence rate as a function of temperature, for a temperature of -1.67°C (29°F), the average tunnel convergence was 0.038 in/day (0.978 mm/day). Rough approximations of the roofs (silt) vertical displacement data as presented by Thompson and Sayles (1972) suggest a creep rate of approximately 0.8 mm/day. Johansen and Ryer (1982) present data on the displacement of the CRREL tunnel ceiling over a 3 month period. They concluded that the tunnel roof was creeping at a rate of 0.002 in/day (0.05 mm/day). No information is mentioned as to the location and temperature conditions at the place of measurement.

A geotechnical testing program was conducted in the CRREL permafrost tunnel with the use of pressuremeter tests (Ladanyi et al, 1991) and cone penetrometer tests (Ladanyi and Huneault, 1989). The results of both tests will be discussed below as they provide important data on the in-situ strength properties of the permafrost soils.

The results from the cone penetrometer tests are presented by Ladanyi and Huneault (1989). The soil from the test location was described as silt without visible ice with water contents from 96-130%. As will be shown (Chapters 3 and 4), the soil most likely contains micro-lenticular

cryostructure based on the water contents given. The tests were conducted in the winze. The cone penetrometer tests were performed primarily in the frozen silt but tests were also conducted in wedge ice. The cone penetrometer tests were load controlled. It was found that the resistance of the point could be plotted against displacement rates of the penetrometer on log-log axes. The data could then be related to a flow law similar to Equation 2.2. From the plot, the creep exponent n could be determined. It was found that for displacement rates less than $3.5x10^{-6}$ m/s, n was equal to 2.97. For displacement rates greater than $3.5x10^{-6}$ m/s, n was equal 3.91. This bilinear relationship was primarily seen for point resistance, but not for total penetrometer resistance in the frozen silts. Interestingly, this correlates well to the observation by Yuanlin and Carbee (1987a) that a change in slope occurs on log $\dot{\varepsilon}$-log σ plot for a critical strain equal to $1x10^{-6}$ s^{-1}. Transferring the data into the form of Glen's law, the relationships for frozen silt at temperatures of -2°C are shown in Equations 2.21 and 2.22:

$$\dot{\varepsilon} = 6.683x10^{-10}\sigma^{2.97}, \text{ for } u < 3.5x10^{-6} m/s$$
$$\dot{\varepsilon} = 1.316x10^{-12}\sigma^{3.91}, \text{ for } u > 3.5x10^{-6} m/s \qquad \text{Eq. 2.21}$$

For the wedge ice found in the tunnel, the relationships are:

$$\dot{\varepsilon} = 2.497x10^{-9}\sigma^{2.29}, \text{ for } u < 3.0x10^{-6} m/s$$
$$\dot{\varepsilon} = 4.556x10^{-15}\sigma^{4.15}, \text{ for } u > 3.0x10^{-6} m/s \qquad \text{Eq. 2.22}$$

Where $\dot{\varepsilon}$ is the strain rate (hr^{-1}), A is a constant in $hr^{-1}kPa^{-n}$, σ is the applied stress in kPa, u is the velocity of cone penetrometer.

Results of the pressuremeter tests are reported by Ladanyi et al (1991). The pressuremeter tests were also conducted in the winze on silts with similar water contents. Reduction of the pressuremeter data conforms to a primary creep type equation where time is a variable. The primary creep type equation is of the form shown in Equation 2.23.

$$\varepsilon = A\sigma^n t^b \qquad \text{Eq. 2.23}$$

Where ε is the strain, σ is the applied stress, n is the stress exponent, t is the time and b is the time exponent. A, n, and b are empirical coefficients. It was found that n varies from n equal to 1.38 at low strains, n equal to 3 for middle strains, and n equal to 4.0 at high strains. No specific strain values were given which correlate to low, medium, or high strains. Interpretation of the available data would suggest that strains less than 4% correspond to low strains, strains from 4 to

20% correspond to medium strains, and strains greater than 20% correspond to high strains. The b values vary from 0.23 at low strains, 0.60 for medium strains, and 0.79 at high strains. If the medium strain region is adopted as representative, the following values for the coefficients in Equation 2.23 can be defined: A is equal to 3.716×10^{-11} min^{-1} kPa^{-n}, n is equal to 3, and b is equal to 0.6. Based on these values, the long term strength as a function of time is expressed in Equation 2.24.

$$\sigma_{lt} = 1025 \cdot t^{-0.2} \qquad \text{Eq. 2.24}$$

Where σ_{lt} is long term strength in kPa, t is the time period for which the long term strength is to be determined in minutes.

Figures 2.5 and 2.6 summarize the data on the minimum strain rate flow laws as described earlier for the various soils and ice data reviewed in the literature. Figure 2.5 shows the data for ice (Nixon and McRoberts, 1976; Morgenstern et al., 1980; Sego and Morgenstern, 1983) and ice-rich undisturbed soils (Thompson and Sayles, 1972; McRoberts et al., 1978; McRoberts, 1988). The dashed lines represent the ice data. Generally the ice data is clustered in a band in which the strain rates across the band vary up to 3 orders of magnitude. However, the data for ice-rich soils tend to show a similar nature. The stress exponent for Fairbanks silt is n equal to 4, as shown by the steeper curve. A common assumption is that the flow law for ice should result in conservative creep rate estimates for frozen soils. The data shown in Figure 2.5 tentatively supports the assumption.

Figure 2.6 shows all the data for laboratory and field studies for remolded and undisturbed Fairbanks Silt. The curves for remolded Fairbanks silt by Yuanlin and Carbee (1987a) show a marked deviation from the other approximations which are derived from undisturbed Fairbanks silt. An abrupt change in slope is seen for the medium density remolded Fairbanks silt at approximately 800 kPa ($\dot{\varepsilon}=3.6 \times 10^{-3}$ hr^{-1}). It was suggested that a change of the deformation mechanism results in the change of slope. As was shown in Figure 2.1 (Pekarskaya, 1965), soils with massive cryostructure tend to show an abrupt decrease in creep rates with a further decrease in stress past some critical stress value as evidences by the increase in the stress exponent n. It is possible that this is a "long-term strength" characteristic that is less strongly expressed in the natural and more ice-rich soils. For low density remolded silt (Yuanlin and Carbee, 1987a), secondary creep approximations more closely resemble those for undisturbed soils. However, the value of the creep exponent n is higher as evidenced from the slope of the curve. The plot of the pressuremeter results (Ladany et al, 1991) is based on the

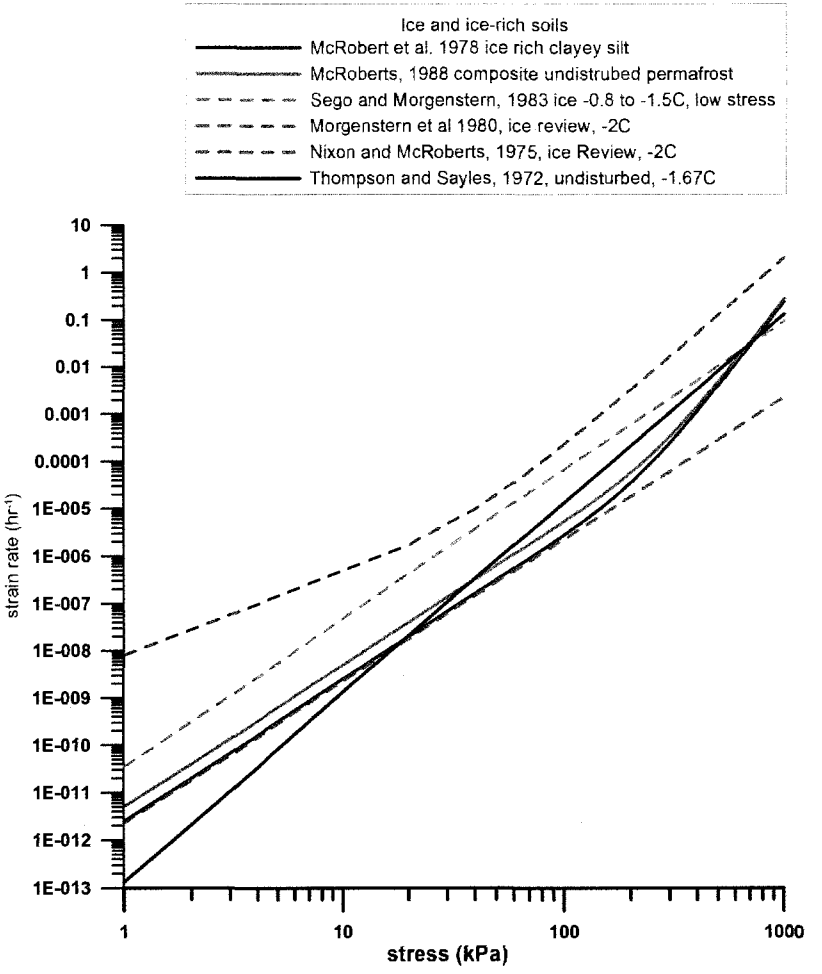

Figure 2.5. Minimum strain rate power law relationships for ice and ice-rich undisturbed soils.

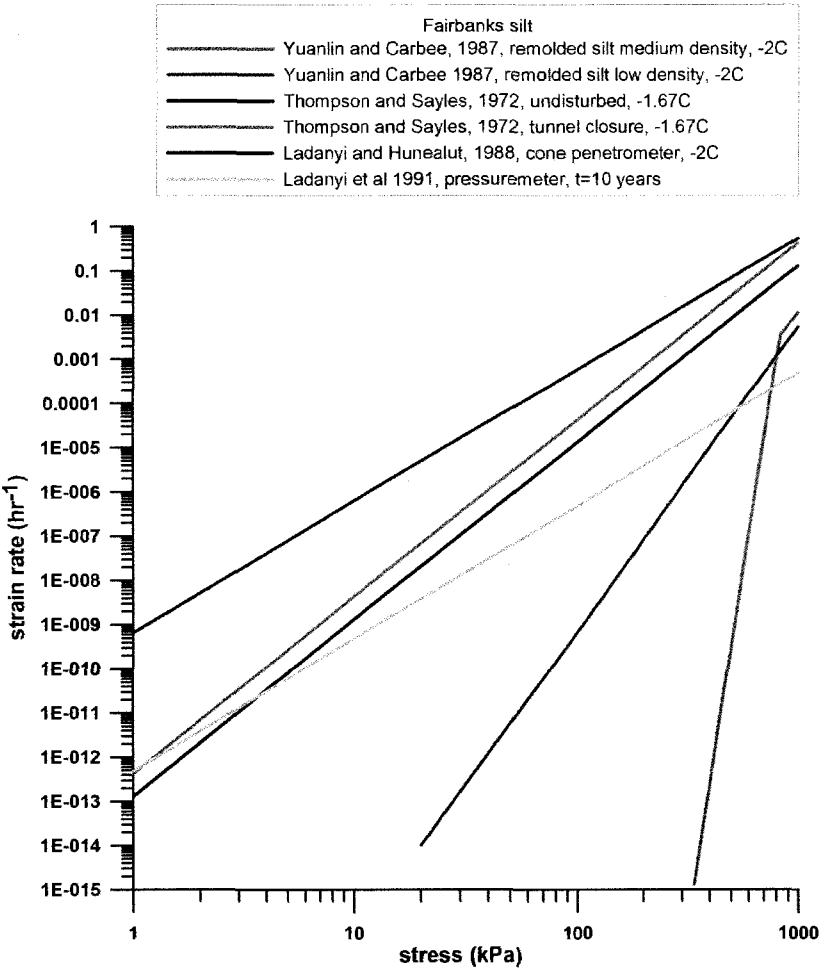

Figure 2.6. Minimum strain rate power law relationships for Fairbanks Silt.

derivative of the primary creep equation (Eq. 2.23) and assumes a time period of ten years for each stress level. Figure 2.6 suggests that data obtained for remolded soils can not be applied to natural soils. In remolded soils, the effects of the depositional and cryogenic genesis (nature of freezing and associated cryostructure) are not reproduced. Further comparison of remolded Fairbanks silt to undisturbed Fairbanks silt is difficult as most studies conducted on remolded soils were conducted at high strain rates (thus high stress levels). Alternatively, most tests on undisturbed soils were conducted at lower strain rates. However, even for the higher displacement rates in the cone penetrometer tests (Ladanyi and Huneault, 1989) the stress exponent n is approximately 4. For the remolded samples the stress exponent n is generally greater than 6 for the low density silt. For medium density silts, n is even larger. The most important conclusion is that results obtained from remolded soils are not applicable to ice-rich undisturbed soils.

2.7 Summary

The few studies that have discussed the effect of cryostructure on the mechanical behavior of frozen soils have shown that cryostructure has an influence on the deformation characteristics. The creep characteristics described by Pekarskaya (1965) remain valid for most of the reviewed data (see Figure 2.1) in which the basic concept is that there is a transition in the creep response in relation to soil cryostructure depending on the applied stress level. Soil cryostructure influences ice lenses orientation as well as total ice content. Based on ice content, the following generalization about the secondary creep behavior can be made. At low stresses, it was shown that soils containing more ice show higher creep rates than soils containing less ice. At higher stresses, soils that contain less ice tend to show higher creep rates than soils containing more ice. Ice is known to creep at low stresses. Soils that contain less ice are generally influenced in part by frictional forces due to motion between particles. When a soil contains more ice, the ice within the soil has the ability to heal or restore its structure as it is strained. For high stresses, the less ice a soil contains, the lower its ability to heal broken bonds that occur during the straining process. As a result, once a certain stress threshold is reached, the bonds in the soils containing less ice are broken thus leading to accelerated strain rates and failure. In contrast, the strain rates for ice and ice-rich soils tend to increase at a
much slower rate for higher stresses in part due to the ability of the ice within the soil to heal its structure.

It was shown that soils with favorably oriented ice lenses show higher creep rates than soil with ice lenses that are not favorably oriented to the applied stress. For example, ice lenses oriented

in the direction of shear planes cause increased strain rates and lower strengths. Ice lenses perpendicular to shear planes resulted in reduced strain rates and higher strengths. Based on this idea, the generalities presented in the preceding paragraph about creep rates, applied stresses, and ice contents cannot be applied without taking into account the ice structure and ice orientation with respect to applied stress and shear planes.

The minimum strain rate flow laws for ice and frozen soils vary. Generally, the stress exponent n varies from 2 to 4 for frozen soils depending on stress. Values of n close to 2 have been shown for low stress conditions in ice. Typically, n is equal to 3 to 4 over most stress ranges that have been studied for ice and ice-rich soils. Remolded Fairbanks silt, showed a marked deviation with n values significantly greater than 3 to 4 (Yuanlin and Carbee, 1987a). The larger n values indicate that the creep rates are highly stress dependent. For stresses less than 750 kPa, the secondary creep rates are lower for remolded Fairbanks silt as compared to undisturbed Fairbanks silt (see Figure 2.6). Therefore, the use of remolded Fairbanks silt is non-conservative when extrapolated to undisturbed Fairbanks silt.

Chapter 3: Permafrost Geology of Soil for Studies

In this chapter, the permafrost geology of the CRREL permafrost tunnel is presented. The permafrost geology was interpreted based on a cryostratigraphic mapping methodology. This methodology is based on the concept that soil cryostucture (pattern of ice inclusions within a soil) has a direct relationship to the depositional and cryogenic genesis. Based on this concept, the permafrost geology was mapped and reinterpreted. This chapter supplies the necessary background in regards to the permafrost geology of the soil used.

The work on the permafrost geology of the tunnel was published in a peer reviewed technical journal, Permafrost and Periglacial Processes. Additional information in regards to the permafrost soil and soil cryostructure has been added in Chapter 4 which was not included in the journal paper. A small amount of overlap is found between Chapters 3 and 4, but it was felt that the paper should be presented in its entirety. A permafrost map of the main tunnel adit is presented. Soil and massive ice descriptions are included.

The mapping and description of the permafrost geology of the CRREL permafrost tunnel was the foundation for the further work on the mechanical properties of the ice-rich permafrost soils that are presented in this work. One of the fundamental ideas behind this work is to relate permafrost geology to the mechanical behavior of a permafrost soils. There is a tendency to ignore the permafrost geology of a frozen soil when interpreting its mechanical behavior. Many studies use remolded soils, which essentially destroys the nature of the original soils. The sediment remains the same, but the nature of the ice inclusion and the sediment relationship to the ice inclusion is altered. The result is essentially a different permafrost deposit. A permafrost soil depends on depositional conditions, but just as important is cryogenic genesis, which refers to how and under what conditions the soil was frozen and formed. Many in-situ studies on the mechanical properties of frozen soils have been performed. One of the deficiencies is an inadequate description of the permafrost geology, especially the soil cryostructure. The soil cryostructure is an important component of a frozen soil, just as joint patterns, weathering patterns, mineral crystallization, and water distributions are in the mechanical behavior of a rock mass. All permafrost is not created equal and therefore should not be treated as such.

3.1 Introduction

The CRREL permafrost tunnel is located at 65° N in the discontinuous permafrost zone of central Alaska, approximately 15 km from Fairbanks (Figure 3.1). The tunnel is excavated within a thick sequence of Late-Pleistocene-age silt (loess), retransported loess, and alluvium that, collectively, are designated as Goldstream Formation (Péwé, 1975). In this paper, additional information is added to recent cryostratigraphic observations (Shur et al., 2004) by presenting a cryostratigraphic map of part of the tunnel walls and describing the characteristic micro-morphology associated with the cryostructures that we recognize. The nature of the various icy bodies and pseudomorphs that are exposed in the tunnel are discussed in more detail.

The length of the CRREL tunnel is ~100m and consists of a main (horizontal) adit and a smaller lower chamber. Our cryostratigraphic map illustrates part of the main adit and is presented as Figure 3.2 and Table 3.1. The ranges of ice content (gravimetric water content) and frozen bulk density values that characterize the tunnel sediments are presented in Figure 3.3.

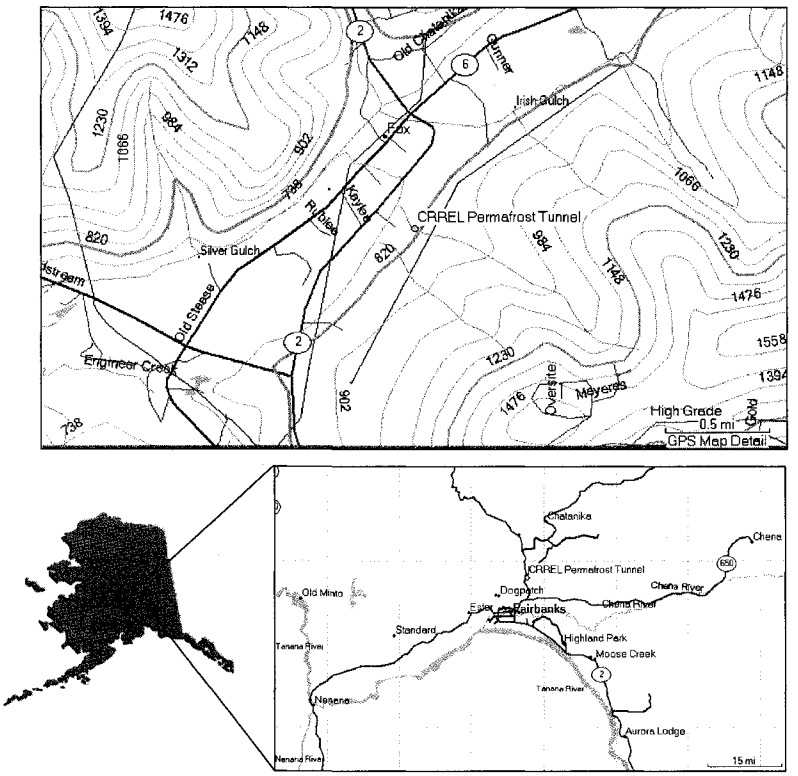

Figure 3.1. Location of the CRREL permafrost tunnel near Fairbanks, Alaska. The CRREL Permafrost Tunnel is located at 64° 57'N and 147° 37.2'W in the zone of discontinuous permafrost.

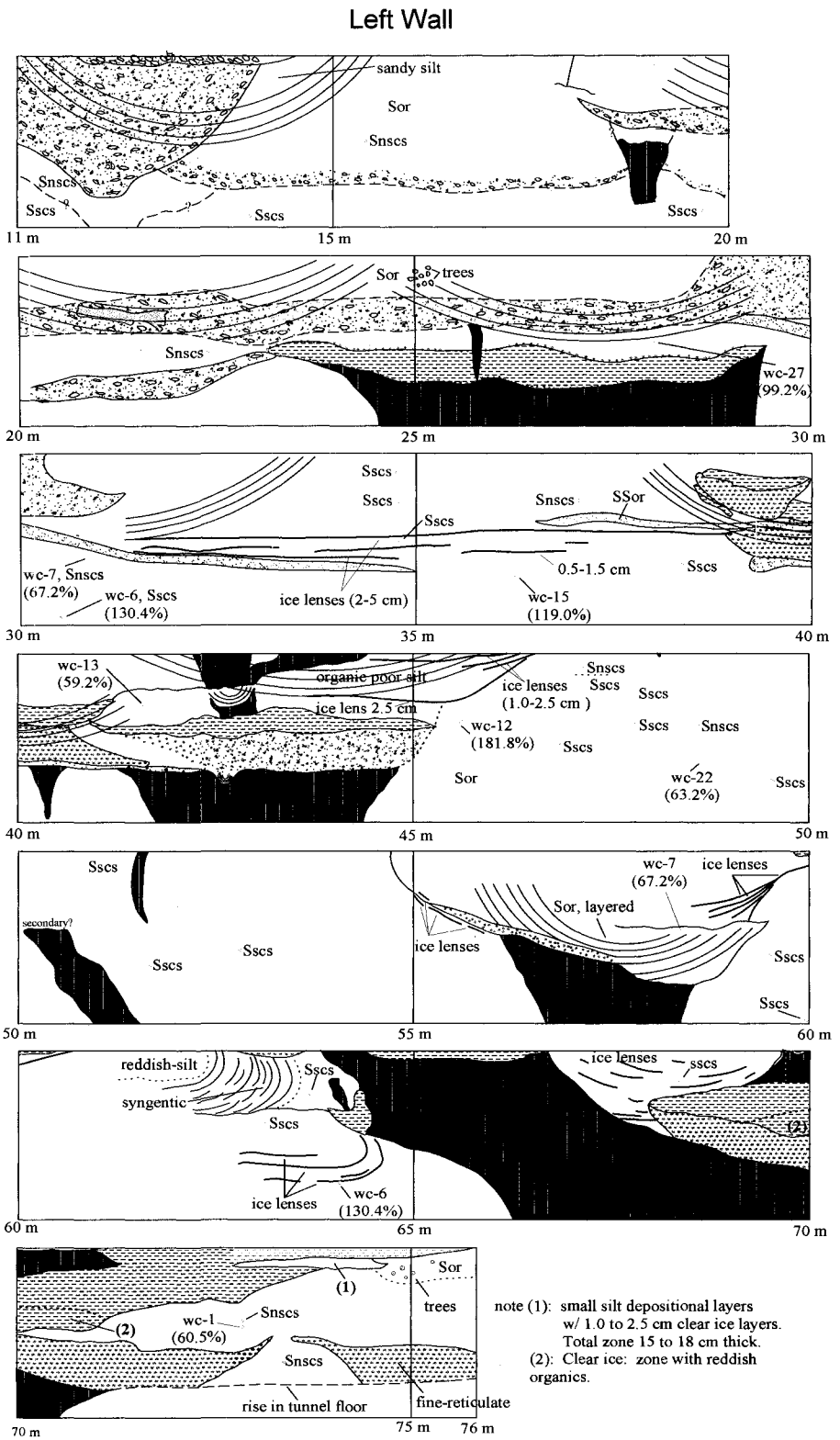

Figure 3.2a. For caption see facing page. Left wall.

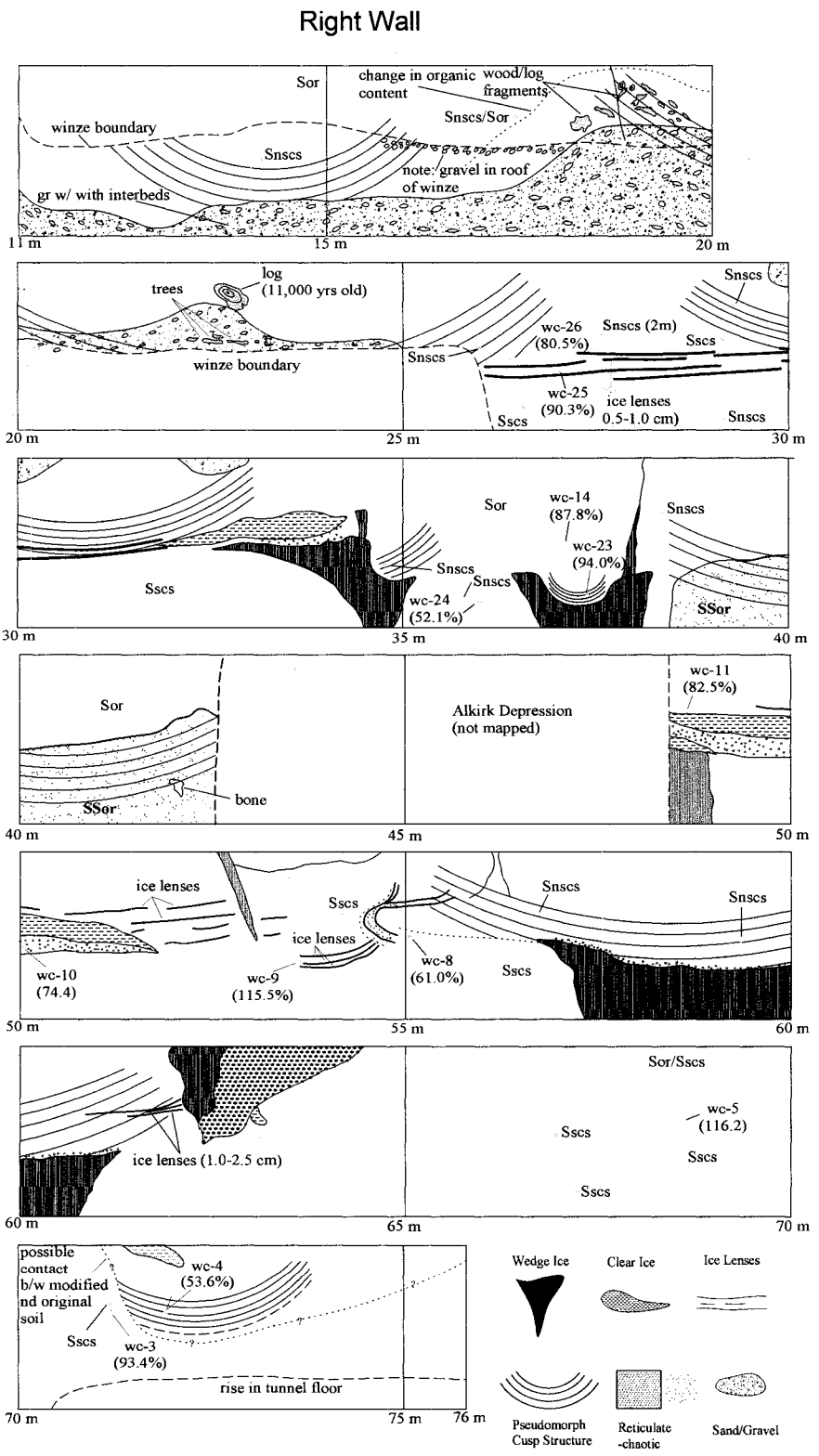

Figure 3.2b. Continued. Right Wall

Table 3.1. Cryo-lithostratigraphic units, ice bodies, and other features that were mapped in the CRREL tunnel (see Figure 3.2).

1. CRYO-LITHOSTRATIGRAPHIC UNITS:	
Sscs:	Fairbanks silt, representative of the orginal syngenetic permafrost, characterized by *micro-lenticular* and *layered* cryostructures. Average gravimetric water content 130%
Snscs:	Fairbanks silt, characterized by a *massive* cryostructure that is indicative of secondary modification. It contains no cryostructures typical of syngenetic permafrost. The average gravimetric water content is 69%.
Sor:	Fairbanks silt with a *massive* cryostructure and possessing organics (rootlets, wood, animal bones etc).
Ssor:	Sandy organic silt with a *massive* cryostructure and containing rootlets, wood and animal bones.
Gr:	Gravel deposits; sandy, silt, imbricated. Where near the tunnel entrance, they may represent slope deposits. Deeper within the tunnel, the gravel deposits are directly related to the fluvial erosion and thaw-modification of ice wedges.
2. ICE BODIES:	
Ice lenses:	Lenses of ice that range in length from ~10 cm to several meters and with thickness of between ~0.5 to~10 cm. They form part of the *micro-lenticular* and *layered* cryostructures.
Clear ice:	Lenticular-shaped ice bodies, often with aligned bubbles towards outer edges, and usually associated with *reticulate-chaotic* cryostructures in adjacent sediments. The ice is interpreted as thermokarst-cave ice.
Wedge ice:	Foliated ice with vertical soil laminations, often brownish in color.
3. OTHER FEATURES:	
Pseudomorphs:	Bodies of mineral soil ranging in composition from gravel to silt, commonly possessing high organic contents and often possessing *reticulate-chaotic* cryostructures. Interpreted as replacement deposits within previously thaw-eroded and truncated ice- wedge structures

3.2 Background

Shur et al. (2004) reinterpreted the ice-rich sediments within the context of syngenetic permafrost growth. It was inferred that, under long-continued cold-climate (permafrost) conditions, sediment aggradation was associated with episodes of thermokarst erosion that operated preferentially along ice wedges. This led to the development of gullies and tunnels in the near-surface sediments which, in turn, led to the formation of thermokarst-cave ice ('pool ice') and pseudomorphs. The exact timing of these events are uncertain, but radiocarbon ages obtained from samples of organic material contained within the silt (see Sellman,1967, 19; Shur et al, 2004, 340) suggest these thermokarst events were local and that they probably occurred at various times between ~30,000 and ~14,000 years ago.

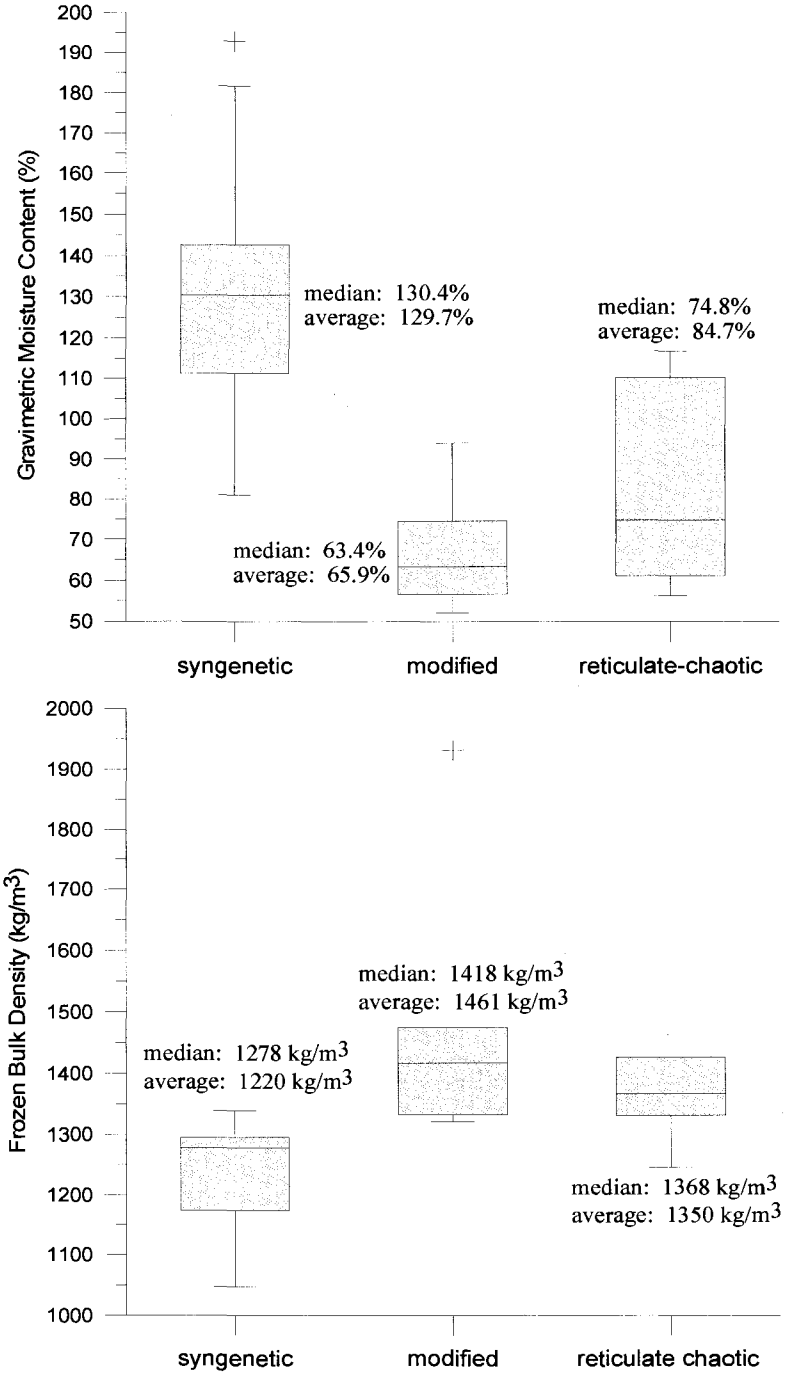

Figure 3.3. The ranges of gravimetric water content (%) (left) and frozen bulk densities (kg) (right) that are diagnostic of tunnel sediments. 'Syngenetic' represents samples containing *micro-lenticular* cryostructures. 'Reticulate-chaotic' represents samples containing *reticulate-chaotic* cryostructures. 'Modified' represents samples taken from pseudomorphs containing *massive* cryostructures.

3.3 Mapping methods

Mapping was conducted by using a cryofacial method first proposed by Katasonov (1960). This is based upon two concepts: (a) that the shape, size and spatial pattern of ice inclusions (i.e. cryostructures) depend on the conditions under which the sediment was deposited and then frozen, and (b) that every cryofacies has its own specific cryostructure. More details of the Russian approach to cryostratigraphy can be found in Kudryavtsev (1978, 302-314), Zhestkova (1982), Shur (1988) and Melnikov and Spesivtsev (2000, 177-343). In the North-American literature, a classification of cryostructures and cryofacies has been presented by Murton and French (1994; see French, 1996, 81-85).

The cryofacial analysis was based on the identification of (i) typical cryostructures, (ii) massive ice bodies, and (iii) ice and soil pseudomorphs. For example, four main cryostructures are recognized in the CRREL tunnel. A *micro-lenticular* cryostructure, which consists of thin, short, straight, wavy lenses of ice, generally less than 0.1mm in thickness and with horizontal to sub-horizontal lengths varying up to a few millimetres. A *layered* cryostructure, which contains larger, more continuous ice lenses with thickness ranging from 0.2 to 5.0 cm. Where the ice lenses are short, with lengths ranging from a few millimetres to 1.0 cm, we describe the structure as *lenticular-layered.* The most striking cryostructure is termed *reticulate-chaotic.* This consists of randomly-oriented ice lenses, 1-5 mm thick and 1.0-5.0 cm long. The fourth cryostructure that we recognize is termed *massive.* This consists of silt cemented together without any visible ice particles.

Massive icy bodies were identified as being of three types: (i) wedge ice, (ii) clear ice, and (iii) clear ice with wedge-ice inclusions. The wedge ice, in response to silt particles and organic staining within the ice, is gray to dark brown in color. The wedges range in apparent width from 1 to 7 m. It is important to stress that only the bottom portions of the wedges are seen in the tunnel. Therefore, their size is difficult to quantify. However, we infer that they are large by normal standards (French, 1996, 90). The clear ice bodies are lenticular shaped and up to 2 m in thickness. The largest apparent horizontal extent of this type of ice that can be viewed in the tunnel is approximately 7 m. In a few places, the clear ice contains wedge-ice inclusions. This indicates that, after truncation and/or replacement of the original wedge ice by clear ice, thermal-contraction cracking continued to occur and veins of wedge ice continued to form.

3.4 Cryogenic Micro-Morphology

The micro-morphology of typical cryostructures in the CRREL tunnel was examined in the laboratory at the University of Alaska-Fairbanks using an environmental scanning electron microscope (ESEM).

Undisturbed samples representing both syngenetic permafrost and modified permafrost were obtained from the tunnel walls using SIPRE augers and saws. The cores were obtained parallel to the surface (i.e. parallel to the ice lensing). Thin sections, between 3-4 mm in thickness, were cut. A surface impression of the soil in question was made. However, it was found that imaging was best achieved by viewing a freshly-fractured surface. Imaging was conducted under a water vapor environment with chamber pressures of 4.9 Torr. With a conventional scanning electron microscope (SEM), typical chamber pressures are in the order of 1×10^{-5} Torr. As result of the higher chamber pressures in the ESEM, and resulting higher vapor pressure of the ice, the soil is viewed under a warmer temperature.

3.5 Cryostructures and Their Associated Micro-Morphology

Typical cryostructures and their associated micro-morphologies in the tunnel are illustrated in Figure 3.4.

In *massive* cryostructures (Figure 3.4a), the soil/ice morphology is dominated by a soil-particle matrix with small randomly-oriented segregated ice lenses. These vary from lens-like to spheroidal in shape and range in thickness from 20-50μm. Because *massive* cryostructures tend not to exhibit ice amounts in excess of the pore space, any presence of excess ice indicates that the soil remained in an unconsolidated state during permafrost formation. It also explains the high water content often found in the secondary (i.e. modified) deposits (see Figure 3.3).

In *lenticular-layered* cryostructures (Figure 3.4b), the ice lenses have a maximum diameter of approximately 1 mm (1000μm) separated by a soil matrix containing smaller lenses, parallel to the larger lenses, which range in size from 20-50μm. The smaller lenses are thickest close to the larger lenses and decrease in thickness with increasing distance from the dominant ice lenses. The smaller lenses have spacing of ~100-250μm between soil particles.

In *micro-lenticular* cryostructures (Figure 3.4c), the ice/soil morphology is essentially one in which mineral soil particles are suspended, with no organized structure, within an ice matrix. The mineral particles range in size from ~25-100μm and the ice crystals range in size from ~20 -

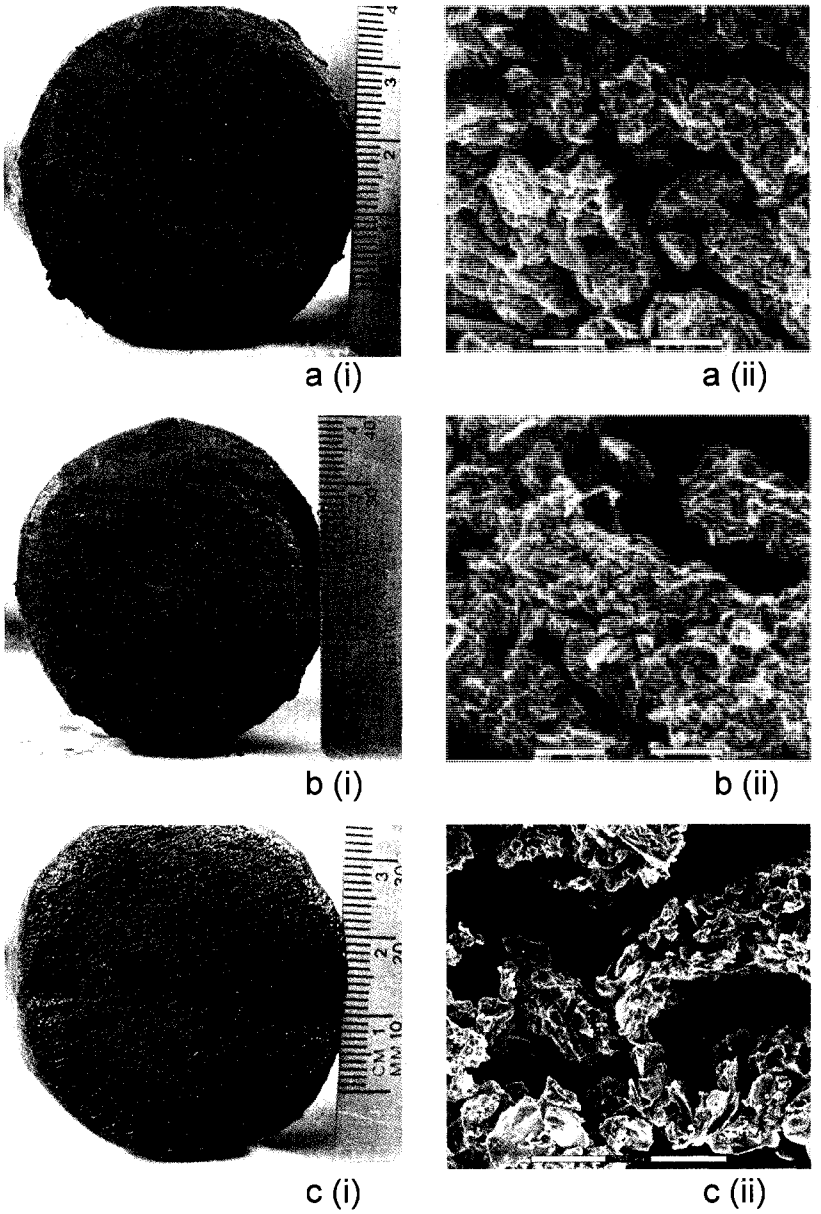

Figure 3.4. Example of cryostructures from the CRREL tunnel viewed conventionally and under ESEM. (a) *Massive* cryostructure. Image (i) is a macro-scale image typical of silt pseudomorphs. Note cm scale. Image (ii) is a micro-scale image using an ESEM. Bar scale indicates 250µm (b) *Lenticular-layered* cryostructure. Image (i) is a conventional macro-scale image. Note cm scale. Image (ii) is a micro-scale image using an ESEM that shows the soil and micro ice-lens morphology. Bar scale indicates 250µm. (c) *Micro-lenticular* cryostructure. Image (i) is a macro-scale image. Note cm scale. Image (ii) is a micro-scale images under ESEM in which soil particles are generally suspended in an ice matrix. Bar scale indicates 250µm

250μm. Grain boundary orientations suggest a preferred ice-crystal orientation with boundaries parallel to the soil depositional surface.

3.6 Discussion

The *micro-lenticular* cryostructure is regarded as diagnostic of syngenetic permafrost. The combination of continuous ice lenses in a *layered* or *lenticular-layered* cryostructure, with a *micro-lenticular* cryostructure in the intervening sediment, is also regarded as diagnostic of syngenetic permafrost. This is based upon field observations of numerous exposures of frozen unconsolidated sediments elsewhere in Siberia, northern Canada and Alaska. In most cases, it has been observed that the soil that separates segregated ice lenses invariably tends to be ice-poor and consolidated in epigenetic permafrost.

It was also observed that both *reticulate-chaotic* and *massive* cryostructures are usually associated with either massive ice related to truncated ice wedges or modified silt sediments related to ice and soil pseudomorphs. Based on observations in the Mackenzie Delta region of Canada, Murton and French (1994) suggest that a 'reticulate-random' cryostructure forms in a semi-closed system. Observations from within the CREEL tunnel support this idea, although the process by which *reticulate-chaotic* cryostructures form is still largely unknown. One possibility is that silty alluvium, in which the *reticulate-chaotic* cryostructure most typically occurs, is very likely to have been temporarily unfrozen during its surface transportation by running water or when it was deposited in water-saturated conditions on a thaw-erosional surface. The thawed sediments then underwent a period of slow freeze-back.

Several indicators enable pseudomorphs to be distinguished from both enclosing syngenetic permafrost and from ice wedges. These include soil composition, the structural relationship of the pseudomorph with the surrounding soil, its cryogenic structure, water (ice) content of the soil, and ice appearance. In the CRREL tunnel, pseudomorphs are composed of gravel, silt or ice, or a combination of all three. Gravel-in-silt and ice-in-silt pseudomorphs are the most readily distinguishable. Silt-in-silt pseudomorphs are less apparent due to the similarity of soil texture between original syngenetic and secondary silty permafrost. However, the cryostructure usually differs between the original silt and the pseudomorph silt deposit. For example, the original syngenetic silty permafrost usually contains almost exclusively *micro-lenticular* cryostructures while the silty pseudomorph contains primarily *massive* cryostructures.

Sellman (1967) and Hamilton et al. (1988) interpreted the elongated clear ice bodies present within the CRREL tunnel as pond ice preserved at the paleosurface by rapid burial. However, convincing examples of buried pond ice in have yet to be observed in Alaska and northern Canada. Therefore, thermokarst-cave ice is the preferred interpretation (Shumskii, 1964, 45-46; Gasanov, 1969) and referred to the ice pseudomorphs consisting of thermokarst-cave ice that are described in the Russian literature (Rosenbaum et al., 1978; Solomatin, 1986). In North America, the colloquial term 'pool ice' has been used (Mackay, 1988, 87; 1997, 20) but little else has been written about this type of ground ice.

In previous studies (Sellman, 1967, 1972; Hamilton et al., 1988), it was inferred that a regional thaw unconformity connected horizontally along the length of the tunnel, as indicated by the numerous flat-topped (i.e. truncated) ice wedges. On the basis of the cryostructures present within the tunnel, an alternative interpretation is proposed in which syngenetic permafrost progressively aggraded under continuous cold-climate conditions. During this period, episodes of local thermal erosion caused formation of mineral pseudomorphs and/or thermokarst-cave ice (i.e. ice pseudomorphs) above thaw-eroded ice wedges. This concept is schematically illustrated in Figure 3.5.

The most intriguing pseudomorph structure is the ice pseudomorph. This consists of clear massive ice that has replaced a portion of the original ice wedge. The ice differs from wedge ice in that no foliations exist and it has a different structure and texture. Previously, ice-wedge pseudomorphs have not been described. The genesis of ice pseudomorphs is related to 'pool ice', or thermokarst-cave ice.

The presence of ice pseudomorphs in the CRREL tunnel indicates that ice-wedge modification cannot be solely attributed to a stalled paleosurface during a regional warming event. In several instances, ice wedges can be seen to continue into the ceiling of the tunnel even though a portion of the wedge in the tunnel wall has been replaced by thermokarst-cave ice. In some places, it can also be observed that ice-wedge growth has continued after formation of the clear ice, as shown by foliated wedge-ice bodies that penetrate the clear ice.

Examples of thermokarst-cave ice from within the CRREL tunnel are shown in Figure 3.6. There appears to be a common relationship between nearly all of the thermokarst-cave ice bodies and a silt unit possessing a well-developed *reticulate-chaotic* cryostructure. This is illustrated in Figure 3.6a. It would appear that the formation of thermokarst-cave ice is episodic because the ice often

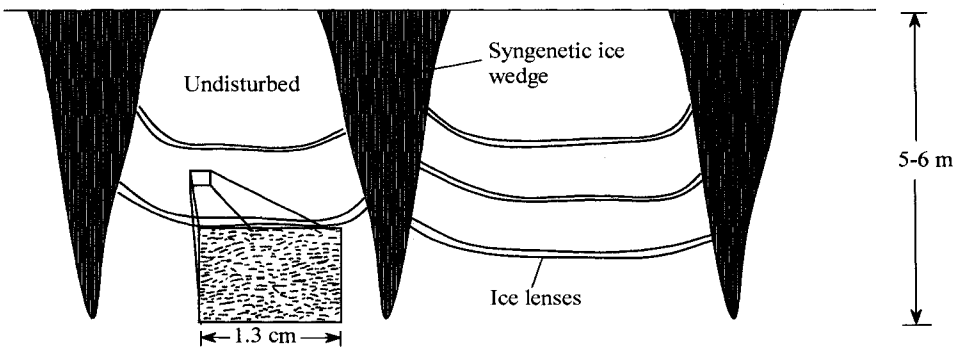

(a).

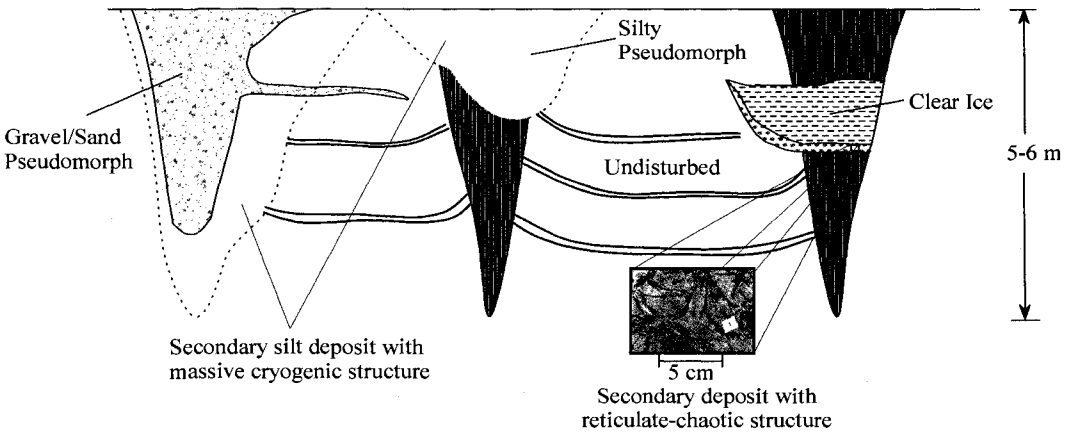

(b).

Figure 3.5. Schematic diagram of (a) undisturbed syngenetic permafrost and (b) a typical modified permafrost exposure within the CRREL tunnel. In (a), the expanded image represents a *micro-lenticular* cryostructure, a reliable indicator of syngenetic permafrost. In (b) an idealized schematic shows typical secondary modification of original syngenetic permafrost. Expanded images represent *micro-lenticular and reticulate-chaotic* cryostructures. The *reticulate-chaotic* cryostructure is associated with 'clear ice', here interpreted as thermokarst-cave ice ('pool ice').

shows several layers of ice deposition. This is illustrated in Figure 3.6b where distinct laminations are visible. Sometimes, thermokarst-cave ice will not completely replace the wedge ice (see Shur et al., 2004, figure 4, p.344).

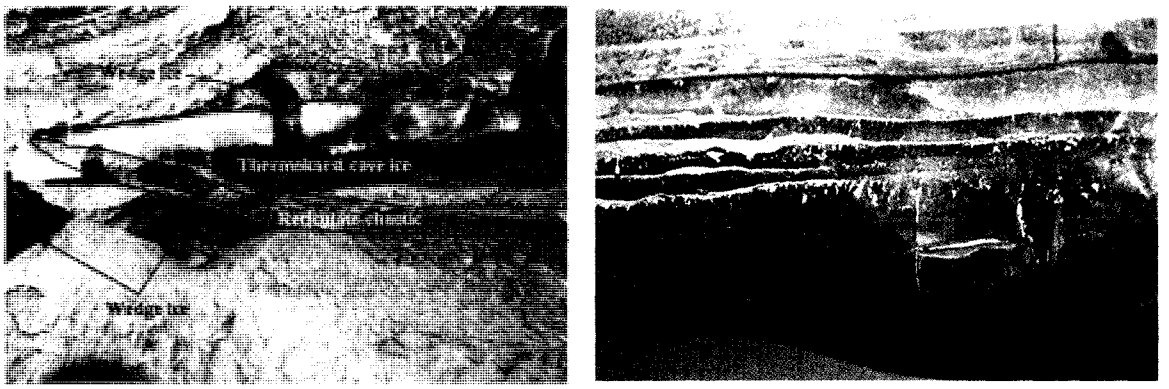

(a) (b)

Figure 3.6. Examples of thermokarst-cave ice from within the CRREL permafrost tunnel. Photo (a) shows the typical relationship between foliated wedge-ice, silt with reticulate-chaotic cryostructure, and thermokarst-cave ice. This photo illustrates location 2+25 to 2+35 on Figure 3.2. Photo (b) shows distinct layering indicating episodic deposition of ice layers.

3.7 Conclusions

The latest cryostratigraphic observations from the CRREL tunnel reinforce earlier conclusions (Shur et al., 2004) regarding the nature of syngenetic permafrost growth in ice-rich and unconsolidated sediments. In such conditions, as might occur in valley-bottom and deltaic situations, *layered* and *lenticular* cryostructures typically develop. Long-continued syngenetic permafrost growth is often accompanied by episodic fluvio-thermal erosion that acts preferentially along ice wedges. Sediment redeposition, lateral stream undercutting, and localized slumping of thawed material can all occur. The result is the formation of *reticulate-chaotic* and *massive* cryostructures that reflect epigenetic freezing in those areas of localized thermal erosion and re-deposition. These secondary, or modified, deposits are described as pseudomorphs. They reflect localities where gullies and eroded ice wedges have been replaced or infilled by gravel, sand, silt or variable silt-ice complexes. Ice pseudomorphs reflect the formation of thermokarst-cave ice, or 'pool ice'.

Chapter 4: Soils and Cryostructures

Chapter 3 supplied information on the permafrost geology of the tunnel. Included was a description of the soil and soil cryostructure. The aim here is to add additional information for each soil cryostructure that was used in the testing program. The cryostructures of soils used include horizontal and vertical micro-lenticular, reticulate-chaotic, massive, and remolded massive. In addition, ice facies that were used include massive syngenetic wedge ice and basal glacial ice and englacial ice from the Matanuska Glacier, Alaska.

4.1 Grain Size Distribution

A sequence of samples was taken from the base of a clear ice body downwards at tunnel station 35 m. See Chapter 3 for permafrost map of the tunnel. The exposure is shown in Figure 4.1 and the base of the clear ice body is labeled as 0 cm. The data is courtesy of Daniel Fortier. Table 4.1 summarizes the water content, organic content, and particle size breakdown. The grain size distribution was not determined for the samples tested in this program. The data presented in Table 4.1 and Figure 4.2 is assumed to be representative of the silt used in this study. Generally, the tunnel soil is composed of re-transported loess silt with small fractions of sand, gravel, and clay. The undisturbed, ice- rich syngenetic permafrost generally is composed of silt of uniform grain size. Secondary reworked sections influenced by fluvial-thermo erosion and deposition, result in a coarser sediment distribution. Stations 2-50 cm are located in the reworked section of Figure 4.1. Stations 50-162 cm are in the original syngenetic permafrost. The grain size distributions below 50 cm are displayed in blue in Figure 4.2. A high degree of uniformity is seen for the original syngenetic permafrost. The soil is poorly sorted with a narrow range of grain sizes. This is typical for wind deposited sediments. The silty soil is not plastic with the plastic limit being approximately 34%.

The reworked sediments from this profile (see Figure 4.1) have a much coarser sediment distribution than the surrounding syngenetic permafrost in the same profile. This is evidenced by the grain size distribution curves in Figure 4.2. In many cases the original silts are just reworked and re-deposited. In this case, grain size distribution curves are not reliable indicators of reworked sediments. However, the reworked sediments typically have lower water contents than the original syngenetic permafrost. The water contents of reworked sediments can be high if large quantities of organics are present in the soil.

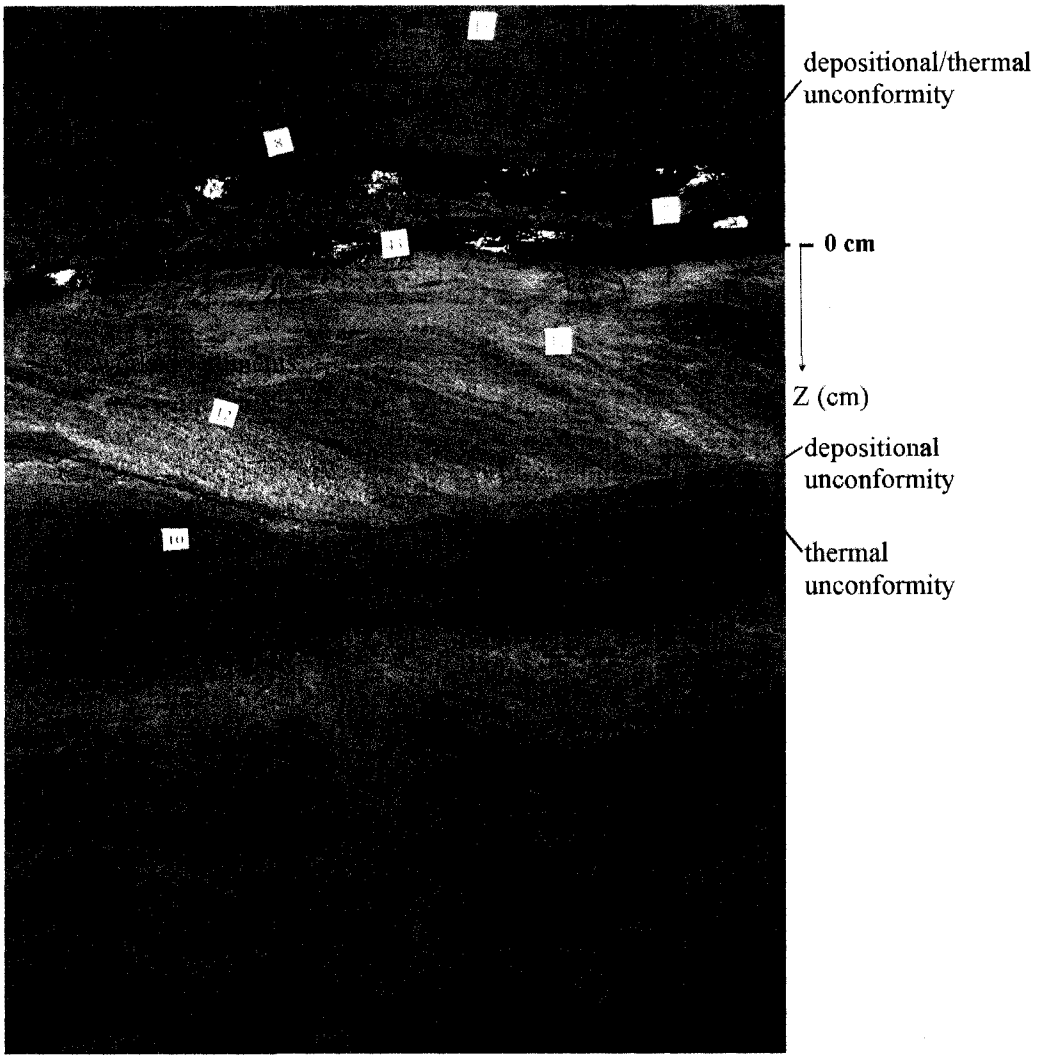

Figure 4.1. Soil profile for grain size distributions for tunnel station 35 m shown in Table 4.1 and Figure 4.2. A region of reworked sediments is bounded above and below by syngenetic permafrost (undisturbed). The reworked sediments are characterized by fluvial stratified silts and sands. Photo courtesy of Daniel Fortier.

4.2. Soil Cryostructure

As outlined in Chapter 3, soil cryostructure can supply information about how a sediment was deposited and under what conditions it was frozen. A soil's cryostructure is the pattern of ice inclusion found within the soil. It is dependent on soil type, depositional characteristics, and freezing conditions. For example, in the tunnel, the original syngenetic permafrost is characterized by micro-lenticular cryostructure. Alternatively, reworked silts in the tunnel are characterized by reticulate-chaotic and massive cryostructure. The same silt, just different depositional and freezing history. The next sections will describe and outline the different soil

Table 4.1. Water content, grain size, and particle size breakdown summary for tunnel station 35 m, left wall. Stations are in centimeters beginning from the lower clear ice deposit, downwards (see Figure 4.2 for profile).

station (cm)	grav. water content (%)	organic content (%)	sand	silt	clay
2-10	187.8	3.82	22.3	70.7	7.0
10-18	99.6	4.48	35.3	63.6	1.1
18-26	168.6	2.51	67.5	30.8	1.6
26-38	349.4	6.82	4.2	86.9	8.9
34-50	75.2	4.93	23.9	69.5	6.6
50-74	116	6.75	5.1	91.0	3.9
82-98	115.9	7.52	3.2	92.4	4.4
98-122	121.3	10.03	6.3	86.8	6.9
122-146	109.5	6.55	2.5	92.4	5.1
146-162	89.2	10.63	5.8	89.5	4.7

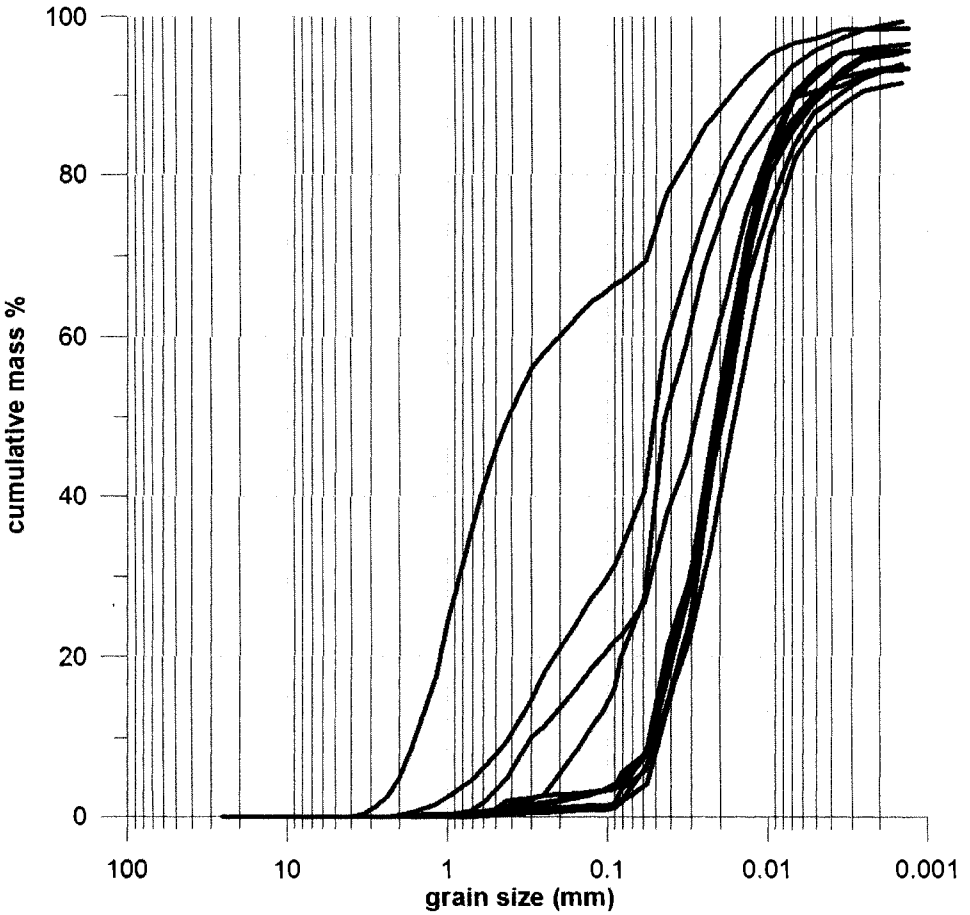

Figure 4.2. Grain size distribution for tunnel station 35 m, left wall (Table 4.1).

cryostructures used in the testing phase of the program. The ice facies tested will also be described.

4.2.1 Micro-lenticular Cryostructure

As seen in Chapter 3, micro-lenticular cryostructure is a diagnostic feature of syngenetic permafrost as seen in the CRREL permafrost tunnel. The soil from the tunnel is re-transported loess and silt frozen during the Pleistocene under syngenetic growth conditions. Syngenetic permafrost forms by the gradual upward growth of the active layer due to sediment deposition. The water rich bottom of the active layer is incorporated into the upward growing permafrost table. The result is typically a large sequence of ice-rich permafrost soils. Due to the nature of the active layer processes occurring on the bottom of the active layer, the frozen soils acquire a very ice-rich open structure. The ice lenses are less than 1 mm thick and up to 3 to 4 mm in length. The lenses are straight to wavy and lenticular in shape. Figure 4.3 shows a soil with micro-lenticular cryostructure as viewed in the field or with the naked eye. Figure 4.4 shows a CT scan rendered image of soil with micro-lenticular cryostructure. Figure 4.5 shows a micrograph image taken with an ESEM (environmental scanning electron microscope) of a 4.7 mm transect perpendicular to ice lens and sediment deposition/growth. As seen in the micrograph, the soil appears to be suspended in an ice matrix rather than ice in a soil matrix. Little quantitative data can be derived in regards to ice crystal orientation. However, from the image, the grain boundaries can be seen in the micrograph, suggesting that average ice crystal size ranges from approximately 20-100 microns. The basic assumption is that the ice crystals are randomly oriented.

Soils with micro-lenticular cryostructure are very ice-rich, unconsolidated sediments with thaw strains reaching 0.4 to 0.6. Typical gravimetric water contents in the tunnel range from 90 to 180%. Water contents exceeding 200% are not uncommon. Typical frozen bulk densities range from 1.25 to 1.35 g/cm^3 and organic contents range from 2 to 10%. Strata layers formed under faster sedimentation rates generally contain lower organic contents.

In the testing program, two orientations of micro-lenticular cryostructure were used (see Figure 4.3) and include vertical micro-lenticular (vml) and horizontal micro-lenticular (hml) cryostructures. Soils with vertical micro-lenticular (vml) cryostructure were obtained by sampling horizontally into the tunnel wall or parallel to the strata. The result was vertically oriented ice lenses or ice lenses parallel to the long axis of the core. Soils with horizontal micro-lenticular (hml) cryostructure were sampled by removing a block from the right tunnel wall at station 30 m (0+98 to 0+100 feet). The

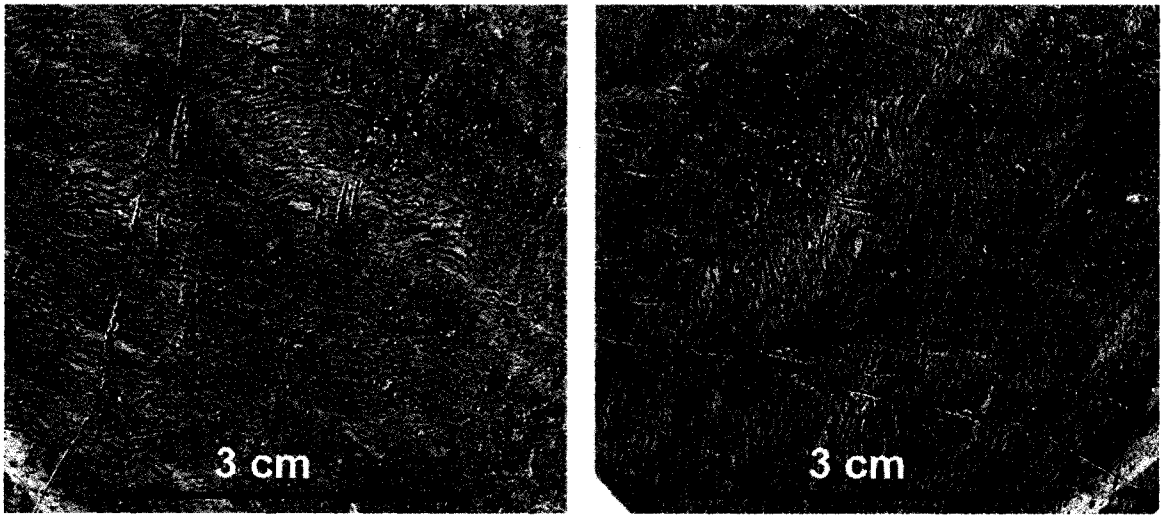

Figure 4.3. Soil with micro-lenticular cryostructure. The left image is horizontal micro-lenticular (hml) cryostructure. The right image is vertical micro-lenticular cryostructure (vml).

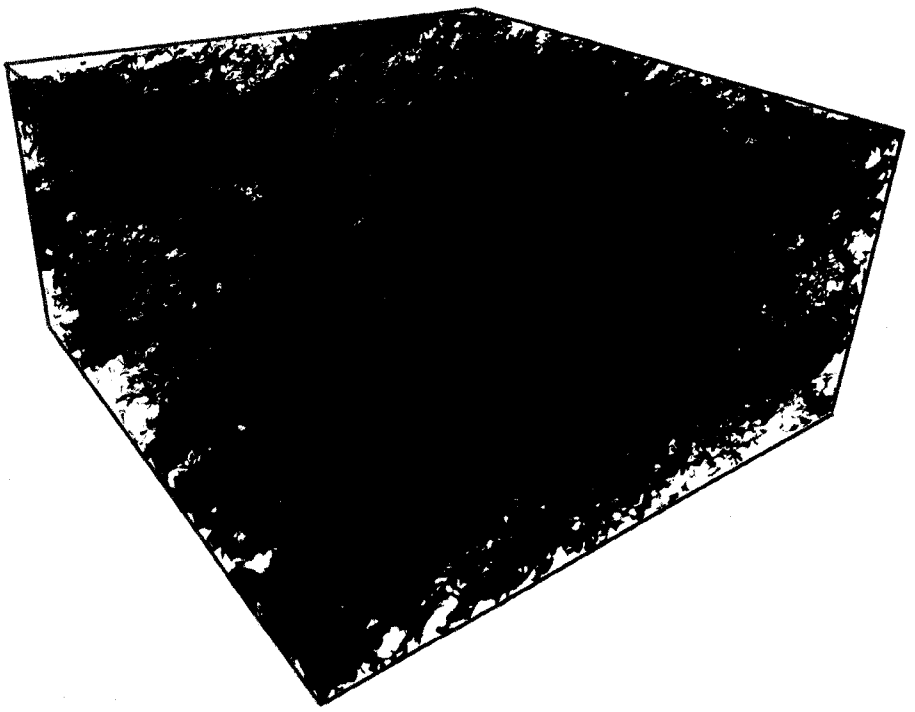

Figure 4.4. CT rendered image of soil with vml cryostructure with vertically oriented ice lens. Blue objects represent ice. White matrix is soil. Box height is 10 mm.

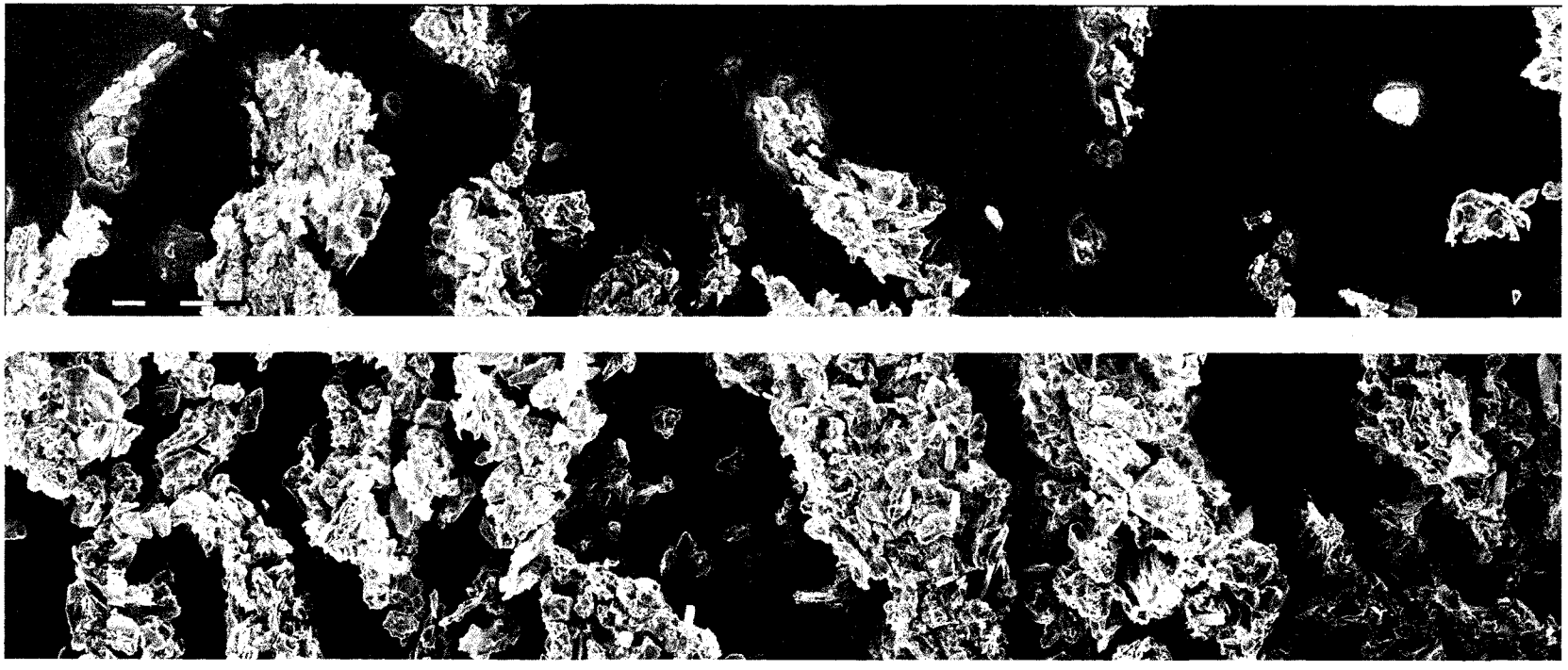

Figure 4.5. ESEM micrograph of soil with micro-lenticular cryostructure. The micrograph represents a 4.7 mm transect across the soil. The dark areas are ice and the lighter aggregates are sediment particles. The transect is viewed from left to right with the left of the lower image being a continuation of the right of the upper image. The scale is located in lower left of the upper image. Scale is 250 µm.

cores were then extracted from the permafrost block in a direction perpendicular to the strata. The result was horizontally oriented ice lenses or ice lenses perpendicular to the long axis of the core. The short notation of hml is used for horizontal micro-lenticular cryostructure. The short notation of vml was used for vertical micro-lenticular cryostructure. The cores sampled horizontally produced relatively uniform ice structure throughout the length of the core. In most of the vertically sampled micro-lenticular soils (hml samples), a small zone at the bottom of the core contained a lower ice lens density, resulting in a slightly less ice saturated region. Even in relatively uniform syngentic permafrost sequences with micro-lenticular cryostructure, the growth and nature of micro-lenticular distribution varies with strata position. The rate of deposition and active layer movement affects that nature of the micro-lenticular cyrostructure. Slower rates of deposition and permafrost growth result in a thicker, more ice-rich micro-lenticular cryostructure.

4.2.2 Undisturbed Massive Cryostructure

Massive cryostructure is generally characterized by frozen soil that contains ice in the pore spaces and does not contain visible segregated ice inclusions. One sample containing undisturbed massive cryostructure was tested. However, the nature of the massive texture is important as the more ice poor sections of the soil had a tendency to show higher creep strains. Figure 4.6 shows a macro scale image of soil with massive cryostructure taken from the permafrost tunnel. Soils with massive cryostructure are generally located in the reworked sediments (secondary deposits) found within the tunnel. Figure 4.7 is derived from a CT scan of the soil. Figure 4.8 shows a micro scale image taken with an ESEM. The particles have no preferred orientation. Seen on the micro scale, the soil has voids in excess of normal pore space geometry with just particle to particle contact. This suggests either segregation processes occurred on a small scale or the soil froze under a supersaturated, open state. The measured water contents are above typical saturation values, thus supporting the observation from the ESEM images.

4.2.3 Remolded Massive Cryostructure

Remolded soil was created using the silt from the tunnel. The silt used was sublimated silt that had fallen to the tunnel floor at tunnel station 30 m (0+98 to 1+00 ft). The soils with horizontal micro-lenticular cryostructure were extracted from a block removed from the tunnel wall at station 30 m. Soils containing vertical micro-lenticular cryostructure were also extracted from this same region. Therefore, the silt uniformity of the remolded soils as compared to the other undisturbed samples should be high.

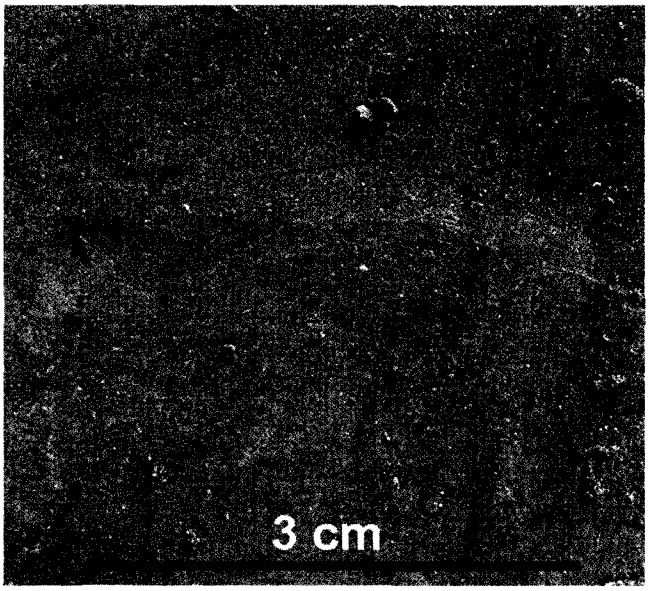

Figure 4.6. Undisturbed soil with massive cryostructure from the tunnel. The image depicts a silt with massive cryostructures from a reworked deposit.

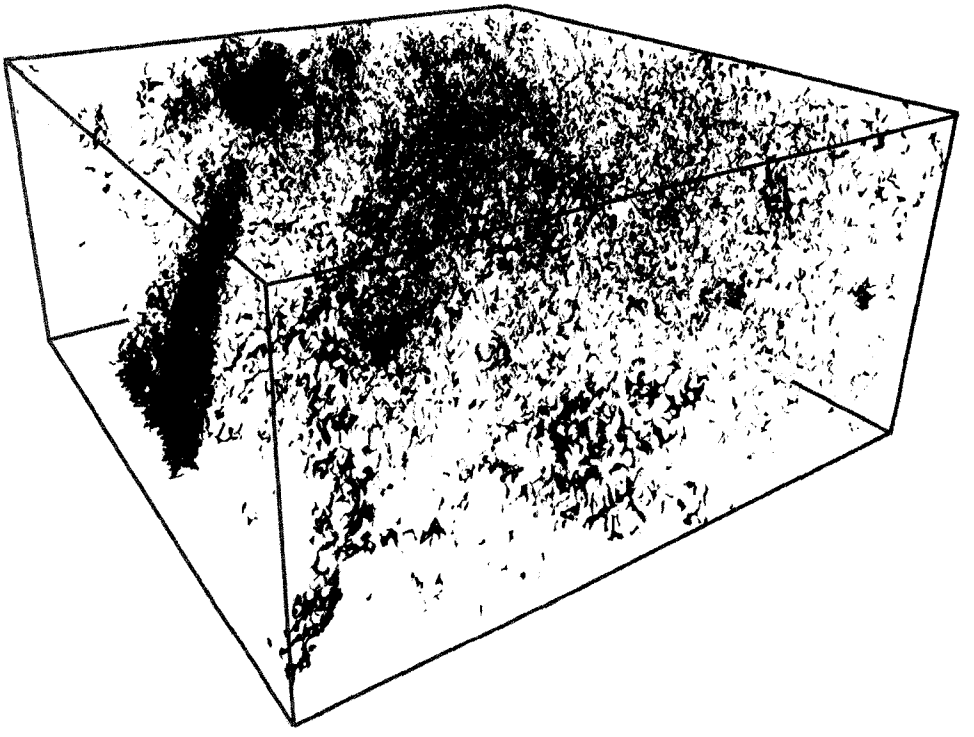

Figure 4.7. CT scan of undisturbed soil with massive cryostructure. Blue object represent ice and the white matrix represent sediment. Box is height is 10 mm.

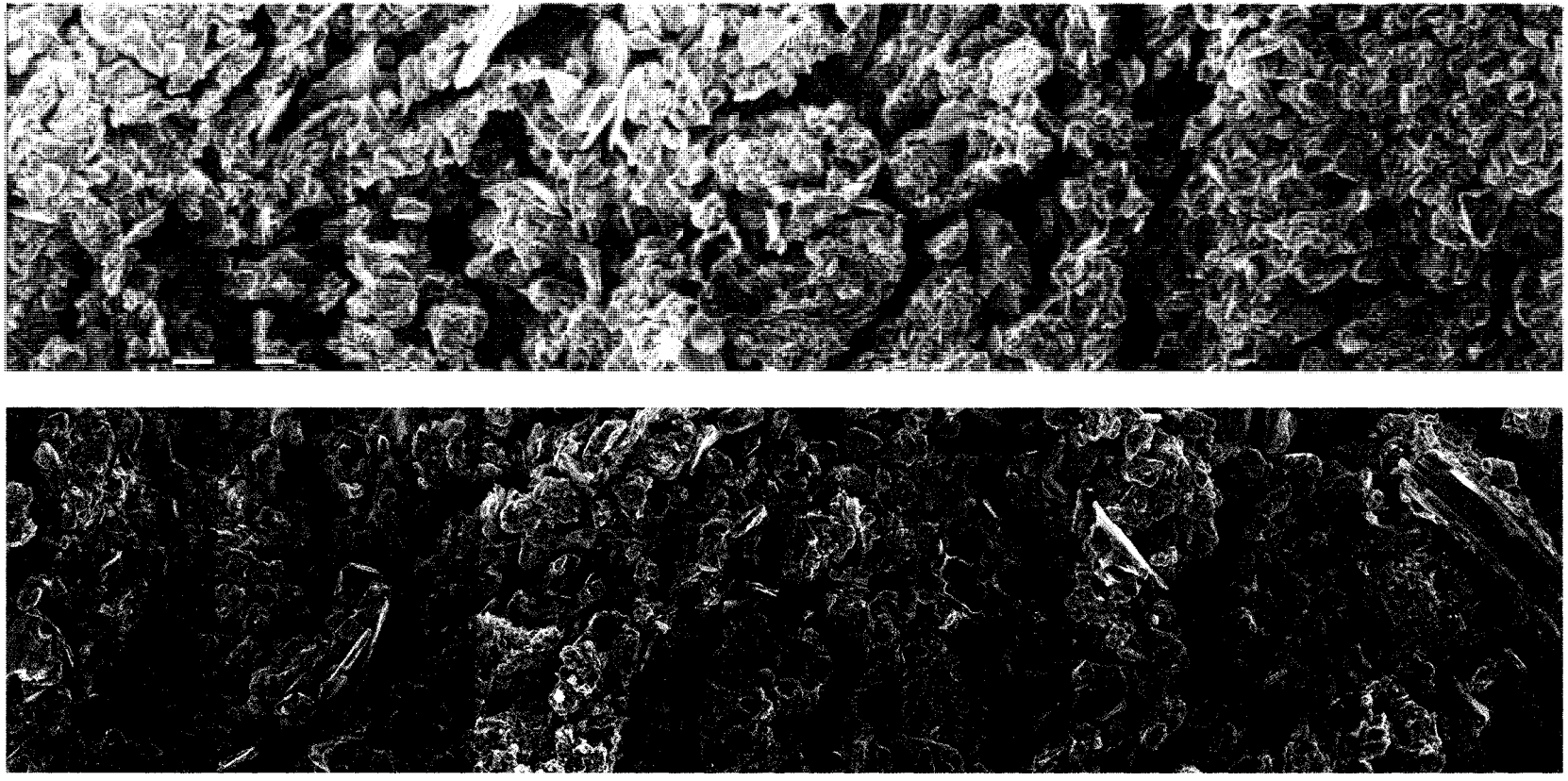

Figure 4.8. ESEM micrograph of undisturbed soil with massive cryostructure. The micrograph represents a 3.9 mm transect. The transect is viewed from left to right with the left of the lower image being a continuation of the right of the upper image. The scale is in lower left of upper image. Scale is 250 µm.

To create remolded samples, deionized water was added to the dry silt to create a saturated slurry. The initial gravimetric water content of the saturated slurry ranged from 60 to 63%. The saturated slurry was then poured into a PVC tube with an inner diameter of 7.6 cm (3 inch). Filter paper was fitted to the bottom of the tube and held in place with a plastic end cap. Holes were drilled into the end cap to allow for water drainage. The silt slurry was poured into the tubes in approximately four layers. After each layer, the slurry was probed with a knife or spoon to help the soil settle and remove any large air pockets. After the last layer was added, the sample was vibrated for two minutes on a vibrating table. Significant amounts of air were removed during this process. The tops of the tubes were then covered with plastic wrap and the soil samples were allowed to drain by gravity for 24 hours. After drainage was complete, samples were placed in an environmental chamber set to -45°C and allowed to freeze for 18 to 24 hours. A temperature of -45°C was used in an attempt to prevent segregated ice from developing in the sample. The frozen samples were then removed from the environmental chamber and ejected from the plastic molds. During the freezing process, excess water was expelled from the soil. This was evidenced by the presence of ice on the bottom and top portions of the sample. After removal of the samples from the molds, they were wrapped in plastic wrap and then aluminum foil and stored in a freezer set to -10°C until tested.

The gravimetric water content of remolded soils with massive cryostructure varied from 48 to 58%. The average water content was 52.9% (n=24). In initial test runs, the remolded soils were created under drained and undrained conditions as well as variable initial slurry water contents. The cores were then cut into sections with water contents measured. It was found that the top and bottom of drained samples had the lowest water contents. Typically, the water contents throughout the entire sample varied by no more than 2-3%. In addition, during trimming of samples for testing purposes, the top and bottom section are removed.

Due to the preparation method, air was entrapped into the soil and remained so in the frozen state. Generally the air pockets are on the order of 100 to 500 μm in diameter and tend to be spherical in shape. From a CT scan of the soil, the volume of air is estimated to be approximately 2%. Figure 4.9 shows a macro scale image of soil with remolded massive cryostructure. Figure 4.10 is CT rendered image of soil with remolded-massive cryostructure. Figure 4.11 is an ESEM image of soil with remolded massive cryostructure. The sediments are randomly oriented with an open packing. The sediment morphology is similar to the sediment morphology of the silt that exists between ice lenses in soils with reticulate-chaotic cryostructure as described below.

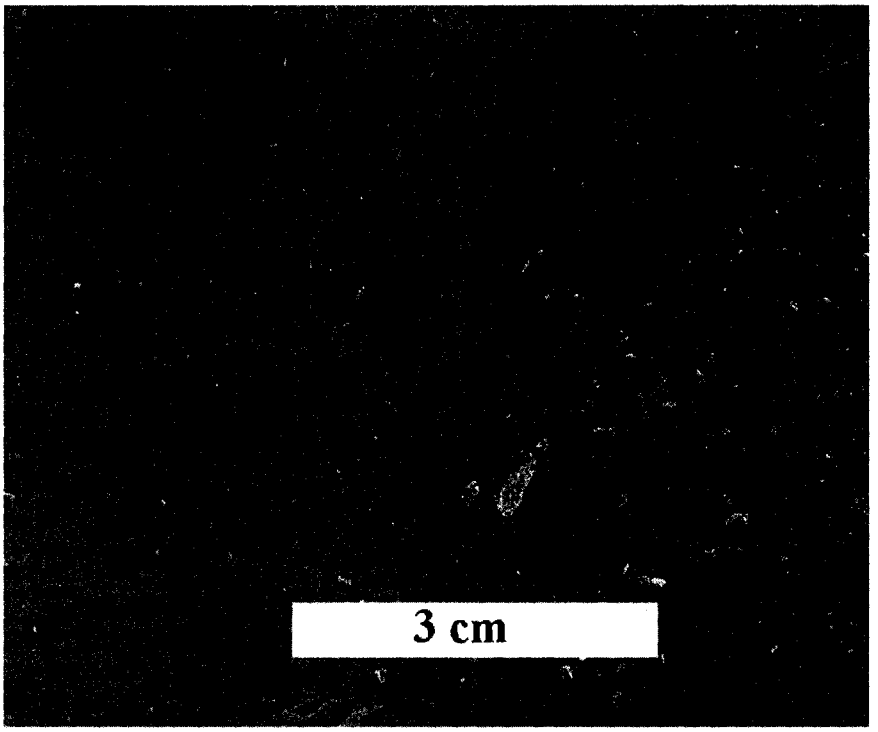

Figure 4.9. Image of soil with remolded-massive cryostructure.

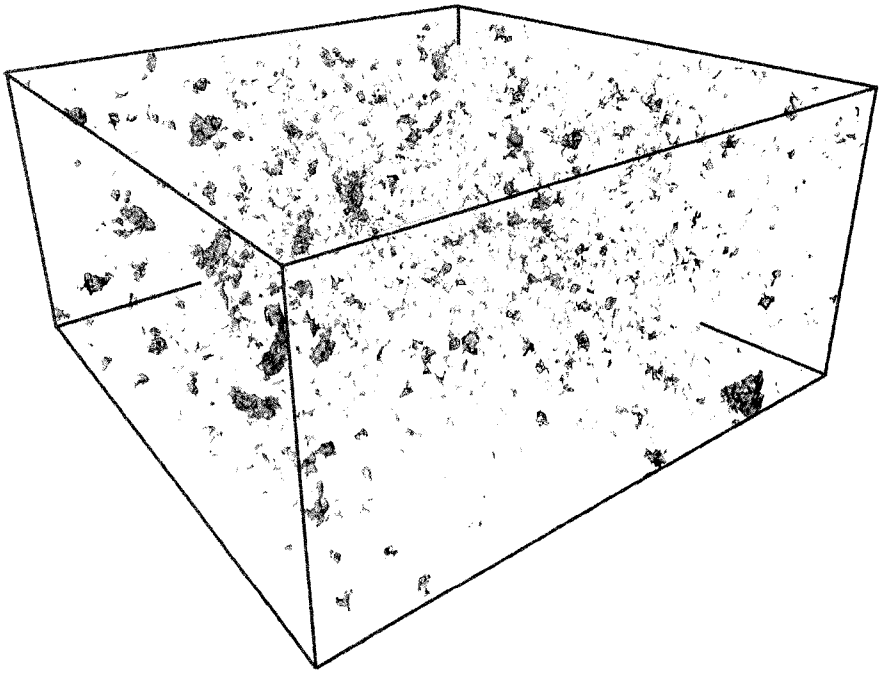

Figure 4.10. CT rendered image of soil with remolded massive cryostructure. Gray objects in image represent air. White matrix consists of sediment. Box height is 10 mm.

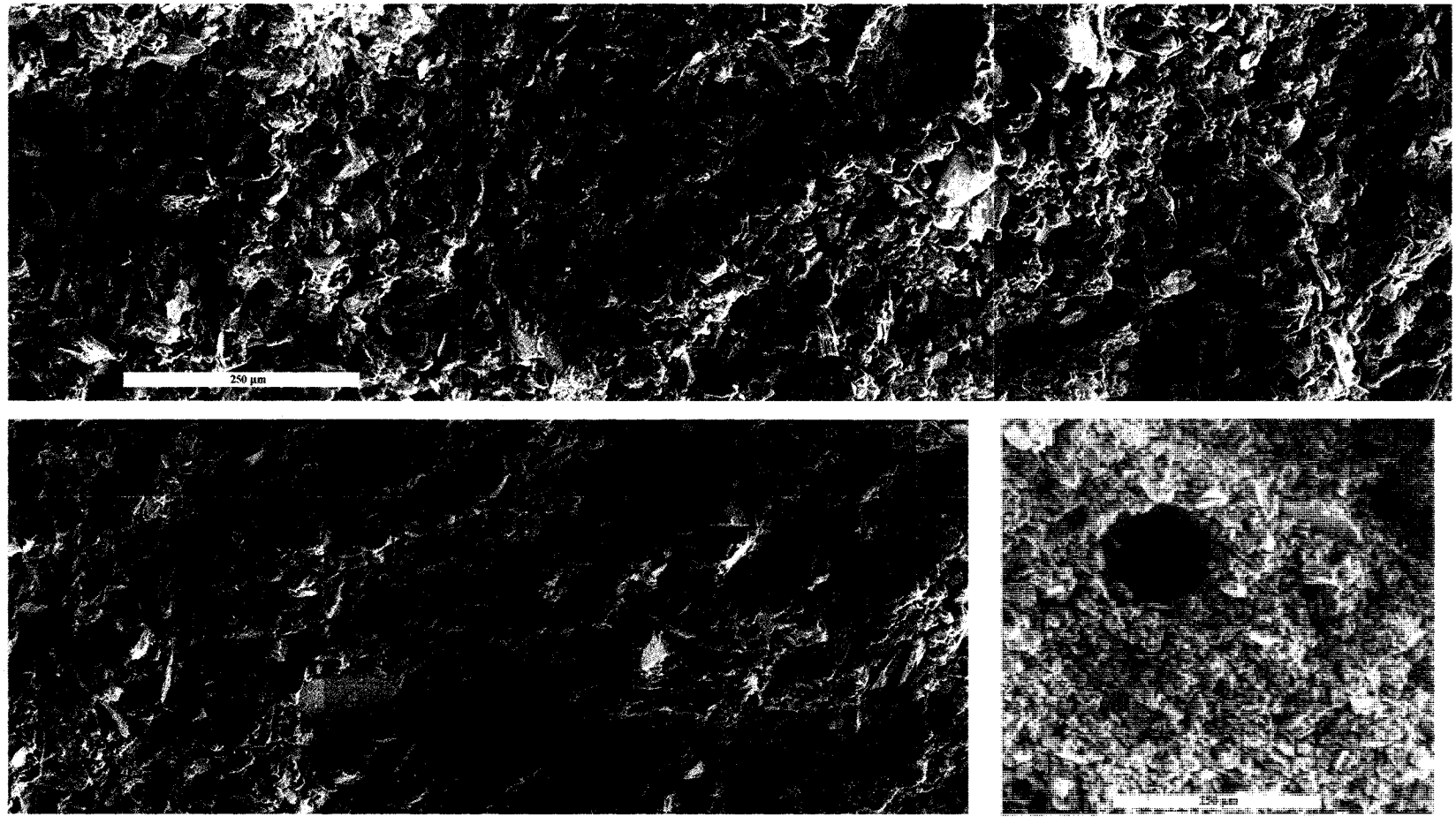

Figure 4.11. ESEM micrograph of soil with remolded massive cryostructure. The micrograph represents a 2.5 mm transect. The transect is viewed from left to right with the left of the lower image being a continuation of the right of the upper image. The scale is in lower left of upper image. Scale is 250 µm. The lower right image shows a typical air pocket. Scale is 250 µm.

4.2.4 Reticulate-Chaotic Cryostructure

Soils with reticulate-chaotic (RC) cryostructure are very distinctive within the tunnel. It is not a widely spread cryostructure, but it does occur in predictable patterns. Soils with reticulate-chaotic cryostructure only occur in reworked deposits. As an underground cavity is formed by fluvial-thermo erosion processes, water rich sediments are deposited. Typically ice lenses form perpendicular to the erosional surface and radiate away from the boundary. In addition, soils with reticulate-chaotic cryostructure always occur if clear ice deposits are present. In Chapter 3, the clear ice was termed thermokarst cave ice. It is a separate massive ice body from wedge ice. Soils with reticulate-chaotic cryostructure form in the sediments beneath the clear ice deposits. The lenses are thicker towards the clear ice and gradually diminish in size towards the erosional/depositional surface.

The cores containing soil with reticulate-chaotic cryostructure were sampled horizontally, from the left wall at station 71 m (2+35 ft). This portion of the tunnel contains a well developed clear ice deposit situated over an ice wedge. The clear ice deposit is labeled pond ice with a sign in the tunnel and is the largest thermokarst cave ice currently accessible in the tunnel. The cores were sampled in the disturbed silty sediments below the thermokarst cave ice body. The ice lenses radiate upwards towards the thermokarst cave ice body and are well developed in this location. Figure 4.12 shows a macro scale image of soil with reticulate-chaotic cryostructure sectioned along the long axis of the core. Figure 4.13 shows a raw CT scan image of soil with reticulate-chaotic cryostructure. The ice lenses tend to feather out and are generally oriented from 0 to 30 degrees on either side of the vertical axis of the core. In an individual core, the ice lenses tend to be oriented in a dominant direction. Generally, a group of ice lenses tend to run in the opposite direction but at a similar angle forming a "conjugate" group. The word "conjugate" is used here as a descriptive term and is not meant to imply a shear displacement genesis of the ice lenses. The ice lenses range from 1 to 4 mm thick and up to 8 to 10 cm in length. Soils with reticulate-chaotic cryostructure have frozen bulk densities that range from 1.33 to 1.50 g/cm^3 and gravimetric water contents ranging from 71.4 to 115.7%.

Figure 4.14 shows an ESEM micrograph of a soil with reticulate-chaotic cryostructure. The upper image is a 2.9 mm transect across a smaller ice lens running through the soil. The soil particles are randomly oriented along the ice-soil contact. The lower image is taken of the soil between the ice lenses. The soil particles are randomly oriented. As compared to the soils with undisturbed massive cryostrucuture, the sediment between the ice lenses in reticulate-chaotic

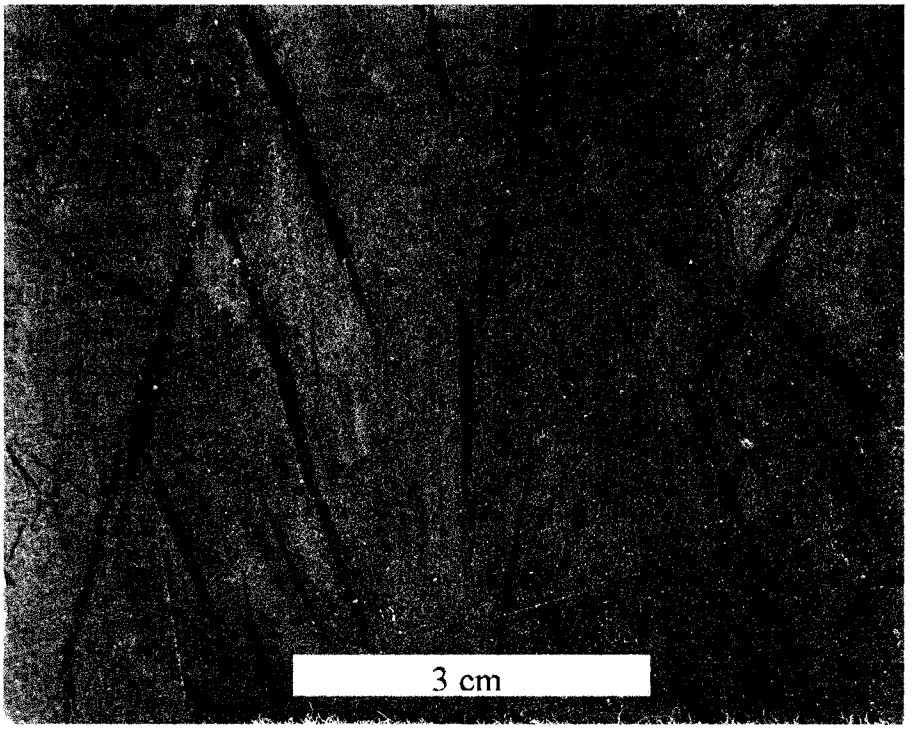

Figure 4.12. Soil with reticulate-chaotic cryostructure.

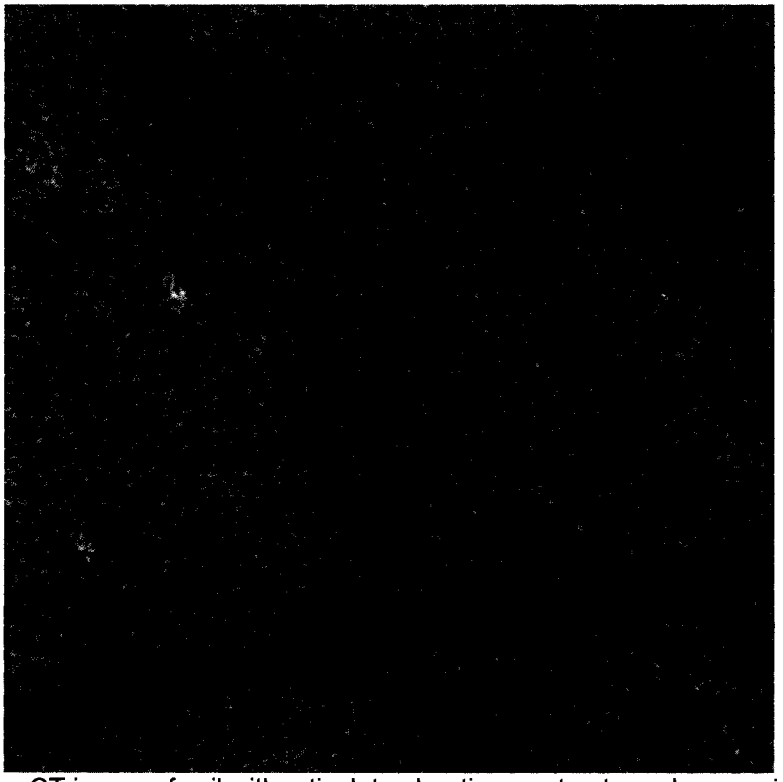

Figure 4.13. Raw CT image of soil with reticulate-chaotic cryostructure. Image width is 20 mm.

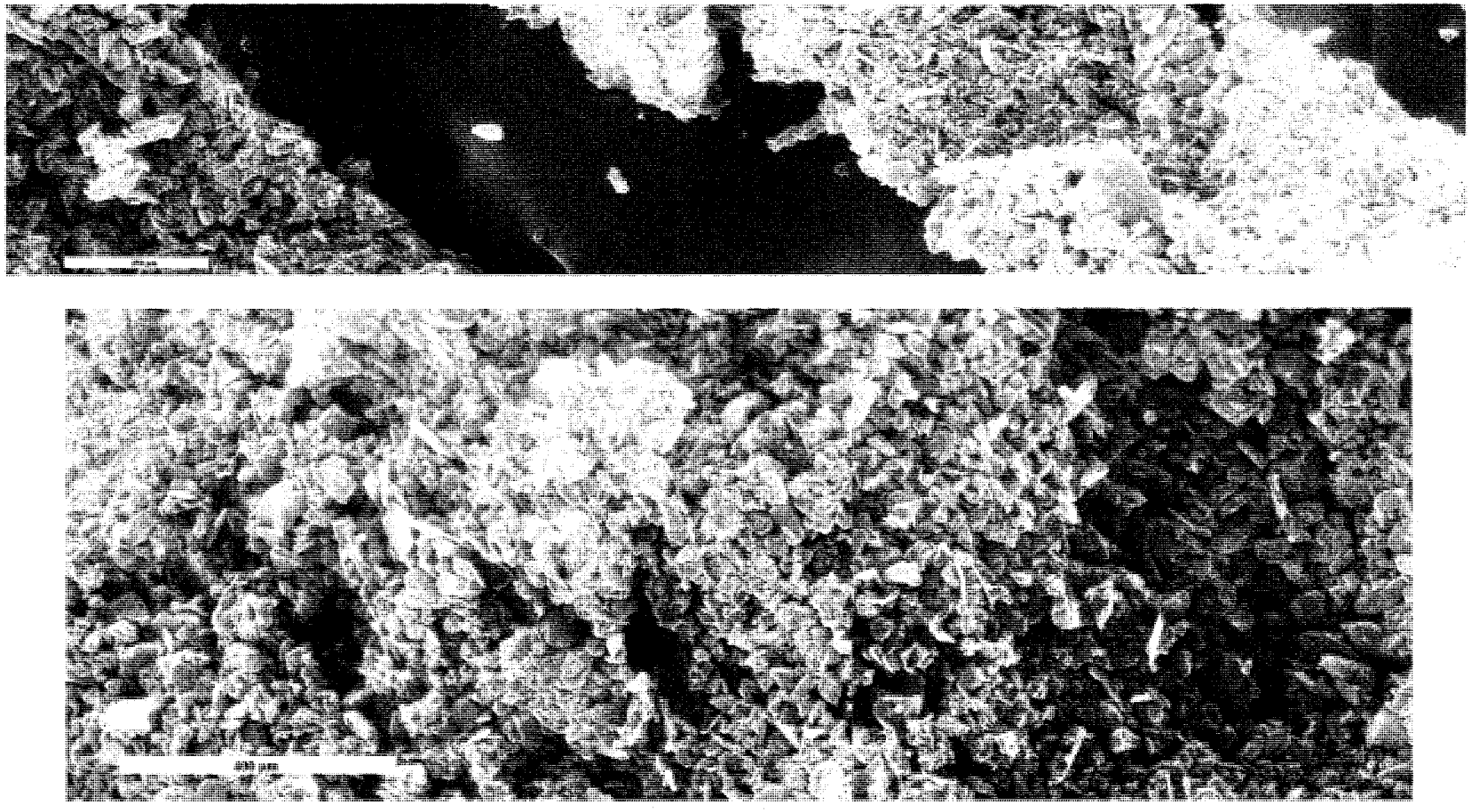

Figure 4.14. ESEM micrograph of soil with reticulate-chaotic cryostructure. The upper image shows a 2.7 mm transect. The transect is viewed crossing an ice lens inclusion. The scale is in the lower left of the image. Scale is 250 µm. The lower image is a 1.9 mm transect across the massive cryostructure portion of the reticulate-chaotic cryostructure. The scale is located in lower left of the upper image. Scale is 400 µm.

cryostructures shows a more compact grain particle packing. The sediment packing is similar to silt with remolded massive cryostructure.

4.2.5 Wedge Ice

Ice wedges are the most prevalent form of massive ice found in the CRREL permafrost tunnel. The ice wedges are syngenetic ice wedges, thus they formed during deposition of the sediment. In the main tunnel adit, the bottom portions of the ice wedges are seen. They are brownish gray in color due to sediment foliation planes. Dark colored ice wedges are typical of the Yedoma syngenetic permafrost deposits of which the tunnel permafrost is included. The apparent widths of ice wedges exposed in the tunnel range from 1 to 7 m. The true widths range from 2-4 m. Sediment is bent upwards along the ice wedge boundaries. In some instances, ice wedges were truncated by thermokarst cave ice. In many cases, foliated wedge ice is seen to grow into and through the thermokarst cave ice and thus indicates that ice wedge growth was not terminated as a result of the modification.

The foliation planes consist as thin sediment bands. In some instances the sediment inclusion can be up to 5 to 10 mm thick, however, they are generally less than 1 mm thick. The air bubble inclusions are elongated approximately perpendicular to the foliation planes. In some instances, the air bubbles may run at an angle of 60 degrees from the foliation plane. Figure 4.15 shows several ice wedge sections. Figure 4.15 (a) shows a sediment rich zone. Only one core that was tested contained a sediment rich section. Figure 4.15 (b) shows typical wedge ice used in the testing program. The wedge ice was sampled horizontally from the tunnel walls. An effort was made to sample perpendicular to the soil-ice wedge contact. The goal was to obtain wedge ice with horizontal foliations or foliations perpendicular to the long axis of the core. The result was foliation planes that varied from 0 to 30 degrees from horizontal. A CT scan of a small portion of an ice wedge suggests that the volumetric components are 1.2% air, 1.9% sediment, and 96.9% ice. The image of the wedge ice used in the CT scan is shown in Figure 4.15 (c). From gravimetric and volumetric reduction of samples (n=11), the average volumetric components are 3.45% air, 0.29% sediment, and 96.40% ice. For the volumetric estimates, it was assumed that the density of ice is 0.9197 g/cm^3 and the specific gravity of soil particles is 2.68. The average frozen bulk density of the wedge ice was 0.894 g/cm^3. Figure 4.16 shows an ESEM micrograph of wedge ice. The sediment (or foliation) plane that was imaged show sediment particles that are randomly orientated. The air bubbles are circular in diameter and elongated. The lower left image shows a sediment plane cross cutting an air bubble. Sublimation of the ice indicated that the sediment was not just on the surface of the bubble but extends in the picture.

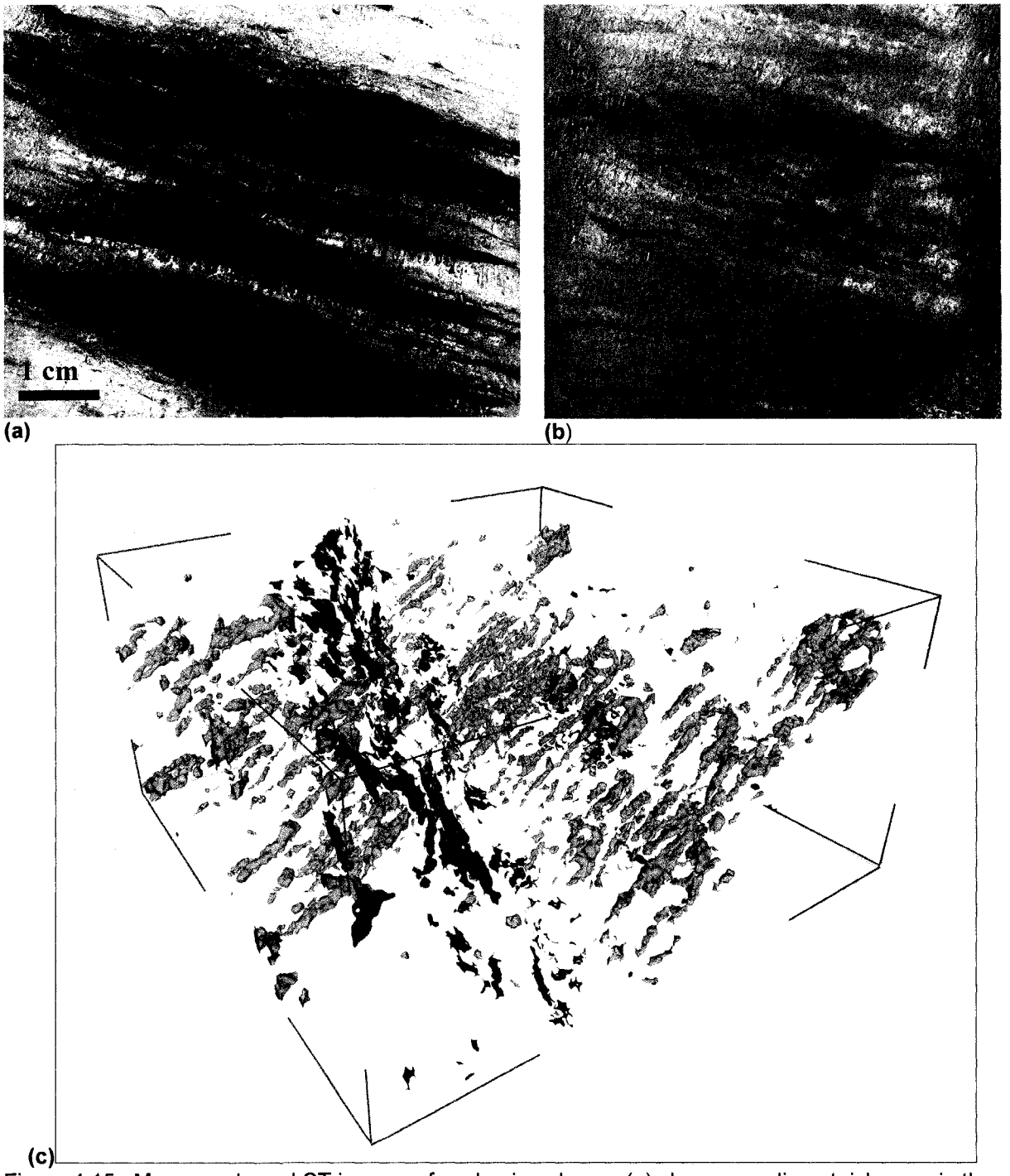

Figure 4.15. Macro scale and CT images of wedge ice. Image (a) shows a sediment rich zone in the wedge ice. Image (b) is typical of the wedge ice tested. Image (c) is a CT scan of wedge ice where gray objects represent air, the brown objects represent sediment, and the white matrix represents ice. Box height is 10 mm.

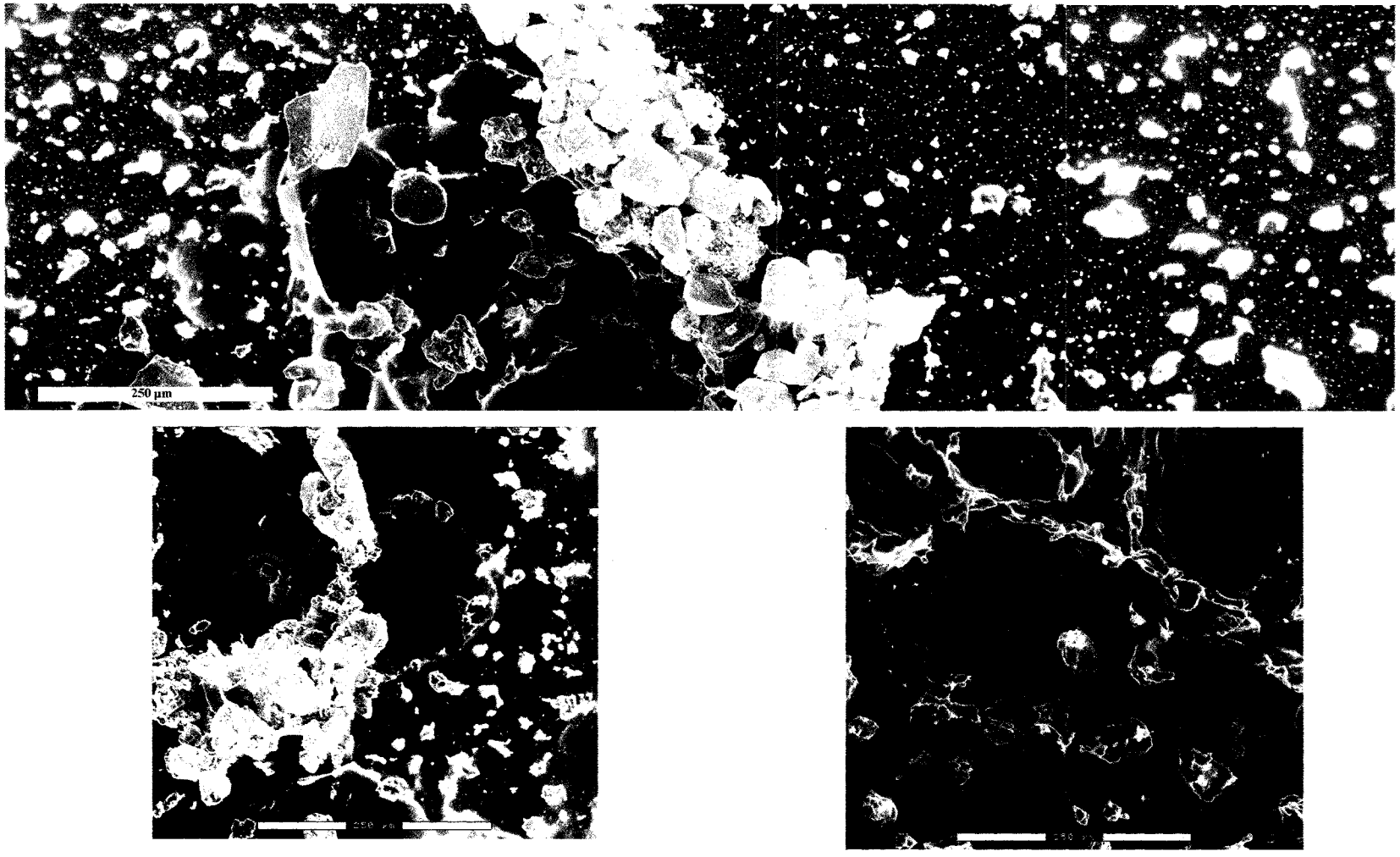

Figure 4.16. ESEM micrograph of wedge ice. The upper image is a 1.5 mm transect across a sediment foliation plane. The scale is 250 µm The two lower images show typical air pocket formed in the wedge ice. The lower left image shows a circular shape air bubble with a sediment plane crossing it. The lower right shows elongated are bubbles. Scale is 250 µm.

4.2.6 Matanuska Basal Glacial Ice and Glacial Ice

In addition to permafrost soils and massive ice from the permafrost tunnel, a few cores were tested from the Matanuska Glacier, Alaska. Basal ice is an ice facies that generally develops at the base of the glacial ice system. Basal ice features are exposed through thrust faults or the melting of ice. Basal ice is defined here as ice that contains sediment inclusion either in the form of sediment bands or dispersed sediment grains and is a deposit of basal glacial origin. The amount of ice varies with different basal ice facies. In this study, three samples were tested. One consisted of suspended sediment bands running diagonally across the sample. The second is a suspended facies with small sediment inclusion suspended in a highly icy matrix. The third sample contains micro-lenticular cryostructure superimposed with a stratified cryostructure. This sample was classified as Matanuska basal ice ML. Figure 4.17 shows the three basal ice samples and their associated cryostructure.

The Matanuska glacial ice has high optical transparency. Very small amounts of sediment inclusion occur and if present, are only found as single sediment grains. Crystal size appears to be 0.5 to 1 cm as viewed with the naked eye. The glacial ice generally contained thin bands of air bubble inclusions primarily concentrated along crystal boundaries. Figure 4.18 shows a macro image of the glacial ice used in experiments.

4.3 Water Content and Frozen Bulk Density

Utilizing all of the available data, the gravimetric water content vs. the frozen bulk density is plotted in Figure 4.19 for the three primary soil cryostructures. The total cumulative sample size is n=57. Easily seen on the curve are the distinct zones for the different soil cryostructures. Soils with vml and hml are grouped together as expected since they represent the same soil cryostructure. Instead of presenting soils with vml and hml together, they are shown separately as there were slight variations in the ice distribution between soils with vml and hml cryostructure. This was due to the difference in the sampling direction and changes in ice distribution along the strata profiles. Soils with RC and RM cryostructure are grouped in separate zones. The best fit regression is a simple power law. The gravimetric water content (ω) as a function of frozen bulk density (γ_{bf}) is shown in Equation 4.1.

$$\omega(\%) = 340.5 \cdot \gamma_{bf}^{-4.1} \qquad \text{Eq. 4.1}$$

(a)

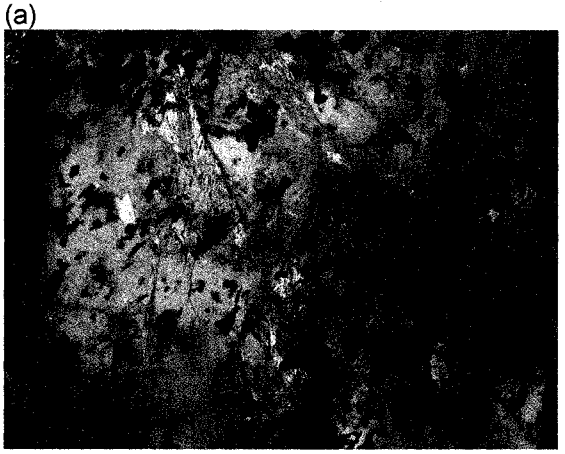

(b)

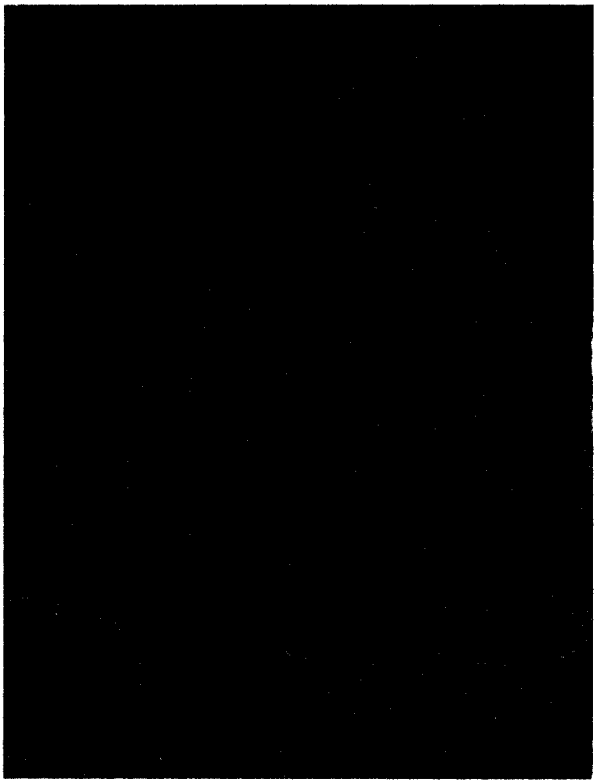

(c)

Figure 4.17. Matanuska basal ice facies tested include a) suspended stratified, b) suspended, and c) micro-lenticular, stratified.

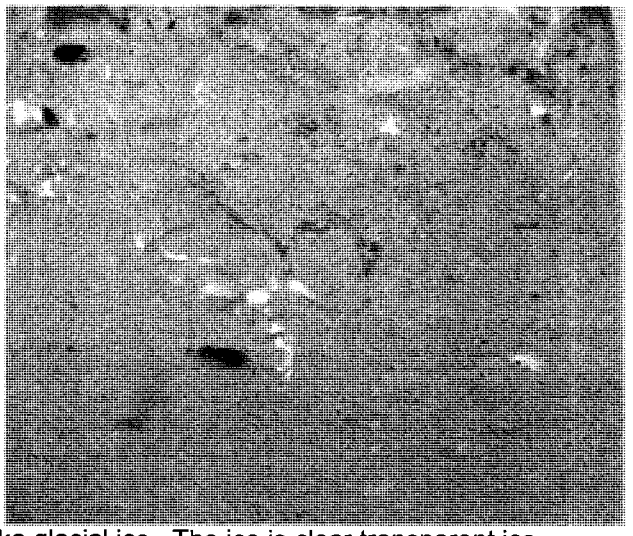

Figure 4.18. Matanuska glacial ice. The ice is clear transparent ice.

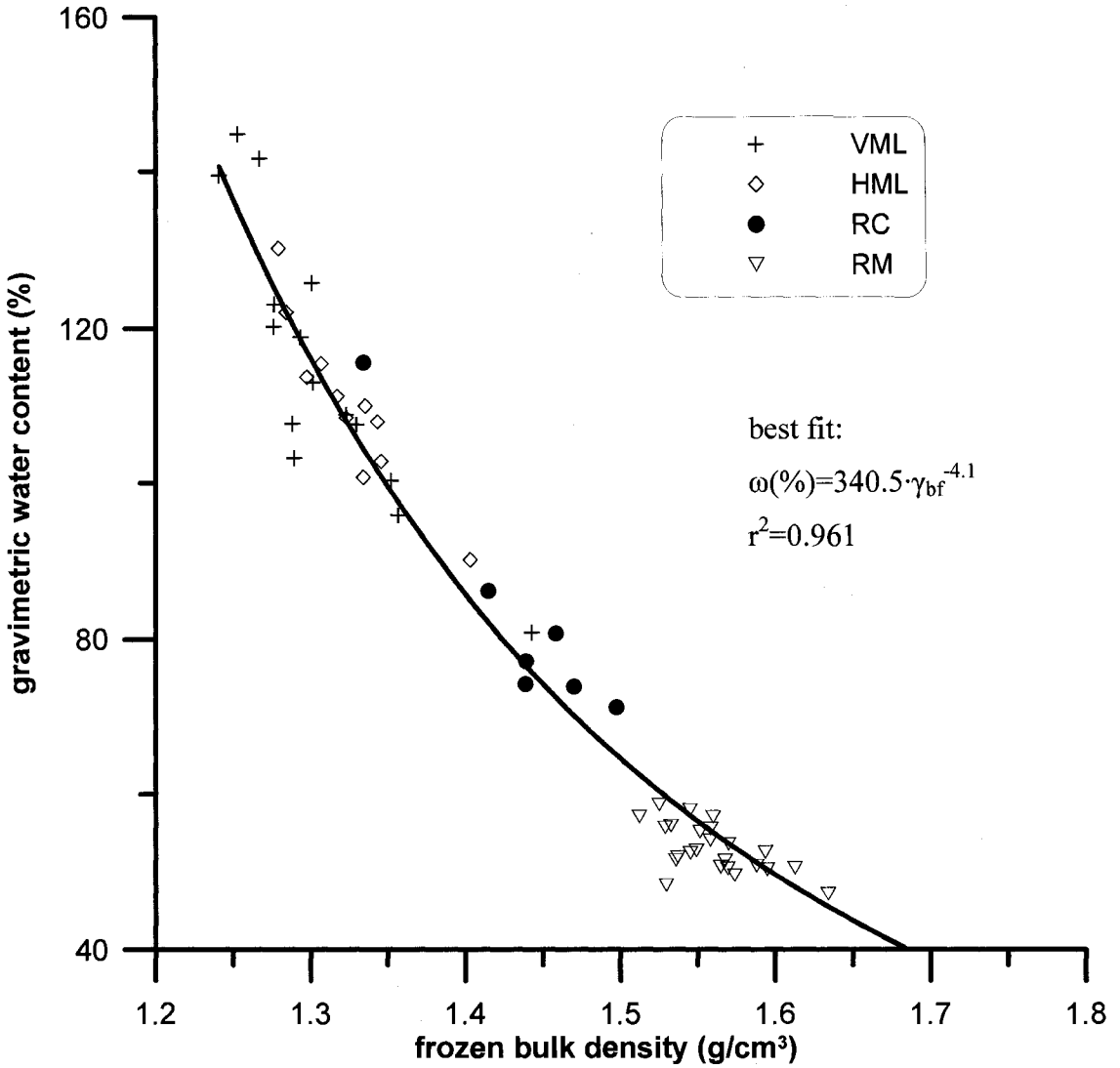

Figure 4.19. Gravimetric water content vs. frozen bulk density for soil cryostructures.

Table 4.2. Average gravimetric water contents and frozen bulk density for soil cryostructures

	VML	HML	RC	RM
Gravimetric water content (%)	115.5	110.3	82.8	52.9
Frozen bulk density (g/cm^3)	1.31	1.32	1.44	1.56
Sample size	15	11	7	24

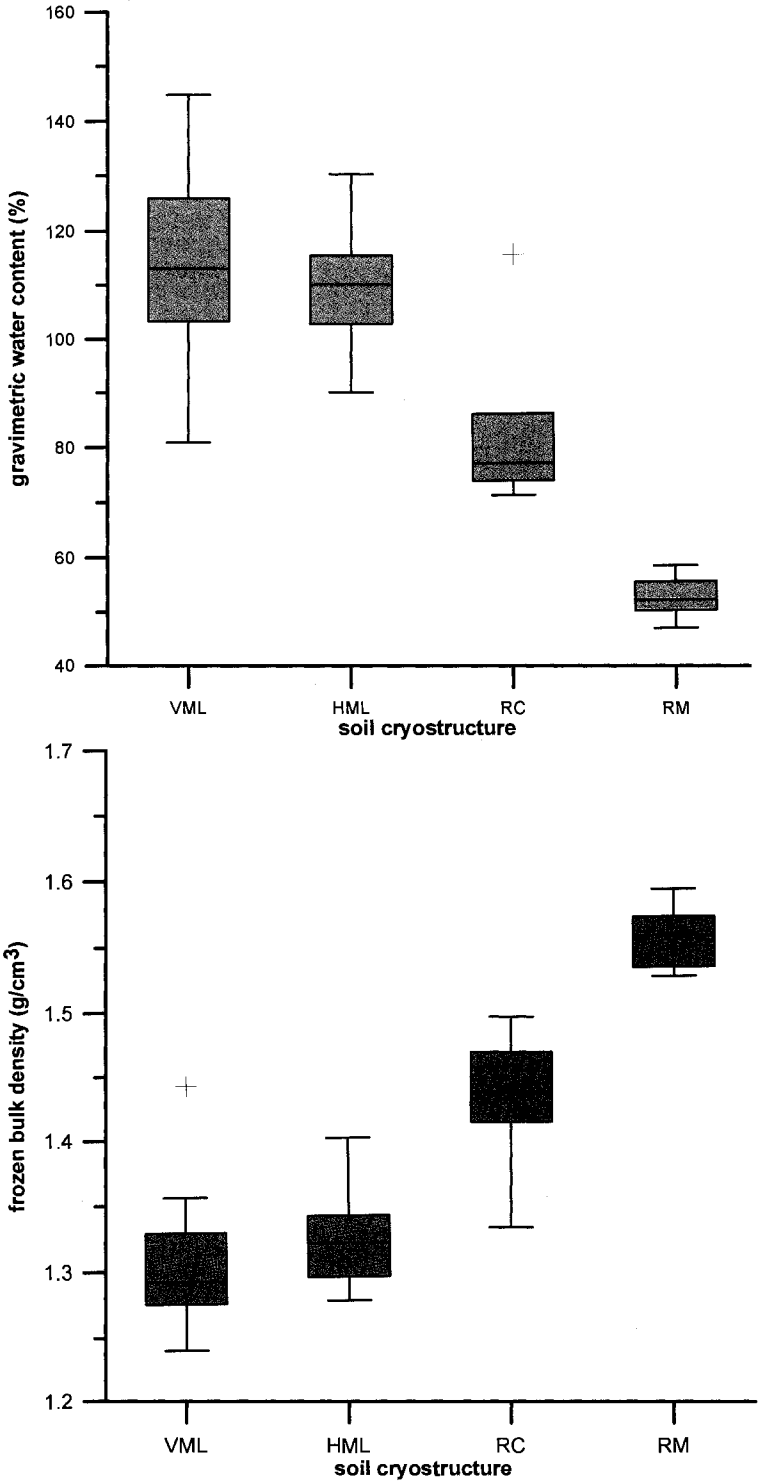

Figure 4.20. Whisker plot showing the breakdown of gravimetric and frozen bulk density for the four primary silt soils with vml, hml, RC, and RM cryostructures.

Table 4.2 gives a summary of the average values for the four silty soils with cryostructures defined in this study. Figure 4.20 shows the relative distribution of water content and frozen bulk density for the four primary soil cryostructures used from the permafrost tunnel

For the permafrost tunnel silt, the soil cryostructures appear to have a relationship to water content and frozen bulk density. Some overlap occurs for the various cryostructures. However, they generally tend to fall into distinct regions. Based on this concept, it is potentially possible to define the various cryostructure based on water content and frozen bulk density alone. In addition to the soils with remolded-massive cryostructure, two additional soils with massive cryostructure were tested from the tunnel. The first soil was undisturbed silt with massive cryostructure (shown in Figure 4.6 (above)) which had a gravimetric water content of 50.8% and a frozen bulk density of 1.59 g/cm^3. The water content is similar to the silt with remolded-massive cryostructure. The second soil was undisturbed sandy silt with massive cryostructure which had a gravimetric water content of 38.5% and frozen bulk density of 1.78 g/cm^3.

4.4 Unfrozen Water Content

Measurements of the volumetric unfrozen water content were conducted on undisturbed cores sampled from the CRREL permafrost tunnel. A Vitel Hydra Probe (Stevens Water Monitoring Systems Inc.) was used for the measurements. The Hydra Probe was designed to measure the volumetric water content of unfrozen soils. Recently, it has been used to measure unfrozen water content (Romanovsky and Osterkamp, 2000; Yoshikawa and Overduin, 2005). The Hydra Probe is a 50 MHz FDR (frequency domain reflectometry) capacitance probe, which measures the bulk dielectric constant.

A Campbell Scientific CR10X data logger with a switched 12V excitation was used to record measurements. The 12V excitation was applied just before measurements and switched off once the measurements were completed. Measurements were performed every 10 minutes. The probe output consists of four voltages. Voltages 1 through 3 relate to the electrical properties of the soil. The fourth voltage measures the temperature. In the case of the hydra probes used, the temperature is measured in the head of the instrument. The dielectric constant and volumetric water contents are determined by inserting the four measured voltages into a proprietary binary computer software program. The output parameters include the real and imaginary part of the dielectric constant, probe temperature, volumetric water content, salinity, and soil conductivity.

The purpose of this phase of the program was to get a general idea about the unfrozen water content in relationship to the soil cryostructure. The soil cryostructures used include horizontal micro-lenticular (hml), vertical micro-lenticular (vml), and remolded-massive (RM), and reticulate-chaotic (RC). Wedge ice was also tested. The probes were installed into undisturbed permafrost cores taken from the CRREL permafrost tunnel. Each core was trimmed parallel with use of a diamond tipped circular chop saw. Each sample was then measured and weighed to determine the frozen bulk density. Pictures were taken of each sample. Using a jig that matched the probe tine configuration, four holes were drilled into the sample using an upright drill press. The holes were created using a 3.97 mm (0.156 in) diameter drill bit. On either side of the probe, holes were drilled for the insertion of thermistor probes located 180 degrees apart. The Hydra Probes were then inserted into the sample. It was found that a tight fit was achieved. Once inserted, the probe was extremely difficult to remove from the soil. After insertion of the probe, each sample was wrapped with plastic wrap to minimize sublimation. For each temperature cycle, two soil samples were tested. The samples were wrapped together and then placed in an insulated polystyrene box which was transferred to an ESPEC LHU-113 environmental chamber. The data logger was located outside of the chamber. The chamber was then set to a temperature between -8°C to -11°C. The sample was allowed to cool to equilibrium with the environmental chamber set point. Data was recorded during the cooling process. The main measurements occurred on the warming side. The procedure used for temperature control of the warming side is described below. The temperature was increased by 2°C increments every 24 hours up to -6°C. The temperature was then increased every 24 hours by 1.5°C increments up to -3°C. The temperature was then increased every 24 hours by 1°C increments to -1°C. The temperature was then adjusted by 0.2°C to 0.5°C increments up to 0°C. Temperature adjustments between -1°C and 0°C were made based on temperature equilibriums rather than defined time increments. The last 1°C of warming generally took over one week to complete. Total test times for the two samples ranged form 2 to 3 weeks. The ending temperature ranged form -0.3°C to -0.1°C.
As the thawing temperatures are approached, it is important to adjust the temperature increments slowly. In order for the phase change (in our soils, this primarily occurred for temperatures warmer than -2°C) to be in balance with the temperature measurements, the temperature increase needs to occur slowly. If large temperature increments are used in this region, the temperature and phase measurements do not equilibrate with each other. For temperatures colder than -2°C, the phase transitions of water do not play a significant role and therefore, it was found that larger temperature adjustments could be made without significant effects. For other soils with significant amounts of unfrozen water at colder temperature, smaller temperature adjustments would likely need to be made.

Table 4.3 shows the basic weight and volumetric data of the samples used in this study. Figures 4.21 to 4.23 show the volumetric unfrozen water content and the real part of the dielectric constant vs. temperature for the soil cryostructures. The curves are separated into soils with micro-lenticular cryostructure (vml and hml), soils with remolded-massive (RM) cryostructure, and soils with reticulate-chaotic (RC) cryostructure. Figure 4.24 shows the data curve for the real part of the dielectric constant vs. temperature for wedge ice, since the probe output data did not indicate any unfrozen water. However, the real part of the dielectric constant indicates a change with temperature especially for temperatures warmer than -0.5°C. Table 4.4 summarizes and condenses the volumetric unfrozen water content in tabular form. The most common expression relating the unfrozen water content to temperature was presented by Anderson and Tice (1973) in the form of a simple power law. The empirical coefficients are shown in Table 4.5 for the volumetric unfrozen water determined in this study. The relationship in a dimensionally stable form (Tice et al., 1989) is shown in Equation 4.2.

$$w_v = A\left(\frac{\theta}{\theta_{-1}}\right)^b \qquad \text{Eq. 4.2}$$

Where w_v is the volumetric unfrozen water content, θ is the temperature in °C, θ_{-1} is -1°C, A and b are experimentally determined coefficients. Equation 4.2 is generally expressed in the terms of gravimetric unfrozen water content. However, in this work, the equation is adopted to volumetric unfrozen water content.

It was assumed that the manufacturer output data in regards to volumetric unfrozen water and real part of the soil dielectric constant represent the actual soil values. The values expressed in Figures 4.21 to 4.24, are based on the manufacturers output values. The validity of this assumption can be questioned. Yoshikawa and Overduin (2005) evaluated commercial FDR and TDT sensors for determining unfrozen water content in relation to NMR analysis. It was concluded that the probes are sensitive to changes in unfrozen water content. However, it was also concluded that the commercial probes yield higher unfrozen water content values than NMR analysis. It was assumed that the NMR results represent true unfrozen water contents. As a result, calibration equations were based on the real part of the dielectric constant in relationship to the unfrozen water content as determined from NMR analysis. A calibration was given for a Fairbanks silt (sampled from a road cut at 7 mile Chena Hotsprings Road) based on data for a Hydra probe. The Fairbanks silt was reported to have a gravimetric water content of 28.4%, a

Table 4.3. Properties of undisturbed soil samples tested for unfrozen water content using the Vitel Hydra Probe.

Vitel Probe sample number	Soil cryostructure:	frozen bulk density (lb/ft^3)	frozen bulk density (g/cm^3)	Gravimetric water content, w (%)	dry density (g/cm^3)	volumetric ice content (%)	volumetric sediment content (%)	volumetric air content (%)
V1	RC	91.06	1.459	80.79	0.807	70.87	29.13	--
V2	RC	89.83	1.439	74.33	0.825	66.71	33.29	--
V3	HML	81.00	1.297	113.79	0.607	75.09	24.91	--
V4	VML	77.46	1.241	139.48	0.518	78.58	21.42	--
V5	IW	55.80	0.894	--	0.894	97.21	0.05	2.82
V6	IW	55.68	0.892	--	0.892	96.56	0.20	3.35
V7	RM	99.07	1.587	50.00	1.058	57.52	42.48	--
V8	RM	97.24	1.558	54.00	1.011	59.39	40.61	--
V9 (PF tunnel RM CORE 12)	RM	96.73	1.549	52.70	1.015	58.14	41.86	--
V10 (PF tunnel RM CORE 13)	RM	97.38	1.560	57.00	0.994	61.58	38.42	--
V11	VML	79.10	1.267	141.69	0.524	80.77	19.23	--
V12 (PF tunnel 032506 0+98b RWH Relax)	VML	78.22	1.253	144.82	0.512	80.59	19.41	--
V13	VML	90.10	1.443	80.92	0.798	70.19	29.81	--
V14 (PF tunnel 121906 2+35 LWH RC CORE b)	RC	93.49	1.498	71.35	0.874	67.80	32.20	--

note: If a description is given below the vital probe sample number, then the sample is from a tested core used in the relaxation part of the testing program.

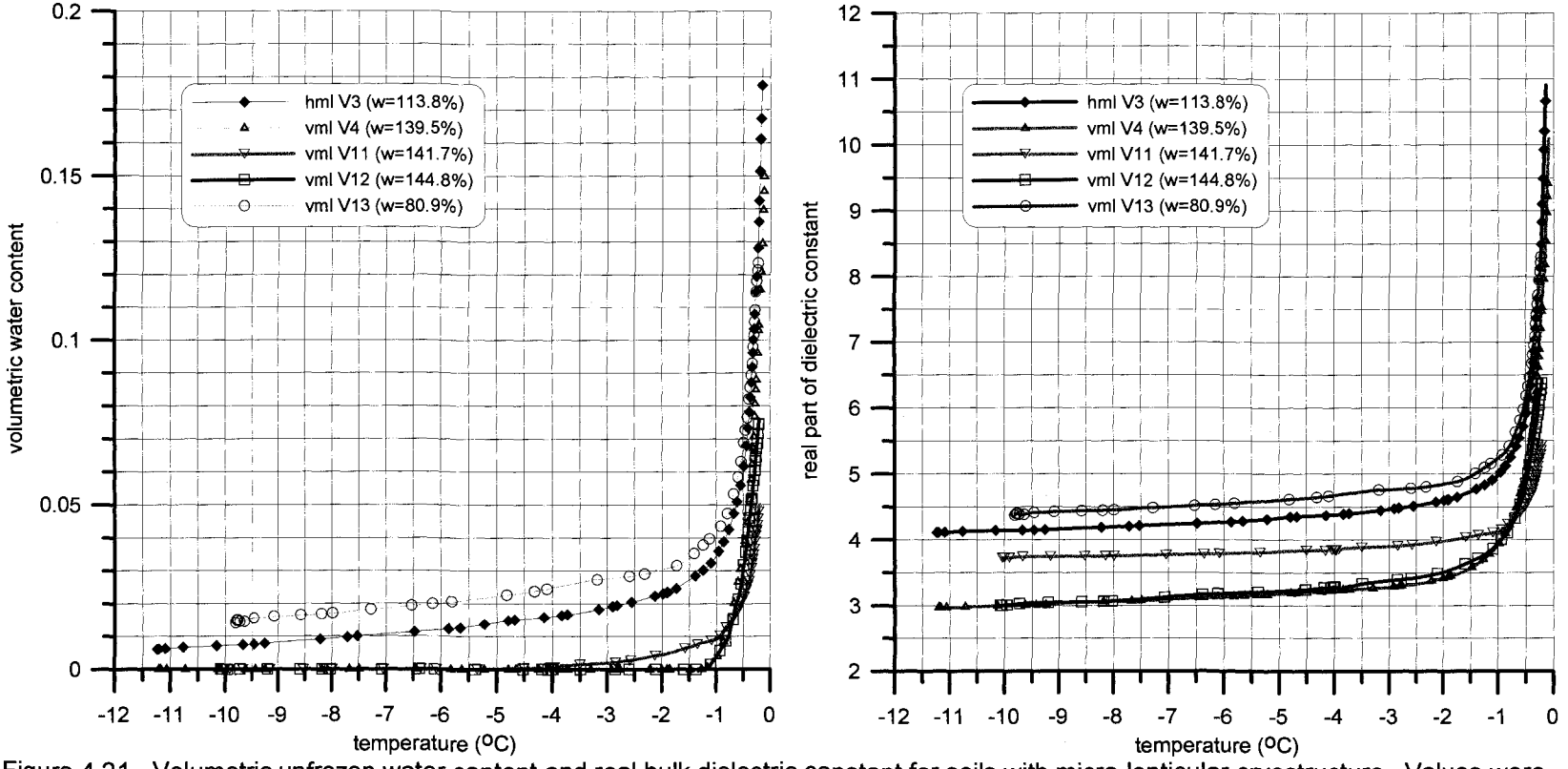

Figure 4.21. Volumetric unfrozen water content and real bulk dielectric constant for soils with micro-lenticular cryostructure. Values were measured with a Vitel Hydra Probe. Data symbols are plotted for every 50 data points. Solid curves are plotted from data recorded every 10 minutes.

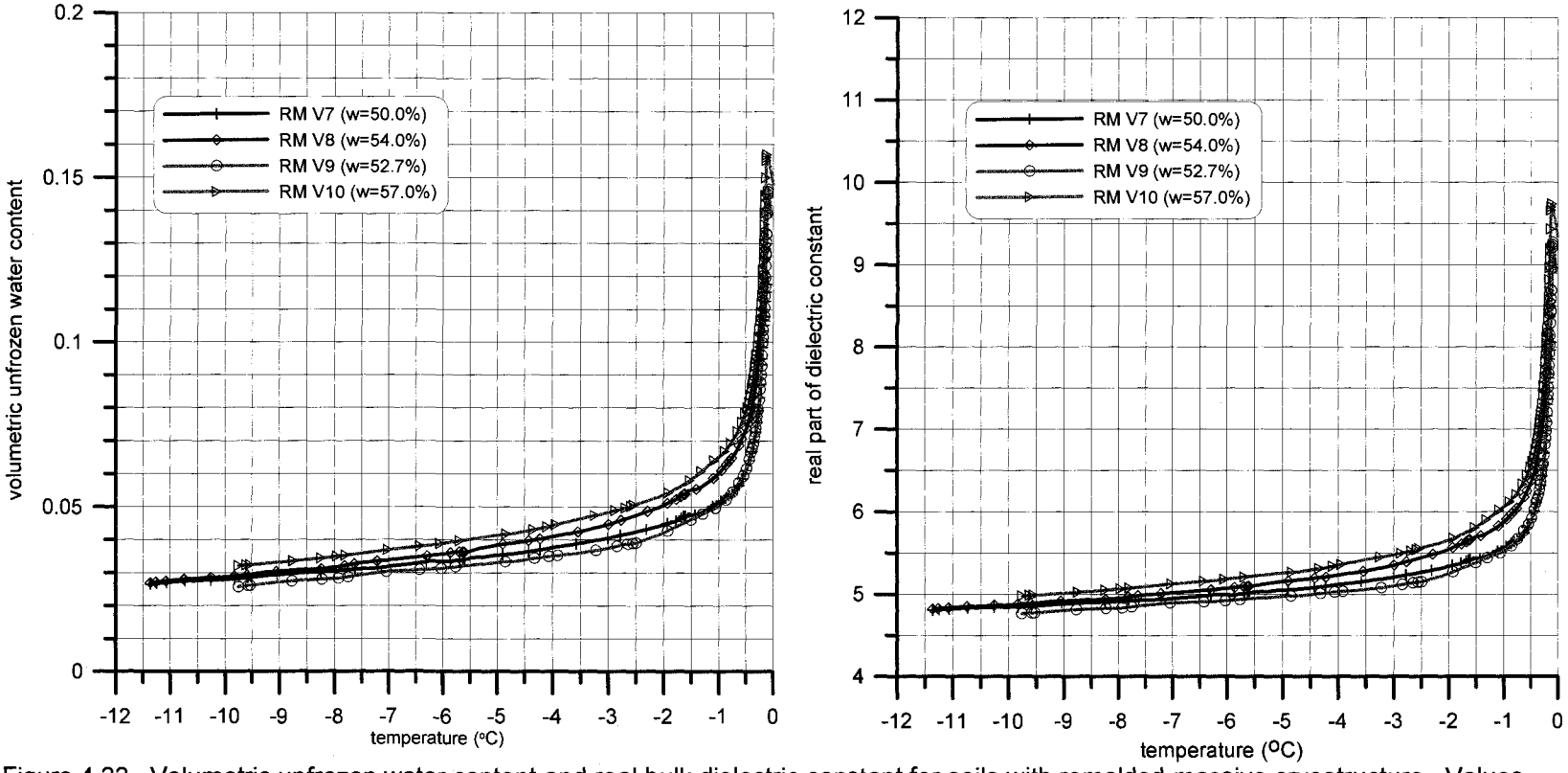

Figure 4.22. Volumetric unfrozen water content and real bulk dielectric constant for soils with remolded-massive cryostructure. Values were measured with a Vitel Hydra Probe. Data symbols are plotted for every 50 data points. Solid curves are plotted from data recorded every 10 minutes.

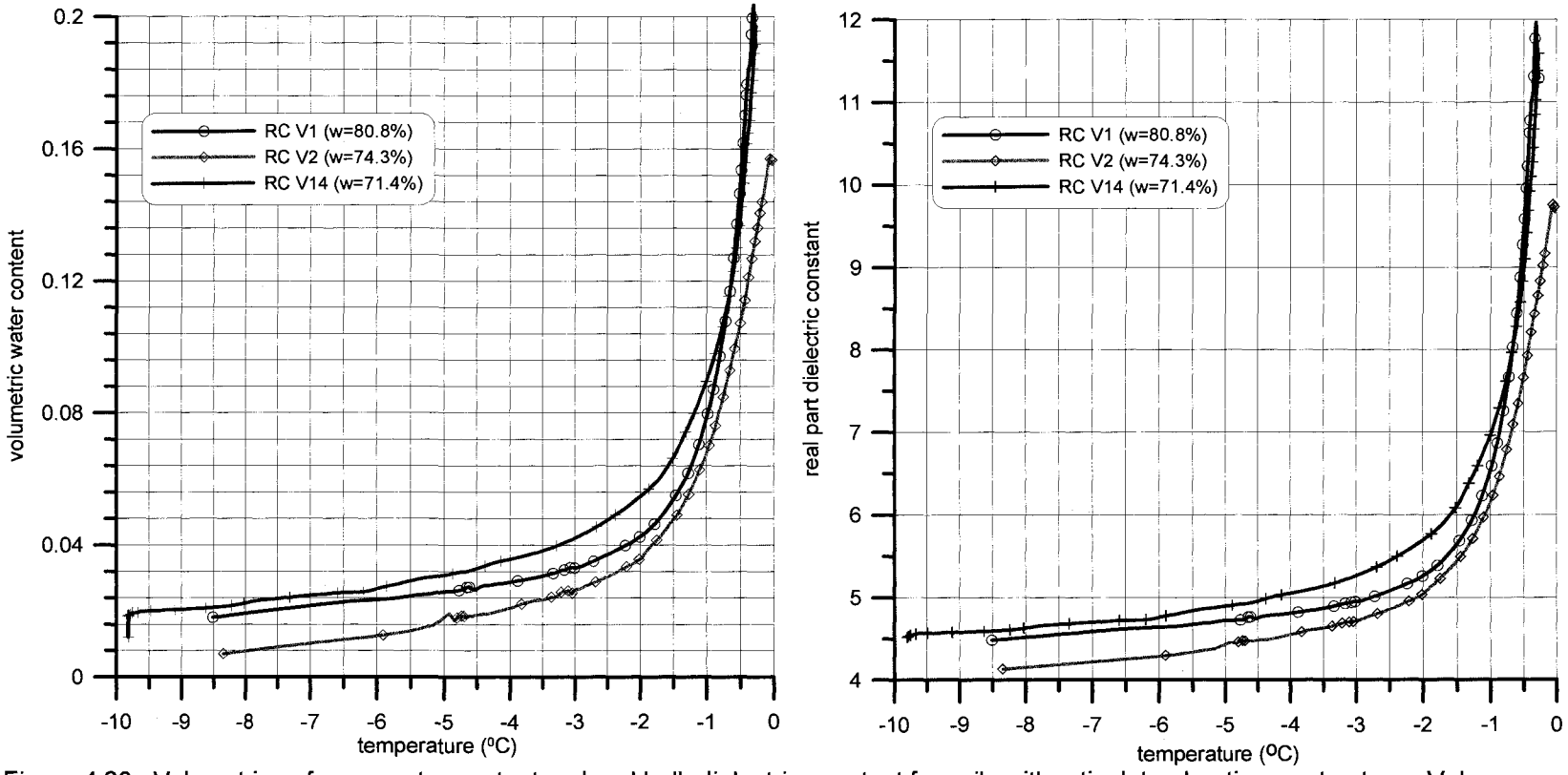

Figure 4.23. Volumetric unfrozen water content and real bulk dielectric constant for soils with reticulate-chaotic cryostructure. Values were measured with a Vitel Hydra Probe. Data symbols are plotted for every 50 data points. Solid curves are plotted from data recorded every 10 minutes.

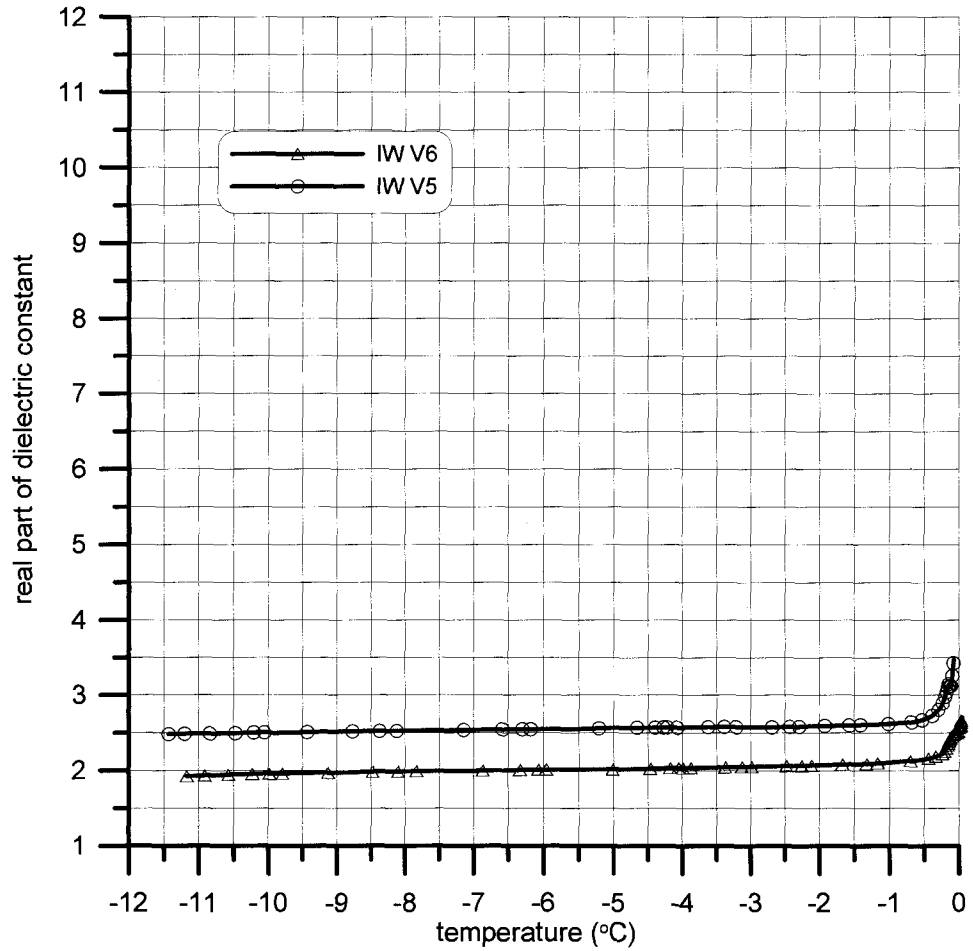

Figure 4.24. Real bulk dielectric constant for wedge ice. Values were measured with a Vitel Hydra Probe. Data symbols are plotted for every 50 data points. Solid curves are plotted from data recorded every 10 minutes. Volumetric unfrozen water was not plotted as the proprietary software output data indicated no unfrozen water (see text).

Table 4.4. Summarized volumetric unfrozen water content determined from Vitel Hydra probe. Values are expressed as volume fractions.

	temperature (°C)													
soil cryostructure and vitel sample number	-11	-10	-9	-8	-7	-6	-5	-4	-3	-2	-1	-0.5	-0.3	-0.2
RC V1	--	--	--	0.0192	0.0216	0.0234	0.0257	0.0288	0.033	0.0426	0.0785	0.15	0.205	--
RC V2	--	--	--	0.0078	0.01	0.0125	0.0183	0.021	0.0266	0.0359	0.0678	0.1072	0.1309	0.1424
HML V3	0.0064	0.0072	0.0082	0.0093	0.0107	0.012	0.0142	0.016	0.0188	0.023	0.0343	0.0597	0.1	0.1434
VML V4	0	0	0	0	0	0	0	0	0	0	0.0032	0.035	0.0703	0.1057
IW V5	0	0	0	0	0	0	0	0	0	0	0	0	0	0.0005
IW V6	0	0	0	0	0	0	0	0	0	0	0	0	0	0
RM V7	0.0271	0.028	0.0294	0.0306	0.0319	0.0336	0.0354	0.0377	0.0406	0.0447	0.0514	0.0609	0.0743	0.0942
RM V8	0.0276	0.0288	0.0305	0.0317	0.0339	0.0358	0.0385	0.0411	0.0447	0.0504	0.0601	0.0734	0.0892	0.1114
RM V9	--	--	0.0272	0.0283	0.0304	0.0315	0.0332	0.0352	0.0376	0.0422	0.0504	0.0608	0.0759	0.0942
RM V10	--	--	0.0332	0.0349	0.037	0.039	0.0415	0.0444	0.0484	0.0537	0.0652	0.0788	0.0969	0.119
VML V11	--	0	0	0	0	0.00004	0.00018	0.00056	0.00192	0.00449	0.0092	0.0215	0.0354	0.0501
VML V12	--	0	0	0	0	0	0	0	0	0	0.004	0.0306	0.0574	0.0758
VML V13	--	--	0.0162	0.0171	0.0186	0.0202	0.0224	0.0249	0.0277	0.0304	0.0419	0.0674	0.1005	0.1273
RC V14	--	--	0.0205	0.0225	0.0247	0.0267	0.0309	0.0358	0.0421	0.0548	0.0893	0.1398	0.188	--

Table 4.5. Equation parameters and r^2 values for Equation 4.2.

Sample/Eq. coefficients	RC V1	RC V2	HML V3	VML V4	IW V5	IW V6	RM V7	RM V8	RM V9	RM V10	VML V11	VML V12	VML V13	RC V14
A	0.08261	0.0536	0.04021	0.00170	2.2E-10	n/a	0.0556	0.0630	0.0553	0.0685	0.0049	0.0034	0.0495	0.0871
b	-0.7951	-0.5638	-0.7316	-2.6794	-7.9776	n/a	-0.3038	-0.3335	-0.3507	-0.3353	-1.8852	-2.3934	-0.5301	-0.6700
r^2	0.991	0.873	0.993	0.616	0.632	n/a	0.979	0.993	0.970	0.981	0.803	0.7182	0.988	0.994

note: parameters A and b apply to power equation of the form $w_v = A(\theta/\theta_{-1})^b$. Where w_v is volumetric unfrozen water content, θ is temperature in °C and θ_{-1} is -1°C, A and b are experimentally determined parameters.

volumetric water content of 47.9%, a S.G. of 2.65, and a dry density of 1.38 g/cm^3. The calibration equation for Fairbanks silt is expressed in Equation 4.3.

$$\theta_v = 0.000009 \cdot e^{2.0087 \cdot \varepsilon_{real}} \qquad \text{Eq. 4.3}$$

Where θ_v is the volumetric unfrozen water content and ε_{real} is the real part of the soil dielectric constant. The calibration equation was applied to the real part of dielectric constant as determined from the Hydra probe. It was found that the calibration equation yielded much larger volumetric unfrozen water contents than the manufacturer output values. This is in contradiction to observations by Yoshikawa and Overduin (2005). As temperatures warmed, the predicted volumetric unfrozen water content increased extremely quickly. This results since the calibration function is an exponential relationship as shown in Equation 4.3. It was felt that the values determined from Equation 4.3 are unrealistic in application to the soil tested in this study. The potential reason for this is that the calibration is based on a temperature range of 0°C to -50°C.

Romanovsky and Osterkamp (2000, Fig. 2, p. 224), show a curve depicting the Hydra probe measured volumetric unfrozen water content in comparison to a calculated volumetric unfrozen water content based on best fit modeling of thermal conditions. It was found that the values are in general agreement. It is our interpretation that the measured values reported are direct probe output values. Based on this study, there seems to be some support for the measured values from the Vitel Hydra Probe. Comparing volumetric unfrozen water curves for similar silts with massive cryostructure (Tice et al, 1989; Romanovsky and Osterkamp, 2000; Bray, 2003, Huang et al., 2004), the values determined in this study from the Hydra probe appear comparable.

In both studies described above (Yoshikawa and Overduin, 2005; Romanovsky and Osterkamp, 2000), the average gravimetric water content is less than 30% for the silt samples. In comparison, the gravimetric water contents range from 50 to 144.8% for the soils tested in this study. This translates into soil that contains significantly larger quantities of ice. As is evident in this study, the greater the amount of ice, the lower the unfrozen water content. The values of the A coefficient listed in Table 4.5 for Equation 4.2, are significantly lower than for those listed in the literature for similar silts (Tice et al, 1989; Romanovsky and Osterkamp, 2000; Yoshikawa and Overduin, 2005). We attribute this to the large volume of ice found within the soils. Figure 4.25 shows the relationship between coefficients A and b to volumetric ice content. A rough linear relationship can be seen for coefficient A vs. volumetric ice content. The apparent outliers

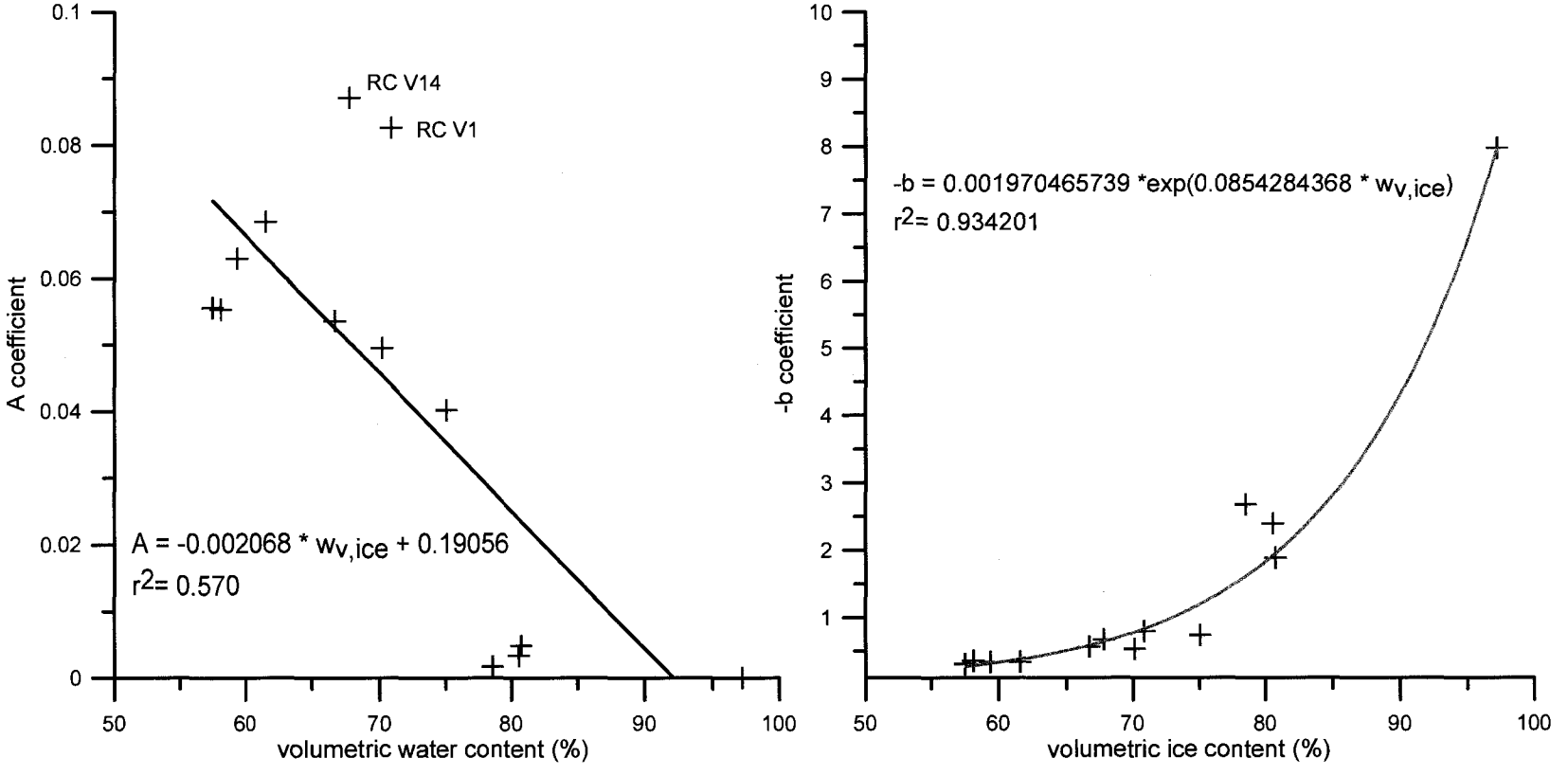

Figure 4.25. The A and b coefficients in Equation 4.2 expressed as a function of volumetric ice content.

appear to be RC V1 and RC V14. The ice is not distributed uniformly in soils with reticulate-chaotic cryostructure. The sediment between ice lenses contains a lower volume of ice than is predicted by the total sample ice volume (water contents). It seems reasonable to assume that the probe is actually measuring a soil with a lower ice content which would in effect pull the two soils closer to the trend. When -b is plotted against volumetric ice content, an exponential relationship is seen. Therefore the b coefficient appears to have a direct relationship to the volume of ice (water content) of the soil.

Figure 4.26 shows the volumetric unfrozen water content relative to sediment volume for temperatures of -0.3°C, -0.5°C, -1°C, -2°C, -3°C, -4°C. For temperatures of -2°C, -3°C, and -4°C the volumetric unfrozen water content for the undisturbed soils (soil with micro-lenticular and reticulate-chaotic cryostructure) and remolded soils (soil with remolded-massive cryostructure) show a correlation to the volume of sediment. This can be contributed directly to the sediment influence due to adsorbed unfrozen water films and capillary films. As the temperature warms to -1°C, soils with remolded-massive cryostructure deviate from the trend shown by the undisturbed soils. As the soils continue to warm past -1°C, the volumetric unfrozen water content trend for the remolded soils progressively deviates from the undisturbed soils since the volumetric unfrozen water content increases at a faster rate than the remolded soil. The average increase in the volumetric unfrozen water from -1°C to -0.3°C was 0.096 for soils with reticulate-chaotic cryostructure, 0.051 for soils with micro-lenticular cryostructure, and 0.027 for soils with remolded-massive cryostructure. The development of unfrozen water at the boundary between ice crystals is not a controlling mechanism for the increase in the volumetric unfrozen water as evidenced by the smaller increase in the unfrozen water for soils with micro-lenticular cryostructure. Deionized water was used to create the remolded soils in contrast to the natural ground water found in the undisturbed soils. It is likely that the soil water in the undisturbed soils have a slightly higher salinity. An increase in the salt content would lead to an increase in the volumetric unfrozen water content.

Insertion of the probes into wedge ice was found to be very difficult. The wedge ice is highly sensitive to fracture during drilling of the holes and insertion of the probe. In an attempt to prevent fracture of the sample during insertion of the probe, the tines were heated. The result was a small thaw pocket that developed just under the head of the hydra probe in the IW V6 sample. As result, the data presented for the wedge ice may be influenced to some degree by the air pocket. The result would be a dielectric constant which is smaller than reality. However, it was felt that the data was reasonable and was included to show the trend for a highly icy sample.

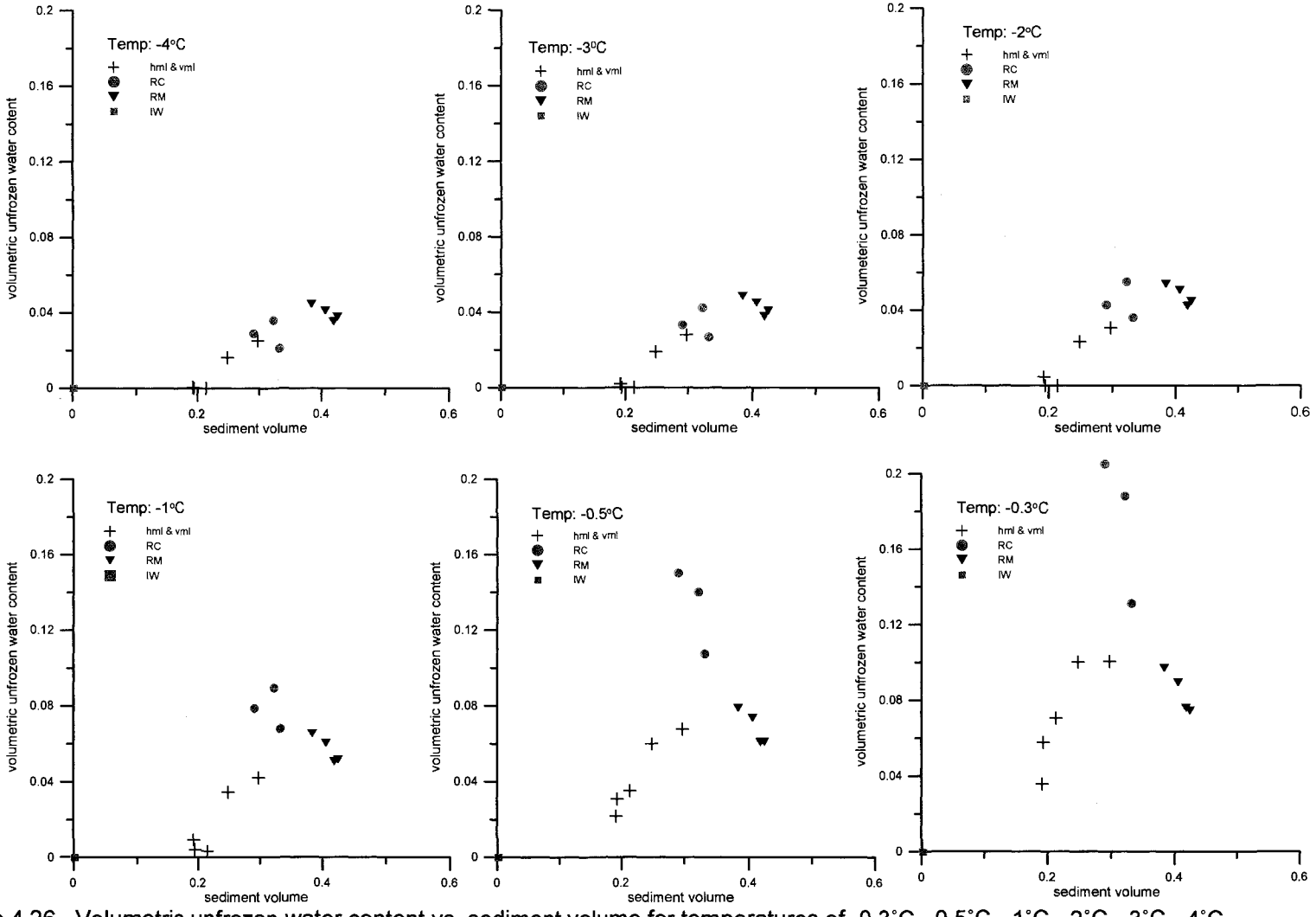

Figure 4.26. Volumetric unfrozen water content vs. sediment volume for temperatures of -0.3°C, -0.5°C, -1°C, -2°C, -3°C, -4°C.

Qualitatively, the results can be summarized as follows. The larger the ice content of the soil, the lower the volumetric unfrozen water content for most of the temperature range measured. At a temperature of -0.2°C, soils with micro-lenticular cryostructure tend to have volumetric unfrozen contents which exceed those for soils with remolded-massive cryostructure. Changes in the unfrozen water content of wedge ice are noticeable at temperatures warmer than -0.5ºC. This is primarily registered as a change in the real part of the dielectric constant. It was observed that as the temperatures warm past -2°C the volumetric unfrozen water content for undisturbed soils increase at a faster rate than the remolded soils. This was attributed to the potential increase of the soil water salinity in the undisturbed soils as compared to the remolded soils which were created using deionized water. The results suggest that the volume of sediment is an important factor controlling the volumetric unfrozen water. The results also suggest that volumetric water contents are influence by the quantity of ice as well as the ice distribution. Evenly distributed, high ice contents result in lower volumetric unfrozen water contents (i.e. soils with micro-lenticular cryostructure). Soils with high ice contents, but with a portion of that ice distributed in large lenses results in higher volumetric unfrozen water contents due to the concentration of mineral grains (i.e. soils with reticulate-chaotic cryostructure).

To improve this work, a proven method needs to be applied to verify the results of the Hydra probe. Currently, the most accepted method for reliability is NMR analysis. The difficulty with NMR analysis is the sample size is generally quite small. The small sample size creates difficulties when testing undisturbed soils with variable ice distribution patterns. Despite some issues with true accuracies of the Hydra probes, the trends are well defined as the testing method did not change from sample to sample.

4.5 Summary

A detailed description of the soils, soil cryostructure, and ice facies was supplied. Soils with micro-lenticular cryostructure contain large quantities of ice. Micro imaging suggests that the soil is suspended in an icy matrix. Undisturbed silts with massive cryostructure show an open sediment packing distribution suggesting that freezing conditions occurred under a super saturated, unconsolidated state. Soils with remolded-massive cryostructure show a small volume of air. The sediment grains show tighter packing as compared to the undisturbed silt with massive cryostructure. Soils with reticulate-chaotic cryostructure shows distinct ice lenses separated by silt with massive cryostructure. The sediment packing between ice lenses has greater similarities to soils with remolded-massive cryostructure than to undisturbed silt with massive cryostructure. The ice facies tested show variability in sediment and ice distributions.

Wedge ice contains approximately 3% air by volume and less than 1% sediment by volume. Matanuska basal glacial ice is variable with high sediment volume to nearly pure ice. Matanuska glacial ice shows large crystals and ice of high optical clarity.

The gravimetric water contents are directly related to the soil cryostructure. The different soil cryostructure are generally grouped into distinct zones based on gravimetric water content and thus frozen bulk densities. If a thorough cryostructure study is performed for a specific permafrost deposit, it may be possible to relate the soil cryostructure directly to gravimetric water contents.

The volumetric unfrozen water content correlates with soil cryostructure. In general, the more ice presents in the soil, the lower the volumetric unfrozen water contents for a given temperature. The exception is for temperatures right at the phase change boundary where icy soils tend to have a significant volume of unfrozen water as would be expected due to the higher initial volume of ice (water) of the soil. The volume of sediment influences the volumetric unfrozen water content. Soils with reticulate-chaotic cryostructure show the highest volumetric unfrozen water. Soils with micro-lenticular cryostructure show the lowest volumetric unfrozen water. Wedge ice for the temperatures tested show lower volumetric unfrozen water contents than the soils tested in the study. In general, the frozen silts do not show appreciable changes in the volumetric unfrozen water content when soil temperatures are colder than -2°C.

Chapter 5: Testing Equipment and Procedures

In Chapter 4, a discussion of the various frozen soils, ice facies, and soil cryostructures used in this testing program were presented. The purpose of this section is to describe the sampling methods, testing equipment, and test procedures used. Section 5.1 looks at the sampling methods. Section 5.2 focuses on the equipment and methods used for constant stress creep (CSC) tests. Section 5.3 focuses on the equipment, methods, and procedures used during the relaxation test portion of the testing program.

5.1 Field Sampling of Soils

One of the focuses of this program was to look at the mechanical behavior of undisturbed soils in contrast to remolded soils. Undisturbed soils were sampled from the CRREL Permafrost tunnel, Fox, Alaska. The permafrost geology and description of soil types can be found in Chapters 3 and 4. Two types of core barrels were used to obtain undisturbed samples. The first is the SIPRE corer which consists of a stainless steel barrel with flighting running from the cutters to the top of the auger. The auger is approximately 1 m in length. The resulting core diameter is approximately 7.1 cm (2.8 inches). The auger is powered by a portable motor. The cutting teeth consist of 30 degree angled carbide inserts. The SIPRE corer cuts into ice rich permafrost soils effectively when the teeth are sharp. The second corer consisted of a continuous diamond concrete coring bit. The coring bit was driven by a large capacity handheld drill used for concrete coring. This type of auger was very ineffective for wedge ice and ice sampling, but worked adequately for permafrost soils. A small degree of melting generally occurred with this coring method. Any melt "mud" on the outside of the sample was removed immediately upon extraction of the core from the core barrel.

The bulk of the samples were extracted by coring horizontally into the wall of the permafrost tunnel. The two primary reasons for horizontal coring were the ability to accurately determine the soil cryostructure and the ease of coring and sample extraction. Samples obtained from horizontal coring include soils with vertical micro-lencticular cryostructure, soils with reticulate-chaotic cryostructure, soils with massive cryostructure, and wedge ice. Vertical coring met with limited success in that obtaining a uniform cryostructure throughout the length of the testable core was difficult. When necessary to obtain cores in the vertical direction (i.e. perpendicular to sediment deposition), soil blocks were removed from the wall of the tunnel. The blocks were then sampled vertically from the top of the soil block. This was the primary method of obtaining soils with horizontal micro-lenticular cryostructure.

Upon removal of the soil samples from core barrels, the cores were immediately double wrapped. The samples were first wrapped with a layer of plastic wrap and then wrapped with a layer of aluminum foil. Finally, the samples were placed in plastic bags for storage and transport. The environment in the tunnel is maintained under subfreezing temperatures, so immediate frozen storage upon extraction of samples was unnecessary. The samples were then placed in insulated coolers for the 20 minute trip to the University of Alaska Fairbanks. The samples were transferred to a chest freezer which was maintained at a temperature of approximately -10°C. The samples remained in the freezer until tested.

Remolded samples were prepared from dry silt collected from the CRREL tunnel and the method of sample preparation was discussed in Chapter 4.2.3. The dry sublimated silt was collected from the floor at station 30 m (0+98 feet) and placed in 20 liter buckets for later use. The silt came from the same area of the tunnel as many of the undisturbed samples containing micro-lenticular cryostructure. Therefore, the silt is representative of the originally deposited silty sediments.

5.2 CSC Testing

The two main testing methods were constant stress creep (CSC) experiments and relaxation experiments. This section describes the equipment and methods used during the CSC phase of the testing program.

5.2.1 Uniaxial Constant Stress Creep (CSC) Testing Equipment

The uniaxial constant stress creep (CSC) tests were conducted on two hydraulic load frames. The first was a 220 kip (978 kN) capacity MTS cervo-hydraulic load frame. At the load capacity tested, the load fluctuation measured was 30 lbs (133 N). An environmental chamber was fit around the loading pistons with total temperature fluctuations of 0.2°C. Set point temperatures could only be adjusted by increments of 1°C. The second load frame was a COX cervo-hydraulic load frame equipped with a 5000 lb load cell with load accuracy less than 1 lb. The loading piston and frame was built into an environmental chamber with total temperature fluctuation of 0.4°C. Figure 5.1 shows the interior pedestals and loading piston within the COX environmental chamber.

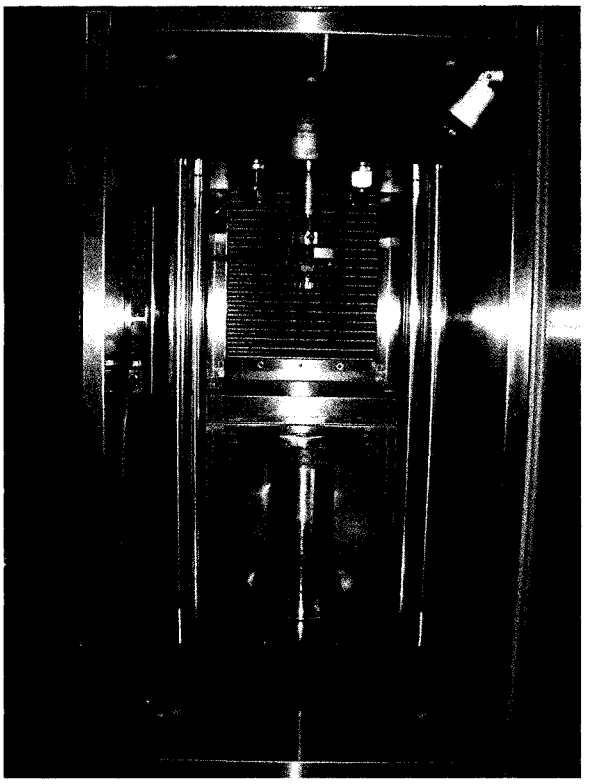

Figure 5.1. COX hydraulic loading frame for CSC (constant stress) tests. A second insulated chamber was placed around the base pedestal and loading piston to further control the temperature.

5.2.2 CSC Temperature Control

Temperature was controlled with redundant environmental chambers. Figure 5.2 shows the general schematic for the redundant chambers and methods used to control the temperature. The first chamber consisted of a commercial temperature control chamber designed to fit around the loading pistons of each frame. The COX environmental chamber was built around the loading supports and actuating piston. The MTS load frame was equipped with an MTS temperature control chamber, which fitted between the loading supports. It was found that the temperature fluctuations of the main environmental chamber were unacceptable for both load frames. To improve temperature control and stability, insulated chambers were constructed from polystyrene blue board (insulation value R-11). The insulated chambers were then placed around the sample.

Temperature of the sample area was maintained by using 20 liter recirculating baths with temperature stability of +/- 0.05°C, by running the fluid at a rate of 20 L/min through a convection driven heat exchanger located inside the insulated chambers. The temperature of the bath was

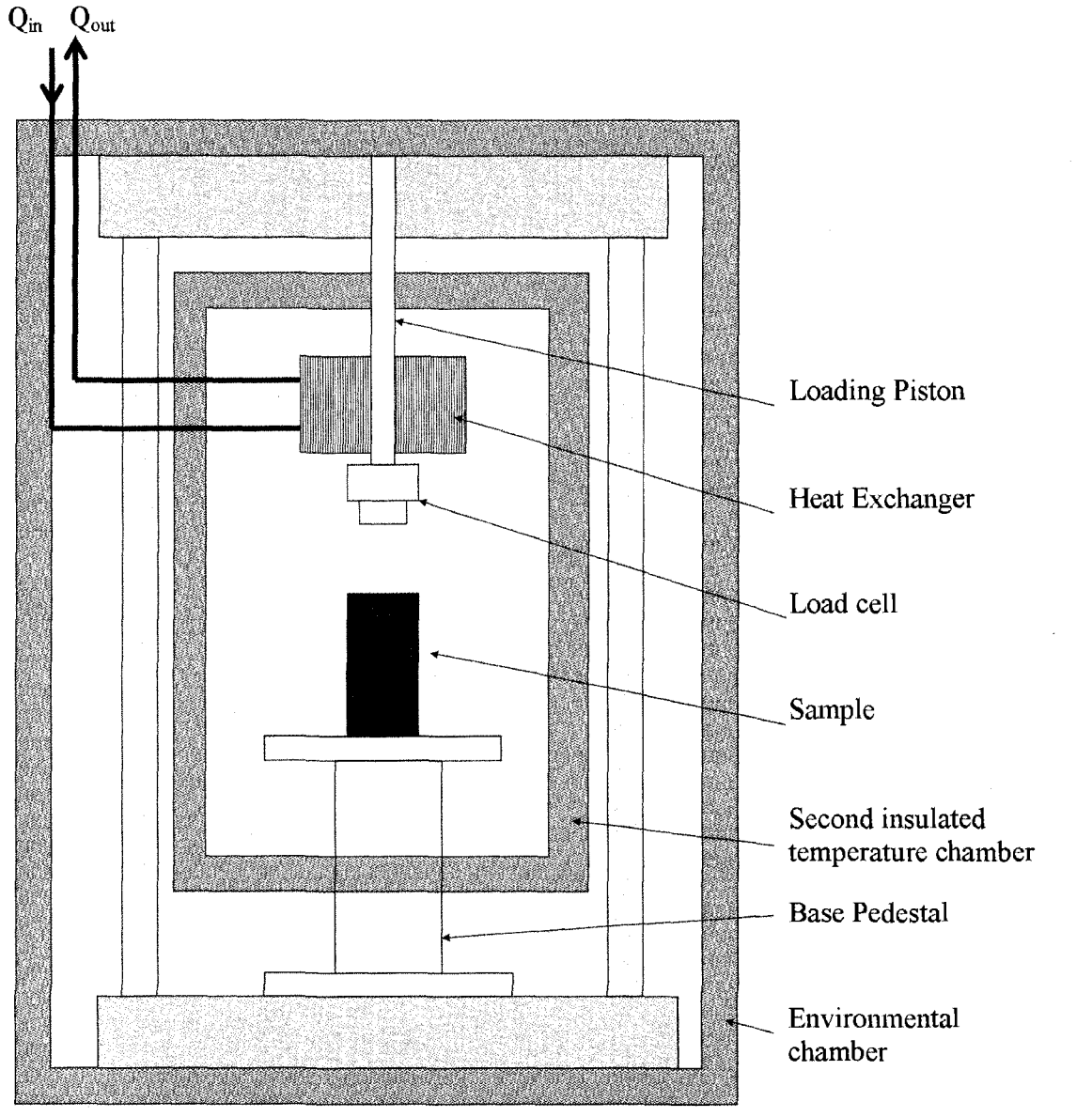

Figure 5.2. Generalization of the COX temperature control set-up. A second temperature chamber is installed within the main environmental chamber and equipped with a heat exchanger connected to a recirculating bath to control temperature and reduce temperature fluctuations.

manually adjusted until the desired set point was achieved. The heat exchanger consists of a copper coil running through a network of fins with a mounted fan designed to blow air over the cooling coils. Using redundant chambers, the temperature stability was generally better than +/- 0.05°C. Generally, the main environmental chamber was set at -5°C. In order to maintain the temperature of the sample, it was important to separate the sample from direct contact with main loading pistons in order to eliminate the impact of heat transfer from the machine to the sample. In order to reduce the heat transfer effects, sufficient airflow is required around the base pedestal and loading piston. This also required that a sufficient area of the base pedestals and loading pistons be exposed to the cooled circulated air. After these two requirements were met, the heat transfer problem to the sample was insignificant.

5.2.3 CSC Testing Procedure

The test samples were removed from cold storage and the top and bottom of the samples were then trimmed parallel with a chop saw equipped with a circular diamond blade in a cold room. The height of each sample did not vary more than 0.005 inches (0.02 to 0.03 mm) as measured from four locations which were measured at 90° increments. Weight measurements were made to an accuracy of 0.1 g. Height and diameter measurements were made to an accuracy of 0.001 inches (0.025 mm) to compute the frozen bulk densities for each soil sample. Pictures and descriptions of cryostructure were taken for each sample before loading. The air convection in the cold chambers tends to produce substantial sublimation of an unprotected sample. Several techniques were tried to counteract this effect. One attempted method was the application of petroleum jelly (Vaseline) to the outside of the sample. If the sample did not undergo large strains, the approach worked well. However, if the sample underwent large deformation, eventually untreated soil was exposed to the air and sublimation occurred. The best and easiest method was the application of a latex membrane around the sample. As long as the membrane fitted tightly around the sample, no to little sublimation occurred. Therefore, latex membranes were used to protect the samples. The samples were then placed in the loading frame and centered. Generally a small seating stress (approximately 50 kPa) was applied to the sample during the period of sample temperature equilibrium. Deformation of the seating load was monitored. The seating load was applied to insure that good contact was achieved for the start of the main test. The sample was allowed to equilibrate for 24 hours to the chamber temperature conditions before the main test was initiated. Several different test approaches were applied. One approach was to hold the temperature constant and apply several load stages (step loaded) to the sample. Each new load stage was applied after stabilization occurred (assumed strain rate of 2.083×10^{-6} hr^{-1} to 2.083×10^{-7} hr^{-1}) or a perceived secondary creep regime was reach for a

period of at least 72 hours. The second approach was to hold a constant stress and adjust the temperature. The third approach was to use one sample, at one stress level, for a given temperature. This was the usual case for samples that exhibited large creep deformation. The load was automatically adjusted through MPT (multi-purpose testware) control software from MTS (Material Testing Systems) Corporation. A common assumption was made that a constant volume was maintained throughout the creep process. Vyalov et al. (1980) indicates that in the steady state region (i.e secondary creep) for frozen supes (silty soils), the Poisson's ratio varies from 0.49-0.54. Based on the assumption of constant volume, the load was adjusted every 0.05 in (0.13 cm) or 0.1 in (0.25 cm) depending on the anticipated level of axial displacement. With the constant volume assumption, the change in cross sectional area was estimated by using Equation 5.1.

$$A_z = \pi \cdot \left(\sqrt{\frac{d_i^2 \cdot l_i}{l_z}} \right)^2 \cdot \left(\frac{1}{4} \right) \qquad \text{Eq. 5.1}$$

where A_z is the cross section at a displacement equal to z in axial direction, d_i is the initial sample diameter, l_i is the initial length of the sample, l_z is the length of sample at displacement z (i.e. $l_z = l_i - \Delta l$). Based on equation 5.1, the increase in applied load was calculated by Equation 5.2.

$$P_z = \sigma \cdot A_z \qquad \text{Eq. 5.2}$$

Where P_z is applied load in pounds or KN, σ is desired stress level, A_z is increase in cross sectional area for a given displacement z (Eq. 5.1).

True strain was used in place of engineering strain with the true strain for compression equal to:

$$\varepsilon_{true} = -\ln\left(\frac{l}{l_0} \right) \qquad \text{Eq. 5.3}$$

where ε_{true} is the true strain, l is the deformed length of the sample at a given moment of time, and l_0 is the original length of the sample. The primary data is strain and time from which the main data of interest, axial strain rate, was calculated. Axial strain rate is the slope of the strain vs. time curve. The strain rate either attenuates or enters a secondary creep regime. The only soils with strain rate attenuation in this study were an undisturbed sandy silt with massive cryostructure and remolded soils with massive cryostructure. All additional undisturbed soils did not show strain rate attenuation.

5.3 Relaxation Tests

The methods and equipment for the CSC test phase of the testing program was described above. This section describes the equipment, temperature control, and testing procedures used during the relaxation phase of the testing program.

5.3.1 Relaxation Test Testing Equipment

The relaxation tests were performed on two electro-mechanical screw driven load frames. A Humboldt Master Loader HM-3000 and a ELE International Digital Tritest load frames were used. Figure 5.3 shows the general instrumentation arrangement relative to the soil sample. The load was monitored in each frame with an Omega S-Beam LC101 10,000 lb (44.5 kN) load cell. Three Omega LD600 LVDT's (linear voltage displacement transducers) were used to monitor the loading platen and sample deformation. One LVDT was used to monitor movement of the loading platen and two LVDT's were used to monitor sample deformation. Agilent/HP 34970A dataloggers and HP BenchLink software were used for data collection. The load was transmitted through the lower loading piston and a large capacity spring (4000 lbs/in or 7 kN/cm).

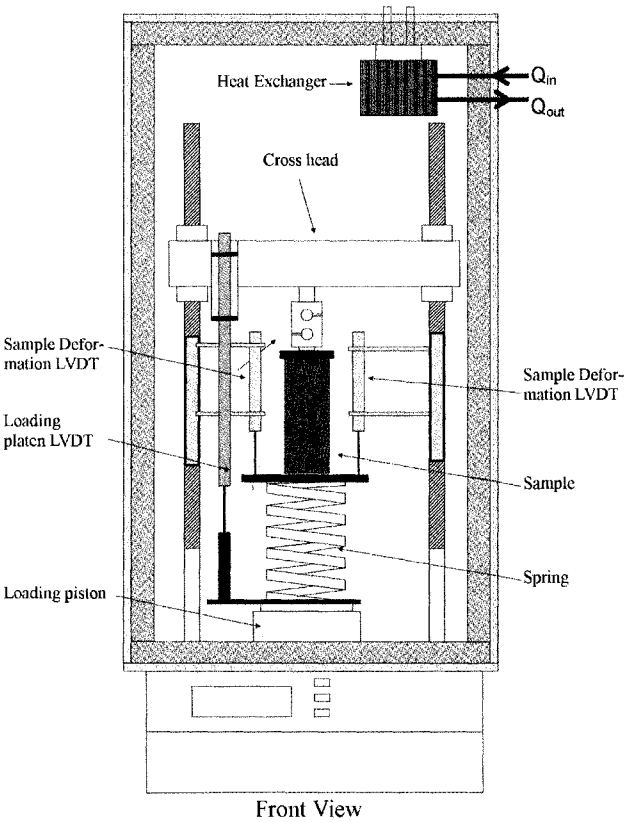

Figure 5.3. Environmental chamber and instrumentation for relaxation tests.

5.3.2 Relaxation Test Temperature Control

The temperature was controlled in much the same way as the CSC temperature control systems. The loading frames were placed in a walk-in cold room. The cold room temperature was maintained at -5°C. Insulated chambers were built to fit around the loading pistons and frame. The electronic portions where left open to the ambient temperature of the cold room. The insulated chambers were constructed from ½" OSB plywood and 2 inch blue extruded polystyrene board insulation. A two pane Plexiglas (acrylic plastic) window allowed for viewing of the sample. Inside of this chamber, a convection driven heat exchanger was placed. A chilled antifreeze fluid was circulated through the heat exchanger via the use of 20 liter recirculating baths with temperature stability of +/- 0.05°C. Figures 5.4 and 5.5 show the insulated chambers and load frames for the relaxation tests.

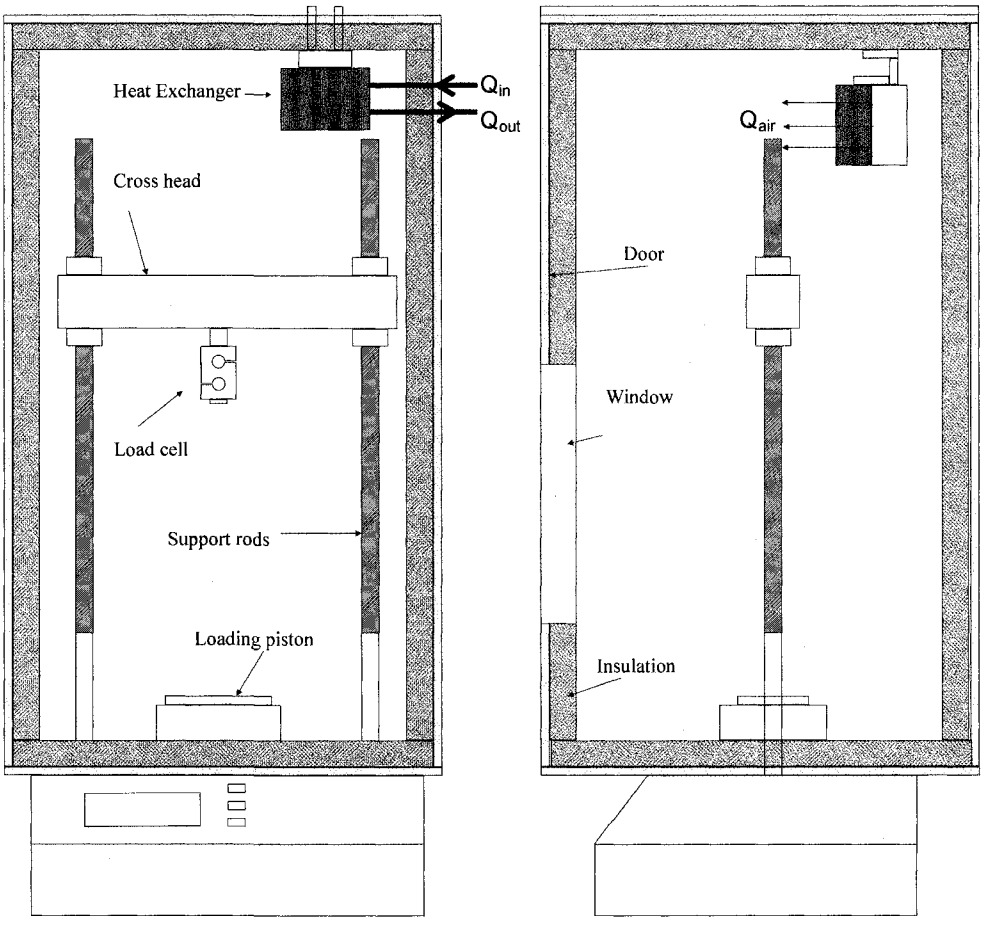

Figure 5.4. General schematic of load frame and insulated chambers fitted around the loading portion of the load frame for relaxation tests. The loading piston is an electo-mechanical screw driven device with loading speed controlled by electronic readout and relays.

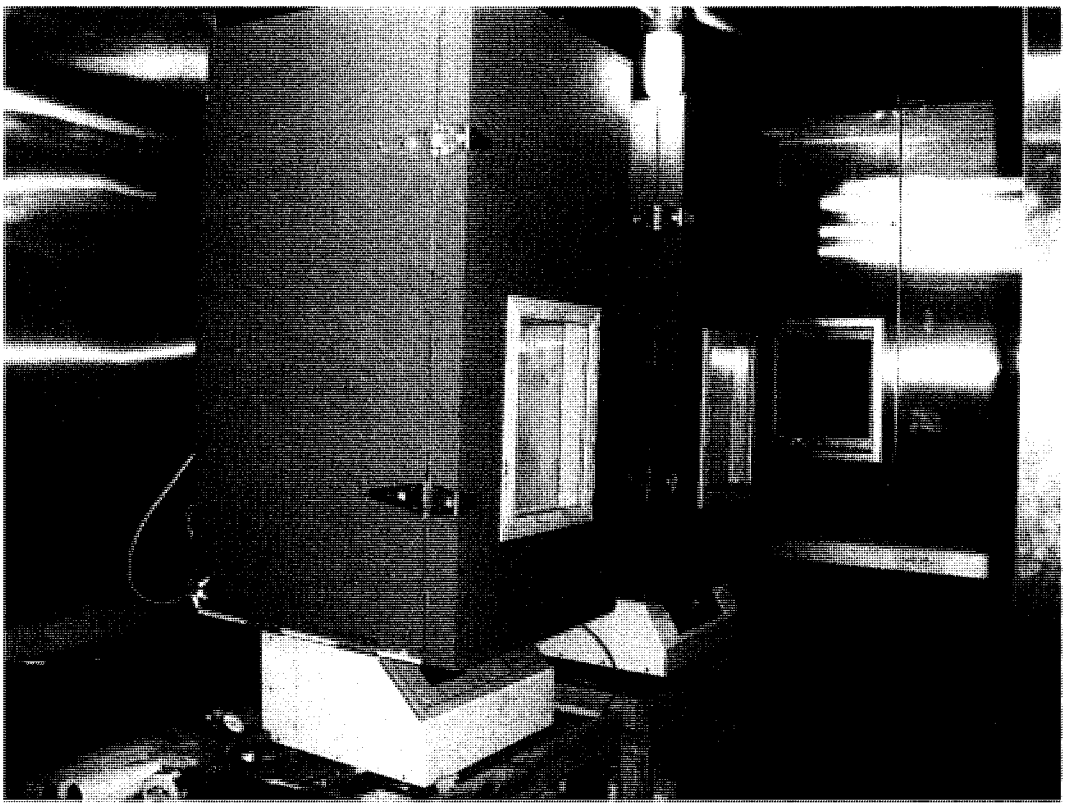

Figure 5.5. Actual insulated chambers placed around load frames for relaxation tests. Load frames are located within a walk in cold room held and set point temperature of -5°C.

Temperature was monitored by two thermistors placed next to the side of the sample and one thermocouple placed in the latex membrane enclosing the sample. It was found that despite the cooling approach, heat transfer still occurred through the lower (loading) platen. This was discovered by having the lower portion of a sample thaw over time when placed on the lower loading platen. It was discovered that heat produced by the electrical system was being transferred through the loading piston to the sample. To counteract this effect, a large 4000 lb/in (7kN/cm) spring was placed on the loading platen with the sample then being placed on spring. The air flow through the spring allowed for decoupling of heat transfer from the loading to the sample. A temperature stability of +/- 0.05°C was able to be obtained around the sample.

5.3.3 Relaxation Test Concepts

The relaxation tests performed in this study are similar to the dynamometer method as proposed by Vyalov et al. (1966) and Vialov and Ermakov (1967). The main purpose of the relaxation test was to explore a viable method for determining creep properties of undisturbed soils.

Undisturbed soils are nearly impossible to replicate from one sample to another. The two biggest constraints for conventional creep testing of undisturbed soils is the need for multiple samples and the large volume of the time required. Conventional creep testing requires either constant stress or constant strain rate tests to be conducted on multiple samples or through step loading of a single sample. In a constant stress test, a sample is loaded to a prescribed stress state and the stress is held constant until sample shows damped creep (stabilization) or either progresses to a secondary or tertiary creep mode. A family of creep curves is then produced from the different stress levels. Ideally, seven to eight different stress levels are tested. At low stresses, it can take months or years to develop a family of creep curves for one soil type at one given temperature. It is the time issue that is the primary constraint of creep tests at lower stress conditions. In a constant strain rate test, a constant strain rate is applied to the sample. Ideally the sample will either stabilize or reach a peak stress value. The same constraint exists were the time to achieve a peak stress or residual stress under slowly applied constant strain rates is large. Therefore, if one can determine creep parameters from one or two samples under relaxation conditions, the process is greatly accelerated. In addition, the use of one or two samples greatly reduces the variability that exists for undisturbed soils. The relaxation tests were primarily used because of the variability among the undisturbed samples.

A conventional relaxation test consists of rapidly straining a sample to a specified strain level. Once this strain level is reached, the machine and sample are fixed and no additional strain will occur during the relaxation process. This is a stress relaxation process whose deformation does not vary with time. The elastic strain stored in the sample during straining, will convert to plastic strain as the sample relaxes and the stress decreases. The sample is then strained to a new strain level and the process is repeated. Ladanyi and Benyamina (1995) present theory, methods, and data for the evaluation of conventional relaxation tests for frozen sands. The relaxation technique used in this study is similar to the dynamometer approach propose by Vyalov (1966) and Vialov and Ermakov (1967). This form of a relaxation test can be considered a relaxation test whose deformation varies with time. Once the sample and spring are strained and the loading platens fixed, the elastic strain stored in the spring and sample is released as the sample undergoes plastic deformation. The result is an active stress relaxation and deformation process with time. The stress relaxation and deformation are considered to be directly related.

The theory and interpretation techniques for dynamometer type relaxation tests are described by Vyalov (1966) and Vialov and Ermakov (1967). Below is a summary of the basic characteristics of the relaxation test. Figure 5.6 shows the basic measurements recorded during the course of a

$l_p(t)$ = time dependent length of sample

$l_s(t)$ = time dependent length of spring

l_o = length of spring and sample after completion of loading

x_p = total deformation of sample

x_{po}= initial sample deformation

$x_{pt}(t)$ = time dependent sample deformation

x_s = total deformation of spring

x_{so} = initial spring deformation

$x_{st}(t)$ = time dependent spring release

P = applied load (or stress)

P(t) = load at time t

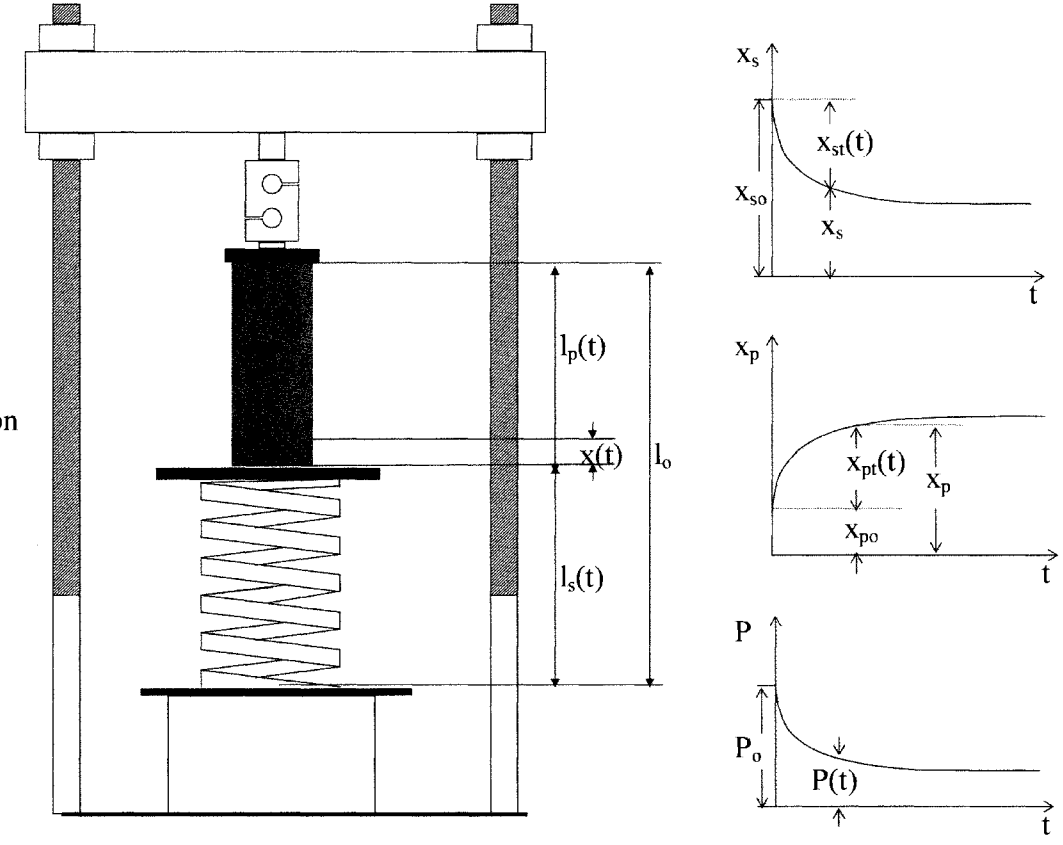

Figure 5.6. Basic principles for the measurements of relaxation test (Based on Vialov and Ermakov, 1967).

relaxation test, which consist of measuring the displacement of the spring and the sample. The load is also measured through the use of a load cell. The total height of the series system, which consists of the load applying spring and the sample, remains constant during the course of the test.

$$l_o = l_p(t) + l_s(t) \qquad \text{Eq. 5.4}$$

where l_o is the total post loading height (length) of the spring and sample, $l_p(t)$ is the time dependent height of the sample, and $l_s(t)$ is the time dependent height of the spring. The deformation of the sample for a given moment in time is:

$$x_p = x_{po} + x_{pt}(t) \qquad \text{Eq. 5.5}$$

where x_p is the total deformation of the sample, x_{po} is the initial deformation of the sample during loading, and $x_{pt}(t)$ is the time dependent deformation resulting from plastic creep of the sample due to release of the elastic strain stored in the spring and soil. The deformation of the spring for a given moment of time is:

$$x_s = x_{so} - x_{st}(t) \qquad \text{Eq. 5.6}$$

where x_s is the deformation of spring, x_{so} is the initial deformation of the spring incurred during loading of the sample, and $x_{st}(t)$ is the time dependent release of the spring. The release of the spring is equal to the plastic deformation of the sample.

$$x(t) = x_{pt}(t) = x_{st}(t) \qquad \text{Eq. 5.7.}$$

The basic operating assumptions for the system are that the load applied through the spring is equal to the load applied to the sample. The total initial deformation is constant. These concepts can be expressed as

$$P = P_s = P_p \qquad \text{Eq. 5.8}$$

$$x_o = x_s + x_p = \text{constant} \qquad \text{Eq. 5.9}$$

5.3.4 Relaxation Test Testing Procedure

A similar storage and sample preparation procedure was used for the relaxation tests as with the CSC creep tests. The samples were stored wrapped in a freezer. The samples were then trimmed to length, pictures taken, and descriptions of cryostructure made. Weight measurements were made to an accuracy of 0.1g. Length and diameter measurements were made to an accuracy of 0.001 inches (0.025 mm) to compute the frozen bulk densities for each soil sample. A latex membrane was then placed around the sample and positioned in the load frame. A small seating load was applied to the sample for a 24 hour period to allow for temperature equilibrium of the sample.

The load was applied to the sample through a large diameter spring and the lower loading piston. The spring constant was approximately 4000 lb/in (7 kN/cm). Typically the samples were loaded to 1000 to 3000 lbs (4.4 to 13.3 kN) depending on soil type and temperature. Therefore, an elastic strain was stored in the spring as the load was applied and the spring strained. The sample would undergo a pseudo-elastic deformation during the loading stage. Once the platen is fixed, relaxation of the sample occurs. This occurs due to creep of the sample and the subsequent release of elastic energy stored in the spring and soil. Sample and spring deformations were described in section 5.3.3. Relaxation is the internal rearrangement of the material in order to reduce stress until a new equilibrium is established.

The creep deformations of the samples were monitored with 2 LVDT's and the fixed platen is monitored with one LVDT. The sample undergoes rapid relaxation in the first portions of the test. The data is recorded at 5 second intervals for the first 30 to 60 minutes. It was then recorded at 5 minute intervals for the next 15 to 24 hrs. The data was then recorded at 15 to 30 minutes intervals for the remainder of the test. The data recorded includes displacement, load, time, and temperature. The temperature is recorded at 5 minute intervals. The tests were typically run for a minimum of 300 hours to 2000 hours. Generally, the test was run until a strain rate of 2.083×10^{-6} hr^{-1} was achieved. Upon completion of the test, weight, length, and diameter were recorded. Post-deformation pictures were taken.

5.4 Summary

Two types of tests were conducted. The first was the conventional constant stress creep (CSC) tests in which the soil deformation with time is monitored for constant stress conditions. Three variations of the CSC tests were conducted and include 1) a step loaded tests in which a single sample was loaded in stages with the temperature held constant, 2) a constant load was

maintained, but the temperature was step changed, and 3) a single constant load was applied to a sample for one temperature state. The second type of test consisted of a relaxation test. The relaxation test is a modification of a pure relaxation condition. During the course of the relaxation tests, the strain and stress varied with time and were directly related. Relaxation test were used as a trial approach to determine the time dependent mechanical properties of frozen soils without the necessity of testing a large number of "identical" undisturbed samples and the large quantities of time required for CSC tests at low stresses. Finding identical samples of undisturbed soils is nearly impossible.

Temperature was controlled through the use of redundant environmental chambers. A commercial environmental chamber was used which was designed to fit around the loading parts of the machine. Inside of this commercial environmental chamber, a second insulated chamber was placed around the sample. The temperature within the second chamber was controlled by circulating a refrigerated fluid from a temperature controlled bath through a convection heat exchanger. It was found that temperature could be controlled within +/- 0.05°C. Without good temperature stability, testing frozen soils at warm temperature is difficult. For temperatures warmer than -1°C a temperature increase by as little as 0.1°C results in a noticeable increase in the strain rate.

Chapter 6: Deformation Patterns

In the previous chapter, the testing equipment and procedures were described for constant stress creep (CSC) tests and relaxation tests. The purpose of this chapter is to describe the physical characteristics of the deformation process as viewed from test data and visual observations. In this chapter, strain vs. time plots for CSC samples will be shown for the various soil cryostructures, massive ice, and ice samples. The chapter will be broken into discussion of the deformation patterns as interpreted for the soil cryostrucures and ice facies.

6.1 Micro-Lenticular Cryostructure

Soils with micro-lenticular cryostructure were tested with the ice lenses either parallel or perpendicular to the applied uniaxial stress. When ice lenses are oriented parallel to the applied stress, this is described as vertical micro-lenticular (vml) cryostructure. When the ice lenses are perpendicular to the applied stress, this is described as horizontal micro-lenticular (hml) cryostructure. The purpose for testing two different orientations was to explore the effects of the ice lens orientation for a relatively "uniform" ice-rich undisturbed syngenetic permafrost soil.

Figure 6.1 shows the strain vs. time plots for soils with vml and hml cryostructure tested at temperatures near -1°C and stresses ranging between 296 to 329 kPa. Samples no. 3, 4, and 5 contain vml cryostructure and samples no. 6, 7, and 8 contain hml cyrostructure (see Chapter 7 for more information on the samples). The curves are similar, however, the soils with hml cryostructure show higher strain rates or increased strains for a given time period. Samples no. 5 and 8 lie on a dashed line which separates soils with vml cryostructure from soils with hml cryostructure.

The remaining strain rate vs. time plots for soils with vml cryostructure are presented in Figures 6.2 and 6.3. Figure 6.2 shows the sensitivity to changes of temperature and stress. The curve for sample no. 5 shows an increased strain rate with an increase in temperature and an increase of the applied stress by 100 kPa. Curves 12(1) and 12(2) represent separate loading cycles for the same sample. The first loading cycle was 12(1). For the two loading cycles, the load was kept constant while temperature was adjusted. Figure 6.3 show the strain vs. time plots for soils with vml cryostructure at temperature near -2°C with larger applied stresses as compared to Figure 6.2. The curve for sample no. 1 shows rapid creep failure. The curve for sample no. 2 shows an increase of the creep rate at the onset of the second loading stage occurring at approximately 310 hrs.

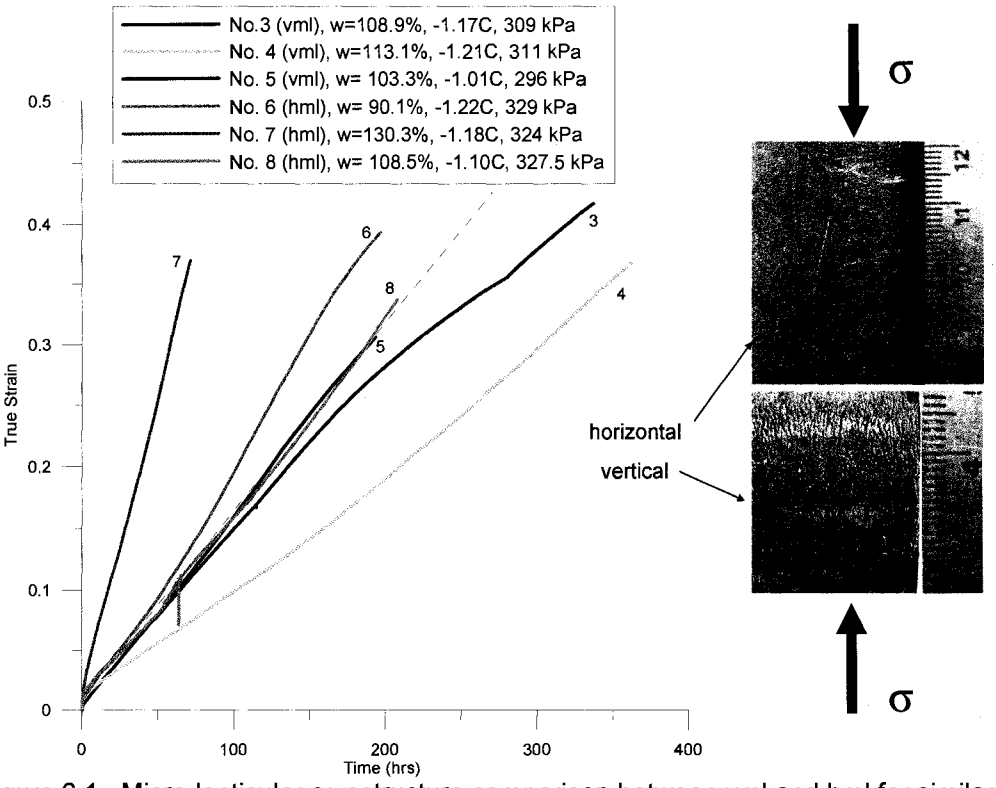

Figure 6.1. Micro-lenticular cryostructure comparison between vml and hml for similar temperature and stress conditions.

The soils with micro-lenticular cryostructure showed different physical characteristics depending on ice lens orientation (i.e. vml vs. hml). Soils with vml cryostructure showed distinct and predictable anisotropic lateral strains. Figure 6.4 shows an image of a deformed soil with vml cryostructure which illustrates this concept. The direction perpendicular to the ice lenses (W1) showed greater lateral strain as compared to the direction parallel to the ice lenses (W2). The ratio of the W1/W2 ranged from 2.1 to 3.3 with an average W1/W2 ratio of 2.8 (sample size n=9). Every soil sample containing vml cryostructure showed this tendency including those tested under relaxation tests. The lateral strain ratios presented are from CSC data as the samples underwent much higher strains than the relaxation tests. Also shown in Figure 6.4, in the upper left corner, is a non-deformed image of the ice lens structure. The upper right image shows a deformed section of the upper left quadrant of the sample in which the ice lenses can be seen to be highly deformed as compared to the original orientation. In some instances they are reoriented to horizontal. It appears that the ice lenses have "flowed". The use of term flow or flow pattern may be incorrect in that flow assumes constant volume. However, a distinct folding of the ice lenses can be seen.

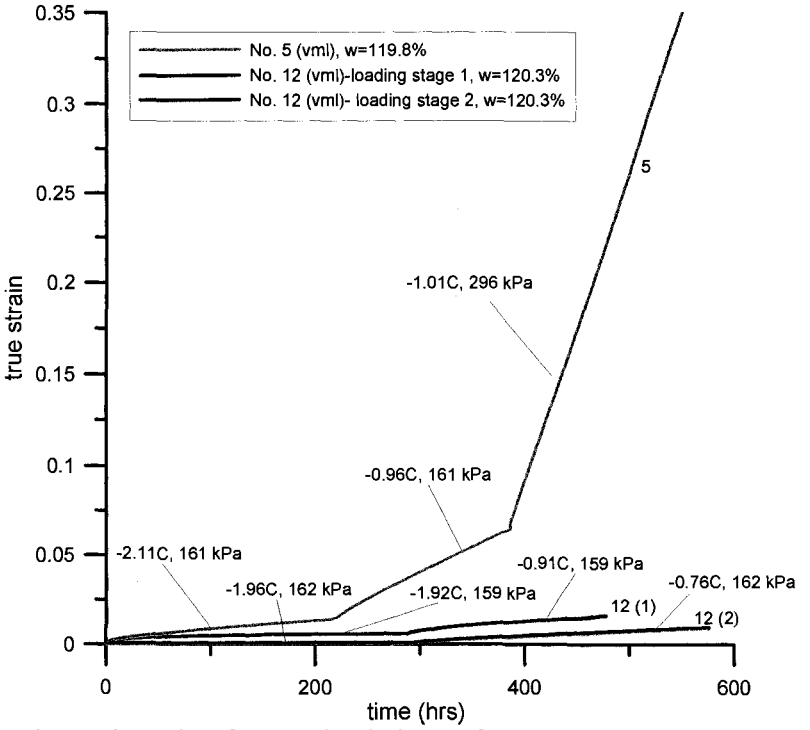

Figure 6.2. Strain vs. time plots for step loaded tests for samples no. 5 and 12 with vml cryostructure.

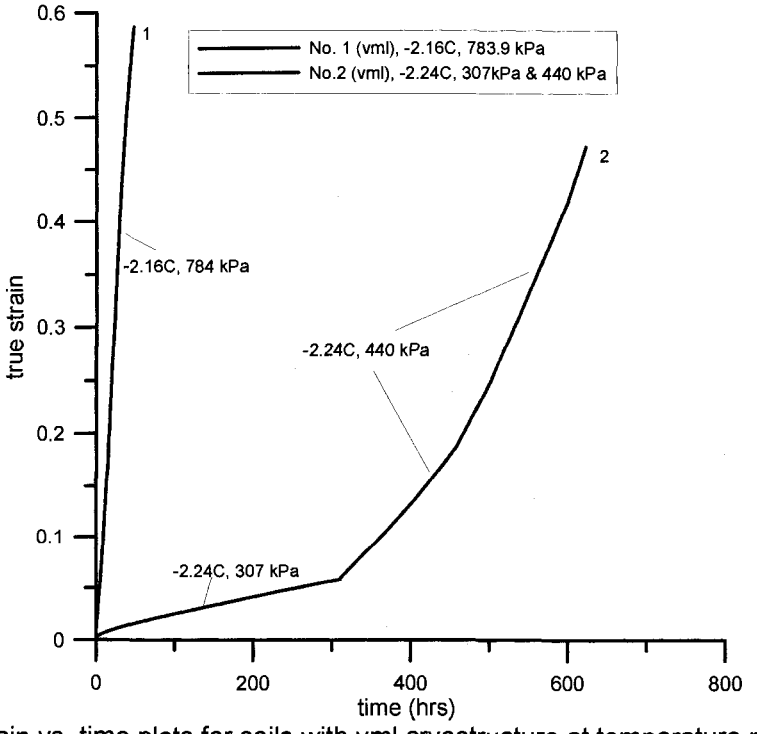

Figure 6.3. Strain vs. time plots for soils with vml cryostructure at temperature near -2°C for samples no. 1 and 2.

In contrast, soils with hml cryostructure showed uniform lateral strains under uniaxial compression. This was true under the constraint that the cryostructure distribution in the sample remained fairly uniform. A common occurrence during the course of this work was the development of pronounced creep lobes for soils with hml cryostructure. Figures 6.5 and 6.6 show the developed creep lobes for samples no. 6 and 11. Sample no. 8 also developed a creep lobe similar to sample no. 11. When analyzed, the creep lobes are concentrated in regions, which contain soil that is dominated by a poorly developed miro-lenticular cryostructure to a massive cryostructure. In Figure 6.5, the creep lobe contains some schist sand sediments, yet a few fine micro-lenticular ice lenses are also present. In Figure 6.6 the creep lobe consists primarily of massive silt in which the silt lobe has a gravimetric water content that is about 25% less than the upper micro-lenticular portion. However, a water content of 97% is still considered quite ice rich. In Figure 6.5, the creep lobe had an average ending diameter of 11.45 cm (4.509 in) as compared to the upper section which had an average ending diameter of 8.82 cm (3.473 in).

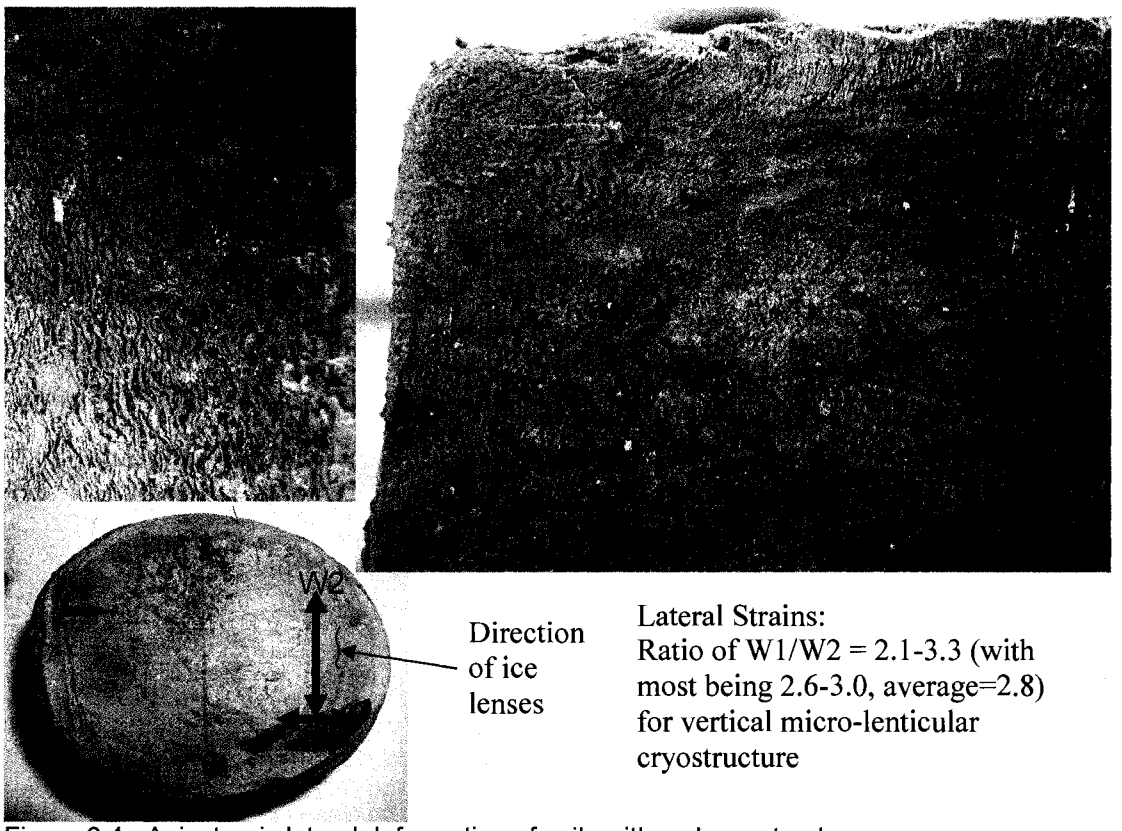

Figure 6.4. Anisotropic lateral deformation of soils with vml cryostructure.

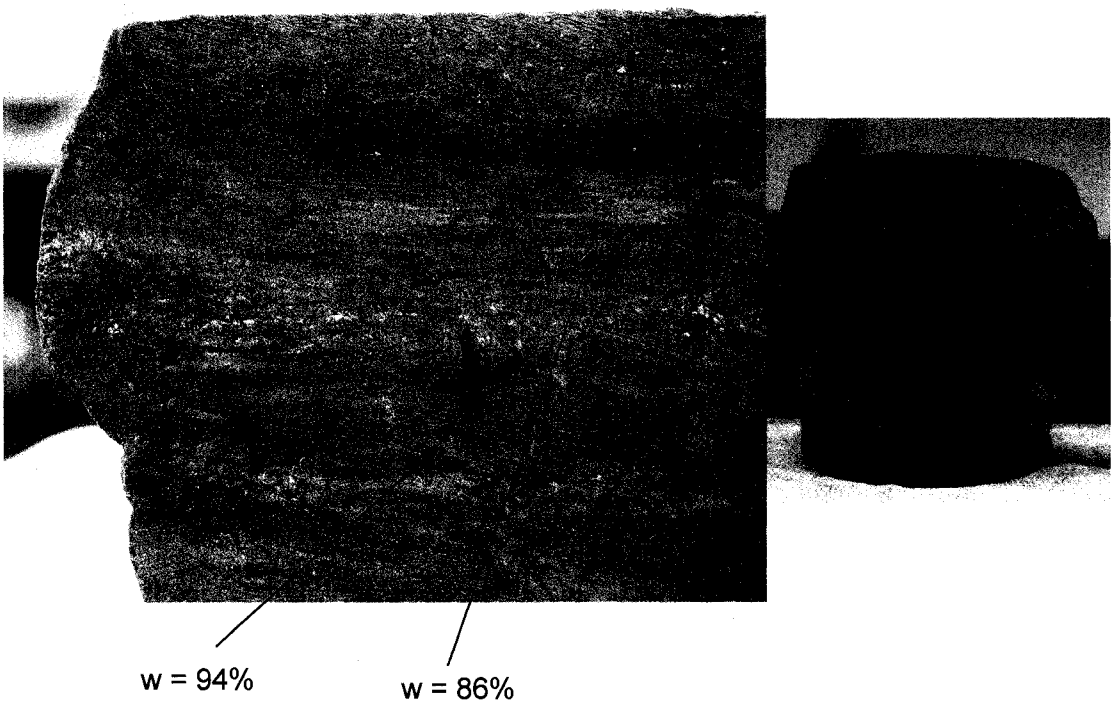

Figure 6.5. Creep lobe developed in soils with hml cryostructure for sample no. 6.

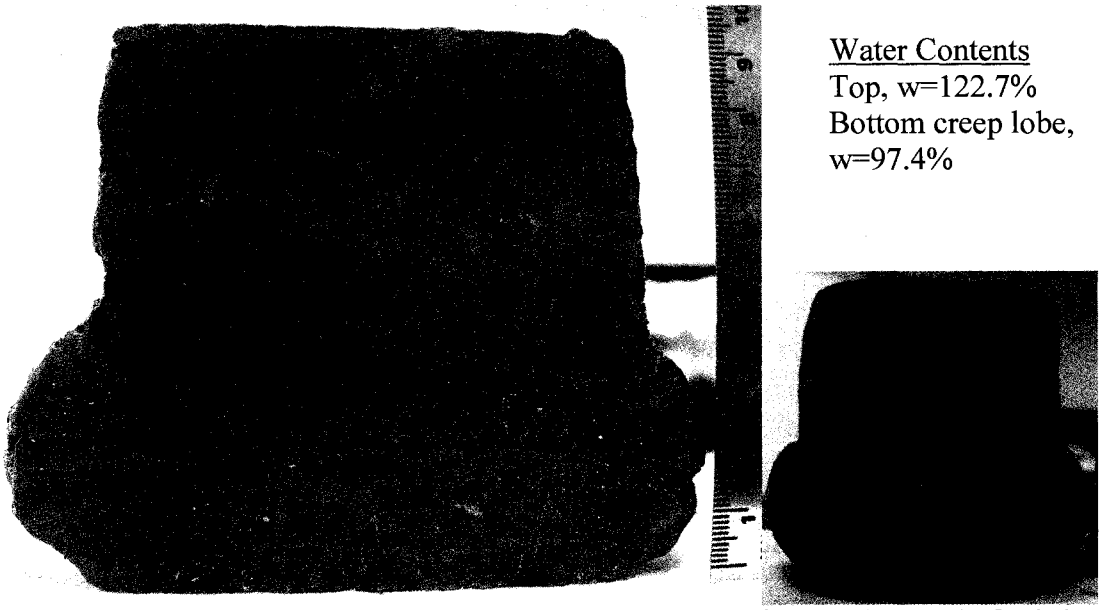

Figure 6.6. Creep lobe developed in soils with hml cyrostructure for sample no. 11. Scale is in centimeters.

In some instances the creep lobe shows cracking on the outer surface of sample as shown in the right images of Figures 6.5 and 6.6. Figure 6.7 shows a sample with hml cryostructure which did not contain a "massive" soil zone and uniform creep along the length of the sample is observed.

As observed from Figures 6.5 and 6.6, it appears that the undisturbed silts with "massive" cryostructure show more intense creep behavior under a given stress condition than the undisturbed silt with micro-lenticular cryostructure. For both cases shown, soil with hml cryostructure is located above and below the more "massive" soil belt. The "massive" soil belt has the appearance of being "squeezed" out between the hml layers. The relaxation samples for soils with hml cryostructure contained a section on the lower half of each sample similar to Figure 6.6. This layer may be partially responsible for the increased creep rates seen for soils with hml cryostructure as compared to soils with vml cryostructure (see Figure 6.1). Possible deformation mechanisms may include consolidation of the more ice poor soil, particle rearrangement, increased creep potential of less icy soils, and increased unfrozen water content. Consolidation does not account for the lateral deformation seen by the development of the creep lobe. Particle reorientations were not visually checked by microscopic methods. As shown in Chapter 4.4, the soils containing lower volumes of ice showed higher volumetric unfrozen water contents. As a result, the more ice poor sections may contain higher unfrozen water contents which may influence the creep rates. It is also likely that the silt particles in these regions are in an open structure thus allowing for reorientation and flow outwards as particles realign due to increased axial strain. However, the exact mechanisms are unknown.

6.2 Undisturbed Massive Cryostructure

Two undisturbed samples with massive cryostructure were tested under CSC conditions. One includes a undisturbed silt and the other a undisturbed sandy silt. In Figure 6.8, strain vs. time data is plotted for the two undisturbed soils with massive cryostructure along with soils containing vml and hml cryostructure for similar temperature and stress conditions. The undisturbed silt with massive cryostructure (sample no. 10) shows creep behavior similar to soils with hml cryostructure despite a much lower water content. Soils with hml and massive cryostructure show higher creep strains and strain rates as compared to the soil with vml cryostructure (sample no. 3). Sample no. 9 shows the strain vs. time curve for sandy silt with massive cryostructure. The resulting behavior deviates from the other undisturbed soils. Initially the sandy silt shows the highest strain rates. As the sample continues to deform, the strain rate shows a continuous decline with time. Due to the sandy sediments, this response is most likely the result of an increase of frictional resistance between soil particles.

Figure 6.7. Soils with uniform hml cyrostructure without a developed creep lobe. Scale is in centimeters

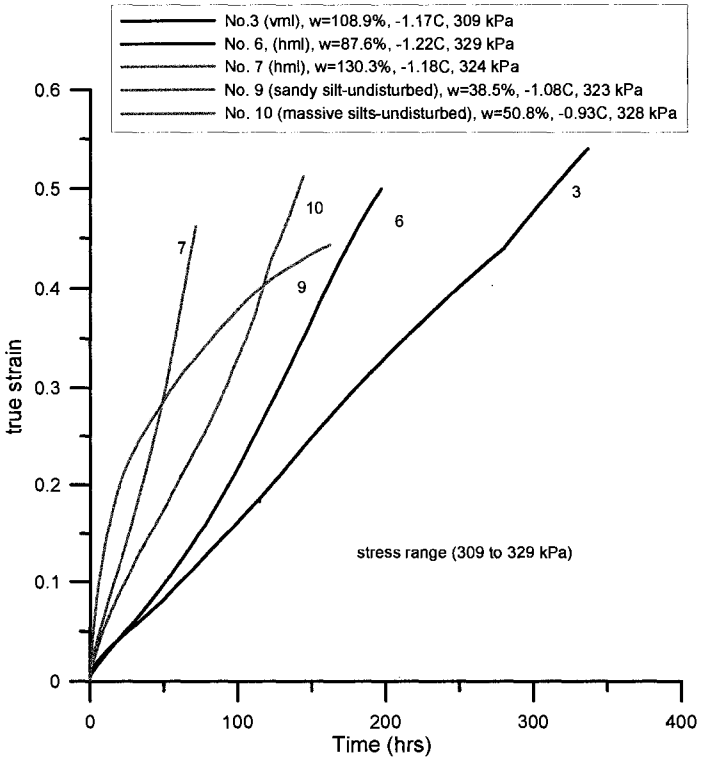

Figure 6.8. True strain vs. time plots comparing undisturbed soils with massive cryostructure with soils containing vml and hml cryostructure under similar temperature and stress conditions.

The data seems to suggest that undisturbed soils with massive cryostructure may have the tendency to creep at higher rates under a given loading condition than more ice-rich undisturbed soils. This observation is opposite of the common assumption that ice-rich soils show greater creep tendencies. The validity of this observation was not explored to lower or higher stresses. In contrast to the undisturbed soils with massive cryostructure, the remolded soils with massive cryostructure appear to show lower creep rates for a given stress. This is valid for the stress range tested.

Bjella (2008) analyzed recent slab failures that have occurred in the CRREL permafrost tunnel. Soil blocks have fallen from the roof of the tunnel near station 80 m (2+62 ft). It was noted that the soils blocks failed due to preferential delamination acting primarily along interbedded silt and gravelly sandy silts. Visual observations by the author also support this concept. Starting approximately at station 75 m (chapter 3), the sediment lithology of the main tunnel adit changes. A coarser sediment distribution is found with interbedded sandy silts apparently derived from a schist parent material as evidenced by the prevalence of mica minerals in the sandy sediment. It is along these coarser sediments (i.e. soils with massive cryostructures) that the failure zones are occurring. This is further evidence, which may suggest that soils with massive cryostructure may be more susceptible to creep deformations and ultimately failure. This portion of the tunnel was not mapped by the author due to the instability of the tunnel roof.

Images of the deformed undisturbed silt and sandy silt with massive cryostructure are shown in Figures 6.9 and 6.10. The undisturbed silt with massive cryostructure (sample no. 10, Figure 6.9) shows relatively uniform deformation with little observable structural changes. The undisturbed sandy silt with massive cryostructure (sample no. 9, Figure 6.10) shows a creep lobe which developed on the bottom left corner of the sample. Visual observation shows a relatively uniform distribution of sediment in the upper half of the sample. The lower half of the sample is characterized by alternating layers of silt and fine sand oriented at a slight 10-20° angle. The creep lobe emerges from the contact between a silt and sand layer. It is most likely that a shear zone acted along this contact layer.

6.3 Reticulate-Chaotic Cryostructure

Soils with reticulate-chaotic (RC) cryostructure are characterized by large diagonally oriented ice lenses. In Chapter 7, a bilinear stress relaxation pattern is shown for soils with RC cryostructure. Deformation and subsequent rapid stress relaxation at high stresses is contributed to creep

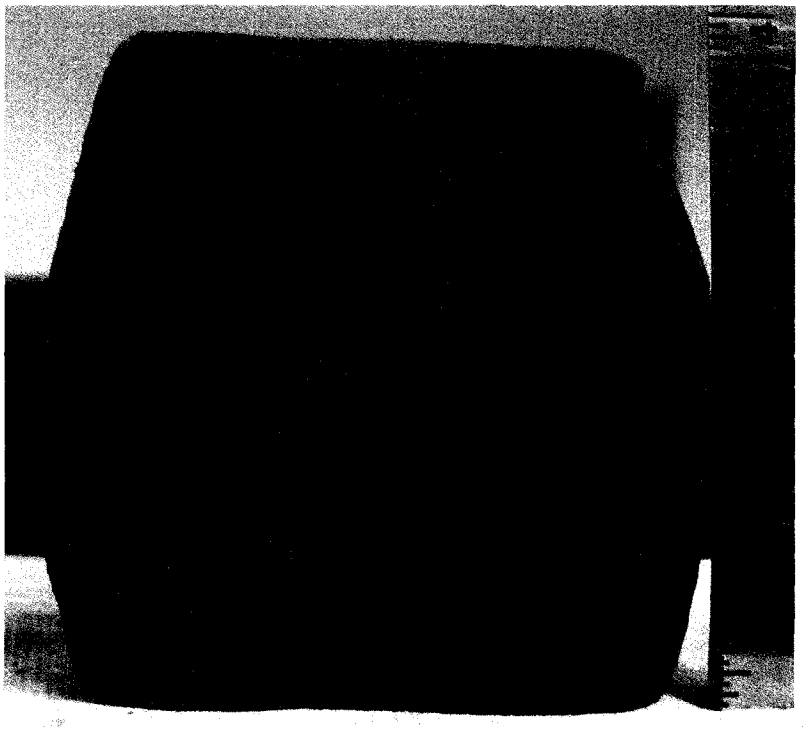

Figure 6.9. Post deformation image of sample no. 10 for undisturbed silt with massive cryostructure. Scale is in inches.

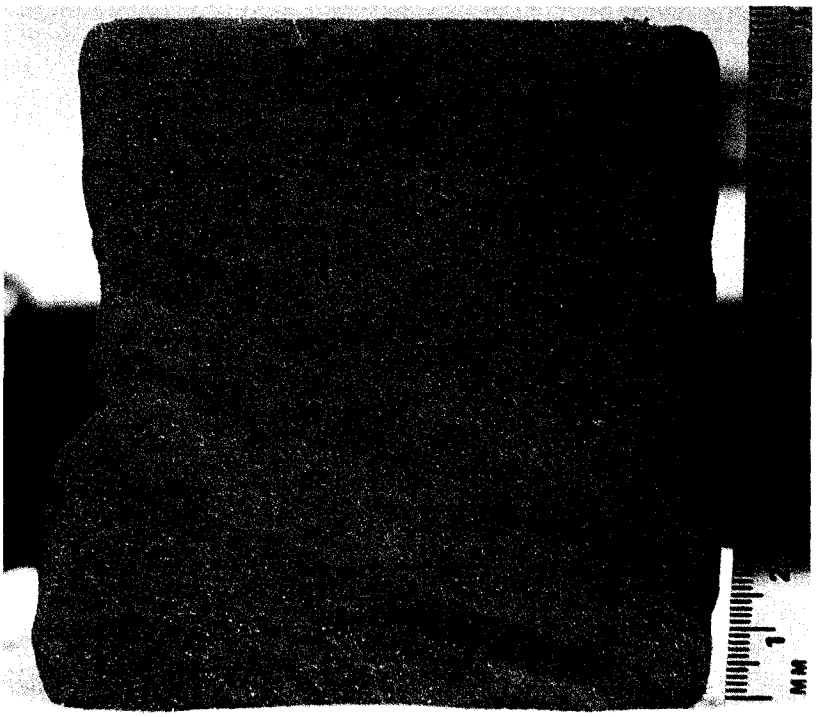

Figure 6.10. Post-deformation image of sample no. 9 for undisturbed sandy silt with massive cryostructure. Scale is in centimeters.

displacement along the ice lens-soil contact. Deformation and stress relaxation at low stresses was contributed to creep in the massive silts between ice lenses.

The role of ice lenses in the deformation process for soils with RC cryostructure can be seen in Figure 6.11. Image (a) is the whole core, (b) is a cut section of the core along the center line, (c) is close up image of lower creep lobe, and (d) is a cut section of lower creep lobe. As can be seen, deformation occurred along the ice lenses. On the outer edges of the sample, deformation along the ice lenses created creep lobes. On other samples, these lobes were even more developed. Image (c) shows a close up image of the lower creep lobe. Planar motion can be seen to have occurred along the diagonally oriented ice lenses. Due to motion along the ice lens, tensile cracks developed at the contact with vertically oriented or favorably oriented ice lenses. The cut sections (images (b) and (d)) show that internal fractures are not visible even though they are rather common on the outer edges of the samples.

Based on the motion, the contact between the ice lens and the frozen silt appears to represent a distinct zone of weakness. The ice lenses are oriented such that they correlate well with the predicted shear stress regions that develop during uniaxial compression. Would the same deformation patterns be seen if the ice lenses were oriented differently for the RC soils? This is a question that was not answered in this work. It is our feeling that the creep response would be different. However, it is readily seen that if well developed ice lenses are oriented in direction of maximum shear, motion along the silt ice lens contact will control the deformation behavior up to a certain stress limit. Based on the change of slope in the stress vs. time plots, at lower stresses there is a stress limit below which deformation along the ice lenses no longer dominate. The limit changes with temperature. In Chapter 4, measurements of the unfrozen water content suggest that soil with RC cryostructure have the largest unfrozen water content at warmer temperatures. It is possible that increased unfrozen water contents can cause an increase in the pore water pressures which act along the ice lenses and help facilitate motion. Work on undisturbed clayey soils by Savigny and Morgenstern (1986a) showed a similar trend where ice lens orientation had a controlling influence on the creep patterns. One particular image shows diagonally oriented ice lens which developed creep lobes very similar to those seen in Figure 6.11 (Savigny and Morgenstern, 1986a, p 524, Fig. 13).

6.4 Remolded-Massive Cryostructure

Soils with remolded-massive (RM) cryostructure contain no segregrated ice lenses. Small air pockets can be found in the soil due to the preparation method. The volume of the air is not

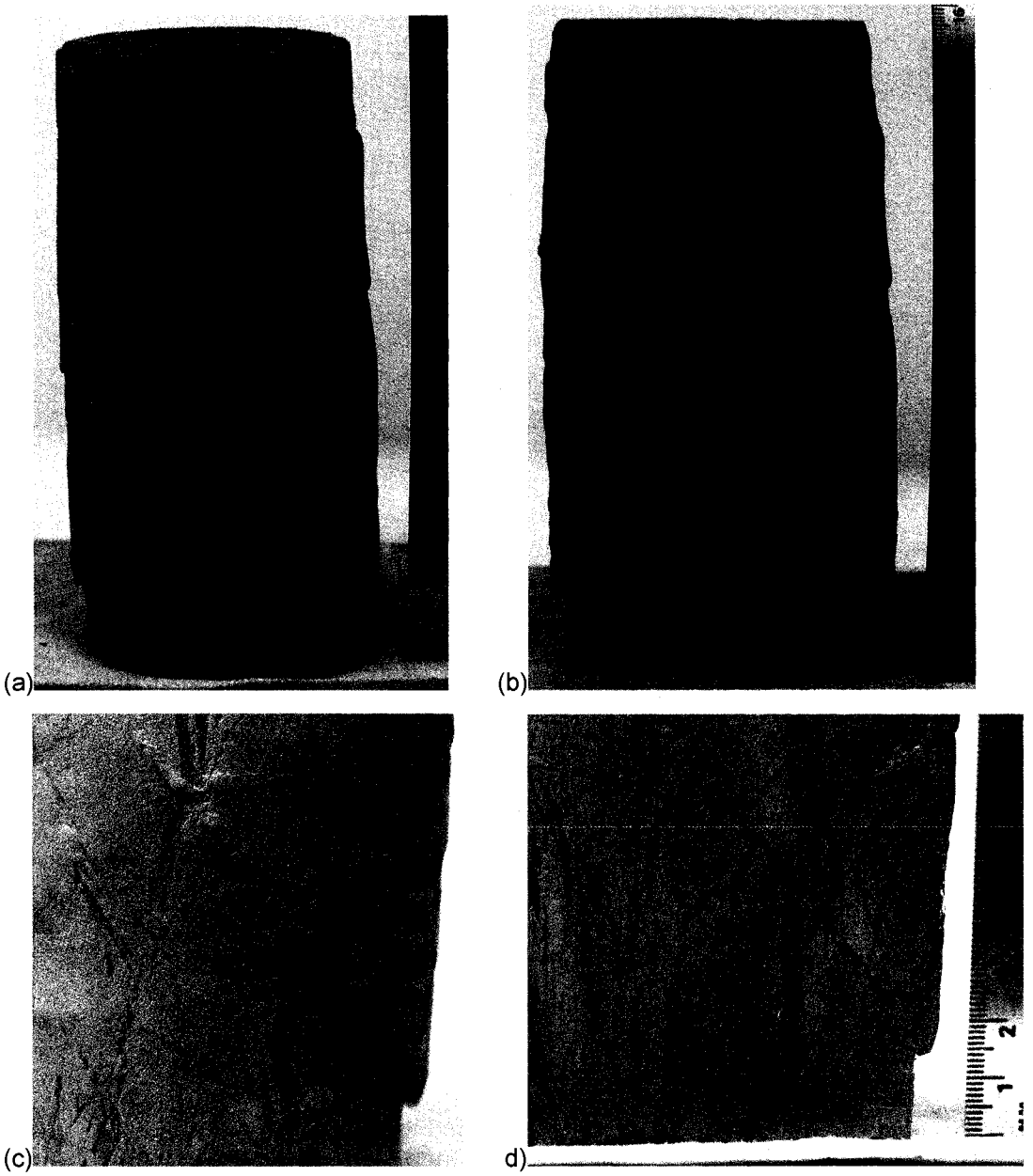

Figure 6.11. Image of ice lens influenced deformation behavior for soils with reticulate-chaotic cryostructure. Image taken from sample no. 33. (a) whole core, (b) cut section of whole core, (c) lower creep lobe, (d) cut section lower creep lobe. Scales are in centimeters.

excessively large by percent volume. The initiation of a progressive creep mode occurs at much higher stresses as compared to the undisturbed soils. However, once a threshold stress limit is reached, the strain rate can increase quickly with further increases of stress which eventually leads to failure.

Strain vs. time plots for soils with RM cryostructure at -1°C for CSC creep tests are shown in Figure 6.12. Sample no. 20 underwent 7 separate load stages. Increasing the stress from 393 kPa to 462 kPa, caused a rapid increase in the resulting strain rate. This same trend is seen for sample no. 21 (3 load stages) where a small stress increase results in a significant increase in the creep rate. Sample no. 22 was initially loaded with a stress of 621 kPa and went rapidly into tertiary creep.

Figures 6.13 and 6.14 show images of the deformation patterns seen for soils with RM cryostructure. When subjected to large strains (> 0.2), internal tensile gaps develop in the samples. Figure 6.13 is a cut section of sample no. 21 showing both sides of the cut. A large gap is seen to have developed in the central part of sample. The crack shown in the image is the largest seen for the soils with RM cryostructure. Figure 6.14 shows the external failure patterns. The image to the left shows a full core. The image to the right is a close up of the left image. In the central area of sample, wing type fracture cracks can be seen on the outer surface. In

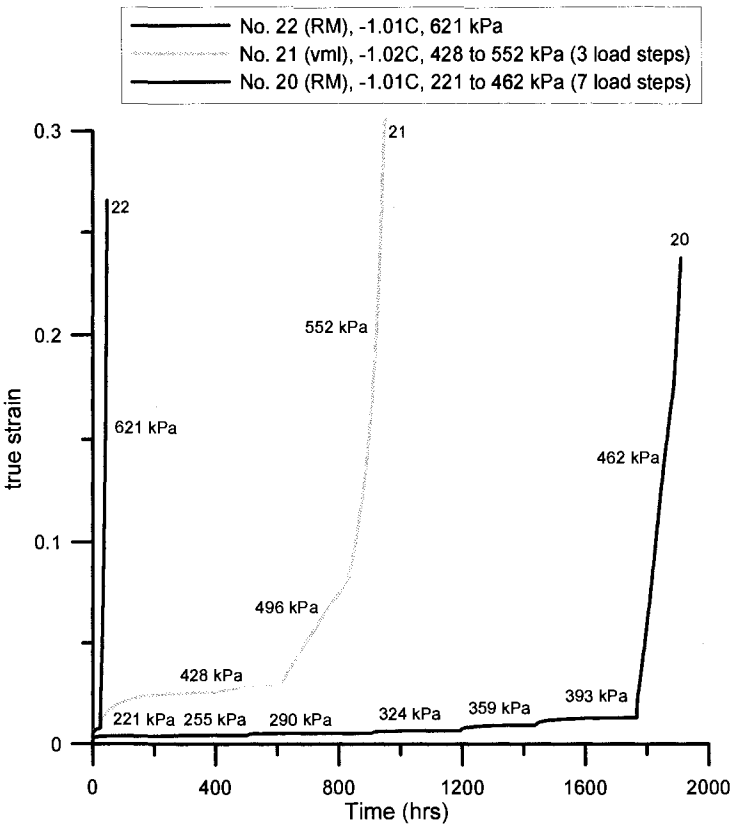

Figure 6.12. Strain vs. time plots for step loaded CSC creep tests for soils with RM cryostrucuture at -1°C. Stress values are given for the various load stages.

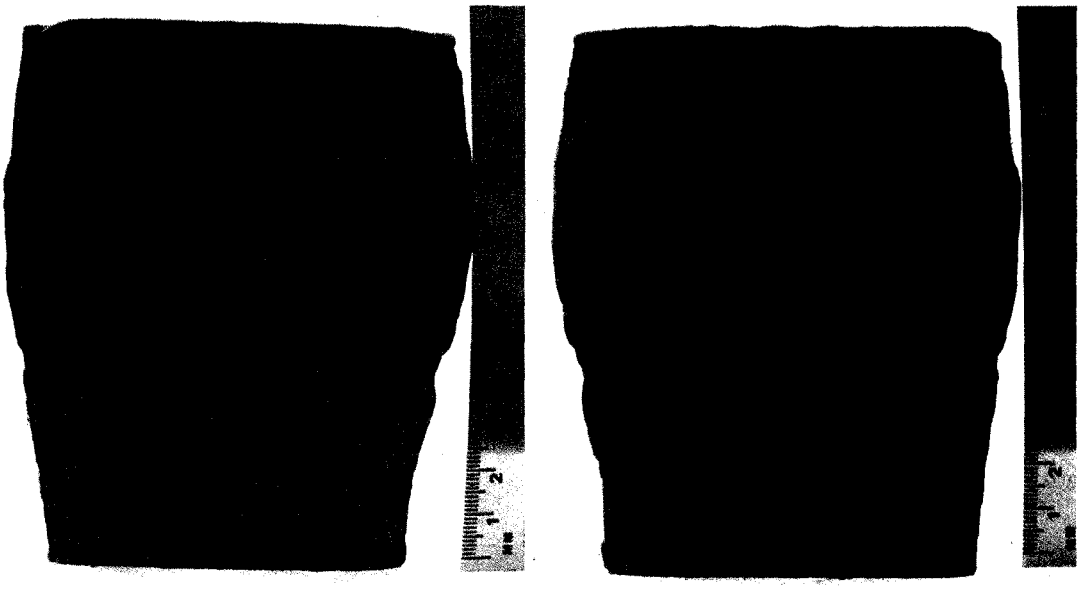

Figure 6.13. Central fracture gap of sample no. 21 for soil with remolded-massive cryostructure. The images represent both sides of the cut core. Scales are in centimeters.

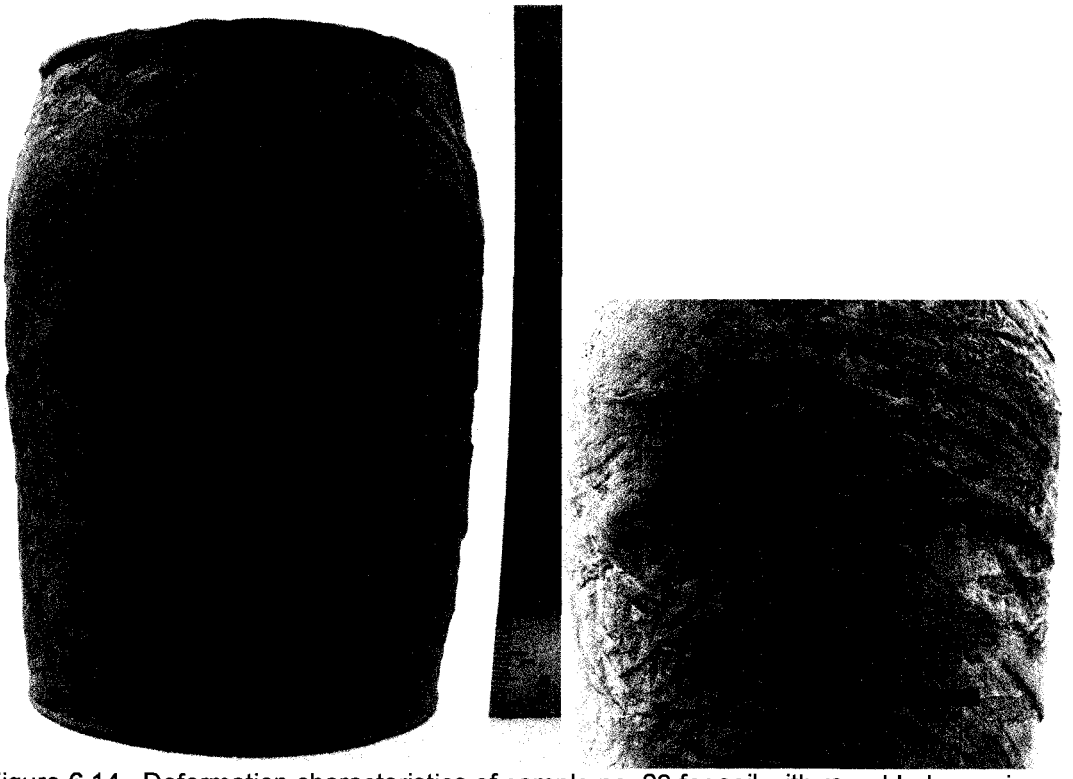

Figure 6.14. Deformation characteristics of sample no. 22 for soil with remolded-massive cryostructure. The image to the right is a close up of the upper creep bulge from the left image. Scale on the left image is in centimeters.

addition, the sample exhibits a fair number of smaller conjugate type shear fracture patterns. No conjugate fracture sets are seen in the inner part of the sample based on visual observations of the cut sections. The relaxation tests do not show any interior gaps or fractures.

Post analysis of one cut section suggests than the inner core has water contents that are approximately 4% lower than the outer 2/3 of the sample. It is assumed that during freezing of the sample, some water migration occurs away from the central part of the core. The result is a slight desiccation of the inner part of the sample. This may result in a weaker zone that is subject to tensile failure at high strains. The exact mechanism of the inner gap/fracture is unknown.

6.5 Ice Facies

Wedge ice (IW), Matanuska basal glacial ice (BI), and Matanuska glacial ice (GI) represent the ice facies tested in this study. Two CSC tests were performed, one on wedge ice and one on Matanuska glacial ice. Both tests were conducted at a temperature near -1°C and a stress of 220.6 kPa. The goal was to compare the results from the ice facies to the results for soil cryostructures.

The results of the two CSC tests on wedge ice and glacial ice are shown in Figure 6.15. The tests results from Matanuska glacial ice (sample no. 17) show a very important feature. Ice is known to undergo recrystallization or reorientation in order to minimize its resistance to deformation when subjected to an applied stress and more importantly to an applied shear strain (Kamb, 1972). When the initial stress is applied (sample no. 17), the strain rate decreases and begins to stabilize at about 100 hrs into the test, which correlates to a strain of about 2%. The strain rate at the first minimum was 1.004×10^{-5} hr^{-1}. The strain rate then accelerated for the next 300 to 400 hours. After which a small plateau in the strain rate emerges. The strain rate of the plateau was approximately 1.2×10^{-4} hr^{-1}. Therefore, for the same stress conditions, the second strain rate "stabilization" was an order of magnitude larger than the first minimum. At a time close to 1000 hrs, the stress level was reduced and a new constant strain rate was quickly reached and whose magnitude was larger than the first minimum observed at the higher stress level. Thin sections were not analyzed to confirm the exact mechanism. The mechanism is interpreted as recrystallization of ice grains, which may be facilitated by the warm test conditions (i.e. -1°C). The term recrystallization is loosely used and indicates that basal slip systems of the ice grains have been reoriented for favorable motion. This can include processes that promote new crystal growth. The presence of an apparent stabilized tertiary creep strain rate (or a second secondary creep rate) lend credibility that new ice grains formed, which were more favorably oriented for basal slip. The curve for wedge ice (sample no. 16) is shown on the same plot.

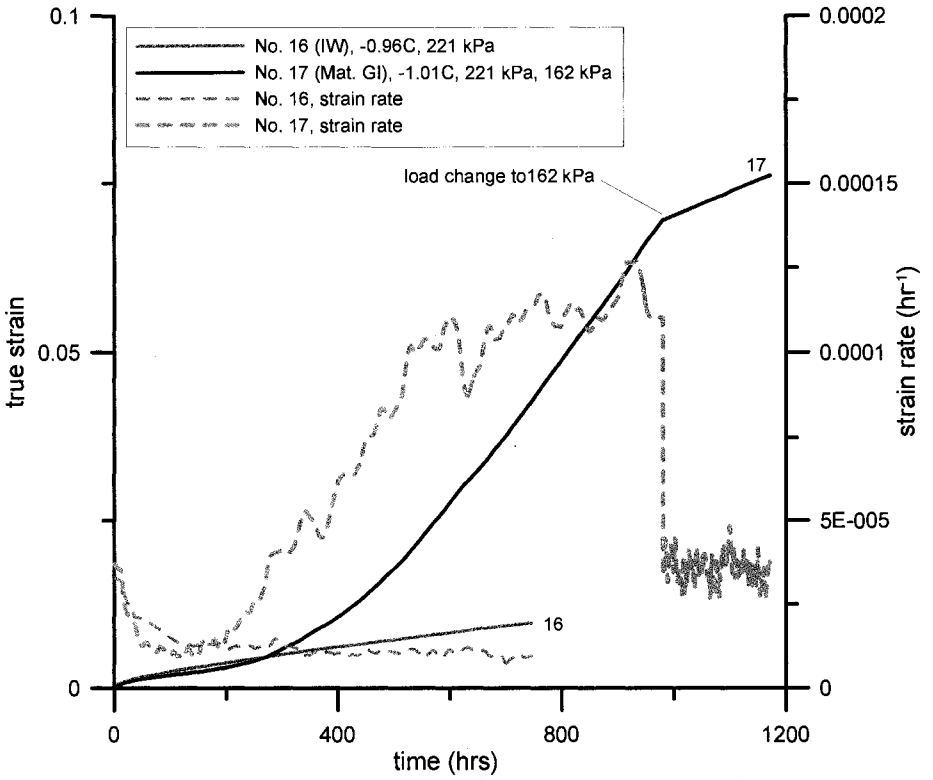

Figure 6.15. Recrystallization strain rate increase for Matanuska glacial ice as compared to wedge ice.

Interestingly, the strain vs. time curves are very similar until the glacial ice begins to undergo recrystallization. However, wedge ice does not show any increase in strain rate with time. No "recrystallization" type strain rate increase was seen for any other sample during the testing program. This does not mean recrystallization processes do not occur in soil or wedge ice; it just indicates that permanent recrystallization or fabric reorientation does not proceed to a degree where a permanent increase in the strain rate is observed. It has been suggested that the presence of particles and impurities in ice cause a continual process of recrystallization (Song et al., 2005). Frozen soils and wedge ice contain a large number of impurities, including sediment particles and air bubbles. This continual recrystallization process resulting from impurities may be partially responsible for a secondary creep regime.

Post deformation pictures are shown for Matanuska basal glacial ice samples no.43 and 44 and wedge ice sample no. 39 in Figure 6.16. Looking closely at image (a), there are fracture pattern that extends through center of the sample. This is characterized by wing type fracture cracks and opaque ice. It was found that when loading ice facies, such as glacial ice and icy basal ice, the

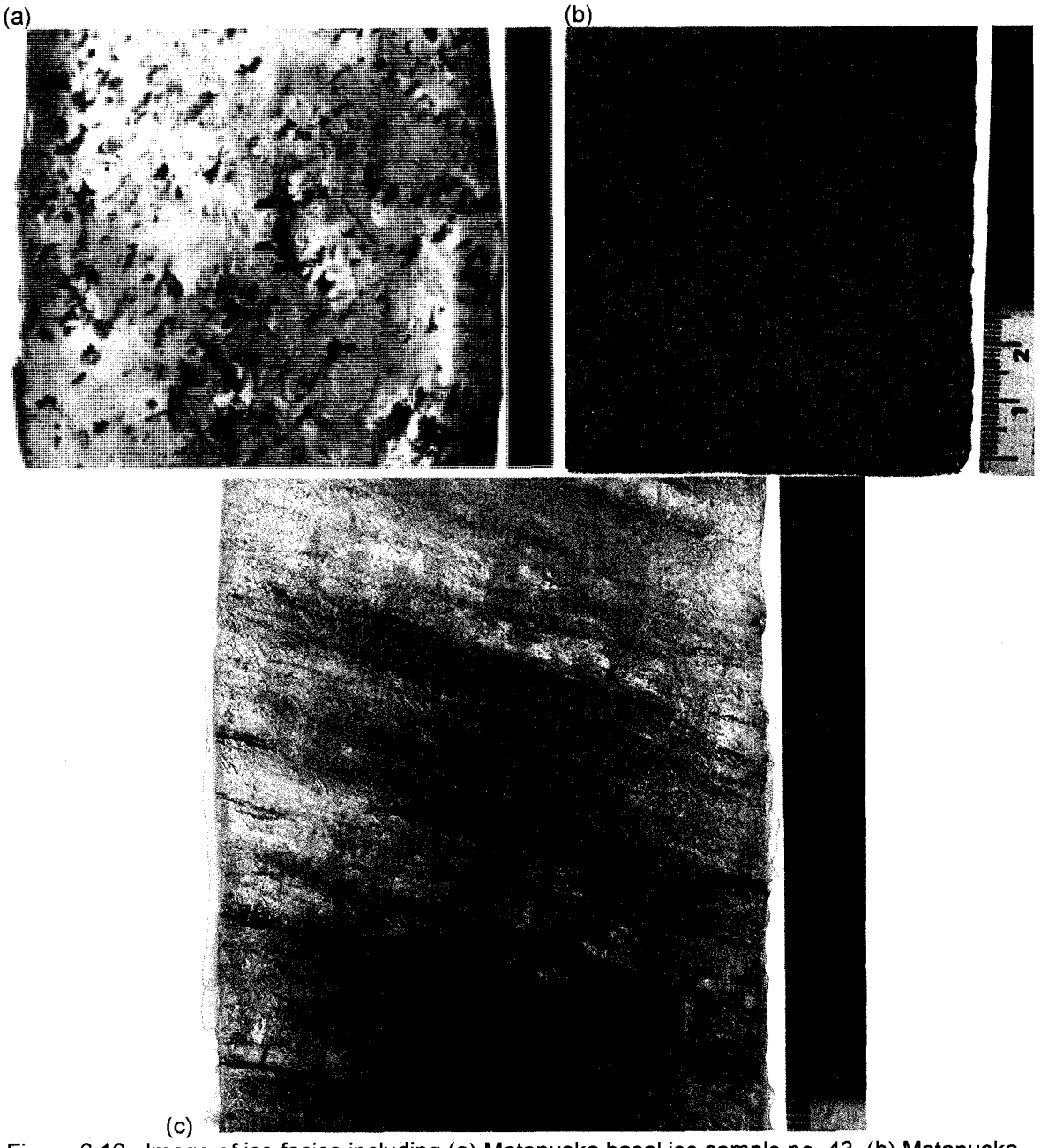

Figure 6.16. Image of ice facies including (a) Matanuska basal ice sample no. 43, (b) Matanuska basal ice sample no. 44, and (c) wedge ice sample no. 39. Scale rulers are in centimeters.

initial load needed to be substantially less than for similar permafrost soils. The ice samples experienced internal fracture at much lower loads. This internal fracture did not lead to complete rupture of the sample. Images (b) and (c) show Matanuska basal glacial ice and wedge ice, respectively. No fracture patterns can be seen. Wedge ice was able to sustain much higher initial loads without fracturing than samples of relatively pure ice found in glacial ice and basal glacial ice (samples no. 43 and 44).

6.6 Conclusions

This section presented some of the physical characteristics of the deformation processes for frozen soils and ice facies. The soil cryostructure were compared and it was found that the nature of the ice lenses influenced the deformation behavior. The deformation of the individual ice facies varied as well.

Soils with micro-lenticular cryostructure appeared to be influenced by the orientation of the ice lenses. Soils with vertical micro-lenticular (vml) cryostructure showed lower strain rates for a given stress than soils with horizontal micro-lenticular (hml) cryostructure. The lateral strains for soil with vml cryostructure varied depending on ice lens orientation. The lateral strains perpendicular to ice lenses was 2.8 times greater than the lateral strains parallel to ice lenses. In contrast, in the presence of a uniformly distributed micro-lenticular cryostructure, soil with hml cyrostructure showed uniform lateral strains. Soil with hml cryostructure generally contained a zone of "massive" cryostructure in which well defined creep lobes developed. Evidence suggests that undisturbed silt with massive cryostructure has a tendency to creep at a faster rate for a given stress than silt with uniformly distributed micro-lenticular cryostructure. This is a significant observation in that undisturbed soils with massive cryostructure may have greater creep tendencies that undisturbed soils with higher ice contents. The validity of this concept needs to be explored further.

The oriented ice lenses for soil with reticular-chaotic (RC) cryostructure controlled the movement during deformation. The ice lenses were oriented in approximately the same direction as the developed maximum shear planes. As a result, planar motion was seen to occur along the ice lenses for higher stress conditions. The planar motion along the diagonally oriented ice lenses resulted in the formation of tensile cracks along vertically oriented ice lenses. The motion along the ice lenses seems to support the concept that at high temperatures, the bond between ice lenses and soil may represent a zone of weakness.

Soils with remolded-massive cryostructure showed well developed central tensile cracking for strains higher than 0.2. In additional, tensile wing type fracture cracks and conjugate shear planes were shown to develop. The strain vs. time data for constant stress conditions showed that once a certain stress threshold was reached, an additional increase in the stress resulted in a rapid increase in the strain rates.

CSC tests on glacial ice with large crystals showed that recrystallization processes can occur such that the resistance to creep deformation is reduced. The expected result is the development of ice grains which are more favorably oriented for slip along the basal planes. This was evidenced by an order of magnitude increase of the strain rate for a constant applied stress. Polycrystalline wedge ice did not show a strain rate increase. The creep curves for glacial ice and wedge ice were similar up to a strain of about 2%.

Chapter 7: Testing Results and Discussion

The purpose of this chapter is to present the data interpretation and test results derived from CSC (constant stress creep) tests and relaxation tests. This chapter includes a summary of the soils and conditions used for the CSC and relaxation tests. The first main part presents results based on the interpretation of the CSC test data in the context of a minimum strain rate flow law. The next main part will explore the relaxation process and the long term strength of soil with different cryostructures and ice facies. The long term strength interpretations for the relaxation tests are based on a strain rate criteria and stress relaxation with time. Long term strength interpretations for CSC tests are based on stress relaxation as derived from minimum strain rates and application of Vialov's long term strength equation.

7.1 Constant Stress Creep (CSC) Tests-Minimum Strain Rate

Chapter 5 summarized the equipment and testing techniques used for constant stress creep (CSC) tests. The primary goal of the CSC tests was to determine the minimum strain rate flow law parameters for a flow law of Glen type (Glen, 1955) as seen in Equation 7.1.

$$\dot{\varepsilon} = A\sigma^n \qquad \text{Eq. 7.1}$$

Chapter 2.3 describes the background for the determination of minimum strain rates. A portion of that information will be represented here. The use of minimum strain rate vs. stress is widely adopted for determination of a constant rate flow law for ice and frozen soils (Arenson and Springman, 2005a,b; Glen, 1955; Andersland and Ladanyi, 1994; McRoberts, 1988; Nixon and Lem, 1984; Nixon and McRoberts, 1976; Savigny and Morgenstern, 1986a; Sego and Morgenstern, 1983). In order to compare the results to the majority of creep data available for frozen soils, a minimum strain rate approach is necessary. Physically, the minimum strain rate (or secondary creep) represents the condition where the plastic flow of material is in balance with the processes which act to relieve the internal stresses. In other words, it represents a condition where the internal processes act in such a way that continued plastic deformation of the material is possible. In contrast, the internal processes for primary creep are not in balance and lead to a strengthening of the material as seen from the continual decrease in the strain rate. If a balance is not achieved, the material will continue in the primary creep phase until deformation ceases. It is assumed that a secondary or minimum strain rate must be achieved before the onset of tertiary creep. By using a minimum strain rate approach, the flow law represents a condition where continual flow is possible.

The CSC tests were conducted at temperatures ranging from -1°C to -2°C. The undisturbed soils were tested under a narrow range of uniaxial stress conditions mainly ranging from 159 to 329 kPa. Several samples were tested above 329 kPa with a maximum stress of 784 kPa. The primary cryostructures tested include vertical micro-lenticular (vml) and remolded-massive (RM). In addition, a small number of soils with horizontal micro-lenticular (hml) cryostructure, undisturbed sandy silt with massive cryostructure, and undisturbed silt with massive cryostructure were tested. One sample of wedge ice and one sample glacial ice was also tested. Tables 7.1 to 7.4 summarize the test conditions and soil properties for samples used for CSC testing.

The sample designation is typically of the following form: PF tunnel 100705 1+05 RWH 25-43 cm or PF tunnel 032506 ml block CORE 1. PF tunnel indicates it came from the CRREL permafrost tunnel, Fox, Alaska. The next term represents the date the sample was obtained. Therefore 100705 indicates a sampling date of 10/07/2005. The next two terms are the location from which the sample was extracted. For example 1+05 RWH indicates that the sample was obtained from tunnel station 105 feet (multiply by 0.3048 for meters) from the inlet riser and was sampled from the right wall horizontally. Other sampling directions may include LFV (left floor vertical), RFV (right floor vertical), and LWH (left wall horizontal). Right and left are referenced from the tunnel inlet looking down the tunnel away from the inlet. The final term designates depth from the tunnel surface from which the sample was obtained from the soil core with 0 cm representing the surface of the tunnel. The term ml block represents a block of soil with micro-lenticular cryostructure that was extracted from the right wall at stations 0+98 to 1+00 (station 30 m). CORE 1 is just a designation of a core that was extracted from this block. So PF tunnel 1+05 RWH 25-43 cm can be written in long form as a sample obtained from the CRREL permafrost tunnel at station 105 feet (32 m), sampled horizontally from the right tunnel wall, with the tested core obtained at a depth of 25-43 cm from the tunnel surface.

7.1.1 Determination of Strain Rates

The primary goal of the constant stress creep tests was to determine a minimum strain rate (creep rate). This minimum strain rate is then related to stress for application into a simple power type flow law. The determination of the minimum strain rate is also subject to much controversy especially under low stress condition for both ice and frozen soil creep tests (Sego and Morgenstern, 1983; Savigny and Morgenstern, 1986a). It has been shown that under low stress

Table 7.1. Summary of testing conditions for undisturbed permafrost samples tested under CSC conditions.

No.	Sample	cryostructure	T (°C)	σ (kPa)	t (hr)	$\dot{\varepsilon}_{min}$ (hr^{-1})	ε_{true}	Comments
1	PF tunnel 100705 1+05C RWH 25-43 cm	vml	-2.16	783.9	49.5	8.784E-03	0.5872	min strain rate
2	PF tunnel 100705 1+05C RWH 45-74 cm	vml	-2.24	306.8	310.8	1.561E-04	0.0584	SS approx.
	--	--	-2.24	439.5	311.8	7.947E-04	0.473	min strain rate
3	PF tunnel 100705 1+05C RWH 119-134 cm	vml	-1.17	308.9	337.1	1.577E-03	0.54	min strain rate
4	PF tunnel 100705 1+04b RWH 0-14 cm	vml	-1.21	311.0	362.8	8.518E-04	0.368	min strain rate
5	PF tunnel 100705 1+04b RHW 44-59 cm	vml	-2.11	161.3	217.0	4.038E-05	0.014	ss approx.
	--	--	-0.96	161.3	165.9	2.794E-04	0.064	Temp fluc., SS approx
	--	--	-1.01	296.1	193.6	1.632E-03	0.394	min strain rate
6	PF tunnel 100705 1+20 LFV 24-39 cm	hml	-1.22	329.0	196.9	1.660E-03	0.5	min strain rate
7	PF tunnel 100705 1+02 LFV 89-105 cm	hml	-1.18	324.2	71.5	4.829E-03	0.462	min strain rate
8	PF tunnel 032506 ml block CORE 1	hml	-1.1	327.5	208.0	1.358E-03	0.411	min strain rate?
9	PF tunnel 100705 1+02 LFV 118-133	sandy silts	-1.08	322.5	162.2	8.198E-03	0.443	damped creep
10	PF tunnel 042806 0+58 LWH 0-15 cm	massive silt	-0.93	328.2	144.3	2.840E-03	0.512	min strain rate
11	PF tunnel 032506 ml block CORE 2	hml	-0.96	327.5	169.8	1.069E-03	0.532	min strain rate
12	PF tunnel 032506 0+98b RWH CORE 1	vml	-1.92	159.1	270.0	3.203E-06	0.0059	min strain rate?
	--	--	-0.91	159.1	190.0	3.292E-05	0.01599	SS approx.
	--	--	-1.96	162.0	290.0	8.109E-07	0.01631	min strain rate
	--	--	-0.76	162.0	286.0	2.207E-05	0.02524	SS approx.
13	PF tunnel 121906 1+00b RWH CORE a	vml	-1.99	259.7	478.8	4.522E-05	0.0284	SS approx.
	--	--	-1.03	259.7	738.0	1.010E-04	0.1341	SS approx.
14	PF tunnel 030907 1+02 RWH	vml	-2.07	220.6	425.0	1.326E-04	0.0589	SS, min reached
15	PF tunnel 030907 0+97 RWH CORE 3	vml	-1.14	220.6	1037.6	3.070E-05	0.0445	SS approx.
	--	--	-0.79	220.6	424.0	2.596E-04	0.169	Temp fluc., SS aprox.
16	PF tunnel 020207 1+95 RFV IW CORE 8	IW	-0.96	220.6	745.5	1.041E-05	0.009545	SS, min
17	Matanuska glacial ice CORE 4	MAT GI	-1.01	220.6	980.8	1.004E-05	0.0694	Min strain rate
	--	--	--	162.0	191.3	3.561E-05	0.0762	SS,. min
18	PF tunnel 1+00 ml block RWH small core	vml	-0.97	220.6	311.25	1.059E-04	0.0372	SS, min

T is test temperature, σ is applied uniaxial stress, t is duration of load stage, $\dot{\varepsilon}_{min}$ is minimum strain rate, ε_{true} is total cumulative true strain at end of load stage. See text and figures meaning of the comments.

Table 7.2. Summary of physical properties for undisturbed permafrost soils and ice samples tested under CSC (constant stress creep) conditions.

No.	Sample	cryostructure	γ_{bf} (lb/ft^3)	γ_{bf} (g/cm^3)	γ_{dry} (g/cm^3)	w_{grav} (%)	$w_{vol,ice}$ (%)
1	PF tunnel 100705 1+05C RWH 25-43 cm	vml	--	--	--	94.9	--
2	PF tunnel 100705 1+05C RWH 45-74 cm	vml	84.4	1.35	0.68	100.3	73.6
3	PF tunnel 100705 1+05C RWH 119-134 cm	vml	82.6	1.32	0.63	108.9	75.0
4	PF tunnel 100705 1+04b RWH 0-14 cm	vml	81.4	1.30	0.61	113.1	75.2
5	PF tunnel 100705 1+04b RHW 44-59 cm	vml	80.5	1.29	0.59	119.8	76.5
6	PF tunnel 100705 1+20 LFV 24-39 cm	hml	87.6	1.40	0.74	90.1	72.3
7	PF tunnel 100705 1+02 LFV 89-105 cm	hml	78.7	1.26	0.55	130.3	77.6
8	PF tunnel 032506 ml block CORE 1	hml	82.3	1.32	0.63	108.5	74.6
9	PF tunnel 100705 1+02 LFV 118-133	sandy silts	111.4	1.78	1.29	38.5	53.9
10	PF tunnel 042806 0+58 LWH 0-15 cm	massive silt	99.2	1.59	1.05	50.8	58.2
11	PF tunnel 032506 ml block CORE 2	hml	83.2	1.33	0.63	110.1	76.0
12	PF tunnel 032506 0+98b RWH CORE 1	vml	79.7	1.28	0.58	120.3	75.8
13	PF tunnel 121906 1+00b RWH CORE a	vml	83.0	1.33	0.64	107.6	74.9
14	PF tunnel 030907 1+02 RWH	vml	81.2	1.30	0.58	125.9	78.9
15	PF tunnel 030907 0+97 RWH CORE 3	vml	84.7	1.36	0.69	95.8	72.2
16	PF tunnel 020207 1+95 RFV IW CORE 8	IW	55.1	0.88	--	--	--
17	Matanuska glacial ice CORE 4	MAT GI	58.2	0.93	--	--	--
18	PF tunnel 1+00 ml block RWH small core	vml	75.4	1.21	--	--	--

γ_{bf} is frozen bulk density, γ_{dry} is dry density, w_{grav} is gravimetric water content, $w_{vol,ice}$ is the volumetric ice content

Table 7.3. Summary of testing conditions for remolded soil samples tested under CSC (constant stress creep) conditions

No.	Sample	cryostructure	T (°C)	σ (kPa)	t (hr)	$\dot{\varepsilon}_{min}$ (hr^{-1})	ε_{true}	comments
19	PF tunnel remolded massive CORE 4	RM	-1.00	162.0	332.3	1.461E-06	0.000976	min strain rate, sample compromised
20	PF tunnel remolded massive CORE 7	RM	-1.01	220.6	262.5	damped	0.00219	
	--	--	--	255.1	241.3	damped	0.00266	
	--	--	--	289.6	401.0	damped	0.00356	
	--	--	--	324.1	286.8	damped	0.004881	
	--	--	--	358.5	243.3	damped	0.00747	
	--	--	--	393.0	330.3	1.099E-06	0.01117	SS approx.
	--	--	--	461.9	142.8	1.177E-03	0.236	min strain rate
21	PF tunnel remolded massive CORE 16	RM	-1.02	427.5	596.0	4.576E-06	0.0297	min strain rate
	--	--	--	496.4	212.8	2.189E-04	0.0816	SS, min
	--	--	--	551.6	118.7	7.504E-03	0.306	min strain rate
22	PF tunnel remolded massive CORE 21	RM	-1.01	620.5	22.0	5.884E-03	0.266	min strain rate

T is test temperature, σ is applied uniaxial stress, t is duration of load stage, $\dot{\varepsilon}_{min}$ is minimum strain rate, ε_{true} is total cumulative true strain at end of load stage.

Table 7.4. Summary of physical properties for soils with remolded-massive cryostructure tested under CSC (constant stress creep) conditions

No.	Sample	cryostructure	γ_{bf} (lb/ft^3)	γ_{bf} (g/cm^3)	γ_{dry} (g/cm^3)	w_{grav} (%)	$w_{vol,ice}$ (%)
19	PF tunnel remolded massive CORE 4	RM	99.1	1.59	1.05	50.7	58.1
20	PF tunnel remolded massive CORE 7	RM	98.0	1.57	1.04	50.4	57.2
21	PF tunnel remolded massive CORE 16	RM	97.9	1.57	1.04	51.4	57.9
22	PF tunnel remolded massive CORE 21	RM	97.3	1.56	1.01	54.0	59.4

γ_{bf} is frozen bulk density, γ_{dry} is dry density, w_{grav} is gravimetric water content, $w_{vol,ice}$ is the volumetric ice content

conditions, the time to reach a minimum or constant strain rate can be large extending to hundreds or thousands of hours. For some ice rich soils, the initiation of a steady state (constant strain rate) can be reached rather quickly (within 100 hours) (Thompson and Sayles, 1972). In Tables 7.1 and 7.3, each individual load or temperature stage contains a notation as to if a minimum or steady state creep regime was reached (found in comments column). If a "min strain rate" is indicated in the comments then a well defined minimum was reached followed by an increase in the strain rate. "SS, min" indicates that the strain rate appears to reach a steady state creep condition where the strain rate has reached a constant value. "SS approx." indicates that the curve was interpreted as steady state, but a minimum or constant value may not have been reached at the end of the load stage. The method for determining the three strain rate conditions are described below. Damped creep is interpreted as a continually decreasing strain rate with time, which in theory should finally approach zero. For the undisturbed soils, the sample containing massive sandy silt showed a well defined damped creep behavior. The remolded soils with remolded-massive cryostructure showed damped creep behavior in the lower stress regions as evidenced by CSC creep data.

Figure 7.1 shows the axial strain rate and true strain vs. time for sample no. 11 (PF tunnel 032506 ml block CORE 2) and illustrates the case where a well defined minimum is reached (i.e. min strain rate in Tables 7.1 and 7.3) and acceleration into a tertiary creep mode occurs. When a well defined minimum strain rate is seen, the time interval to reach the minimum is determined. To determine the axial strain rate, a linear best fit regression was applied to the true strain vs. time curve for the specified time interval. If two minimum strain rates are seen for the frozen soils, the second is generally the result of the software failing to adjust the load in order to account for an increase in the cross sectional area of the sample resulting from axial deformation. Figure 7.2 shows the axial strain rate determination for a steady state minimum situation (i.e. SS, min in Tables 7.1 and 7.3). Figure 7.2 shows test data for sample no. 14 (PF tunnel 030907 1+02 RWH). In the course of this work, it was assumed that the sample maintained constant volume (Vylalov et al., 1980). Therefore, load adjustments were performed based on axial displacement as outlined in equations 5.1 and 5.2. For sample no. 14, the loads were adjusted automatically for every 0.05 inches (0.127 cm) of axial deformation. The test data in Figure 7.2 shows the sensitivity of the strain rate to the load adjustments. Beginning at approximately 90 hours the strain rate begins to stabilize with a gradual decrease in the strain rate. At test times of approximately 96, 227, and 360 hours, the applied load was adjusted for an increase in the cross sectional area. At each load adjustment, the strain rate jumps slightly and is followed by a gradual decrease in the strain rate. With an increase in load, the strain rate jumps to a value

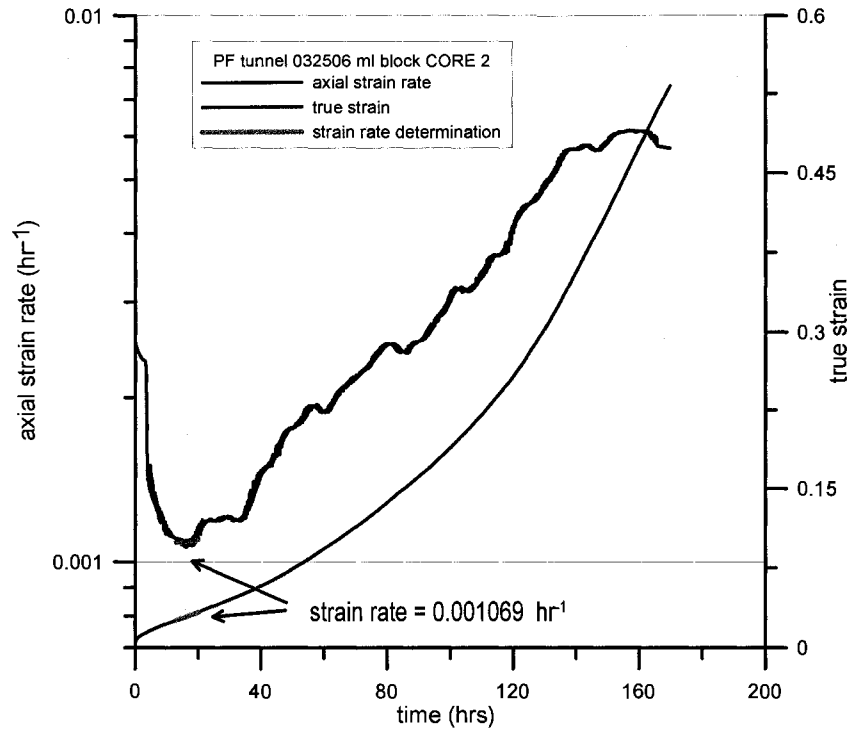

Figure 7.1. Determination of minimum strain rate for a well defined minimum strain rate. Sample no. 11 is shown at a test temperature of -0.96°C and a stress level of 327.5 kPa.

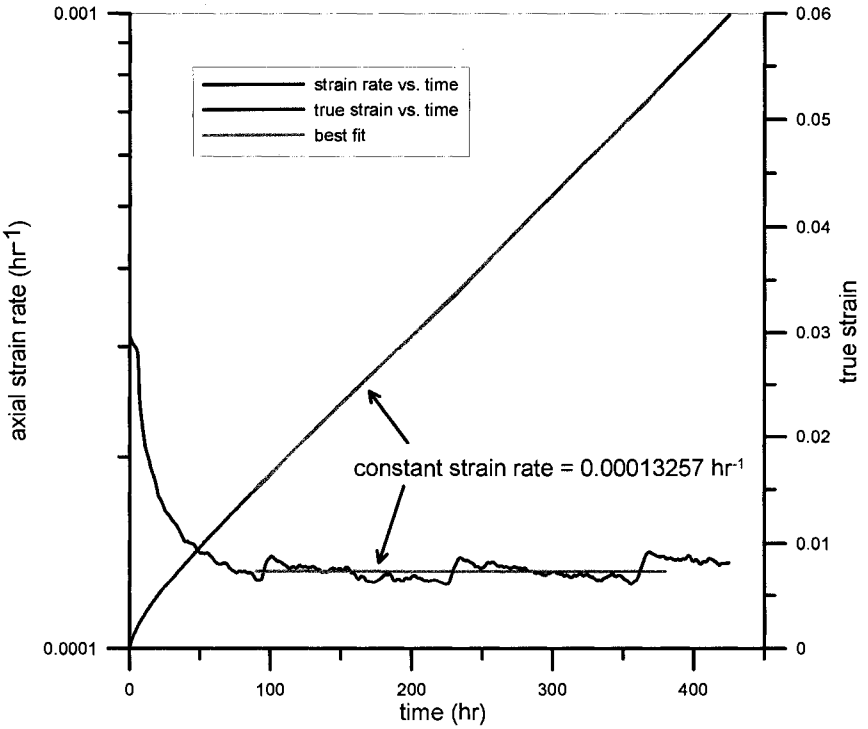

Figure 7.2. Determination of minimum strain rate for a steady state creep regime. Sample no. 14 is shown at a test temperature of -2.07°C and a stress level of 220.6 kPa.

similar to that seen for the previous load adjustment. The strain rate gradually decreases again. It is the author's belief that the tendency not to see steady state creep regimes (or minimum strain rate) at lower stresses in the literature is the sensitivity of the samples to the increase in the cross sectional area. This observation relies on the assumption stated previously that a constant volume is maintained. In this study, sample diameters with changing axial displacements were assumed from axial deformation and were not directly measured during the course of an experiment.

Figure 7.3 shows test data for sample no. 13 (PF tunnel 1+00b RWH CORE a) at a test temperature of -1.99°C. This curve correlates to the steady state approximation (SS approx.) as seen in Tables 7.1 and 7.3. As seen in the curve, a load adjustment occurred at test time of approximately 194 hrs. After the load adjustment, the strain rate continued to decrease below the level achieved before the first load adjustment. Since the total true strain was rather low for the test, another load adjustment had not occurred. For this test, the load adjustments were set to perform every 0.1 inches (0.254 cm). At the end of the test stage, the test was only 0.02 inches (0.051 cm) from an automatic load adjustment. Comparing to Figure 7.2, in which the load adjustments occurred every 0.05 inches (0.127 cm), it is plausible to assume that with the next load adjustment the strain rate would increase. As a result the strain rate would appear constant in contrast to a continual decrease with time. Based on this concept, when a steady state or minimum creep regime was not observed as in Figure 7.3, a steady state approximation was used. The steady state approximation was a best fit linear regression using the last 48 to 72 hours of the test on the true strain vs. time plots. It is felt that the resulting strain rate is not a gross overestimation of a minimum strain rate value. For most of the ice-rich undisturbed samples tested, a secondary creep regime tended to dominate the process.

Table 7.5 shows the predicted and ending diameters for a select number of CSC test samples. The predicted diameters are the expected diameters of the sample based on a constant volume assumption and axial deformation. The ending diameters are actual measurements of the sample at the end of the test. For several of the earlier samples, only the max ending diameters were recorded and are notated as avg. max. One set of measurements consist of two diameter measurements oriented perpendicular to each other. The samples notated with avg. top and max indicate that two sets of measurements were made with one them being the maximum diameter. Samples notated with avg. top, mid, bottom indicate that three sets of measurements were made at the top, middle, and bottom, and may or may not represent the maximum ending diameter. The predicted end diameters tend to be less than or comparable to the actual ending diameters.

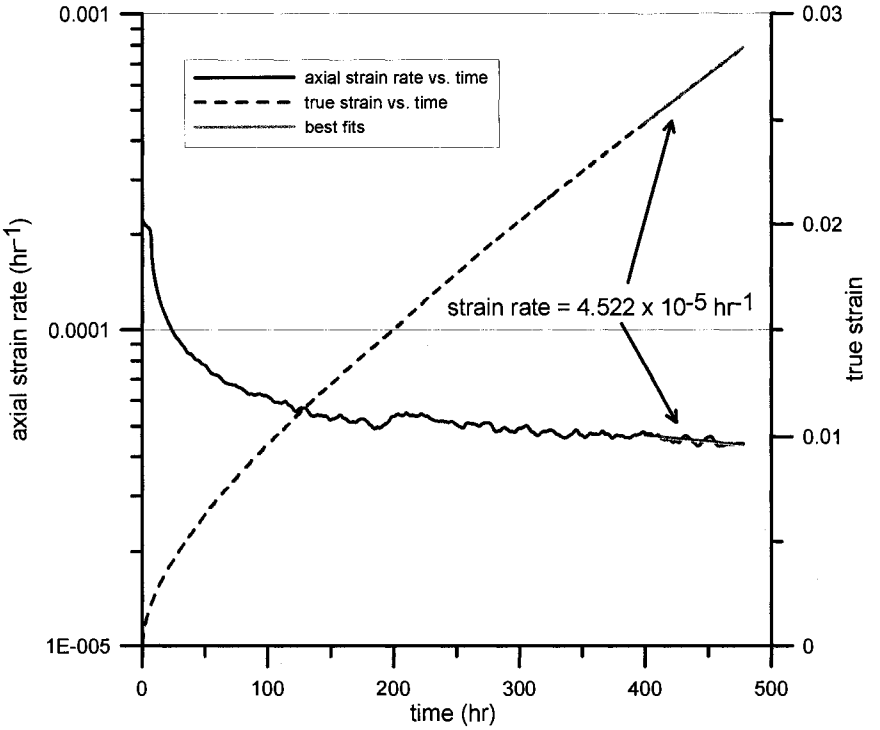

Figure 7.3. Determination of minimum strain rate for steady state approximation (SS approx. tables 7.1 and 7.3). Sample no. 13 is shown at a test temperature of -1.99°C and a stress level of 259.7 kPa.

Table 7.5. Predicted and measured ending diameters for select CSC samples.

No.	Sample	ending diameter (cm)		comments
		predicted	average measured	
4	PF tunnel 100705 1+04b RWH 0-14 cm	8.60044	9.171	avg max
5	PF tunnel 100705 1+04b RHW 44-59 cm	8.74776	9.223	avg max
6	PF tunnel 100705 1+20 LFV 24-39 cm	9.25322	10.748	avg max
7	PF tunnel 100705 1+02 LFV 89-105 cm	8.85444	9.261	avg max
8	PF tunnel 032506 ml block CORE 1	9.31418	9.211	avg top and max
9	PF tunnel 100705 1+02 LFV 118-133	8.8011	9.358	avg top and max
10	PF tunnel 042806 0+58 LWH 0-15 cm	8.30072	10.137	avg max
11	PF tunnel 032506 ml block CORE 2	9.79678	9.828	avg top and max
12	PF tunnel 032506 0+98b RWH CORE 1	8.10006	8.285	avg top, mid, bottom
13	PF tunnel 121906 1+00b RWH CORE a	8.99414	9.582	avg top and max
14	PF tunnel 030907 1+02 RWH	8.44042	8.428	avg top, mid, bottom
15	PF tunnel 030907 0+97 RWH CORE 3	8.04418	8.767	avg top, mid, bottom
20	PF tunnel remolded massive CORE 7	9.23544	9.169	avg top, mid, bottom
21	PF tunnel remolded massive CORE 16	8.90016	9.127	avg top, mid, bottom
22	PF tunnel remolded massive CORE 21	8.7249	9.197	avg top, mid, bottom

The constant volume assumption expects a uniform increase in area along the entire length of the sample. In most cases, this was not the case. Therefore, the measured diameters should have a tendency to be larger than the predicted. The predicted diameters in Table 7.5 are given for the total deformation of the sample. The predicted diameters as a function of sample axial deformation are the basis for the automatic load adjustments performed in the CSC creep tests. Based on the observations that the predicted values are less than or comparable to the actual, then the load adjustments are actually conservative in nature in that the stress values do not exceed the target stress. This would suggest that minimum strain rates are also conservative and that the steady state approximations may not be a large over estimation of minimum strain rates.

7.1.2 Minimum Creep Rate Relationships

The most common way to present creep data is based on the presentation of minimum strain rates as a function of stress and temperature through the use of power law relationships. The relationships are generally based on the simple power law proposed by Glen (1955). The primary purpose of the CSC portion of the testing program was to define the minimum strain rate flow law in relation to several of the tested soil cryostructures for a given temperature. Refer to section 7.1 for information on the minimum strain rate concept and its application. The primary emphasis was on soils with vertical micro-lenticular (vml) cryostructure and soils with remolded-massive (RM) cryostructure. In addition a small number of tests were performed on soils with horizontal micro-lenticular (hml) cryostructure, undisturbed silts and sandy silts containing massive cryostructure, wedge ice, and Matanuska glacial ice. The purpose of these tests was to produce data points for comparison to the more intensive series of tests conducted for soils with vertical micro-lenticular and remolded-massive cryostructure.

Figure 7.4 shows the interpreted minimum strain rates for vml cryostructure in a temperature range from -0.76°C to -1.21°C and a uniaxial stress range from 159 to 311 kPa. The plot clearly shows a high degree of data scatter with axial strain rates varying by an order of magnitude for a given stress condition. The large degree of scatter makes determination of a highly correlated power law fit difficult. However, best fit power law regressions were applied to the strain rate equation of the form shown in Equation 7.1. As shown in Figure 7.4, a best fit was applied to the cumulative data (average) along with upper and lower bounds. The purpose of the upper and lower bounds is to supply a comparison for min and max flow conditions for the data presented. The resulting flow laws correlating to Equation 7.1 are presented in Figure 7.4. The resulting flow laws are highly sensitive to interpretation of the data. The average curve (cum data) relationship

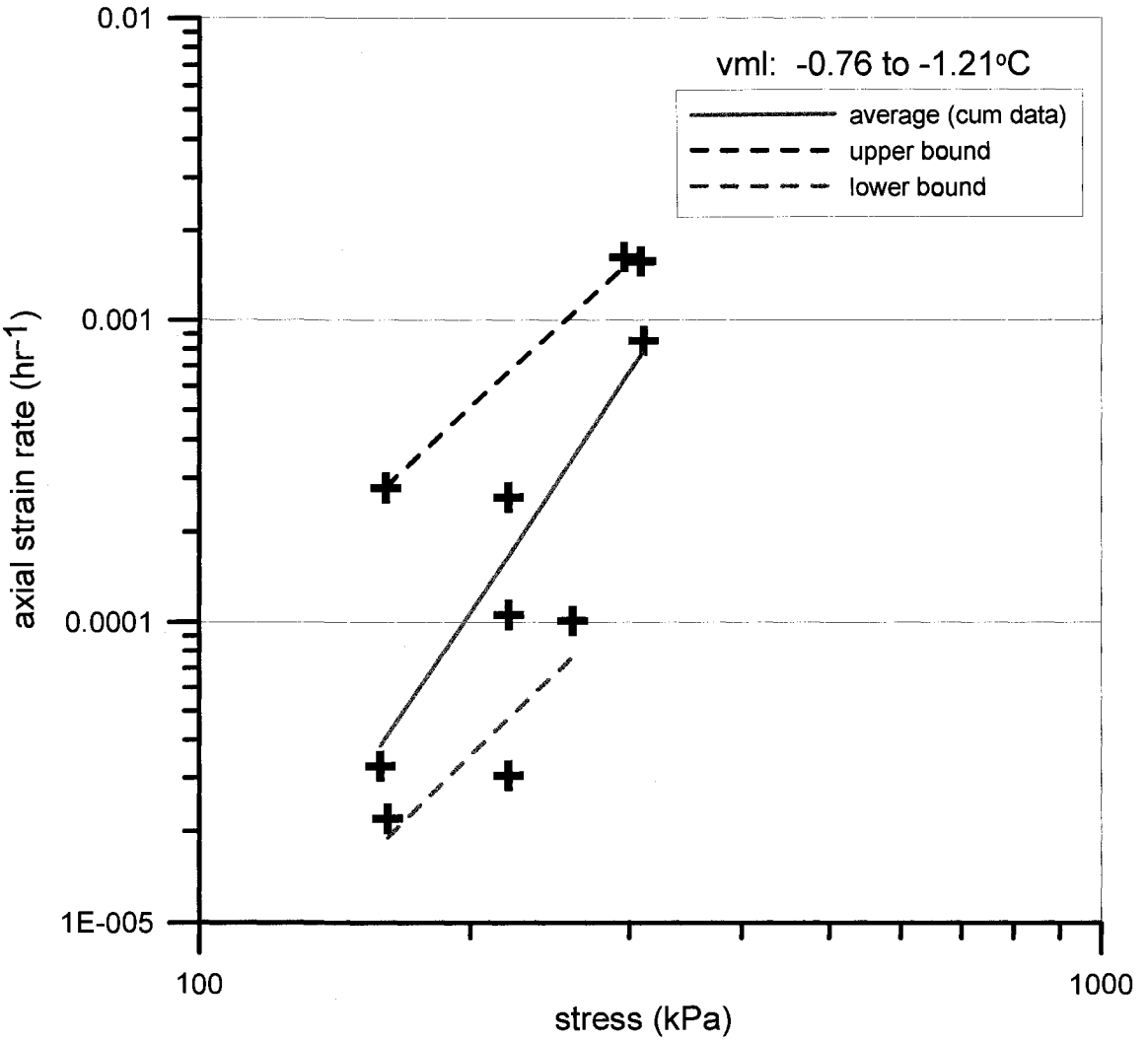

curve	strain rate equation $hr^{-1}=(hr^{-1}kPa^{-n})*(kPa^{n})$ $(hr^{-1}=(hr^{-1}psi^{-n})*(psi^{n}))$	r^2	Sample No.
average (cum data)	$\dot{\varepsilon} = 4.7791x10^{-15}\sigma^{4.498}$ $(\dot{\varepsilon} = 2.8251x10^{-11}\sigma^{4.498})$	0.556	3, 5, 12, 13, 15, 18
upper bound	$\dot{\varepsilon} = 2.1614x10^{-10}\sigma^{2.769}$ $(\dot{\varepsilon} = 4.5371x10^{-8}\sigma^{2.769})$	0.994	3, 5
lower bound	$\dot{\varepsilon} = 5.9983x10^{-12}\sigma^{2.942}$ $(\dot{\varepsilon} = 5.9983x10^{-9}\sigma^{2.942})$	0.777	12, 13, 15

Figure 7.4. Minimum strain rates as a function of stress for soils with vertical micro-lenticular (vml) cryostructures for a temperature range of -0.76°C to -1.21°C.

in Figure 7.4 could be easily fit to the data so that the slope of the curve (i.e. n coefficient) is similar to the upper and lower bound relationships. The A parameter then changes accordingly.

Figure 7.5 reduces the cumulative data shown in Figure 7.4 into two data sets. One data set has been reduced to the data which is nearest to -1°C, with a temperature range of -0.91°C to -1.03°C. The other data set is confined to the data near -1°C, but also meets the condition that a minimum or steady state strain rate was identified (SS approximations were not included.). The resulting best fit flow law equations are presented in Figure 7.5. The data scatter is still rather large for both conditions. However, the power laws are in better agreement to those cited for undisturbed Fairbanks silt (Thompson and Sayles, 1972, Law, 1987; Ladanyi and Huneault, 1989). The "minimum or steady state" data set and associated minimum creep rate relationship (see Figure 7.5) will be adopted as the representative flow law, as determined from CSC tests, for the soils with vertical micro-lenticular (vml) cryostructure at -1°C.

Figure 7.6 shows the minimum axial strain rates for soils with vml cryostructure at temperatures near -2°C (temperatures ranges from -1.92°C to -2.24°C). The amount of data scatter is reduced when compared to soils with vml cryostructure at -1°C. However, an appreciable amount of data scatter is still seen at the lowest stress range where the axial strain rates vary by almost two orders of magnitude. As the stress increases, the data comes together and results in an improved correlation. As seen in Chapter 4 (Section 4.4), the unfrozen water content increases significantly at temperatures warmer than -1°C. As a result, it is possible to expect that temperature variations close to -2°C have less influence than at temperatures close to -1°C. Alternatively, testing at high stresses generally supply a well defined minimum strain rate and therefore, more accurate determinations of minimum strain rates can be made thus improving the correlations. As seen in Figure 7.6, the lower the applied stress, the greater the variation in the minimum strain rate.

Figure 7.7 shows the minimum axial strain rates for soils with RM cryostructure for test temperatures of -1.01°C to -1.02°C. Tests with the creep data interpreted to be damped creep, were not included. The data is more tightly grouped than for the undisturbed samples shown earlier. Possible reasons for this may include a tighter range of test temperatures and higher uniformity between samples. The flow law is considerably different than the undisturbed soils presented earlier. This can also be observed by comparing data for remolded Fairbanks silt (Yuanlin and Carbee, 1987a) with data for undisturbed Fairbanks silt (Thompson and Sayles, 1972; Law 1987, Landany and Huneault, 1989; Ladanyi et al., 1991). The creep exponent n was determined to be 19.86 for soils with remolded-massive cryostructure as compared to 4.17

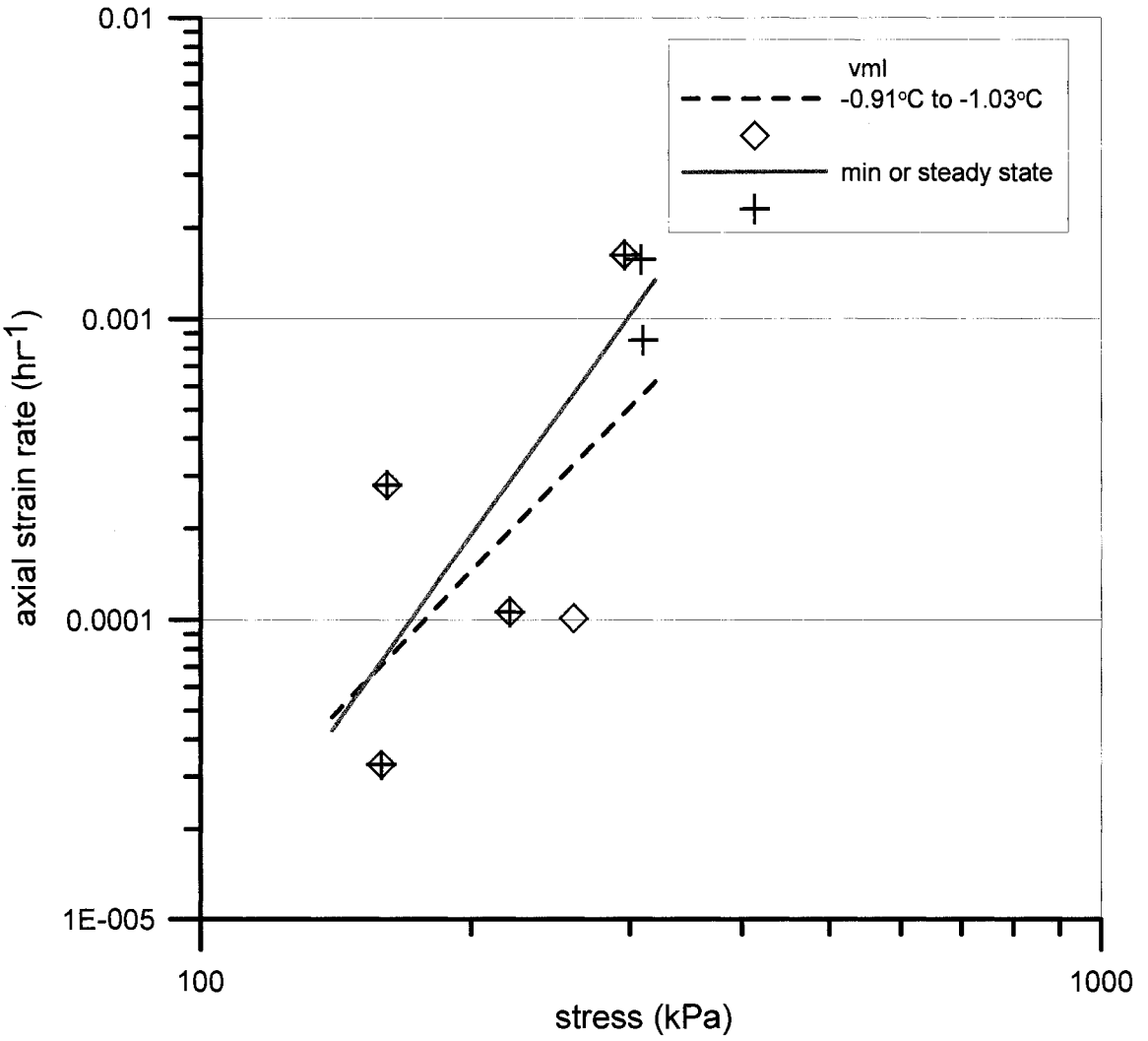

curve	strain rate equation $hr^{-1}=(hr^{-1}kPa^{-n})*(kPa^{n})$ $(hr^{-1}=(hr^{-1}psi^{-n})*(psi^{n}))$	r^2	Sample No.
-0.91˚C to -1.03˚C	$\dot{\varepsilon} = 1.04264x10^{-11}\sigma^{3.103}$ $(\dot{\varepsilon} = 4.16884x10^{-9}\sigma^{3.103})$	0.351	5, 12, 13, 18
min or Steady state	$\dot{\varepsilon} = 4.87502x10^{-14}\sigma^{4.167}$ $(\dot{\varepsilon} = 1.52114x10^{-10}\sigma^{4.167})$	0.701	3, 4, 5, 12, 18

Figure 7.5. Minimum strain rates as a function of stress for soils with vertical micro-lenticular (vml) cryostructure near -1˚C. One curve combines the samples with tests run near -1˚C. The other curve combines test data in which a minimum or steady state strain rate was identified.

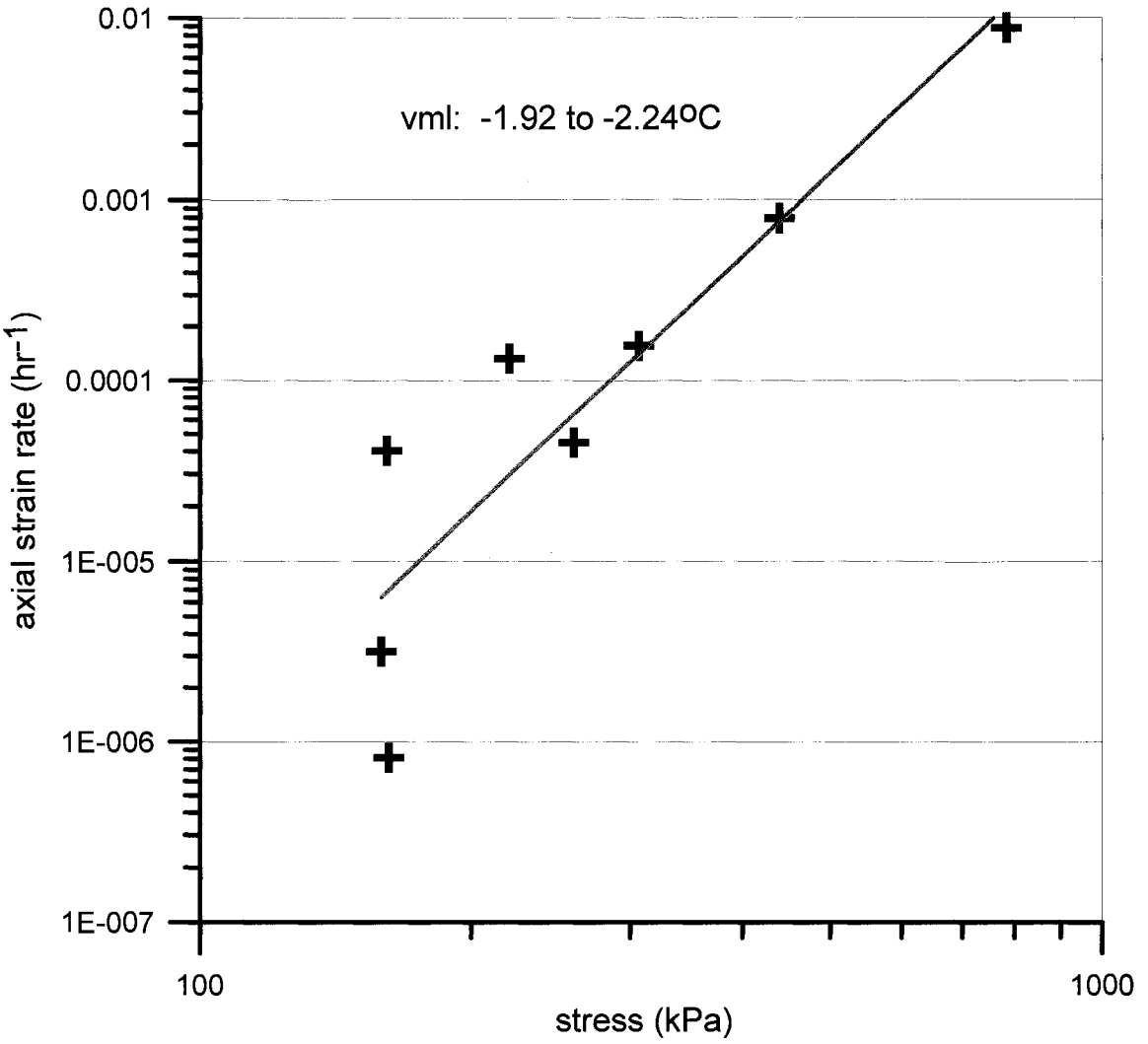

curve	strain rate equation $hr^{-1}=(hr^{-1}kPa^{-n})*(kPa^{n})$ $(hr^{-1}=(hr^{-1}psi^{-n})*(psi^{n}))$	r^2	Sample No.
vml @ -2°C	$\dot{\varepsilon} = 2.80116x10^{-16}\sigma^{4.704}$ $(\dot{\varepsilon} = 2.46305x10^{-12}\sigma^{4.704})$	0.822	1, 2, 4, 5, 12, 13, 14

Figure 7.6. Minimum strain rates as a function of stress for soils with vertical micro-lenticular (vml) cryostructures for a temperature range of -1.92°C to -2.24°C.

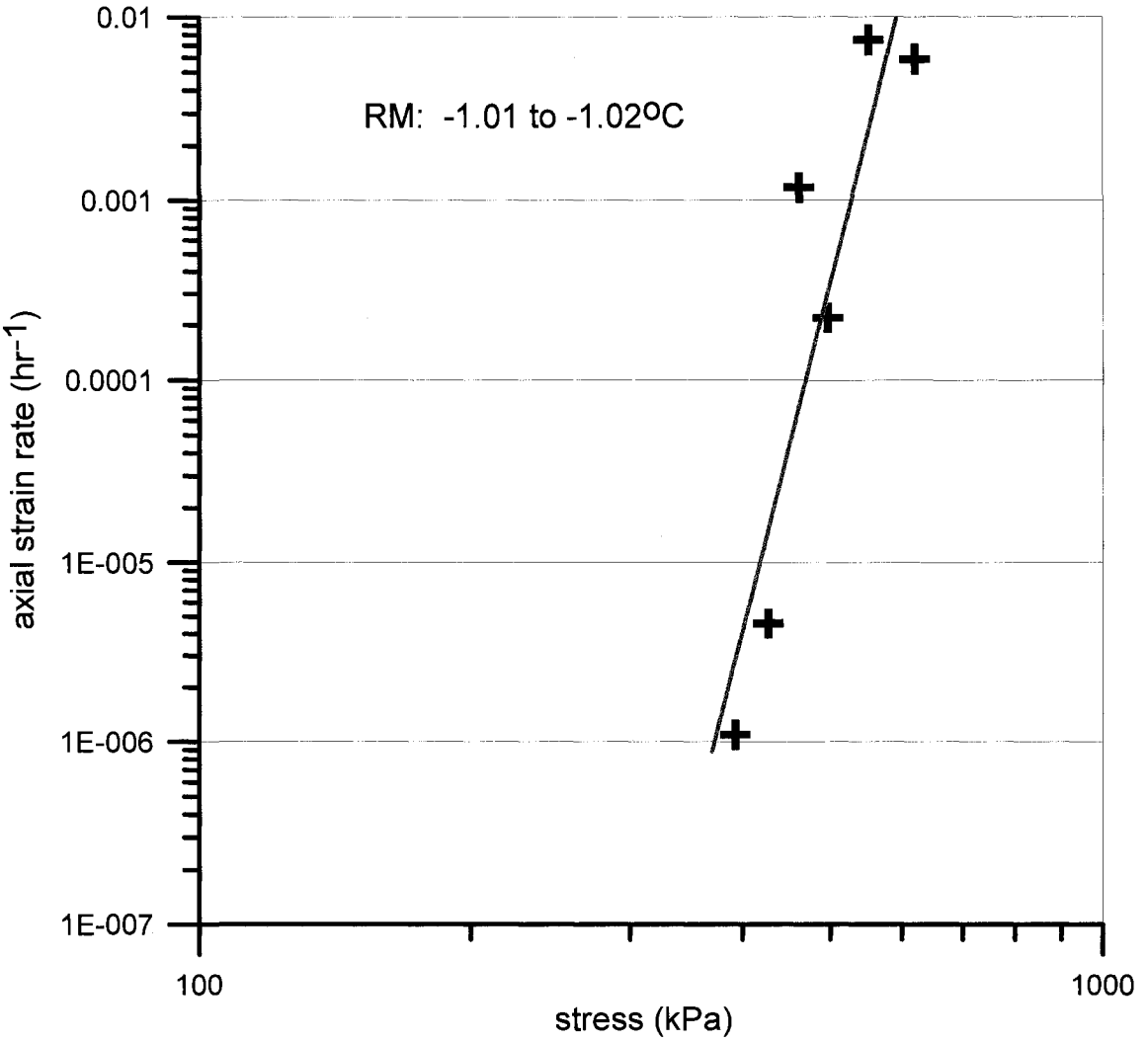

curve	strain rate equation $hr^{-1}=(hr^{-1}kPa^{-n})*(kPa^{n})$ ($hr^{-1}=(hr^{-1}psi^{-n})*(psi^{n})$)	r^2	Sample No.
RM @ -1°C	$\dot{\varepsilon} = 8.62056x10^{-58}\sigma^{19.860}$ ($\dot{\varepsilon} = 3.87667x10^{-41}\sigma^{19.860}$)	0.801	20, 21, 22

Figure 7.7. Minimum strain rates as a function of stress for soils with remolded massive (RM) cryostructures for a temperature range of -1.01°C to -1.02°C.

(vml, -1°C) and 4.70 (vml, -2°C) for soils with vertical micro-lenticular cryostructure. Yuanlin and Carbee (1987a) determined that the creep exponent n was equal to 27.36 for -1°C and strain rates less than 0.0036 hr^{-1}. Yuanlin and Carbee (1987a) hypothesize that the increased creep exponents are influenced by the soil particles, which act to impede motion that is facilitated by creep of the pore ice.

Figure 7.8 summarizes the minimum strain rate data for all of the CSC tests. Included are the best fit power law regressions determined in Figures 7.5, 7.6, and 7.7 for soils with vml cryostructure at -1°C and -2°C and for soils with RM cryostructure at -1°C. Also included are the strain rate vs. stress data points for all of the frozen soils and ice facies that were tested under CSC conditions. A slight decrease in the strain rates for a given stress level occurs as the temperature decreases from -1°C to -2°C for soils with vml cryostructure. Soils with RM cryostructure show a much larger n value (i.e. curve slope). Under the assumption that extension of the strain rate-stress relationships is valid to higher stress conditions, the following observations can be made. At stresses above approximately 650 kPa, soils with RM cryostructure show higher strain rates for a given stress than the icier soils with vml cryostructure. This observation needs further verification. Soils with vml cryostructure show significantly higher strain rates at stresses lower than 650 kPa.

7.2 Minimum Strain Rate Comparison: CSC Tests and Literature Data

Determination of minimum strain rate relationships based on a Glen type flow law (Glen, 1955) was presented for CSC (constant stress creep) tests in section 7.1. The purpose of this section is to compare the results from CSC tests and literature for ice-rich frozen soils. The comparison is primarily based on soils with vertical micro-lenticular (vml) cryostructure at -1°C and -2°C and soil with remolded-massive (RM) cryostructure at -1°C.

Figure 7.9 shows a comparison of minimum strain rate relationships derived from CSC test data for soils with vertical micro-lenticular cryostructure and data from literature sources for soils with a similar cryostructure. The literature sources are derived from in-situ tests in the CRREL permafrost tunnel and include data based on tunnel closure rates (Thompson and Sayles, 1972), data from plate load tests (Law, 1987), and data from cone penetrometer tests (Ladanyi and Huneault, 1989). As indicated in Chapters 3 and 4, water content can be used as an indirect indicator of the type of soil cryostructures found within the tunnel. It is based on the high water contents cited in the literature that the soil tested most likely corresponds to soil with micro-lenticular cryostructure. However, the soil cryostructure were not described in the literature

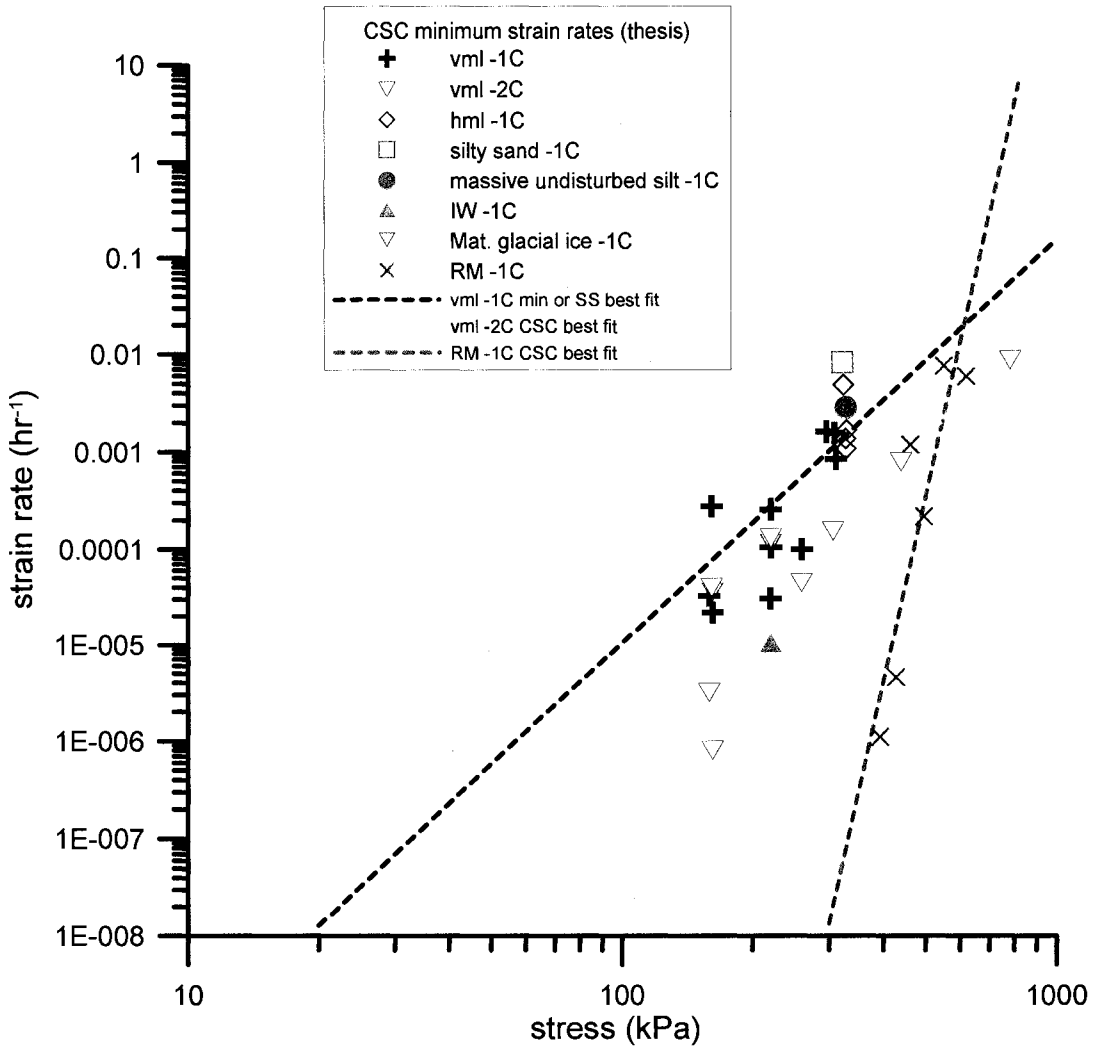

Figure 7.8. Summary of minimum strain rate power relationships determined from CSC tests for soils with vml cryostructure and soils with RM cryostructure. Also included are the minimum strain rates vs. stress data points for all of the samples used in the CSC testing program.

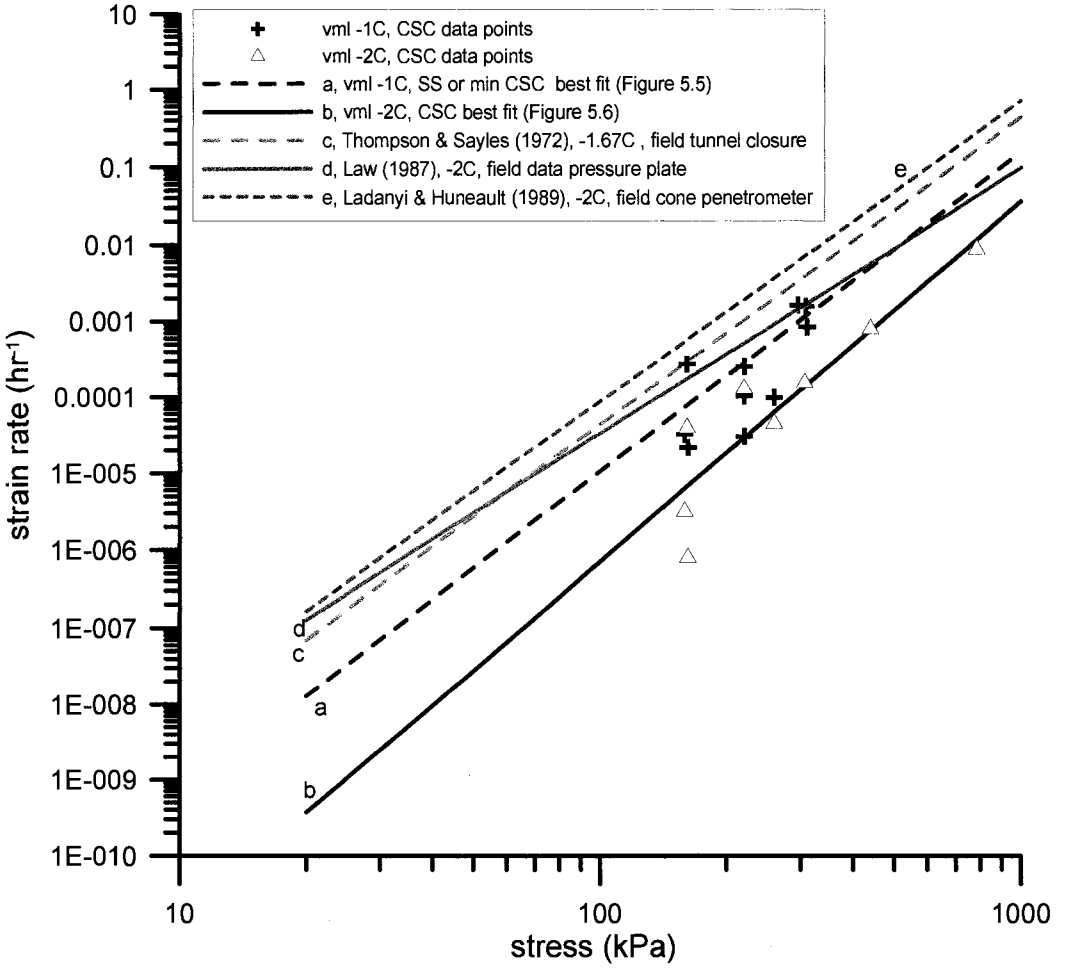

Figure 7.9. Minimum strain rate-stress relationship comparison for CSC test data and literature data for soils with vertical micro-lenticular (vml) cryostructure.

sources. The soil temperatures for the literature sources generally range from -1.7°C to -2°C. For a given stress, the predicted strain rate from the field derived relationships is greater than predicted from the CSC test data is this work. As compared to the CSC vml -2°C curve (Fig. 7.6), the field data predicts strain rates for a given stress which are one to two orders of magnitude larger. The difference may be the result of a field and laboratory scaling effect. Alternatively, the soil cryostructure may be different than micro-lenticular cryostructure, thus resulting in increases strain rates. Finally, it may be possible that laboratory results are not representative of the in-situ soil response. The slopes of the relationships are similar, thus the value of the n exponent in the flow law relationship are similar.

The CSC data in this work for soils with remolded-massive (RM) cryostructure are compared to literature data for remolded Fairbanks silts from the tunnel as presented by Yuanlin and Carbee

(1987a) in Figure 7.10. The CSC data presented corresponds to a test temperature of -1°C. Two power law relationships are shown from uniaxial tests conducted by Yuanlin and Carbee (1987a) for low density silt (bulk density 1.62 g/cm^3) and for medium density silt (bulk density 1.72 g/cm^3) at test temperatures near -2°C. The creep response for soils with RM cryostructure (curve a) in this work appear similar to the creep response for medium density silts at -2°C shown by curve b (Yuanlin and Carbee, 1987a). The main similarity is the slope of the curve (i.e. stress exponent, n). The primary difference is a shift to the right and thus a shift of the A coefficient in the power law relationship. It seems likely that a shift to the right on Figure 7.10 would result from a decrease in temperature from -1°C to -2°C. A shift to the right was observed for soils the vml cryostructure with decreasing temperatures (Figure 7.9). The soils with RM cryostructure used in this study have a frozen bulk density ranging between 1.5 and 1.6 g/cm^3. The frozen bulk density is similar to or less than the low density silts tested by Yuanlin and Carbee (1987a) which are

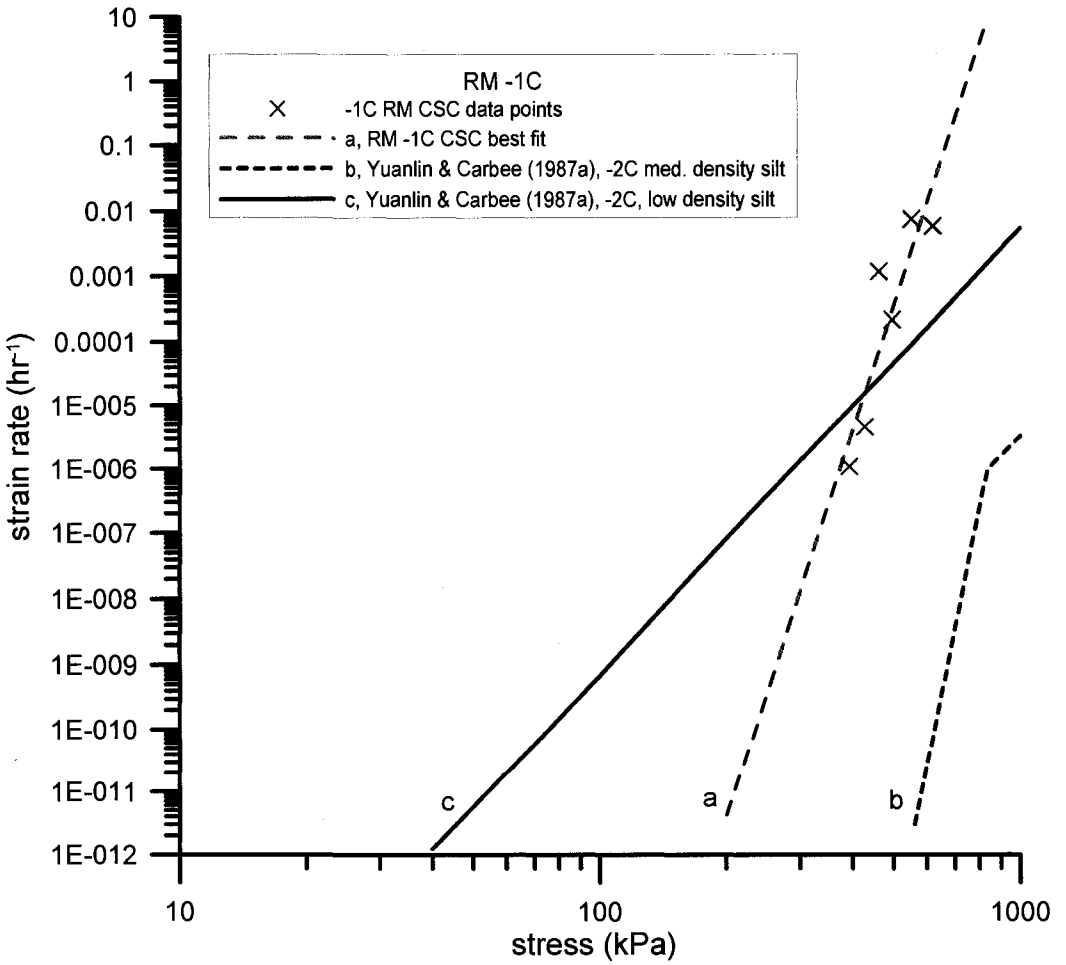

Figure 7.10. Minimum strain rate relationship comparison for CSC test data and literature data for soils with remolded-massive (RM) cryostructure.

shown by curve c in Figure 7.10. Despite this fact, as noted, the creep response is closer to the medium density silts tested by Yuanlin and Carbee (1987a). The strain rate vs. stress curve for medium density silts (Yuanlin and Carbee, 1987a) are shown by curve b in Figure 7.10. A change of the slope occurs at higher stresses which suggest that extrapolation of the minimum strain rate relationships from low stresses to stresses above this change of slope results in over estimation of strain rates. From the CSC data for soils with RM cryostructure, an increase in stress from 551.6 and 620.5 kPa did not yield an appreciable increase in the strain rate. However, a decrease in the strain rate is seen for an increase in the stress from 461.9 kPa to 496.4 kPa (data points shown in Figure 7.10). Therefore, the CSC data is insufficient to confirm whether or not a change in the creep behavior occurs at higher stresses for the soils with RM cryostructure used in this study as predicted by Yuanlin and Carbee (1987a).

Literature data on minimum strain rate flow laws for ice and ice-rich permafrost soils are presented in Chapter 2. These relationships are compared to all of the CSC data points for the different cryostructures, wedge ice, and ice tested in this work for temperatures ranging from -0.76°C to -2.24°C. The results are shown in Figure 7.11. The curves presented by Thompson and Sayles (1972) and Law (1987) were derived from in-situ testing in the CRREL permafrost tunnel at temperatures from -1.7°C to -2.5°C and provide good upper bound estimates for the data presented here. The relationship for McRoberts et al. (1978) was derived from ice-rich Norman wells silt at -1°C with ice layers oriented parallel to the principal stress. McRoberts (1988) presents additional creep data for ice-rich clayey permafrost, which also includes the Norman Wells silts reported by McRoberts et al. (1978). Extrapolation of the Norman Wells silt and clayey permafrost to undisturbed Fairbanks silt is non conservative based on our data. The ice data presented by Nixon and McRoberts (1976) appears to be quite conservative for all of the data tested in this work. The best fit flow laws derived from CSC data for soil with vml cryostructure at -1°C and -2°C are shown by curves a and b, respectively in Figure 7.11.

7.3 Minimum Strain Rate Summary

CSC tests were conducted in order to determine minimum strain rate vs. stress flow laws. Two soil cryostructures were tested. The first was undisturbed soil containing vertical micro-lenticular (vml) cryostructure. The second was remolded soil with the same silt composition as the undisturbed samples except the soil contained remolded-massive cryostructure. Flow law relationships for soils with vml cryostructure were determined for temperatures near -1°C and -2°C and for soils with RM cryostructure at a temperature of -1°C. In addition, a small number of data points were determined for additional undisturbed soil cryostructures and ice facies.

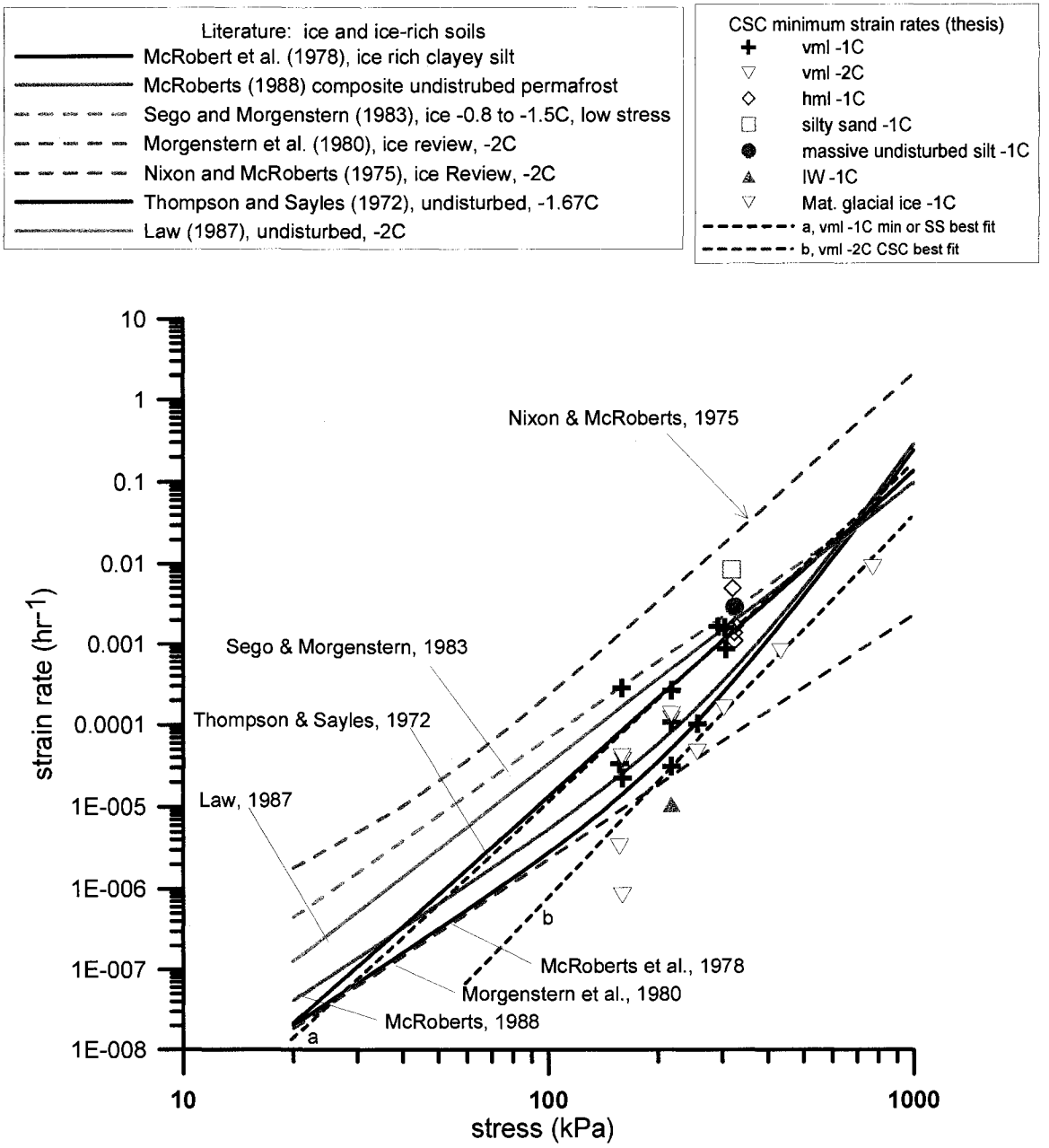

Figure 7.11. Minimum strain rate power law relationships based on literature review for ice and ice-rich soils including all CSC data and power regressions from this work. Note: see text for description of literature ice and ice-rich flow laws.

Additional soil cryostructures include horizontal micro-lenticular (hml) cryostructure, undisturbed silty sand and silts both containing massive cryostructure. Ice facies included syngenetic wedge ice and Matanuska glacial ice. A summary of minimum strain rates for soils with vml and RM cryostructures will be included below.

1. Vertical micro-lenticular (vml) cryostructure was one of the two primary cryostructures used for the determination of minimum strain rates from CSC creep tests. The prevalent data scatter and narrow stress range near -1°C made interpretation of CSC data difficult. Extending the data set to a larger stress range should improve the trend. The data scatter is still quite large for low stresses at -2°C with improved consistency of the data trend at higher stresses. The data scatter can be partially attributed to variability of undisturbed samples. In addition, the strain rate response appears to be more variable at low stresses. As the stress increases, the minimum strain rate trends show increased uniformity. This suggests that at high stresses, a single deformation mechanism drives the creep or plastic flow processes. At lower stress, the deformation mechanism show more variability depending on the specific soil conditions. Equations 7.1 and 7.2 summarize the minimum strain rate vs. stress flow laws for soils with vml cryostructure at -1°C and -2°C.

$$\dot{\varepsilon} = 4.87502 \times 10^{-14} \sigma^{4.167}, \text{ (valid for vml close to -1°C)} \qquad \text{Eq. 7.2}$$

$$\dot{\varepsilon} = 2.80116 \times 10^{-16} \sigma^{4.704}, \text{ (valid for vml close to -2°C)} \qquad \text{Eq. 7.3}$$

Where $\dot{\varepsilon}$ (hr^{-1}) is the strain rate, A ($kPa^{-n} \cdot hr^{-1}$) is an empirical constant, and σ (kPa) is the applied stress.

2. Soil with remolded-massive cryostructure is the only remolded soil used in this study. The resulting creep behavior is noticeably different than for the undisturbed soils with vml cryostructure. The minimum strain rate is significantly influenced by stress for the stress range tested. For stress levels less than 358.5 kPa, all creep deformations were damped with no minimum strain rates. Minimum strain rates were seen for stresses between 393 and 620.5 kPa. No tests were run above 620.5 kPa. Equation 7.3 summarizes the minimum strain rate vs. stress flow law for soils with RM cryostructure at -1°C

$$\dot{\varepsilon} = 8.62056 \times 10^{-58} \sigma^{19.860}, \left(\begin{array}{c} \text{valid for RM close to -1°C} \\ \text{and } 393 \le \sigma \le 620.5 \text{ kPa)} \end{array} \right) \qquad \text{Eq. 7.4}$$

Where $\dot{\varepsilon}$ (hr^{-1}) is the strain rate, A ($kPa^{-n} \cdot hr^{-1}$) is an empirical constant, and σ (kPa) is the applied stress.

The undisturbed soil with vml cryostructure and the remolded soil with RM cryostructure are composed of the same silty sediments. The primary difference is the variation in cryostructure and the associated difference in water content resulting from the variation in cryostructure. Data from CSC creep tests at -1°C show that creep occurs at a much greater rate for undisturbed soils with vml cryostructure than for soils with RM cryostructure for stresses less than 650 kPa. Extrapolation of the minimum strain rate flow laws to higher stresses would suggest that at stress above 650 kPa, soils with RM cryostructure creep at a greater rate than soils with vml cryostructure at -1°C. Additionally, damped creep is seen for soil with RM cryostructure below 359 kPa. Under the stress range tested (161 to 784 kPa), soils with vml cryostructure did not exhibit damped creep.

The testing time for CSC tests to determine flow law characteristics for soils with vertical micro-lenticular at -1°C took up to 12 months. The testing time for CSC tests for soils with RM cryostructure at -1°C was derived over a period of 4 to 5 months. The time indicated above correlates to the determination creep flow laws for one type of cryostructure at one specific temperature. For a range of temperatures, the tests times would be significant. An important limitation to CSC creep tests is the large volume of time required to determine minimum strain rates. It is important to maintain isothermal conditions when running creep tests. The large time intervals required for CSC tests can cause difficulties with strict temperature control in that power outages and mechanical issues with the temperature control equipment are not uncommon. In addition, mechanical issues can arise in the loading apparatuses when test periods are large. Any changes in temperatures and loading conditions have an influence on the creep rates. These affects are magnified when testing at temperatures close to the melting point of the samples.

As the large data scatter indicates, it would be desirable to test an even larger group of samples to help eliminate uncertainties. Detailed analysis on the micro-level could yield information that might explain the variations in strain rate responses. Helpful data could include ice crystal orientation, dominant sediment grain orientations, and characteristics of the soil water system. However, that is outside of the current scope of this work.

7.4 Stress Relaxation

A significant volume of the testing data was produced from relaxation tests. A wide range of frozen soil cryostructures and ice facies were tested, thus allowing for comparative analysis. In this section, the general patterns of stress relaxation for soils with different cryostructures and ice facies will be discussed. Subsequent sections will utilize results from stress relaxation tests to determine long term strength characteristics which are then compared to CSC creep test data (discussed earlier) and literature sources. The appendix interprets relaxation tests in the context of minimum strain rate flow laws. Most of the samples were tested at temperatures ranging between -0.8°C to -3.10°C. Soils containing remolded-massive (RM) cryostructure were tested at temperatures ranging from -0.3°C to -5.01°C. Tables 7.6 and 7.7 list the basic physical properties of the relaxation samples. Table 7.8 lists the test temperatures and loading range experienced by the samples during the course of the test. The high end of the stress range represents the stress level to which the sample was initially loaded. The low end of the stress range represents the stress level at the end of the test. The end stress may or may not represent a stabilized stress value. In most instances for undisturbed soils, it did not.

In the following section, a qualitative discussion of the stress relaxation curves will be presented for the various soil cryostructures and ice facies tested. The stress relaxation curves are grouped separately by type of soil cryostructure or ice facies. Soil cryostructures to be presented include vertical micro-lenticular (vml), horizontal micro-lenticular (hml), reticulate-chaotic (RC), and remolded-massive (RM). Ice facies to be presented include syngenetic wedge ice (IW), Matanuska basal glacial ice (BI), and Matanuska glacial ice (GI). Refer to Chapter 4 for descriptions of soil and ice facies. The stress relaxation curves are presented for both linear and logarithmic axes. Note that nearly all of the stress relaxation curves plotted on linear axes were cropped at a stress of 1000 kPa for presentation purposes.

The stress relaxation curves for soil with vertical micro-lenticular (vml) cryostructure are presented in Figure 7.12. The curves for samples no. 23 and 24 are cropped to 800 hrs on the linear axis plot (Fig. 7.12 (a)). The actual run time was 2067 hrs. A large initial drop of the stress is seen with greater than a 50% reduction of the stress during the first hour. Sample no. 24 (Fig. 7.12 (b)) shows a slower rate of stress relaxation over the first 1 hour of the test. This is primarily due to a lower initial stress. After a period of 1 to 10 hours, the stress relaxation curves tend towards linear on a log stress vs. log time plot. This shows a consistency in the relaxation process. It also shows that a power law relationship can be applied to the stress relaxation process based on the linear trend seen on a log-log plot (as is shown later in this work). In Figure

Table 7.6. Summary of soil properties for undisturbed permafrost samples tested under relaxation conditions.

No.	Sample	cryostructure	γ_{bf} (lb/ft^3)	γ_{bf} (g/cm^3)	γ_{dry} (g/cm^3)	$w_{grav.}$ (%)	$w_{vol,ice}$ (%)
23	PF tunnel 032506 0+98c RWH 3-17 cm	vml	79.7	1.28	0.57	123.1	76.6
24	PF tunnel 032506 0+98c RWH 34-50 cm	vml	80.7	1.29	0.59	118.9	76.4
25	PF tunnel 032506 0+98b RWH	vml	78.2	1.25	0.51	144.8	80.6
26	PF tunnel 032506 ml block CORE 3	hml	82.2	1.32	0.62	111.3	75.4
27	PF tunnel 032506 ml block CORE 4	hml	83.9	1.34	0.65	108.0	75.8
28	PF tunnel 032506 ml block CORE 5	hml	83.3	1.33	0.66	100.8	72.8
29	PF tunnel 032506 ml block CORE 6	hml	81.6	1.31	0.61	115.5	76.1
30	PF tunnel 032506 1+00a RWH	vml	84.0	1.35	0.66	102.8	74.2
31	PF tunnel 121906 2+35 RWH Core a	RC	91.8	1.47	0.84	74.0	68.0
32	PF tunnel 121906 2+35 RWH Core b	RC	93.5	1.50	0.87	71.4	67.8
33	PF tunnel 121906 2+35 RWH Core c	RC	88.4	1.42	0.76	86.2	71.2
34	PF tunnel 121906 2+35 RWH Core e	RC	83.3	1.33	0.62	115.7	77.8
35	PF tunnel IW CORE a	IW	55.8	0.89	0.00	41936	96.9
36	PF tunnel 020207 IW CORE 4	IW	55.9	0.90	0.00	29160	97.0
37	PF tunnel 020207 IW CORE 5	IW	54.8	0.88	0.00	48294	95.2
38	PF tunnel 020207 IW CORE 6	IW	57.2	0.92	0.03	2643	95.9
39	PF tunnel 020207 IW CORE 9	IW	55.4	0.89	0.01	14061	95.8
40	PF tunnel 020207 IW CORE 10	IW	55.9	0.89	0.02	3971	94.9
41	PF tunnel 020207 IW CORE 11	IW	55.9	0.90	0.00	45783	97.2
42	Matanuska Basal ICE CORE 1	BI	69.1	1.11	0.31	259	86.8
43	Matanuska Basal ICE CORE 2	BI	59.1	0.95	0.02	3715	100.2
44	Matanuska Basal ICE CORE 3	BI-micro-lenticular	87.3	1.40	0.76	83.1	69.0
45	Matanuska Glacial Ice CORE 3	GI	57.5	0.92	--	--	--
46	Matanuska Glacial Ice CORE 5	GI	58.2	0.93	--	--	--
47	PF tunnel ml block CORE SM1-conv. relax	vml	75.0	1.20	0.47	157.4	79.9
48	PF tunnel ml block CORE SM2-conv. relax	vml	77.5	1.24	0.50	150.1	81.0

γ_{bf} is frozen bulk density, γ_{dry} is dry density, w_{grav} is gravimetric water content, $w_{vol,ice}$ is the volumetric ice content.

Table 7.7. Summary of soil properties for remolded samples tested under relaxation conditions.

No.	Sample	cryostructure	γ_{bf} (lb/ft^3)	γ_{bf} (g/cm^3)	γ_{dry} (g/cm^3)	$w_{grav.}$ (%)	$w_{vol,ice}$ (%)
49	PF RM CORE 1	RM	99.5	1.59	1.05	52.5	59.7
50	PF RM CORE 5	RM	97.7	1.57	1.04	50.6	57.2
51	PF RM CORE 6	RM	99.6	1.59	1.06	50.2	58.0
52	PF RM CORE 8	RM	95.9	1.54	1.01	51.5	56.8
53	PF RM CORE 9	RM	95.5	1.53	1.03	48.2	54.1
54	PF RM CORE 10	RM	95.7	1.53	0.98	55.9	59.8
55	PF RM CORE 11	RM	96.5	1.55	1.01	52.4	57.8
56	PF RM CORE 12	RM	96.7	1.55	1.01	52.7	58.1
57	PF RM CORE 13	RM	97.4	1.56	0.99	57.0	61.6
58	PF RM CORE 14	RM	97.3	1.56	1.00	55.5	60.5
59	PF RM CORE 15	RM	95.5	1.53	0.98	55.7	59.5
60	PF RM CORE 17	RM	94.4	1.51	0.96	57.1	59.8
61	PF RM CORE 18	RM	95.2	1.52	0.96	58.6	61.3
62	PF RM CORE 19	RM	96.0	1.54	1.01	51.9	57.1
63	PF RM CORE 20	RM	96.9	1.55	1.00	55.1	59.9
64	PF RM CORE 23-conv. relax	RM	96.5	1.54	0.98	57.9	61.6
65	PF RM CORE 24-conv. relax	RM	100.7	1.61	1.07	50.4	58.8

γ_{bf} is frozen bulk density, γ_{dry} is dry density, w_{grav} is gravimetric water content, $w_{vol,ice}$ is the volumetric ice content

Table 7.8. Temperature and stress range for relaxation tests.

No.		T (°C)	$\sigma_{full\ range}$ (kPa)	No.		T (°C)	$\sigma_{full\ range}$ (kPa)
23	vml	-0.77	31.6-1658.0	43	Bl	-1.86	88.3-1784.3
24	vml	-0.86	28.1-1140.8	44	Bl-ml	-1.02	105.8-1642.8
25	vml	-2.78	247.7-2176.8	45	Gl	-1.02	56.3-916.9
26	hml	-0.77	58.2-1239.3	46	Gl	-1.00	141.7-518.2
27	hml	-0.82	58.4-1356.3	49	RM	-1.05	275.9-1423
28	hml	-1.81	151.8-1604.6	50	RM	-0.99	253.3-1335.4
	hml	-2.81	198-1750.0	51	RM	-1.00	204-1327.2
29	hml	-1.86	150-1650.5	52	RM	-1.98	526.7-1613.6
	hml	-2.81	176.3-1869.5	53	RM	-1.99	505.7-1647.8
30	vml	-1.82	151.9-1832.1	54	RM	-3.01	969.2-1903.3
31	RC	-0.88	70.3-1441.7	55	RM	-2.99	714.8-1909.3
31	RC	-2.08	169-1689.6	56	RM	-0.50	141.6-1044.8
32	RC	-1.85	165-1951.7	57	RM	-0.50	131.5-1049.9
33	RC	-2.79	230.2-1761.5	58	RM	-0.30	72.7-953.9
34	RC	-1.85	127.7-1103.8	59	RM	-0.16	14-989.5
35	IW	-0.96	127.8-1566.2	60	RM	-4.02	917.3-2381
36	IW	-0.98	122.6-1226.7	61	RM	-4.01	888.5-2371.2
37	IW	-1.86	209.2-1412.1	62	RM	-5.01	1146.8-2749.8
38	IW	-1.86	200.8-1283.2	63	RM	-5.01	993.6-2520.4
39	IW	-3.1	160.6-1442.2				
40	IW	-3.1	129.3-1456.2				
41	IW	-0.44	207.4-936.2				

note: T is temperature in degrees C and $\sigma_{full\ range}$ is the total range of applied stress experienced by the sample over the course of the relaxation test.

7.12 (b), the slopes of sample no. 23 and 24 (which correspond to tests at -0.77°C and -0.86°C respectively) for times greater than 1 hour are larger than samples no. 25 and 30, which were tested under colder conditions. Alternatively, samples no. 25 and 30 show approximately the same slope for times greater than 1 hour with slope values of -0.212 and -0.214 respectively. The differences in slope suggest that a slightly different relaxation process is occurring for the warmer conditions (i.e. approx. -0.8°C). This most likely is attributed to increased unfrozen water contents. As shown in Chapter 4.4, the unfrozen water content for soils with vml cryostructure at temperatures colder -2°C are small. It increases rapidly for temperatures warmer than -1°C.

The stress relaxation curves for soils with horizontal micro-lenticular (hml) cryostructure are shown in Figure 7.13. The stress relaxation curves are similar to those for soils with

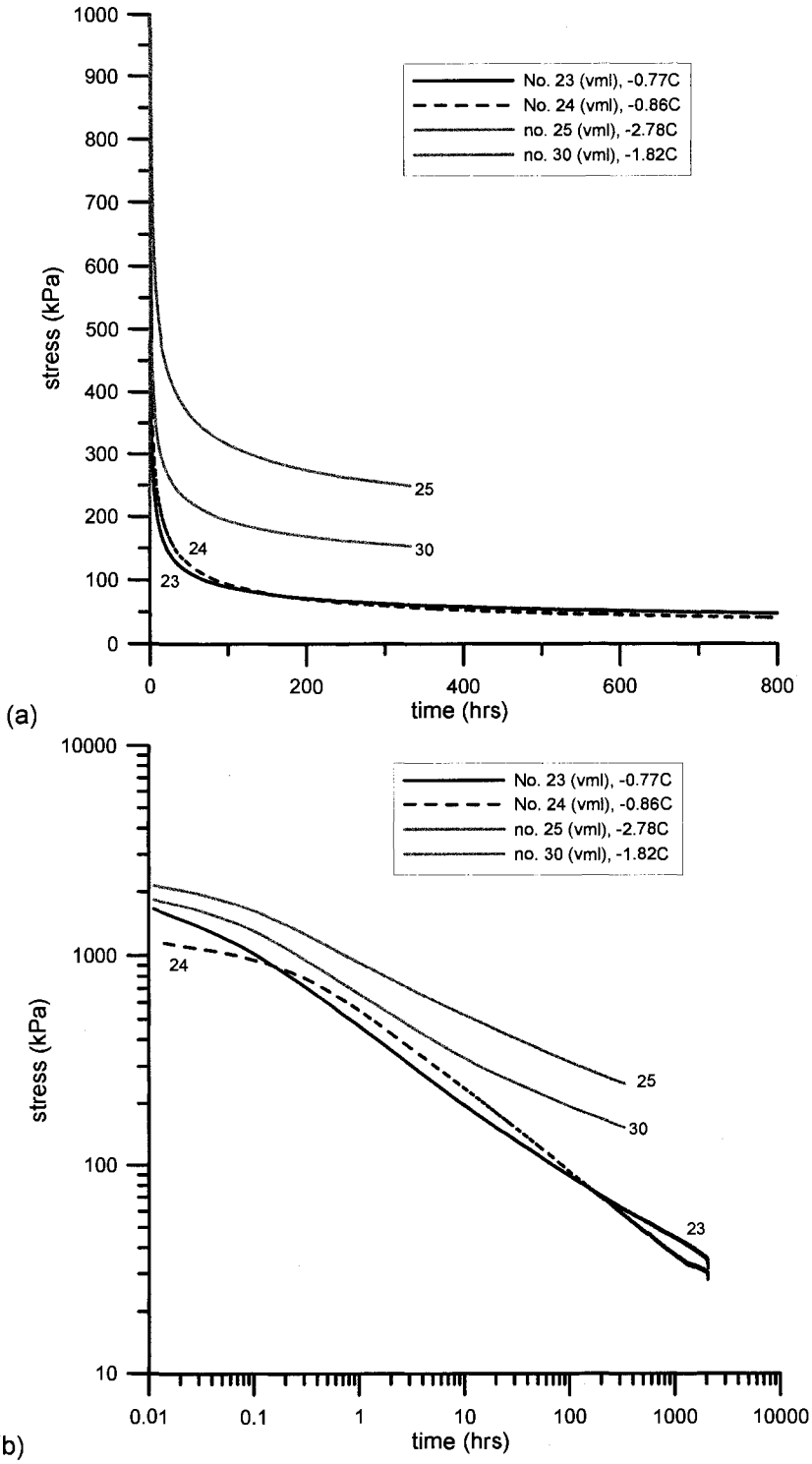

Figure 7.12. Stress relaxation for soils with vertical micro-lenticular (vml) cryostructure on linear axes (a) and on log-log axes (b).

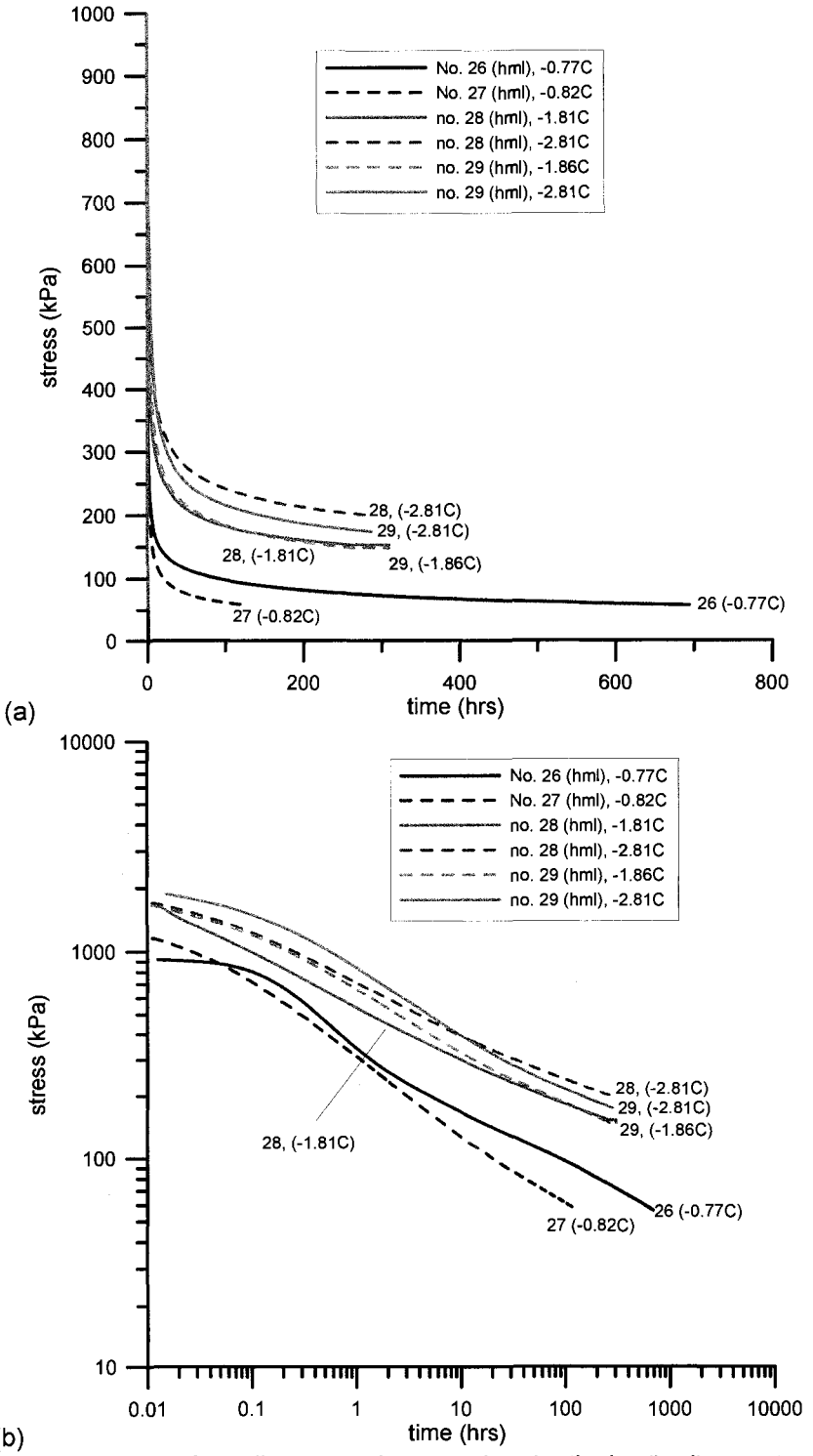

Figure 7.13. Stress relaxation for soils with horizontal micro-lenticular (hml) cryostructure on linear axes (a) and on log-log axes (b).

vml cryostructure. After a time period between 1 to 10 hrs, the slope of the curves (Fig. 7.13 (b)) becomes relatively constant. Similar to the soils with vml cryostructure, the slope of the curves (after 1 to 10 hrs) is larger for warmer soil conditions (samples no. 26 and 27). Some small fluctuations in slope are seen for samples no. 26 and 29. There is more variability of the stress relaxation curves during the relaxation process as compared to soils with vml cryostructure. As mentioned in Chapter 6, this may be attributed to subtle changes in the soil cryostructure of the samples containing hml cryostructure. The soils with hml cryostructure do not exhibit the same degree of uniformity in regards to the ice lens distribution as for soils with vml cryostructure. This is due to vertical sampling through the stratigraphic profile for soils with hml cryostructure as compared to horizontal sampling for soils with vml cryostructure along a narrower stratigraphic zone. In horizontal sampling, an area with a uniform cryostructure can be selected. In vertical sampling, the uniformity is much harder to control due to natural variability of the sediment and cryostructure sequence.

Soils with reticulate-chaotic (RC) cryostructure are characterized by 1-4 mm thick ice lenses running at a diagonal to the long axis of the core. This results in ice lenses that are aligned favorably for shear conditions which develop during uniaxial compression tests. The stress relaxation curves for soils with RC cryostructure are shown in Figure 7.14. The rate of initial rate of relaxation for the first 0.5 hours varies among the samples as evidenced in Figure 7.14 (b). Ignoring the difference in the initial relaxation, the stress relaxation curves in Figure 7.14 (b) show two distinct slope regions. The first occurs from the initial relax period or from 0.5 hrs depending on the sample, to a certain point of time where the slope angle decreases. The time of this transition ranges from approximately 1 hour at a temperature of -0.88°C to 10 hours at a temperature of -2.79°C. This trend is similar to the stress relaxation curves for soils with remolded-massive (RM) cryostructure which will be discussed next. The first linear segment of the stress relaxation curves correlates to a rapid drop is stress shortly after application of the load. This stress drop for samples no. 31 and 32 occurred immediately after application of the load. For samples no. 33 and 34 the stress drop occurred after a short time interval. The second linear segment correlates to a stress relaxation process which occurs at a much slower rate. Due to the technique of the relaxation method, the stress drop is directly related to soil deformation. Therefore, a rapid drop in stress generally is associated with rapid deformation. The first linear segment is attributed to movement occurring along the soil-ice lens contact. As shown in Chapter 6, significant movement was observed to occur along the ice lenses. At some point, deformation along the ice lenses no longer controls the deformation process. Instead, the soil matrix between the ice lenses begins to control the deformation process. The soil matrix between ice lenses

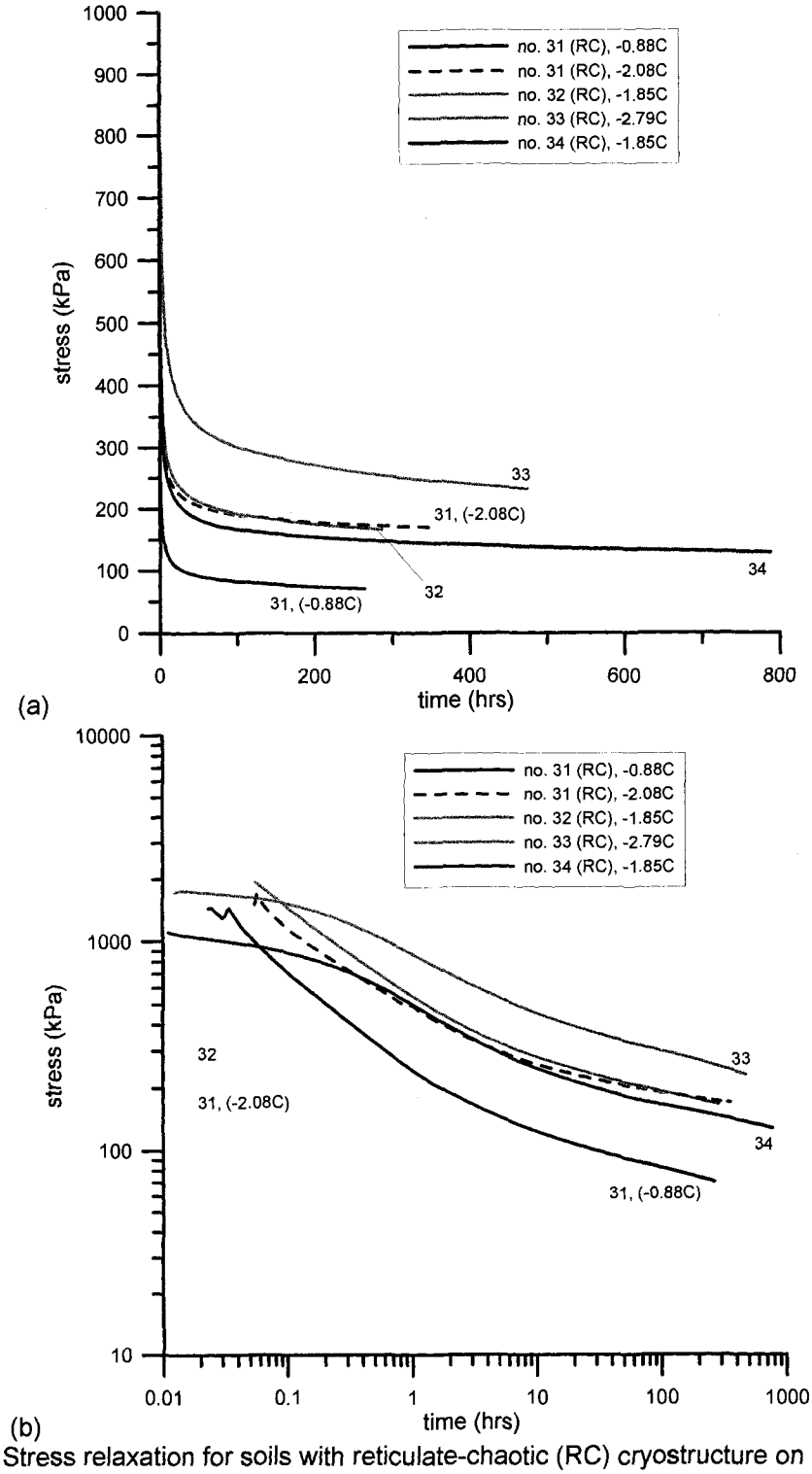

Figure 7.14. Stress relaxation for soils with reticulate-chaotic (RC) cryostructure on linear axes (a) and on log-log axes (b).

generally has a massive cryostructure. The slope of the second linear segment is smaller for soils with RC cryostructure than for soils with vml or hml cryostructure. For example, for sample no. 23 (-0.77°C) containing vml cryostructure the slope is -0.314, for sample no. 26 (-0.77°C) containing hml cryostructure the slope is -0.312, and for sample no. 31 (-0.88°C) containing RC cryostructure the slope is -0.161. As can be seen, the slope of the second linear segment for soils with RC cryostructure differs from the linear section of the stress relaxation process for soils with micro-lenticular cryostructure. Alternatively, the slope of the first linear segment is greater for soils with RC cryostructure than for soils with vml or hml cryostructure.

The stress relaxation curves for soils with remolded-massive (RM) cryostructure are shown in Figure 7.15. For soils with RM cryostructure they are similar in character to the stress relaxation curves for soils with RC cryostructure. Two linear segments are seen with a transition between the two (Fig. 7.15 (b)). The first linear segment indicates that a rapid drop of stress occurs after application of the initial load. This is quite visible in Figure 7.15 (a). In Figure 7.15 (a), little stress relaxation is seen once the initial stress relaxation is complete. This region of little stress relaxation correlates to the second linear segment in Figure 7.15 (b). As evidenced by the stress relaxation curves, the time to the initiation of the second linear segment increases with warming temperatures. The impact of temperature on the stress relaxation process can be seen in Figure 7.15. The onset of second linear segment is interpreted as an "activation" of the long term strength properties of the soil. In other words, a threshold stress level is approached where the deformation mechanisms change.

The stress relaxation of wedge ice (IW) shown in Figure 7.16, provides an important contrast to the stress relaxation behavior of the frozen soils tested. First, the stress relaxation proceeds at a slower rate as compared to the frozen soils. This is illustrated in Figure 7.16 (a) and (b). Secondly, the stress relaxation of wedge ice is practically independent of temperature. This is in sharp contrast with the stress relaxation process for frozen soils which showed a definite trend with temperature. As seen in Figure 7.16, the relaxation curves converge towards a similar stress level as test time increases. Based on this observation, the long term strength of wedge ice is similar for temperatures ranging from -0.44°C and -3.10°C. This is shown quantitatively in section 7.5.1.

Several samples of basal ice and englacial ice from the Matanuska Glacier, Alaska were also tested. The stress relaxation curves are shown in Figure 7.17. Analysis of samples no. 43 and 45 after testing showed that inner portions of the sample have evidence of brittle fracture such as

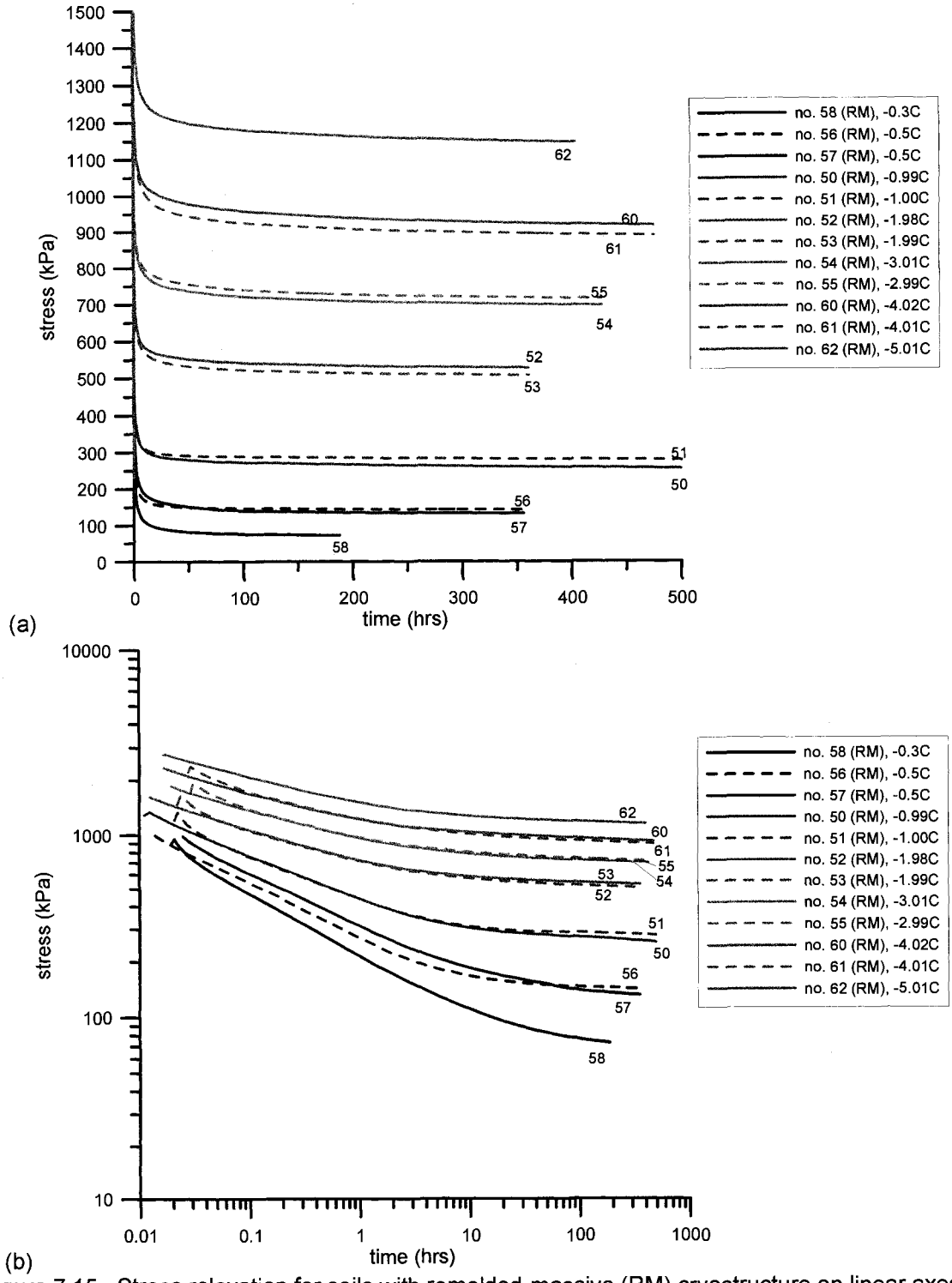

Figure 7.15. Stress relaxation for soils with remolded-massive (RM) cryostructure on linear axes (a) and on log-log axes (b).

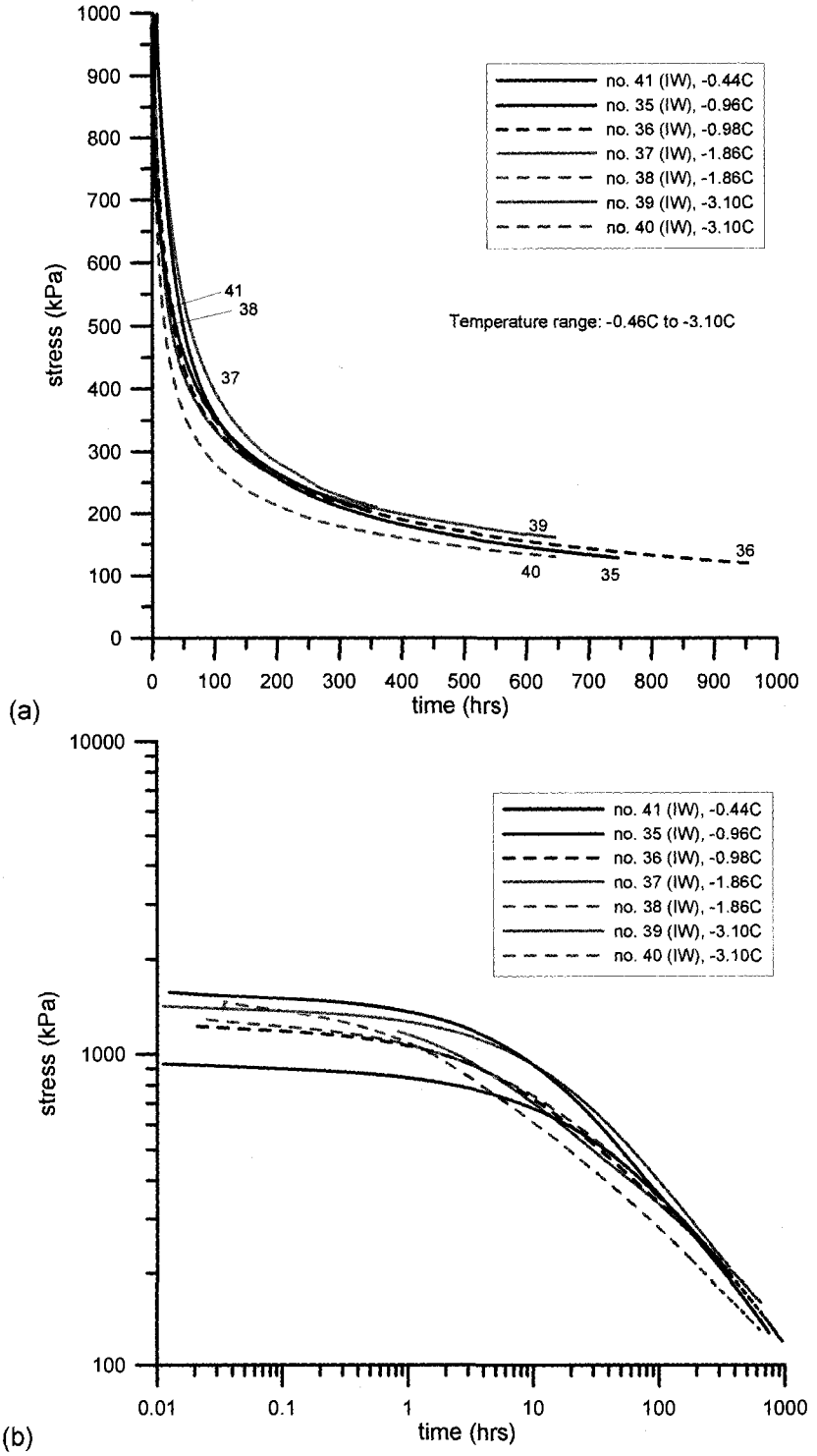

Figure 7.16. Stress relaxation for syngenetic wedge ice (IW) on linear axes (a) and on log-log axes (b).

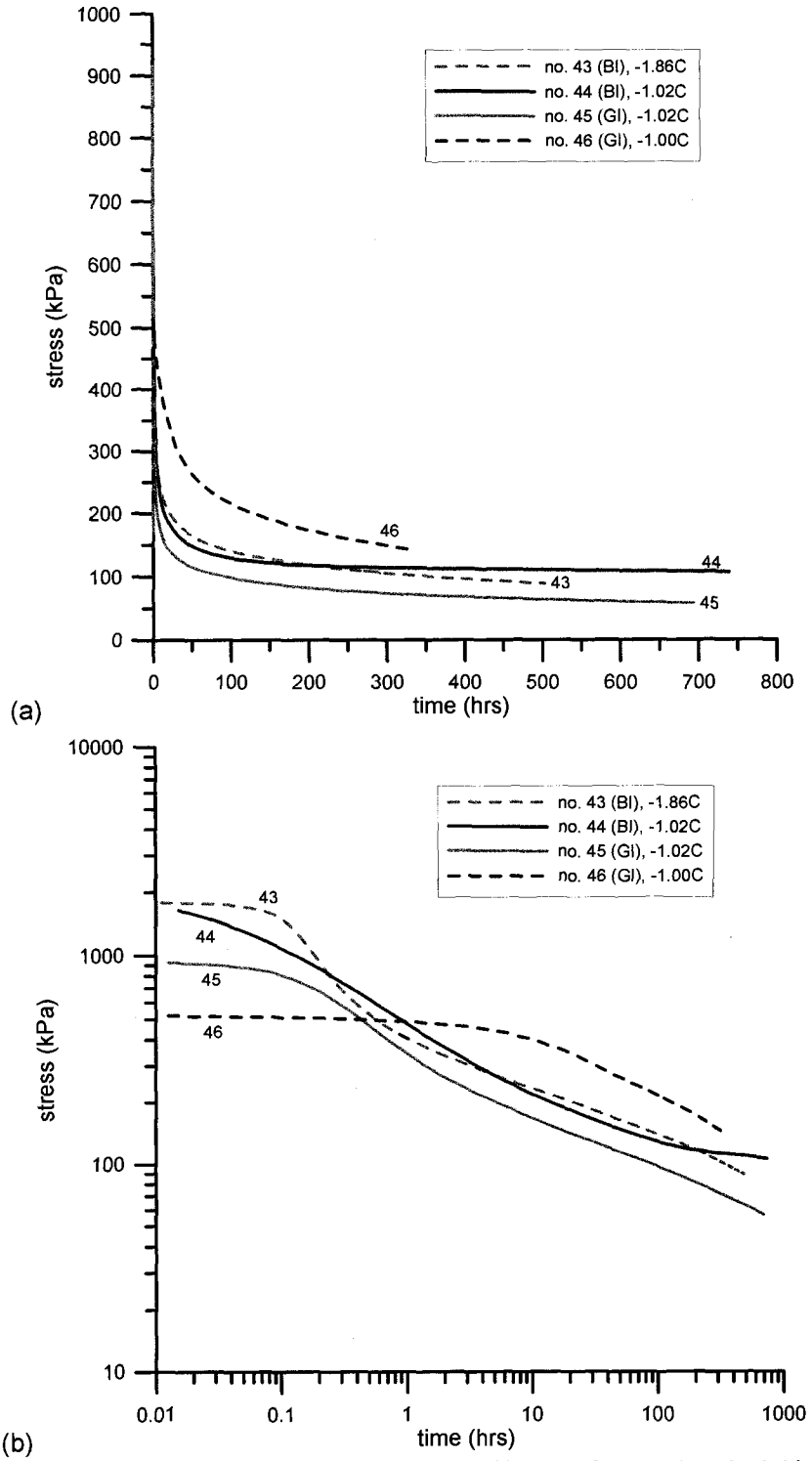

Figure 7.17. Stress relaxation for Matanuska basal ice (BI) and Matanuska glacial ice (GI) on *linear axes* (a) *and on log-log axes* (b).

wing fractures and opaque ice. Both samples were composed primarily of ice of high optical clarity. Both samples experienced an initial period with a slow rate of relaxation followed by a rapid increase of the rate of stress relaxation. Sample no. 44 (basal ice) contains an appreciable amount of silty sand with a well developed micro-lenticular cryostructure. No internal fractures after testing were observed. The stress relaxation follows a linear trend on log-log axes (Fig. 7.17 (b)). At a time period of 100 to 200 hours, the rate of stress relaxation reduces noticeably as evidenced by the inflection point on Figure 7.17 (b). The initial linear segment (Fig. 7.17 (b), sample no. 44) extends for a longer period of time, but the general nature of the curve is similar to those seen for soils with RC and RM cryostructrue in which the frictional forces start to influence the relaxation-deformation process. As described earlier, it can be explained as an "activation" of long term strength deformation mechanisms. Sample no. 46 consisted of englacial ice. In response to the brittle fracture patterns seen for samples no. 43 and 45, the initial loading stress for sample no. 46 was reduced. Analysis after testing showed no visible brittle fracture. The stress relaxation curve is very similar to those for wedge ice in which relaxation process proceeds at much slower rate as compared to frozen soils.

Figures 7.18 to 7.20 show a direct comparison of the relaxation curves for soil cryostructures and ice facies at -1°C, -2°C, and -3°C on linear axes. A few observations regarding the stress relaxation process will be discussed. At -1°C and -2°C, wedge ice shows significantly lower rates of stress relaxation as compared to frozen soils. At-1°C, Matanuska glacial ice also shows a slower rate of relaxation as compared to frozen soils. At -3°C, the relaxation rate of wedge ice still proceeds at a slower rate, but the stress relaxation rates for the soils also slow as compared to -1°C and -2°C. Generally, one can observe that icier the soil, the slower the relaxation rate or more prolonged the relaxation process. The amount of ice is generally associated with the type of cryostructure. For example, for soils with RM and RC cryostructure the stress drops rapidly following by little reduction of the stress as compared to the other icier soils. This relates to the activation of a long term strength resistance as discussed earlier. In addition, as the test temperatures become colder, the rate of relaxation for the frozen soils decreases. As the temperatures warm, the rate of relaxation increases, especially during the early time periods of the relaxation process. This is most likely related to the increased volume of unfrozen water as soil temperature warm.

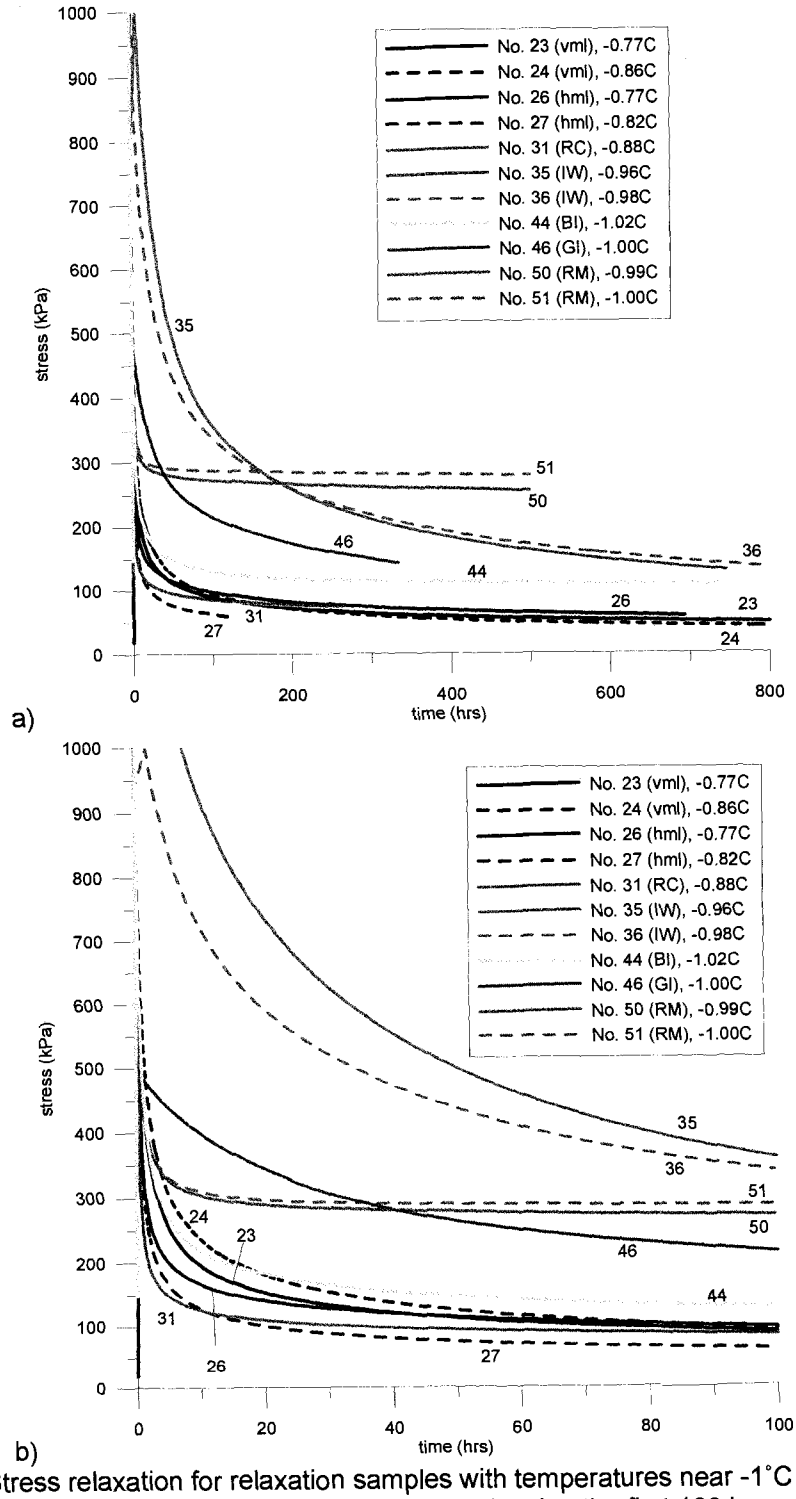

Figure 7.18. Stress relaxation for relaxation samples with temperatures near -1°C with plot a) showing the relaxation curves to 800 hours and plot b) showing the first 100 hours of the relaxation process.

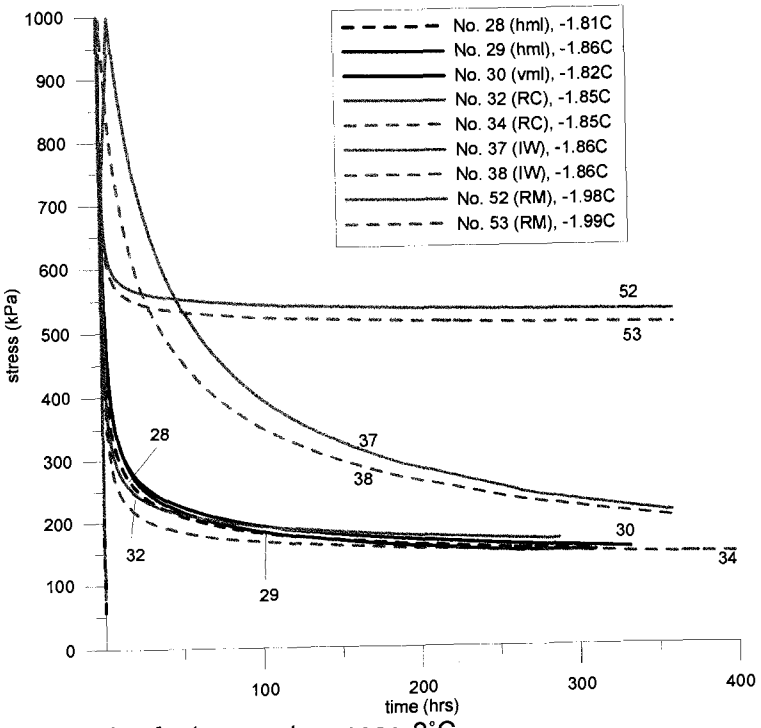

Figure 7.19. Stress relaxation for temperature near -2°C.

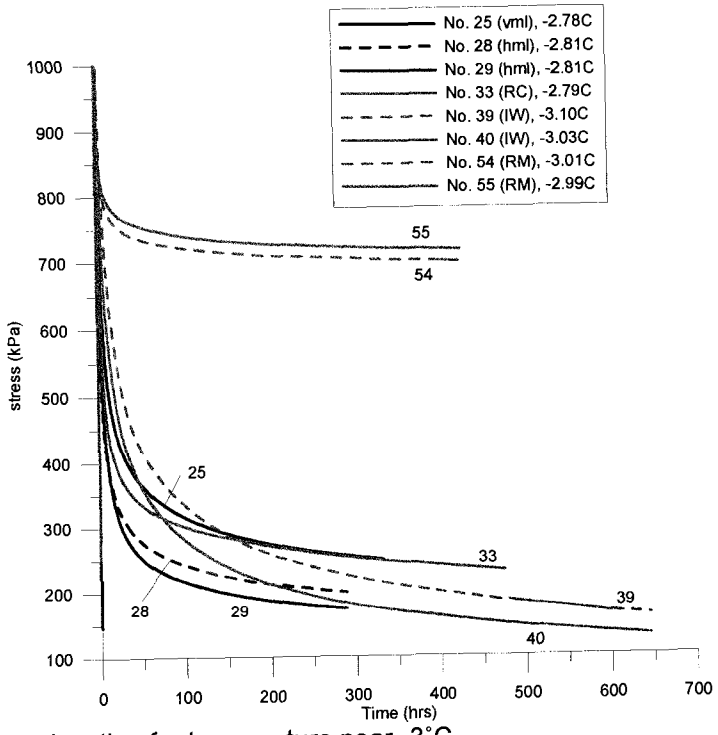

Figure 7.20. Stress relaxation for temperature near -3°C.

7.5 Long Term Strength

The purpose of this portion is to look at the impact of soil cryostructure on the long term strength of ice-rich permafrost. Only a few published studies include information on the long term strength behavior of ice-rich permafrost. In most studies, remolded samples are used. Remolded samples usually contain a massive cryostructure unless special efforts are made to create a different cryostructure. Soils with massive cryostructure may, but in many instances for ice-rich permafrost, do not represent the actual permafrost soil. It has been recognized that the texture has an influence on the resulting strength and creep behavior (e.g. Sayles & Carbee 1981). A few studies have investigated the creep behavior of ice-rich permafrost samples (undisturbed cores) (Arenson & Springman 2005a, McRoberts et al. 1978, McRoberts 1988, Savigny & Morgenstern 1986a). Savigny & Morgenstern (1986a) briefly explored the effects of cryostructure on the behavior of clay permafrost and found that the prominent ice veins or lenses had a large impact on the resulting creep and strength behavior. Research in Russia showed that the orientation of segregated ice in frozen soil also had an impact on the shear strength (e.g. Pekarskaya 1965, Vialov, 1959). Shear strength in the direction of ice lenses was lower than the shear strength perpendicular to ice lenses. Long term strength data for frozen soils presented in this section include soils with horizontal and vertical micro-lenticular (vml & hml) cryostructure, reticulate-chaotic (RC) cryostructure, and remolded-massive (RM) cryostructure. Long term strength data is also presented for massive wedge ice (IW), Matanuska basal ice (BI), and englacial ice (GI).

The long term strength can be classified as the stress above which deformations are no longer damped (Tsytovich 1975, Vyalov et al. 1966). Alternatively, creep strengths are commonly predicted by recording the time to failure for a given stress. Failure is commonly adopted as the transition from secondary to tertiary creep (i.e. at minimum strain rate) or a strain of 20% (Andersland & Ladanyi 1994). Strength vs. time is plotted to represent the long term strength. Experimental approaches for determining the long term strength are outlined by Tsytovich (1975) and Vyalov et al. (1966). They are the ball plunger test and the dynamometer test from which the long term strength is defined as the stress at which deformation ceases (or a prescribed conditional stability is met). Thus, these approaches give directly the value of long term strength.

In the following sections, interpretation of long term strength will be shown for stress relaxation tests and CSC creep tests. Long term strength from relaxation tests will be interpreted in the context of strain rate criteria and stress relaxation vs. time relationships. Long term strength from CSC creep tests are interpreted based on the time to a minimum strain rate for a constant stress condition.

7.5.1 Relaxation Tests: Strain Rate Criteria Evaluation of Long Term Strength

The determinations of long term strengths in this study are based primarily from relaxation tests, which are similar to the dynamometer testing method (Tystovich, 1975; Vyalov et al., 1966; Vialov and Ermakov, 1967). In many instances, complete stabilization (i.e. no deformation) was difficult to reach. Two relaxation tests on vertical micro-lenticular cryostructure lasted for 3 months without stabilization of deformation. Therefore, two strain rates of 2.083×10^{-6} hr^{-1} and 2.083×10^{-7} hr^{-1} were considered as conditional stability states as it was outlined by Vyalov et al. (1966). The basis for the adopted stabilization criteria is that if the deformation rate is small enough, the total accumulated deformation over a period of time should be insignificant from a practical stand point. The first strain rate condition (i.e. 2.083×10^{-6} hr^{-1}) will be referred to as stability condition 1. The second strain rate condition (i.e. 2.083×10^{-7} hr^{-1}) will be referred to as stability condition 2. Consequently, definition of long term strength in this work, as determined from relaxation tests and strain rate criteria, is the stress at which the conditional stability criterions are met. A stress (strength) at a given moment of time correlates to a strain rate, which is the slope of the strain vs. time plot. For example, Figure 7.21 shows stress vs. time and strain vs. time plots for the relaxation test of sample no. 36 (IW). A strain rate can be determined from the slope of the true strain vs. time plot at the any specified time, t, by taking the tangent of the slope at that point. Likewise, at the same time, t, used to determine the strain rate, the corresponding stress can be found from the uniaxial stress vs. time plot. When the strain rate criteria is met (i.e. stability conditions 1 and 2), the stress corresponding to that moment of time is the long term strength.

The long term strength as determined from relaxation tests and the stability conditions described above are presented in Table 7.9. The results are grouped by soil cryostructure. Figures 7.22, and 7.23, show the long term strengths vs. temperature as determined directly from relaxation tests based on the conditional stability criteria. Based on the data plotted in Figures 7.22 and 7.23, the long term strength can be approximated by a simple power law of following form:

$$\sigma_{lt} = A|\theta|^{b} \qquad \text{Eq. 7.5}$$

Where σ_{lt} is the long term strength, A and b are empirical coefficients. The long term strength, σ_{lt}, has units of kPa. The coefficient A has units of $kPa \cdot {}^{\circ}C^{-b}$. Temperature, θ, is the temperature in degrees Celsius. The empirical coefficients A and b from Equation 7.5 are shown in Tables 7.10 and 7.11 for the two stability criteria described earlier. The coefficients are grouped by soil cryostructure and ice facies.

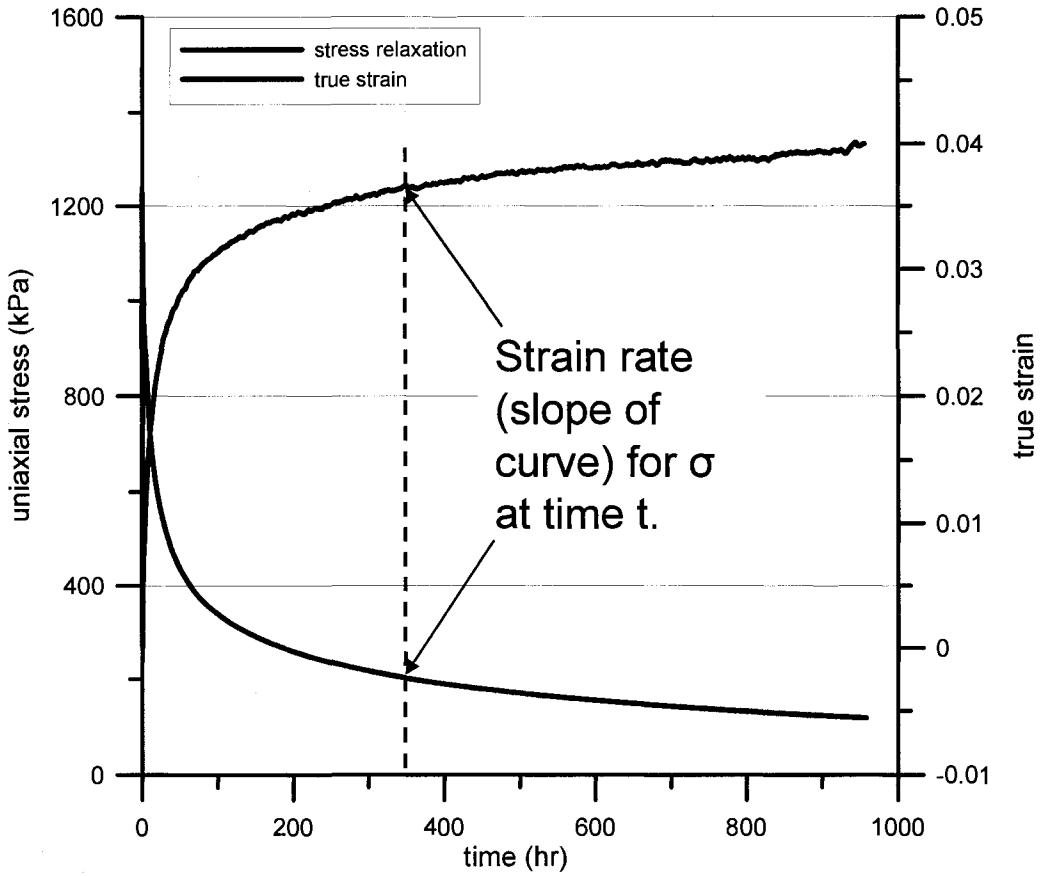

Figure 7.21. True strain and stress relaxation curves for sample No. 36 (IW, -0.98°C). From these two curves, the strain rate vs. stress relationships are established for long term strength estimate.

For soils with micro-lenticular cryostructure, the value of b>1 results in concave upwards inflection of any extrapolation of the curve. The temperature range represented by this data is the zone of the most intensive change in the unfrozen water content. As the temperature decreases, the long term strength for most soils generally increases at a slower rate as the temperature decreases. Therefore, extrapolation of the given equation to lower temperatures should give larger values of long term strength than would be expected. Additional tests at colder temperatures need to be conducted to verify this observation.

The long term strength of soils with vertical micro-lenticular (vml) and horizontal micro-lenticular (hml) cryostructure are similar as evidenced from the coefficients A and b and Figures 7.22 and 7.23. Soil with remolded-massive (RM) cryostructure shows higher long term strength as compared to undisturbed soils. The long term strength is 3 to 4 times larger for soils with RM cryostructure than undisturbed soils for a given temperature. This is significant in that

Table 7.9. Summary of long term strength for stability conditions 1 and 2 as determined from relaxation tests.

vertical micro-lenticular (VML)				horizontal micro-lenticular (HML)				remolded massive (RM)			
σ_{lt} (kPa) stability condition 1	σ_{lt} (kPa) stability condition 2	T (°C)	No.	σ_{lt} (kPa) stability condition 1	σ_{lt} (kPa) stability condition 2	T (°C)	No.	σ_{lt} (kPa) stability condition 1	σ_{lt} (kPa) stability condition 2	T (°C)	No.
69.2	39.9	-0.77	23	56.4	33.9	-0.77	26	72.5	60.7	-0.30	58
46.0	23.0	-0.86	24	48.5	27.2	-0.82	27	146.2	142.0	-0.50	56
127.2	84.7	-1.82	30	162.3	113.1	-1.81	28	136.0	130.2	-0.50	57
217.4	153.0	-2.78	25	115.7	74.8	-1.86	29	270.9	256.7	-1.05	49
				209.5	161.2	-2.81	28	259.0	236.6	-0.99	50
								286.9	278.8	-1.00	51
								532.8	506.2	-1.98	52
								509.9	484.2	-1.99	53
								695.4	654.6	-3.01	54
								715.2	676.8	-2.99	55
								919.0	867.1	-4.02	60
								890.6	844.2	-4.01	61
								1142.2	1092.3	-5.01	62
reticulate-chaotic (RC)				wedge ice (IW)				Mat. basal ice (BI) and glacial ice (GI)			
σ_{lt} (kPa) stability condition 1	σ_{lt} (kPa) stability condition 2	T (°C)	No.	σ_{lt} (kPa) stability condition 1	σ_{lt} (kPa) stability condition 2	T (°C))	No.	σ_{lt} (kPa) stability condition 1	σ_{lt} (kPa) stability condition 2	T (°C)	No.
86.9	63.6	-0.88	31	95.8	39.3	-0.44	41	116.7	83.0	-1.86	43
154.7	118.0	-1.85	32	131.0	63.0	-0.96	35	112.8	93.7	-1.02	44
140.0	110.0	-1.85	34	123.2	60.1	-0.98	36	70.3	45.8	-1.02	45
183.3	138.2	-2.08	31	101.3	42.5	-1.86	37	108.9	61.5	-1.00	46
213.0	151.1	-2.79	33	113.6	53.4	-1.86	38				
				117.7	58.6	-3.1	39				
				113.4	59.0	-3.1	40				

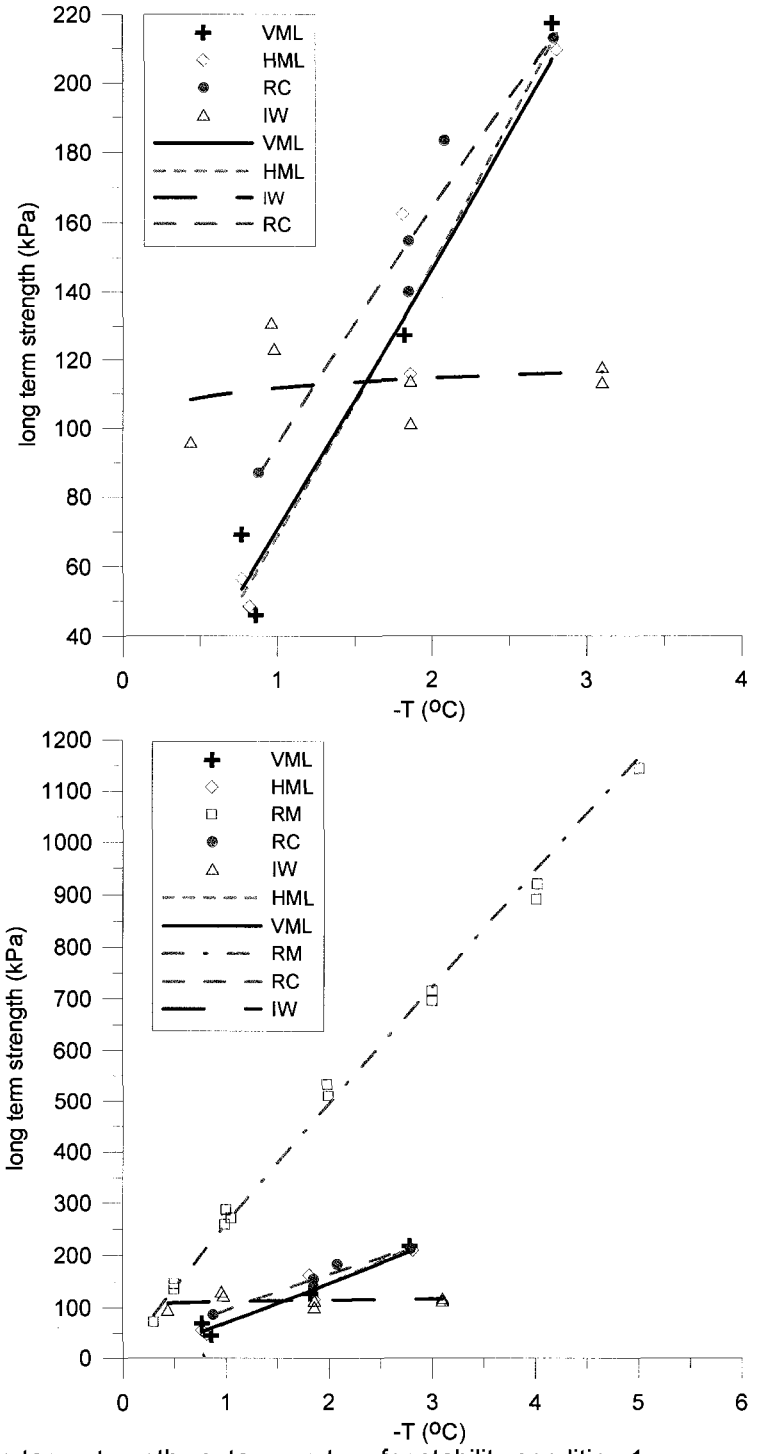

Figure 7.22. Long term strength vs. temperature for stability condition 1 (i.e. $\dot{\varepsilon}=2.083\times10^{-6}$ hr^{-1}).

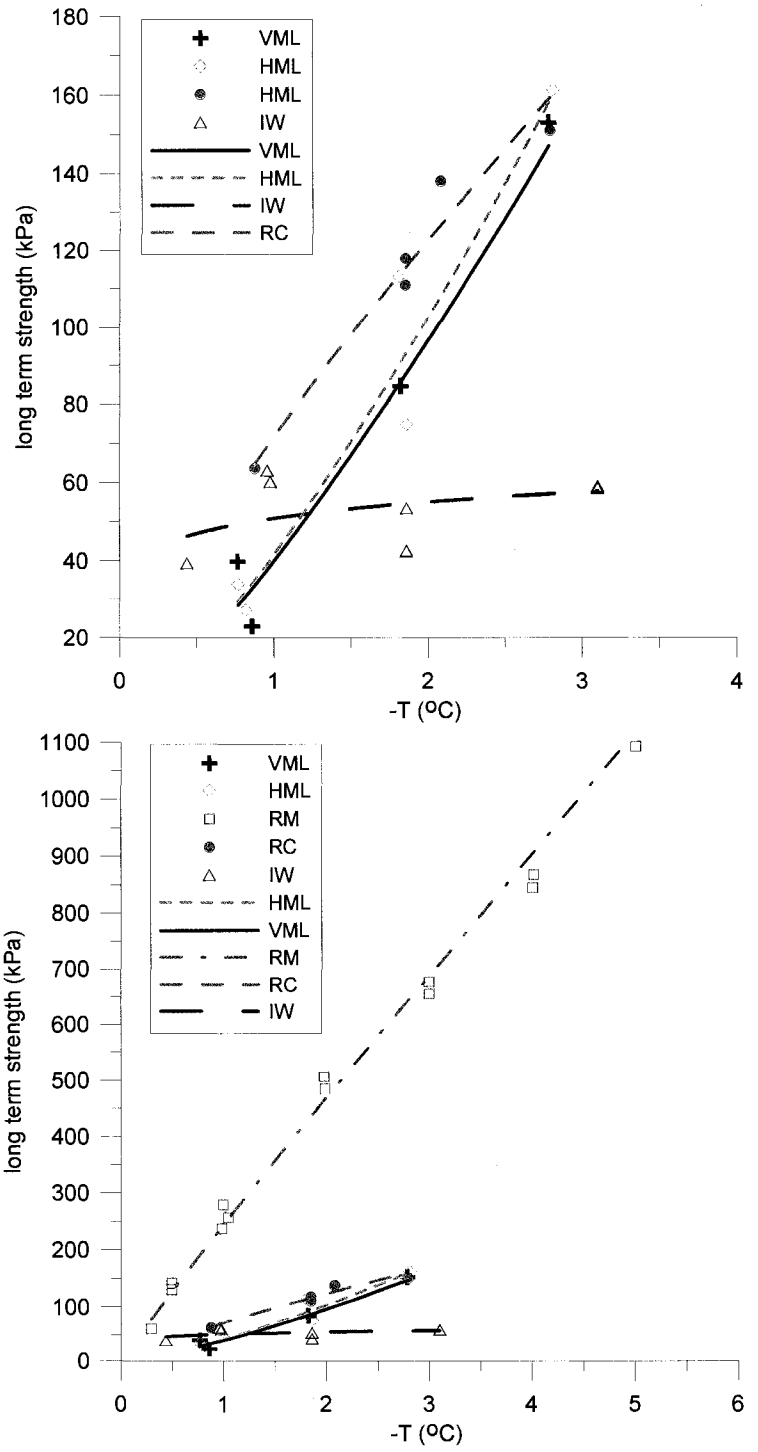

Figure 7.23. Long term strength vs. temperature for stability condition 2 (i.e. $\dot{\varepsilon}=2.083\times10^{-7}$ hr^{-1}).

Table 7.10. Long term strength experimental coefficients A and b for Eq. 7.5 for stability condition 1 (i.e. $\dot{\varepsilon}=2.083x10^{-6}$ hr^{-1}).

Cryostructure	Temp range (°C)	A ($kPa°C^{-b}$)	b (dimensionless)	r^2
VML	-0.77 to -2.78	70.458	1.0533	0.898
HML	-0.77 to -2.81	68.329	1.1061	0.943
RM	-0.30 to -5.01	252.031	0.9327	0.994
RC	-0.88 to -2.79	94.887	0.7886	0.966
IW	-0.44 to -3.10	111.593	0.0365	0.057

$\sigma_{lt} = A|\theta|^b$ (Eq. 7.5). θ is the temperature in °C.

Table 7.11. Long term strength experimental coefficients A and b for Eq. 7.5 for stability condition 2 (i.e. $\dot{\varepsilon}=2.083x10^{-7}$ hr^{-1}).

Cryostructure	Temp range (°C)	A ($kPa°C^{-b}$)	b (dimensionless)	r^2
VML	-0.77 to -2.78	39.934	1.2758	0.884
HML	-0.77 to -2.81	41.336	1.3106	0.937
RM	-0.30 to -5.01	241.823	0.9500	0.987
RC	-0.88 to -2.79	71.422	0.7817	0.972
IW	-0.44 to -3.10	50.747	0.1128	0.187

$\sigma_{lt} = A|\theta|^b$ (Eq. 7.5). θ is the temperature in °C.

extrapolation of results from remolded soils to undisturbed soils may not be conservative, based on our data. The strength values for remolded Fairbanks silt (Yuanlin and Carbee, 1987a) are similar to the strength values for the soils with RM cryostructure used in this work. The strengthening effect may result from the interlocking of soil grains.

In-situ silts with massive cryostructure from the permafrost tunnel were not tested directly using the relaxation method. However, a small number of undisturbed silt with massive cryostructure samples were tested under uniaxial constant stress conditions. Results suggest that the in-situ silts with massive cryostructure show higher deformation for a given stress than soils with micro-lenticular cryostructure. Results from soils with remolded-massive cryostructure should not be extrapolated to the in-situ silts with massive cryostructure. Soils with reticulate-chaotic (RC) cryostructure show a slight increase in long term strength over soils with micro-lenticular cryostructure under the temperature range tested. Wedge ice (IW) shows little increase of long term strength with temperature. Significant scatter of experimental data exists. Only at -0.44°C is a drop in strength observed. Under the temperature range tested, the long term strength can be considered constant. At a temperature of approximately -1.5°C, the long term strength of wedge ice falls below that of the ice-rich soils. The largest drop in long term strength for the stability condition 2 is for wedge ice.

7.5.2 Relaxation Tests: Stress Decrease vs. Time Evaluation of Long Term Strength

In the previous section, long term strength was determined from strain rate stability criteria condition, which was applied to relaxation test data. Mentioned earlier in section 7.4, the stress decrease with time can be approximated by a power law of the form shown in Equation 7.6.

$$\sigma = C \cdot t^{d} \qquad \text{Eq. 7.6}$$

where σ is the uniaxial stress, C and d are empirical constants. The stress relaxation curves are generally characterized by a rapid stress decrease (soils) followed by a slower rate of stress decrease. On log stress vs. log time plots, the stress relaxation data generally results in a linear trend (see section 7.4). Equation 7.6 can be applied to the last linear trend, which extends to the end of the data set. Generally, Equation 7.6 can be applied to soils for times greater than 5 to 10 hours and for wedge ice for times greater than 30 hours. Table 7.12 lists the time range for which Equation 7.6 is valid for all relaxation tests. Extrapolation of the initial parts of the stress relaxation curve generally under predicts the later stress (strength) values. Table 7.12 presents the empirical coefficients C and d for Equation 7.6, as well as the 50 and 100 year strengths determined by extrapolation of the power regressions to the desired time period. The 50 and 100 year strengths are considered the long term strength conditions for this method of long term strength evaluation. In all cases, if Equation 7.6 is applied for 50 or 100 year time periods, the resulting stress (strength) values are lower than predicted by stability conditions 1 and 2 in section 7.5.1.

Figures 7.24 and 7.25 show the empirical coefficients C and d plotted against temperature for the various soil cryostructures and ice facies. Figure 7.24 suggests that the C coefficient is primarily influenced by temperature and increases linearly with decreasing temperature. The values of the C coefficient have a similar dependence on temperature for the studied soils. For wedge ice, the C parameter data has considerable scatter but the C coefficient shows an increasing trend with warming temperatures which is opposite to the soils.

Figure 7.25 shows the empirical coefficient d as a function of temperature for Equation 7.6. The d coefficient appears to be influenced by the soil cryostructure. General observation can be made. The frozen soils tend to be grouped into distinct regions by cryostructure. The general trend is that the d parameter decreases (become more negative) with increasing ice contents. The other observation is that the d coefficient generally decreases for temperatures warmer than -1° to -2°C.

Table 7.12. Summary of experimental coefficients for stress vs. time decay based on relaxation tests for Eq. 7.6.

No.		T (°C)	time range (hr)	C (kPa/hr^d)	d	$\sigma_{50\ yrs}$	$\sigma_{100\ yrs}$	No.		T (°C)	time range (hr)	C (kPa/hr^d)	d	$\sigma_{50\ yrs}$	$\sigma_{100\ yrs}$
23	vml	-0.77	>10	387.78	-0.314	6.6	5.3	43	BI	-1.86	>1 hr	417.20	-0.244	17.5	14.8
24	vml	-0.86	>10	576.53	-0.394	3.5	2.6	44	BI-ml	-1.02	>100	181.12	-0.082	62.8	59.4
25	vml	-2.78	>10	838.88	-0.212	53.5	46.2	45	GI	-1.02	>10	312.07	-0.258	11.0	9.2
26	hml	-0.77	>10	256.94	-0.312	4.5	3.6	46	GI	-1.00	>20	897.33	-0.312	15.5	12.5
27	hml	-0.82	>10	316.90	-0.310	5.6	4.5	49	RM	-1.05	>10	338.65	-0.049	179.3	173.4
28	hml	-1.81	>10	461.77	-0.201	34.1	29.6	50	RM	-0.99	>10	327.35	-0.040	193.5	188.2
	hml	-2.81	>10	613.83	-0.202	44.7	38.9	51	RM	-1.00	>10	317.78	-0.022	238.9	235.3
29	hml	-1.86	>10	540.12	-0.233	26.1	22.2	52	RM	-1.98	>10	613.33	-0.027	434.4	426.5
	hml	-2.81	>10	652.40	-0.238	29.6	25.1	53	RM	-1.99	>10	600.12	-0.030	406.8	398.5
30	vml	-1.82	>10	520.75	-0.214	32.3	27.8	54	RM	-3.01	>10	826.47	-0.029	567.3	556.0
31	RC	-0.88	>10	178.47	-0.161	21.9	19.6	55	RM	-2.99	>10	844.56	-0.028	584.8	573.4
	RC	-2.08	>10	320.85	-0.111	76.0	70.3	56	RM	-0.50	>10	175.56	-0.038	107.2	104.4
32	RC	-1.85	>10	384.30	-0.150	54.7	49.3	57	RM	-0.50	>10	218.45	-0.091	67.1	63.0
33	RC	-1.85	>30	303.85	-0.129	56.6	51.8	58	RM	-0.30	>5	154.25	-0.152	21.5	19.4
34	RC	-2.79	>20	636.77	-0.164	76.1	68.0	60	RM	-4.02	>5	1107.25	-0.031	739.8	724.1
35	IW	-0.96	>10	3234.94	-0.482	6.2	4.4	61	RM	-4.01	>5	1077.69	-0.032	709.4	693.7
36	IW	-0.98	>50	2557.72	-0.436	8.8	6.5	62	RM	-5.01	>5	1333.74	-0.026	953.2	936.3
37	IW	-1.86	>30	3500.10	-0.477	7.1	5.1	63	RM	-5.01	>10	1176.19	-0.029	803.6	787.4
38	IW	-1.86	>30	2268.64	-0.409	11.2	8.4								
39	IW	-3.1	>30	1831.25	-0.372	14.5	11.2								
40	IW	-3.1	>20	1689.31	-0.393	10.2	7.8								
41	IW	-0.44	>30	2203.77	-0.401	12.0	9.1								

Eq. 7.6 $\sigma = C \cdot t^d$, where σ is stress (kPa) and C and d are experimental coefficients.

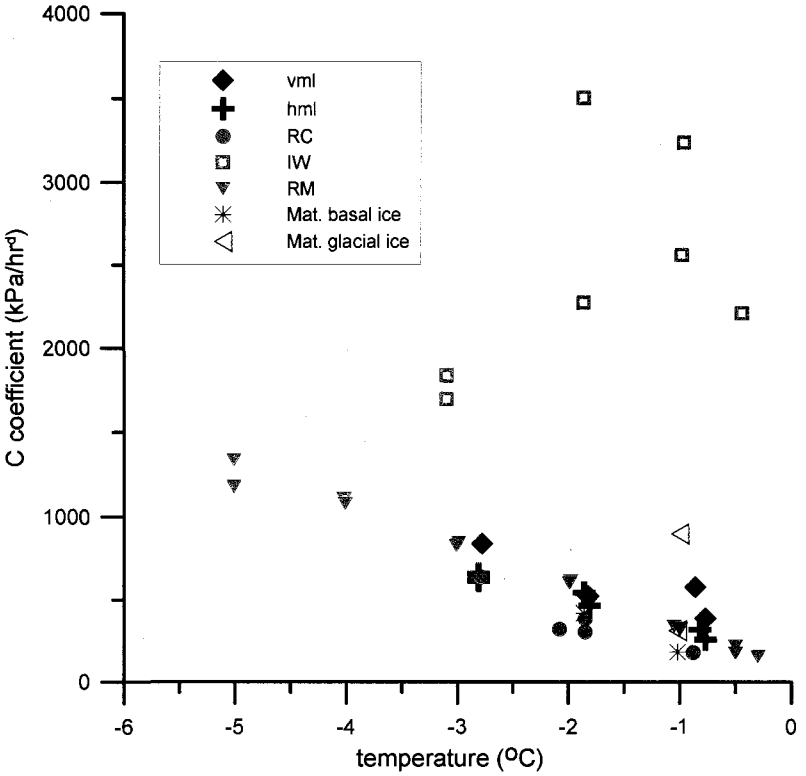

Figure 7.24. The C coefficient vs. temperature for various soil cryostructures.

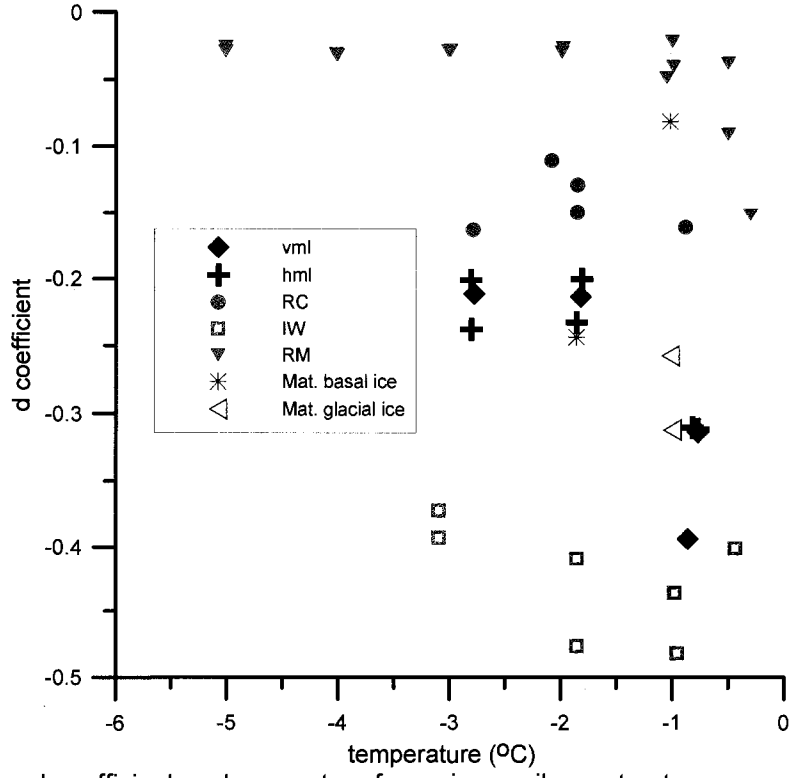

Figure 7.25. The d coefficient vs. temperature for various soil cryostructure.

The trend appears similar to the unfrozen water content trends for these soils as shown in Chapter 4.4. Since the volumetric unfrozen water of each sample was not measured, a representative volumetric unfrozen water content curve was used for each soil cryostructure. Using the predicted volumetric unfrozen water content from Equation 4.3 and Table 4.5 for the various soil cryostructures, the volumetric unfrozen water content can be related to -d coefficient. The curves used for determination of the volumetric unfrozen water include RC V1 for soils with reticulate-chaotic cryostructure, RM V8 for soils with remolded massive cryostructure, hml V3 for soils with horizontal micro-lenticular cryostructure, and vml V11 for soils with vertical micro-lenticular cryostructure. Unfrozen water content was not applied to wedge ice. When plotted as log (-d) vs. log (w_v), the data tends towards linear as shown in Figure 7.26. However, plotting log (-d) versus log (-T) also tends towards linear as shown in Figure 7.27. The results suggest that the d parameter is related to unfrozen water content, which is an affect of temperature. Since temperature is an easy parameter to measure, the relationship of d parameter to temperature will be expressed rather than to volumetric unfrozen water. Empirical best fit regressions show that the d parameter can be fit equally well with either a power or an exponential relationship. A power relationship was therefore chosen. Samples no. 51 and 56 (Table 7.7) for soils with remolded massive cryostructure were removed in order to improve the best fit equation. Table 7.13 shows the C and d parameters as a function of temperature. The C parameter was approximated using a simple linear regression. The d parameter was approximated with a power law regression. Soils with reticulate chaotic cryostructure (RC) and wedge ice have poor correlation coefficients for the d parameter. The wedge ice data scatter is also prevalent in the C parameter correlation coefficient. It is possible that different deformation mechanism occur for wedge ice and soils with RC cryostructure, thus resulting in deviation of the d vs. temperature relationship. For wedge ice, temperature and thus unfrozen water may play a different role as compared to the frozen soils. As seen in Chapter 4.4, wedge ice does not contain any appreciable volumetric unfrozen water for the temperature range tested. Soils with RC cryostructure are anisotropic with the presence of the large diagonal ice lenses that which control deformation slip planes.

Tables 7.14 and 7.15 summarize the stress fraction for undisturbed and remolded-massive samples. The stress fractions are included to visually show the time behavior of the stress relaxation process. The stress fraction is the stress at time t divided by the peak applied stress (i.e. $\sigma_t/\sigma_{\text{peak applied stress}}$). Additional stress fractions are shown which relate to stability conditions 1 and 2 which were used to define the long term strength in section 7.5.1. In this the case, the stress fraction is equal to $\sigma_{\text{stability condition}}/\sigma_{\text{peak applied stress}}$. It is important to note that the peak applied

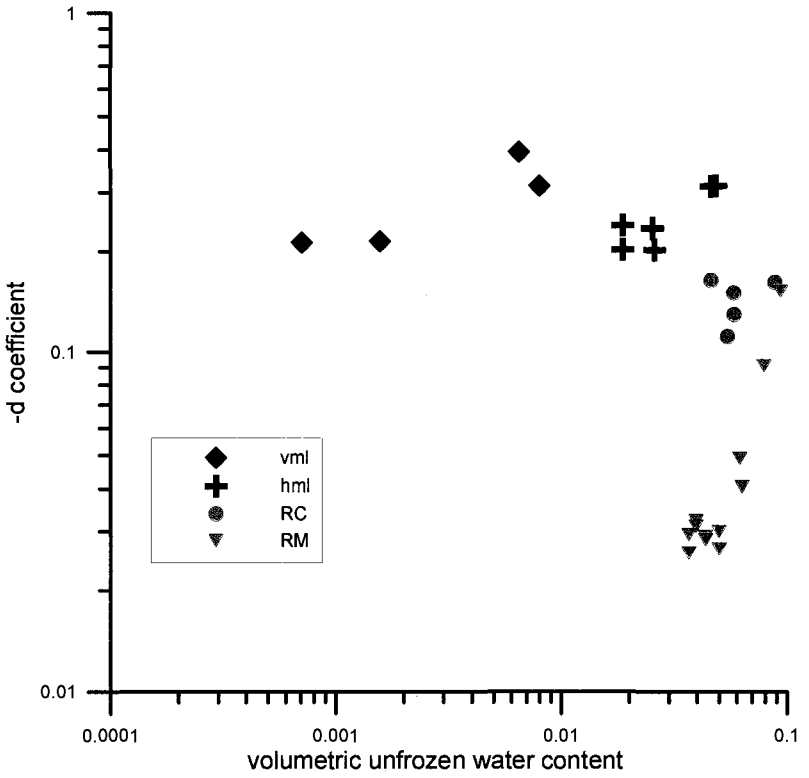

Figure 7.26. Plot of -d coefficient vs. volumetric unfrozen water content.

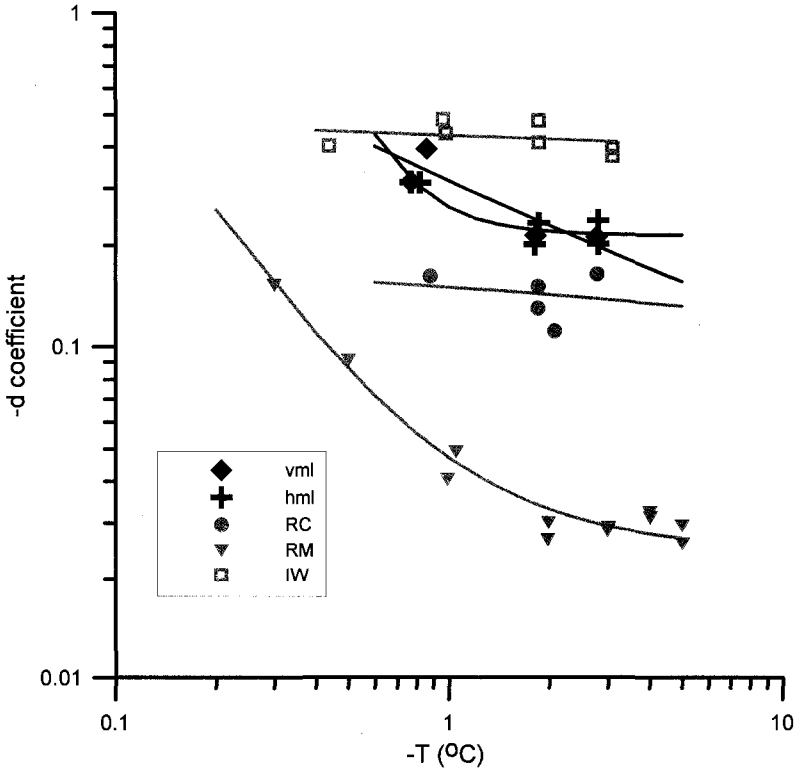

Figure 7.27. Plot of -d coefficient vs. -T.

Table 7.13. Coefficient C and d for Eq. 7.6 as a function of temperature in relation to various soil cryostructures.

cryostructure	C ($kPa \cdot hr^{-d}$)	r^2	d	r^2
vml	315.73 - 170.30·(T)	0.720	$-[0.03260 + 0.2827 \cdot (-T)^{-0.5177}]$	0.752
hml	160.08 - 172.93·(T)	0.952	$-[0.21406 + 0.0479 \cdot (-T)^{2.9967}]$	0.886
RC	-66.12 - 228.92·(T)	0.847	$-[0.24190 - 0.0926 \cdot (-T)^{0.1121}]$	0.049
IW	3041.13 + 325.38·(T)	0.250	$-[0.15641 + 0.2740 \cdot (-T)^{-0.0605}]$	0.085
RM	94.686 - 240.60·(T)	0.989	$-[0.02478 + 0.0220 \cdot (-T)^{-1.46527}]$	0.989

Note: T is the temperature in -°C.

stress may not be the instantaneous or ultimate compressive strength of the soil. Therefore, the stress fraction presented is not the fraction of the instantaneous strength. Figures 7.28 to 7.30 graphically depict the data shown in tables 7.14 and 7.15. Evident in both the tables and figures, the initial drop in stress is rapid for all soil cryostructures. It is notable that the drop in stress for wedge ice initially proceeds at a much slower rate. Pekarskaya (1965) presents data that agrees with the observation that the relaxation of ice proceeds at a slower rate than frozen soils.

For the frozen soils, the stress fraction and in particular the final stress fractions, which correspond to the long term strength stability conditions described earlier (section 7.5.1), appear to be temperature influenced. The final stress fraction decreases as the soil temperatures warm and approach zero. The data set for soil with remolded-massive (RM) cryostructure shows the greatest temperature range from which the decreasing stress fraction trend with warming temperature is readily observed.

For the undisturbed soils (soils with vml, hml, & RC cryostructure), generally the stress fraction drops to 0.4 to 0.6 in the first 0.5 hrs for the temperature range tested. Additional lowering of the stress fraction by 0.4 to 0.5 then proceeds over a larger time period when compared to soils containing RM cryostructures. For soils with RM cryostructures, the major drop in the stress fraction occurs over the first 0.5 hrs. The additional drop in the stress fraction by 0.2 to 0.3 occurs after this interval. This is seen by comparing the data groups (Figures 7.28 to 7.30) which encompasses the stress fraction ranging from 0.5 hr to stability condition 2. The data groups are spread over a larger range for the undisturbed frozen soils as compared to the remolded soil. The exception to this is the narrow data range seen for a soil with RC cryostructure at -0.88°C. The major observations shown from use of stress fraction is that the "stabilized" or long term

Table 7.14. Summary of stress decrease as fractions of peak applied stress vs. time for undisturbed samples for relaxation tests.

Sample no.		Temp	Time (hrs) 0.5	1	2	4	8	12	24	$\sigma_{@\ 2.083x10^{-6}\ hr^{-1}}$ /$\sigma_{peak\ applied}$	$\sigma_{@\ 2.083x10^{-7}\ hr^{-1}}$ /$\sigma_{peak\ applied}$	test time (hr)
23	vml	-0.86	0.362	0.289	0.217	0.167	0.128	0.111	0.087	0.042	0.023	2067.0
24	vml	-0.77	0.602	0.483	0.376	0.291	0.225	0.193	0.147	0.040	0.020	2066.9
25	vml	-2.78	0.508	0.424	0.356	0.299	0.253	0.230	0.197	0.100	0.070	332.4
26	hml	-0.78	0.329	0.253	0.192	0.145	0.112	0.097	0.076	0.046	0.027	118.7
27	hml	-0.82	0.340	0.261	0.202	0.159	0.126	0.109	0.087	0.036	0.020	238.4
28	hml	-1.81	0.404	0.334	0.278	0.233	0.197	0.178	0.153	0.101	0.071	310.4
	hml	-2.81	0.485	0.406	0.340	0.284	0.238	0.216	0.185	0.120	0.092	287.7
29	hml	-1.86	0.490	0.400	0.324	0.260	0.211	0.187	0.155	0.070	0.045	310.4
	hml	-2.81	0.553	0.448	0.357	0.285	0.227	0.200	0.163	0.070	0.046	287.7
30	vml	-1.82	0.447	0.359	0.288	0.233	0.190	0.169	0.144	0.069	0.046	332.4
31	RC	-0.88	0.228	0.165	0.132	0.106	0.090	0.082	0.072	0.060	0.044	264.5
	RC	-2.08	0.360	0.291	0.228	0.187	0.160	0.148	0.134	0.108	0.082	358.0
32	RC	-1.85	0.367	0.280	0.218	0.177	0.150	0.138	0.122	0.079	0.060	287.5
33	RC	-2.79	0.608	0.486	0.393	0.322	0.270	0.247	0.215	0.121	0.086	475.2
34	RC	-1.85	0.565	0.457	0.357	0.285	0.236	0.215	0.188	0.127	0.100	787.8
35	IW	-0.96	0.905	0.866	0.809	0.730	0.627	0.559	0.439	0.084	0.040	746.0
36	IW	-0.98	0.907	0.865	0.805	0.724	0.622	0.559	0.455	0.097	0.047	957.9
37	IW	-1.86	0.924	0.889	0.842	0.777	0.688	0.626	0.510	0.072	0.030	358.6
38	IW	-1.86	0.881	0.828	0.768	0.691	0.604	0.550	0.452	0.089	0.042	358.6
39	IW	-3.10	n/a	0.798	0.716	0.620	0.519	0.461	0.371	0.082	0.041	644.8
40	IW	-3.03	0.822	0.744	0.647	0.542	0.447	0.397	0.318	0.078	0.040	644.8
41	IW	-0.44	0.925	0.897	0.861	0.813	0.746	0.698	0.602	0.102	0.042	334.1
43	BI	-1.86	0.295	0.228	0.188	0.159	0.137	0.126	0.108	0.065	0.047	502.5
44	BI	-1.02	0.377	0.290	0.223	0.176	0.142	0.127	0.106	0.069	0.057	738.9
45	GI	-1.02	0.508	0.372	0.287	0.233	0.193	0.174	0.147	0.077	0.050	693.9
46	GI	-1.00	0.957	0.936	0.909	0.864	0.798	0.744	0.634	0.210	0.119	334.1

Note: The stress fraction for the time intervals are equal to σ_t / $\sigma_{peak\ applied\ stress}$.

Table 7.15. Summary of stress decrease as fractions of peak applied stress vs. time for remolded soils with remolded-massive cryostructure for relaxation tests.

Sample no.		Temp	Time (hrs) 0.5	1	2	4	8	12	24	$\sigma_{@\ 2.083x10^{-6}\ hr^{-1}}/\sigma_{peak\ applied}$	$\sigma_{@\ 2.083x10^{-7}\ hr^{-1}}/\sigma_{peak\ applied}$	test time (hr)
49	RM	-1.05	0.391	0.330	0.282	0.247	0.223	0.213	0.202	0.190	0.180	76.9
50	RM	-0.99	0.387	0.329	0.285	0.253	0.232	0.224	0.215	0.194	0.177	499.7
51	RM	-1.00	0.388	0.329	0.287	0.257	0.238	0.230	0.222	0.215	0.209	499.7
52	RM	-1.98	0.498	0.447	0.411	0.384	0.366	0.358	0.349	0.330	0.314	360.6
53	RM	-1.99	0.482	0.434	0.397	0.369	0.350	0.341	0.331	0.309	0.294	360.6
54	RM	-3.01	0.554	0.503	0.465	0.437	0.417	0.408	0.396	0.365	0.344	427.5
55	RM	-2.99	0.555	0.507	0.471	0.443	0.424	0.415	0.404	0.375	0.354	427.5
56	RM	-0.50	0.316	0.257	0.212	0.183	0.164	0.156	0.148	0.140	0.136	355.3
57	RM	-0.50	0.364	0.296	0.246	0.209	0.183	0.171	0.156	0.130	0.124	355.3
58	RM	-0.30	0.286	0.225	0.180	0.147	0.122	0.111	0.097	0.076	0.064	188.0
59	RM	-0.16	0.231	0.178	0.142	0.114	0.091	0.076	0.060	0.025	0.014	188.0
60	RM	-4.02	0.555	0.512	0.478	0.455	0.438	0.431	0.420	0.386	0.364	475.2
61	RM	-4.01	0.563	0.516	0.479	0.451	0.430	0.420	0.408	0.376	0.356	475.3
62	RM	-5.00	0.595	0.547	0.510	0.484	0.464	0.456	0.445	0.415	0.397	403.4
63	RM	-5.01	0.591	0.540	0.501	0.472	0.449	0.439	0.425	0.393	0.374	403.4

Note: The stress fraction for the time intervals are equal to $\sigma_t / \sigma_{peak\ applied\ stress}$.

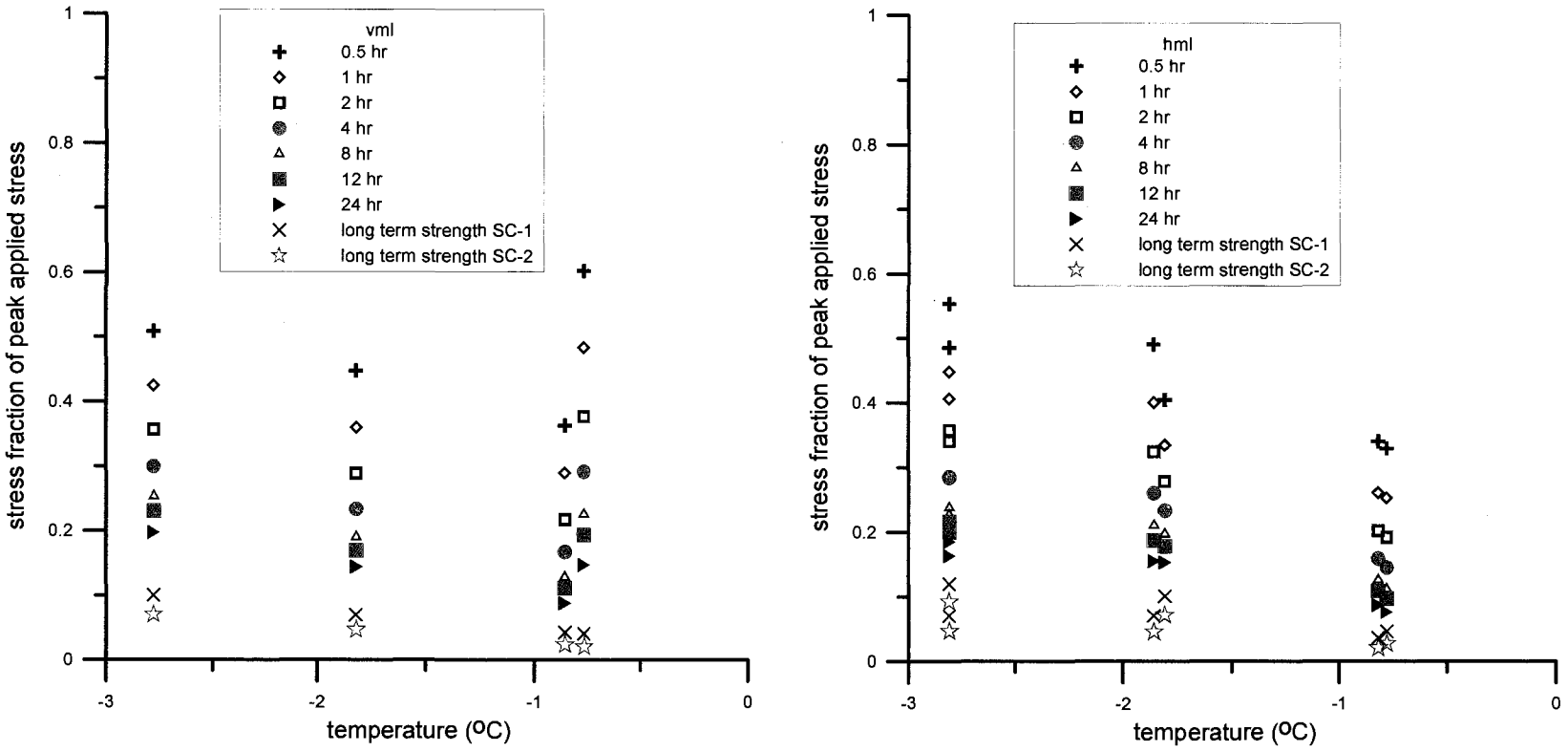

Figure 7.28. Stress fraction vs. temperature for soils with vml and hml cryostructures. The stress fraction is equal to $\sigma_t/\sigma_{\text{peak applied stress}}$. The stress fractions are shown for the long term strength stability conditions 1 (SC-1) and 2 (SC-2) that were used to define the long term strength (section 7.5.1). The additional stress fractions relate to test time.

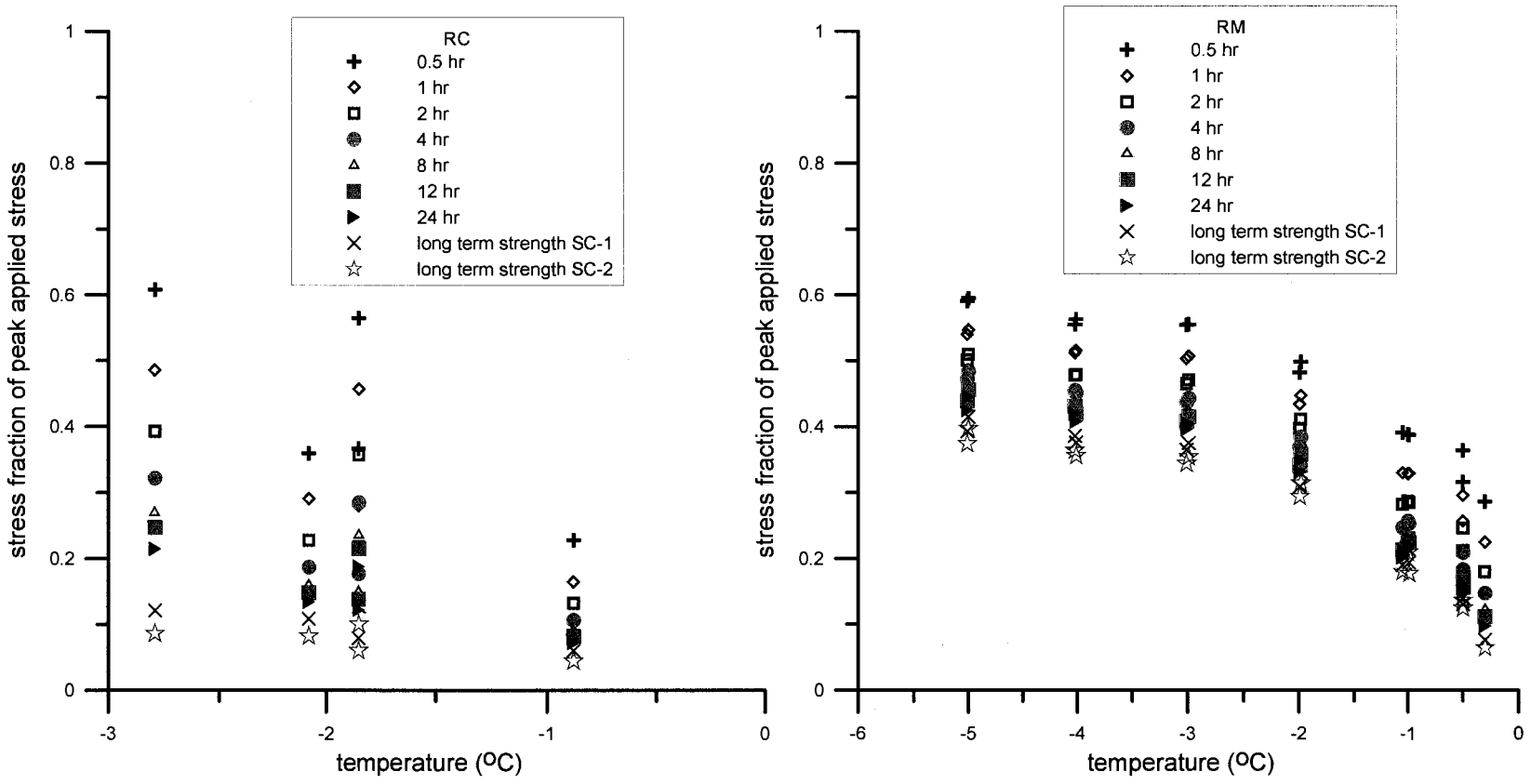

Figure 7.29. Stress fraction vs. temperature for soils with RC and RM cryostructures. The stress fraction is equal to $\sigma_t/\sigma_{\text{peak applied stress}}$. The stress fractions are shown for the long term strength stability conditions 1 (SC-1) and 2 (SC-2) that were used to define the long term strength (section 7.5.1). The additional stress fractions relate to test time.

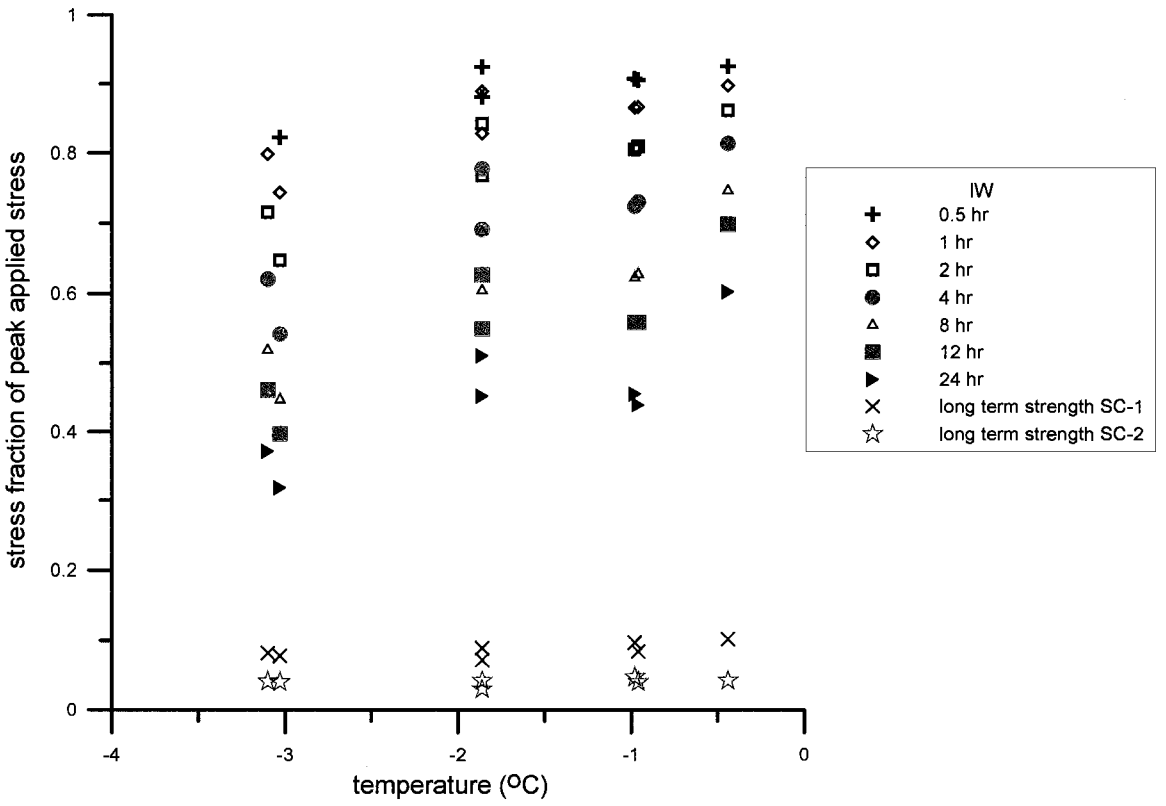

Figure 7.30. Stress fraction vs. temperature for IW (wedge ice). The stress fraction is equal to $\sigma_t/\sigma_{\text{peak applied stress}}$. The stress fractions are shown for the long term strength stability conditions 1 (SC-1) and 2 (SC-2) that were used to define the long term strength (section 7.5.1). The additional stress fractions relate to test time.

strength is much lower than the initial applied stress in our experiments and thus much lower than an instantaneous strength for a given soil. The stress fraction for the stability conditions also show that given enough time, the stress fraction (and thus stress) tendtowards an uniform value for a given temperature, independent of initial variations of the relaxation rate.

Undisturbed soils have the lowest long term strength (and lowest stress fraction). For example, sample no. 23 is a soil with vml cryostructure tested at -0.77°C. The stress at stability condition 1 is 23 times less than the initial applied stress. At stability condition 2, the stress is 43 times less than the initial applied stress. Therefore, the long term strength is even less as compared to an instantaneous compressive strength. The long term strength as compared to an instantaneous strength is significantly lower as determined from our data than those reported by Vialov (1959). Generally, soils with vml, hml, and RC cryostructure, along with IW have ending stress fraction

less than 0.1 for the temperature range tested. The ending stress fractions for soils with RM cryostructure range from 0.06 to 0.4 depending on temperature and are much greater than for undisturbed soil and wedge ice.

The peak applied stress for frozen soils was greater for colder test temperatures. Ice samples were generally loaded to a smaller stress than the frozen soils to avoid brittle fracture. The brittle fracture did not lead to complete failure of sample, however. Figure 7.28 shows the stress fraction "relaxation" of samples no. 23 (-0.77°C) and 24 (-0.86°C) which contain vml cryostructure. The load applied to sample no. 23 was 517 kPa larger than the load applied to sample no. 24. Despite the larger initial stress applied to sample no. 23, the end stress fraction was comparable between the two samples. However, the stress fraction for stability condition 2 for sample no. 23 was slightly lower than for sample no. 24. It would be expected that a higher initial stress should result in a lower "stabilized" stress fraction if the same long term strength is expected.

Figure 7.30 shows the stress fraction plots for wedge ice. The trend with temperature appears to be opposite of the trend observed for frozen soils. It was mentioned in previous sections that the stress relaxation behavior of wedge ice appears to be independent of temperature for the temperature range tested. The initial loading conditions were similar among the samples tested. The initial applied stress to sample no. 41 (-0.44°C) was slightly lower than for the other temperatures. The stress fractions for stability conditions 1 and 2 are similar for the temperature range shown. This shows that the stress fractions for the first 24 hours varied in relation to temperature, but the end values do not. The increasingly brittle nature of wedge ice with decreasing temperature may be a factor behind the reverse trend seen for the stress fraction vs. temperature.

7.5.3 CSC Tests: Long Term Strength.

The methods for the determination of the time to a minimum strain rate for a constant stress test are illustrated in Figure 7.31. Figure 7.31 (a), shows the classic creep curve with primary, secondary, and tertiary creep stages. Defining the long term strength relationships consists of determining a relationship between time to failure and stress. The definition of failure is user dependent. For long term strength conditions, it is common to use the onset of tertiary creep as the failure condition (McRoberts et al. 1978; Pekarskaya, 1965; Vialov et al., 1965; Andersland and Ladanyi, 1994). This is shown in Figure 7.31 (a) by point D and time t_1. The stress level is then related to the time t_1 at point D by plotting stress (strength) vs. time. Point D may serve as an inflection point or may occur after a prolonged secondary creep stage. In this work, the long term strength limit is considered as the onset of a secondary creep stage or minimum strain rate

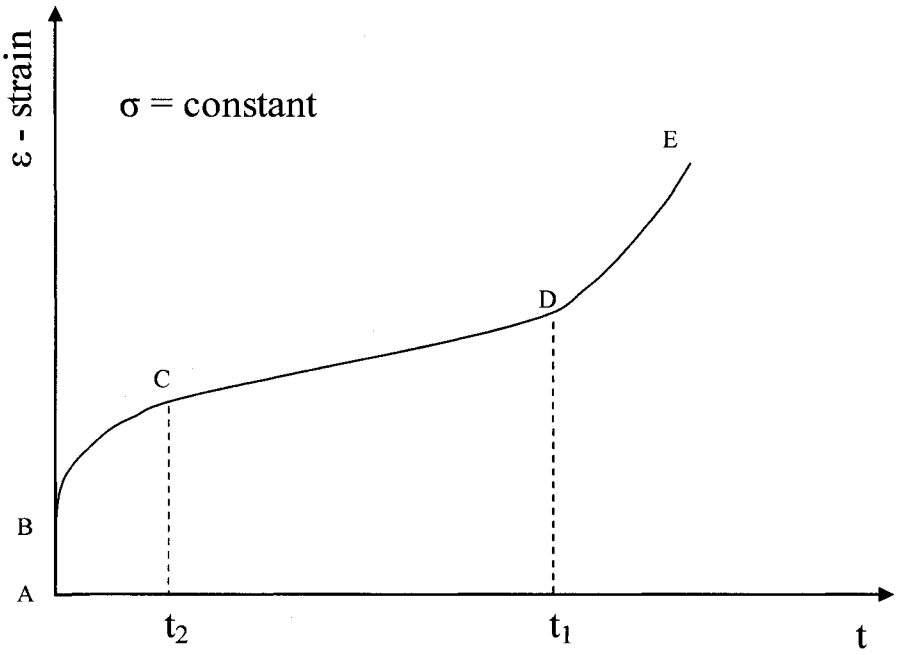

(a)

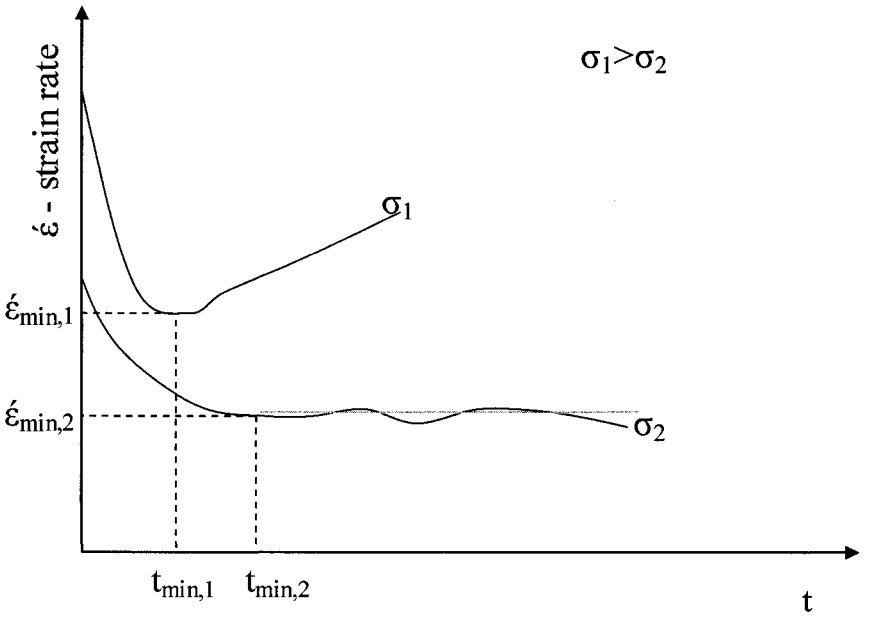

(b)

Figure 7.31. Concepts for the determination of the time to a minimum strain rate for a constant stress creep (CSC) condition.

as indicated by point C and time t_2 in Figure 7.31 (a). This indicates that for stresses below the long term strength, only primary creep exists (Sayles, 1985; Vialov, 1959). Once a secondary creep stage or tertiary creep stage is reached, "flow" of the material occurs and given enough time the sample eventually fails. Figure 7.31 (b) shows the two conditions for which a time to a minimum strain rate was calculated for long term strength estimation. When a well defined minimum strain rate (inflection point) is observed, the minimum strain rate and time are identified as represented by $\dot{\varepsilon}_{min,1}$ and $t_{min,1}$ (Figure 7.31 (b)). In this case the secondary and tertiary creep interpretations of the long term strength limits correspond. When a prolonged secondary creep stage is observed, time t correlates to the onset of the secondary creep stage. The minimum strain rate and time are identified as $\dot{\varepsilon}_{min,2}$ and $t_{min,2}$ (Figure 7.31 (b)). The long term strength relationships are then interpreted based on the stress level (for a constant stress test) and the time period required for the onset of a secondary creep regime or a strain rate inflection point. The long term strength from CSC data is interpreted by two methods. The first method applies a best fit regression to the data derived from time to minimum strain rate for a CSC creep test. So for each constant stress, a time to a minimum strain rate is determined. From the best fit regression, long term strength extrapolations are conducted to the time period of interest. In this work, time periods of 50 and 100 years were used. The second method is application of Vialov's long term strength equation to the CSC data.

7.5.3.1 CSC Tests: Strength vs. Time Evaluation of Long Term Strength

Utilizing the data determined from the CSC tests for soils with vml cryostructure at -1°C and -2°C and soils with RM cryostructure at -1°C, long term strength curves will be presented. For a constant stress creep test, the time to a minimum strain rate is identified (See Figure 2.3). The long term strength curves are then determined by plotting the time required for a minimum strain rate to be reached for an applied constant stress. The result is a stress decrease vs. time curve.

Power law regressions were fit to the CSC data points, which define the long term strength vs. time curves for soils with vml cryostructures and for soils with RM cryostructures. Figures 7.32 to 7.34 show the resulting CSC long term strength curves. Included are the stress relaxation curves derived from relaxation tests for similar soil cryostructures and temperatures for comparison. The long term strength is estimated by extrapolating the power regression to a user identified time period. In this work, 50 and 100 years time periods were used. The long term strength curves determined from CSC data tend to predict higher strength values for vml cryostructure at -1°C and for RM cryostructure at -1°C than the stress relaxation curves determined from relaxation tests (see section 7.5.2). The long term strength curves from CSC tests and relaxation curves

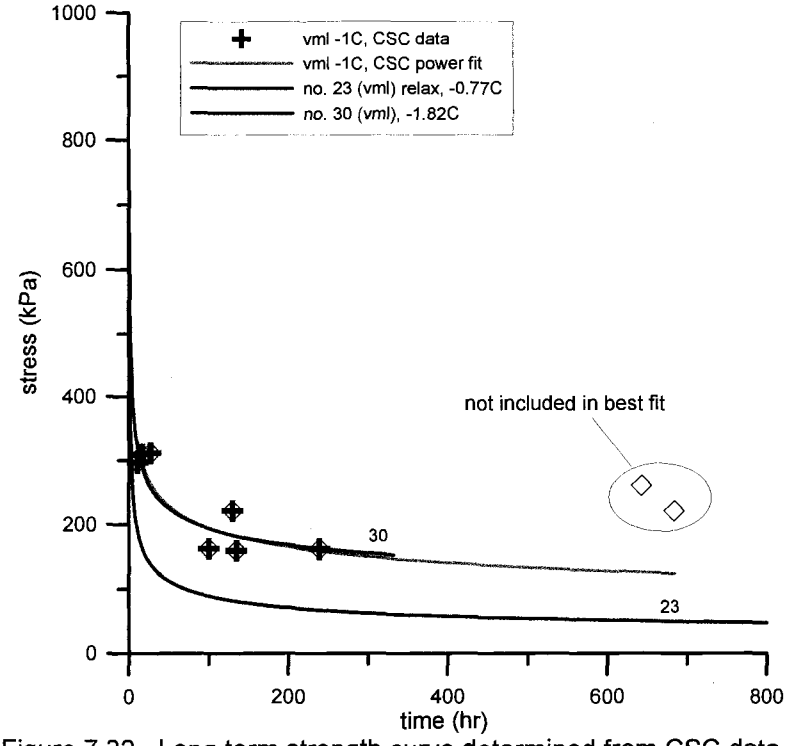

Figure 7.32. Long term strength curve determined from CSC data for soils with vml cryostructure at -1°C. Stress relaxation data from relaxation tests are shown for comparison.

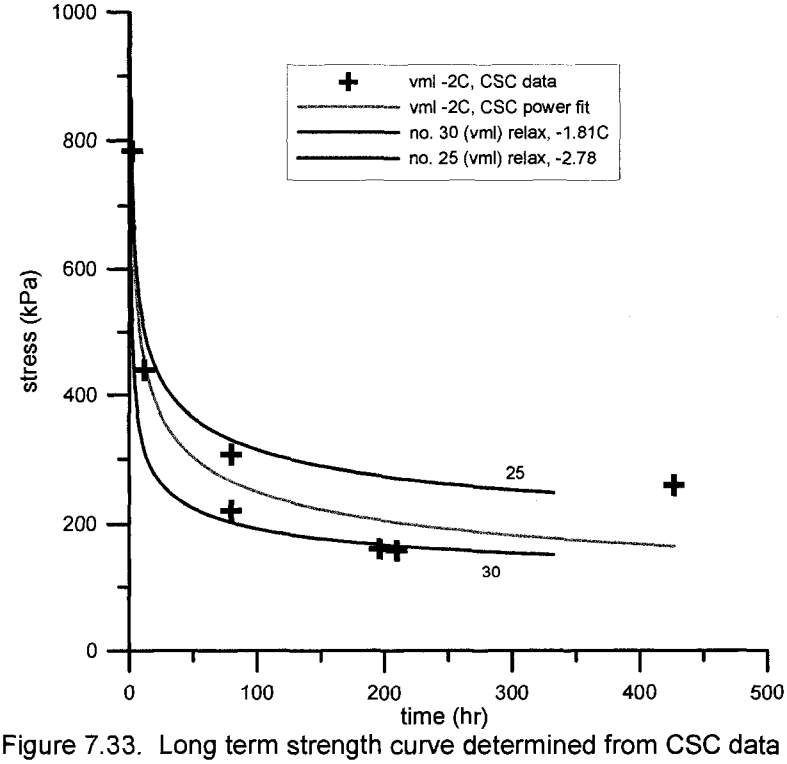

Figure 7.33. Long term strength curve determined from CSC data for soils with vml cryostructure at -2°C. Stress relaxation data from relaxation tests are shown for comparison.

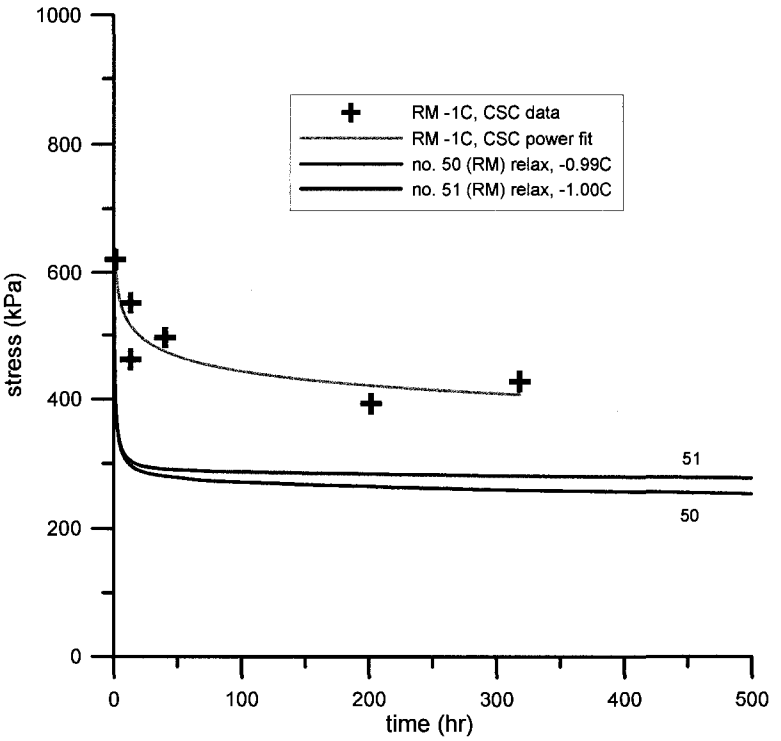

Figure 7.34. Long term strength curve determined from CSC data for soils with RM cryostructure at -1°C. Stress relaxation data from relaxation tests are shown for comparison.

Table 7.16. Long term strength coefficients derived from CSC data for Eq. 7.6 and estimated 50 and 100 year strengths.

CSC data	C (kPa/hr^d)	d	r^2	$\sigma_{50\ year}$ (kPa)	$\sigma_{100\ year}$ (kPa)
-1C vml	577.039	-0.237	0.794	26.6	22.5
-2C vml	908.538	-0.281	0.802	23.6	19.4
-1C RM	623.328	-0.074	0.815	237.7	225.8

from relaxation tests are in relative agreement for soils with vml cryostructure at -2°C (Figure 7.32). Table 7.16 lists the C and d parameters for Equation 7.6, as well as the 50 and 100 year long term strengths estimates for CSC data. Anomalous values are seen for the 50 and 100 year long term strengths for soils with vml cryostructure at -2°C. The long term strength values are predicted to be lower at -2°C than at -1°C. One difficulty with determination of the CSC relaxation curves is the quantification of the time parameter. For the ice-rich soils, a clear minimum strain rate may not be defined. In some instance a prolonged secondary stage is seen. As a result, identifying the time at which a minimum or secondary stage is reached is somewhat subjective. Therefore, acquiring an accurate estimate of the power regression for stress decrease vs. time

can be difficult. The long term strength for soils with vml cryostructure at -2°C are not less than at -1°C.

7.5.3.2 Vialov's Long Term Strength Equation

An empirical relationship for the long term strength was proposed by Vialov (1959). Vialov's long term strength equation has been widespread in use for predicting the long term strength at some time t in the future. Vialov's long term strength equation can be expressed as

$$\sigma_{lt} = \frac{\beta}{\ln\left(\frac{t}{B}\right)} \qquad \text{Eq. 7.7}$$

Where σ_{lt} is the long term strength, t is the time period for which the long term strength is to be predicted, β (units of stress) and B (units of time) are empirical coefficients.

Coefficients β and B are determined by plotting 1/σ vs. log time. The inverse of the slope gives the β parameters. The B coefficient is then calculated from the log 1 intercept and the β coefficient. The method by which the coefficients for Equation 7.7 are determined is shown in Figure 7.35. Figure 7.36 show the test data for soils with vml cryostructure and soils with remolded-massive cryostructure based on the CSC time to minimum strain rates. A best fit logarithmic fit was applied and the β and B coefficients were calculated as indicated in the Figure 7.35.

Vialov's long term strength equation can be used to extrapolate short term data to long term predictions. Table 7.17 gives the β and B coefficients for best fit regressions. Also included are the estimated 50 and 100 year long term strengths. The r^2 value is the correlation coefficient for the best fit logarithmic regression as applied to the CSC data points. As earlier, anomalous values for the long term strength estimates for soils with vml cryostructure at -2°C are seen. Once again this is due to the subjective nature of determining the time to minimum strain rate for a constant stress. Long term strengths for soils with vml cryostructure are in reality higher at -2°C than at -1°C.

7.6 Long Term Strength Comparison: Relaxation, CSC Data, and Literature

Table 7.18 is a summary of the long term strengths as determined by relaxation tests and CSC tests. The relaxation data is based on a strain rate stability criterion (i.e. stability conditions 1 and 2, section 7.5.1) and power law regressions for stress relaxation vs. time (section 7.5.2). Table

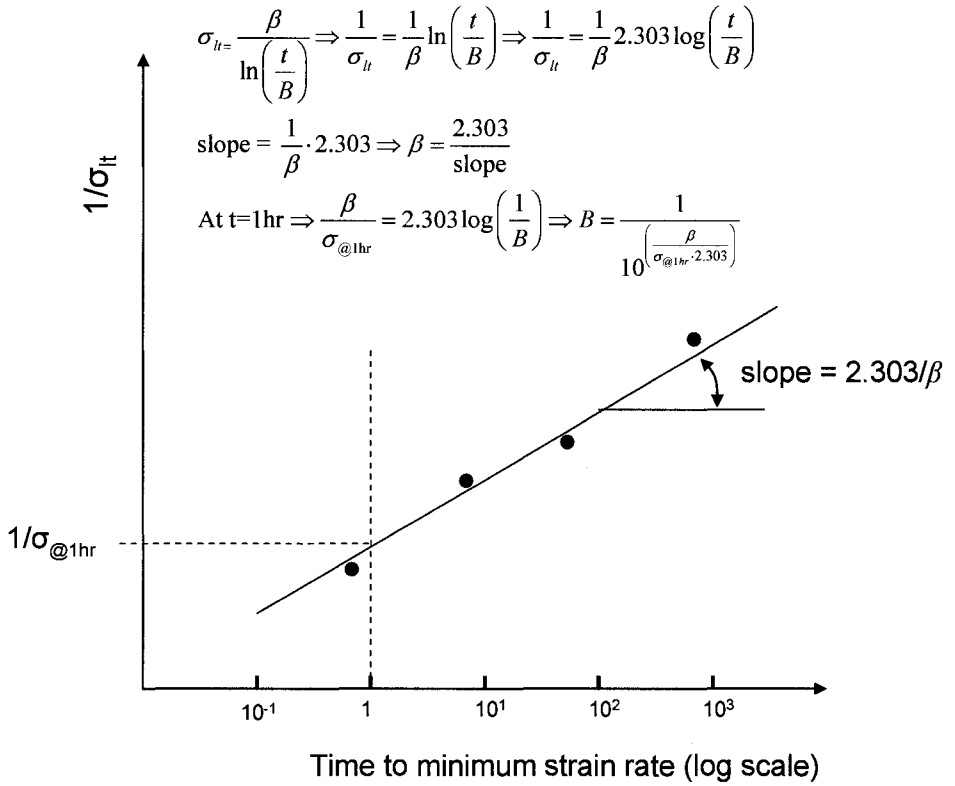

Figure 7.35. Determination of coefficients for Vialov's long term strength equation (Eq. 7.7).

7.18 also summarizes the 50 and 100 year long term strengths as predicted from power law regressions of long term strength vs. time relationships for CSC data and Vialov's long term strength equation based on CSC data. The data has been average if two or more samples were tested under similar conditions and temperatures. Table 7.19 summarizes the long term strengths as determined from literature sources for Fairbanks silt and ice-rich Norman Wells permafrost

Extrapolations of the stress relaxation curves derived from relaxation tests to 50 and 100 years predicts the lowest long term strengths. Extrapolation of Vialov's equation predicts the highest long term strengths. There is some ambiguity of the -2°C strengths as predicted for soils with vml cryostructure from CSC tests. The CSC data predicts lower strengths for -2°C than -1°C. This is not a realistic result as shown from the relaxation tests. This unrealistic result is an example of the difficulties in interpreting CSC data based on data from many different undisturbed samples. The long term strengths show a wide range of values based on the method of determination. For soils with vml cryostructure at -1°C, the long term strength ranges from 4 to 106.2 kPa. For soils

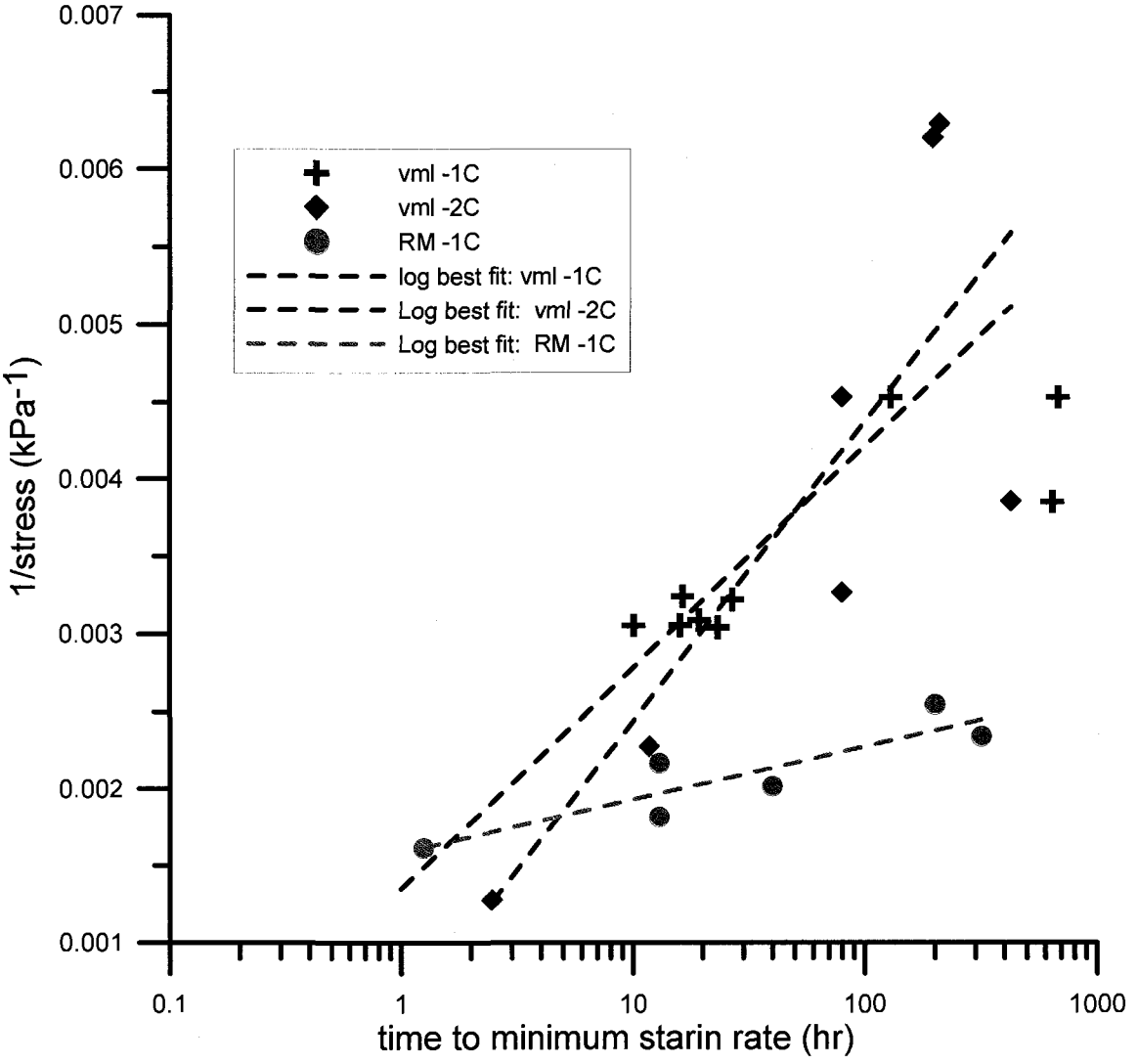

Figure 7.36. Determination of Vialov's long term strength coefficients β and B based on CSC data for soils with vml cryostructure at -1°C and -2°C and soils with RM cryostructure at -1°C.

Table 7.17. Summary of coefficients for Vialov's equation and 50 and 100 year strength estimates.

CSC data	β (kPa)	B (hr)	r^2	$\sigma_{50\ year}$ (kPa)	$\sigma_{100\ year}$ (kPa)
-1C vml	1609.94	0.114	0.867	106.1858	101.5435
-2C vml	1192.89	0.548	0.655	87.76765	83.50881
-1C RM	6657.34	2.401E-05	0.801	281.7681	273.7375

Table 7.18. Summary of long term strengths determined from CSC and relaxation tests.

Test type	Temp (°C)		σ_1 (kPa)	σ_2 (kPa)	$\sigma_{50\ years}$ (kPa)	$\sigma_{100\ years}$ (kPa)
Relax (avg. no 23, 24)	-0.81	vml	57.6	31.5	6.0	4.0
Relax (no. 30)	-1.82	vml	127.2	84.7	32.3	27.8
Relax (no. 25)	-2.78	vml	217.4	153.0	53.5	46.2
CSC (σ vs. time)	-1	vml	--	--	26.6	22.5
CSC (σ vs. time)	-2	vml	--	--	23.6	19.4
CSC (Vialov eq.)	-1	vml	--	--	106.2	101.5
CSC (Vialov eq.)	-2	vml	--	--	87.8	83.5
Relax (avg. no. 26, 27)	-0.80	hml	52.5	30.6	5.1	4.1
Relax (avg. no. 28,29)	-1.83	hml	139.0	94.0	30.1	25.9
Relax (no. 28)	-2.81	hml	209.5	161.2	37.2	32.0
Relax (no. 31)	-0.88	RC	86.9	63.6	21.9	19.6
Relax (avg. no. 32, 34)	-1.85	RC	147.4	114.0	55.7	50.6
Relax (no. 33)	-2.79	RC	213.0	151.1	76.1	68.0
Relax (no. 58)	-0.3	RM	72.5	60.7	21.5	19.4
Relax (avg. no. 56, 57)	-0.5	RM	141.1	136.1	87.2	83.7
Relax (avg. no. 49, 50, 51)	-1.00	RM	272.3	257.4	203.9	199.0
Relax (avg. no. 52, 53)	-1.99	RM	521.4	495.2	420.6	412.5
Relax (avg. no. 54, 55)	-3.00	RM	705.3	665.7	576.1	564.7
Relax (avg. no. 60, 61)	-4.01	RM	904.8	855.7	724.6	708.9
Relax (no. 62)	-5.01	RM	1142.2	1092.3	953.2	936.3
CSC (σ vs. time)	-1	RM	--	--	237.7	225.8
CSC (Vialov eq.)	-1	RM	--	--	281.8	273.7
Relax (no. 41)	-0.44	IW	95.8	39.3	12.0	9.1
Relax (no. 35, 36)	-0.97	IW	127.1	61.6	7.5	5.5
Relax (no. 37, 38)	-1.86	IW	107.5	48.0	9.2	6.8
Relax (no. 39, 40)	-3.10	IW	115.6	58.8	12.4	9.5
Relax (no. 44)	-1.02	BI	112.8	93.7	62.8	59.4
Relax (no. 46)	-1.00	GI	108.9	61.5	15.5	12.5

note: σ_1 is the long term strength based on stability condition 1 (section 6.5.1), σ_2 is long term strength based on stability condition 2 (section 6.5.1), $\sigma_{50\ year}$ is the strength extrapolated to 50 years, and $\sigma_{100\ years}$ is the strength extrapolated to 100 years. Relax indicates data derived from relaxation tests. CSC indicates data derived from constant stress creep tests.

Table 7.19. Literature summary for the long term strength for Fairbanks silt and other ice-rich silt.

long term strength (kPa) stability condition 1	long term strength (kPa) stability condition 2	Temp (°C)	soil	source	comments
319.7	228.5	-2.0	Fairbanks silt	Yuanlin & Carbee 1987a	low density, remolded
62.9	35.4	-1.7	Fairbanks silt	Thompson & Sayles 1972	lab test on undisturbed cores
46.8	26.3	-1.7	Fairbanks silt	Thompson & Sayles 1972	permafrost tunnel closure rates
45.1	23.2	-2.0	Fairbanks silt	Law, 1987	pressure plate permafrost tunnel
15.0	6.9	-2.0	Fairbanks silt	Ladanyi & Huneault, 1989	cone penetrometer permafrost tunnel

*note: above values are based on steady state power law creep relationships

100 Year Strength Approximations

$\sigma_{100\ yrs}$	Temp (°C)	soil	source	comments
191.2	-0.5	Fairbanks silt	Yuanlin & Carbee 1987a	med. density, remolded
343.2	-1.0	Fairbanks silt	Yuanlin & Carbee 1987a	med. density, remolded
608.0	-2.0	Fairbanks silt	Yuanlin & Carbee 1987a	med. density, remolded
864.0	-3.0	Fairbanks silt	Yuanlin & Carbee 1987a	med. density, remolded
29.3	-1.7	Fairbanks silt	Ladanyi et al. 1991	pressuremeter relaxation, field, med. strains
133.8	-1.7	Fairbanks silt	Ladanyi et al. 1991	pressuremeter relaxation, field, low strains
171.0	-1.0	Norman Wells silt	McRoberts et al. 1978	lab tests, undisturbed cores, ice-rich
220.0	-3.0	Norman Wells silt	McRoberts et al. 1978	lab tests, undisturbed cores, ice-rich

with vml cryostructure at -2°C, the long term strength ranges from 27.8 to 127.2 kPa. For soils with RM cryostructure at -1°C, the long term strength ranges from 199 to 281.8 kPa. In general, the long term strength predicted for stability condition 2 from relaxation tests are relative agreement with the long term strengths predicted from CSC data.

Table 7.19 shows strength data for Fairbanks silt (Ladanyi & Huneault, 1989; Ladanyi et al., 1991; Thompson & Sayles, 1972; Yuanlin & Carbee, 1987a; Law, 1987) along with data for ice-rich silts (McRoberts et al., 1978). Data is reduced from minimum strain rate flow laws (secondary) and primary creep equations. Yuanlin & Carbee (1987a) worked with remolded

Fairbanks silt from the permafrost tunnel. For low density silt (γ_d =1.07-1.10 g/cm^3), the strength corresponding to stability conditions 1 (2.083x10^{-6} hr^{-1}) and 2 (2.083x10^{-7} hr^{-1}) were 319.7 kPa and 228.5 kPa at -2°C. Values were obtained from tests with strains rates greater than 2.88x10^{-4} hr^{-1}. Hundred year long term strength (data extrapolated to 100 years) for medium density silt (γ_d =1.18-1.23 g/cm^3) yielded strengths of 191.2 kPa, 343.2 kPa, 608.0 kPa, and 864 kPa at temperatures of -0.5°C, -1°C, -2°C, and -3°C respectively. The strength data for soils with remolded massive cryostructure falls between the low and medium density silts. The dry densities for soil with remolded-massive cryostructure are close to the low density silts tested by Yuanlin & Carbee (1987a). Ladanyi et al. (1991), performed in-situ pressuremeter relaxation tests in the permafrost tunnel. For medium strains, 100 year strength is equal to 29.3 kPa. For low strains, the 100 year strength is equal to 133.8 kPa. Test temperatures varied from -1.7°C to -2°C. Ladanyi and Huneault (1989) performed cone penetrometer tests in the permafrost tunnel. The data was fitted to a minimum strain rate power law relationship. From the minimum strain rate conditions, the strength for stability conditions 1 and 2 were 15.0 kPa and 6.9 kPa respectively for a temperature of approximately -2°C. Thompson & Sayles (1972) measured closure rates of the permafrost tunnel and performed laboratory creep tests of undisturbed soil cores. Based on minimum strain rates for laboratory tests, the strengths are 62.9 kPa and 35.5 kPa (for stability conditions 1 and 2 respectively) at -1.67°C. Test strain rates were greater than 0.0018 hr^{-1}. Steady state creep conditions for the tunnel closure data yielded strength values of 46.8 kPa and 26.3 kPa. McRoberts et al. (1978) reported 100 year strengths for ice-rich Norman Wells silt with strength values of 171 kPa and 220 kPa at temperatures of -1°C and -3°C respectively.

Based on water contents listed in the field study reports from the permafrost tunnel, the soils tested most likely contained micro-lenticular cryostructure. However, detailed permafrost descriptions were not available so this cannot be confirmed directly. Generally, the field tests yielded lower long term strengths as compared to the strain rate criteria interpretation of relaxation tests conducted in this study. The 50 and 100 year long term strength estimates from relaxation tests offer better agreement to the field tests reported in the literature. It is important to note that results of the laboratory tests on undisturbed soils are extrapolations from higher strain rates under which the tests were conducted to lower strain rates. Experience indicates that extrapolation to lower strain rates generally will yield lower strengths than is normally seen. The low strain conditions (Ladanyi et al, 1991) are in the same range as soils with micro-lenticular cryostructure. The -1°C long term strengths are generally higher for ice-rich Norman Wells silt as

compared to soils with micro-lenticular and reticulate-chaotic cryostructure. The -3°C long term strengths are comparable.

The determination of long term strengths based on strain rate criterion and relaxation tests yield comparable results to other testing methods. An important observation is that soils with remolded-massive structure had long term strengths 3 to 4 times greater than the undisturbed soils. This indicates that long term strengths from remolded soils are not conservative for undisturbed soils. In the temperature range tested, soils with reticulate-chaotic cryostructure have greater long term strength than soils with micro-lenticular cryostructure or wedge ice. The long term strength for wedge ice had little temperature influence in studied range. Soils with horizontal and vertical micro-lenticular cryostructure had similar long term strength patterns.

7.7 Long Term Strength Summary

The long term strength was determined by four methods of analysis and two testing methods. The long term strength from relaxation tests were interpreted based on a strain rate stability criteria and stress relaxation vs. time. The strain rate stability method assumed that the long term strength is the stress which correlates to a specified strain rate. In this study, two strain rate criteria were defined as 2.083×10^{-6} hr^{-1} and 2.083×10^{-7} hr^{-1}. The second method of interpretation based on relaxation tests involved fitting the stress relaxation vs. time data curve with a power law regression. The strength is then estimated for a user identified time period. In this work, strengths for a 50 and 100 year time period were used.

Long term strengths from CSC tests were interpreted based on a stress vs. time relationship and the second method was application of Vialov's long term strength equation. The stress vs. time curves are defined by determining the time to a minimum strain rate for a constant stress conditions. The data is then fitted with a power regression and the strength is estimated by extrapolating the regression to a user identified time period. The CSC data was applied to Vialov's long term strength equation from which the long term strength is determined for a user specified time.

Generally, Vialov's long term strength equation produced the highest long term strength estimates. The stress relaxation vs. time based on relaxation test data produced the lowest long term strength estimates. The strain rate criteria conditions generally produced higher long term strength estimates than the CSC long term strength vs. time approach.

Interpretation of CSC data is subjective in the selection of strength time data. CSC strength-time data is a composite of numerous constant stress creep tests. Relaxation tests give direct results from one sample. In general, more data is needed to clarify the results. Based on the data presented above, the long term strength estimates vary depending on testing method. What is the best approach to use for estimation of the long term strength? The icier the soil, the lower the long term strength when using the stress relaxation vs. time as interpreted from relaxation tests. This is supports the concept that ice has little to no long term strength and the strength approaches zero with infinity. Soils with micro-lenticular cryostructure and wedge ice show this trend with small long term strengths as based on 50 and 100 year estimates. Less ice rich cryostructures such as RM cryostructure show a long term strength condition that changes little as 50 and 100 year estimates are determined. From an engineering view point, the strain rate stability criteria may be a viable option. The user identifies what is a permissible strain rate for their structure, foundation, tunnel, etc. and then uses that condition for the determination of the long term strength. The 50 and 100 year estimates from the stress relaxation curves, as derived from relaxation tests, supply the most conservative results. It is the author's opinion that the relaxation tests are a valuable alternative in that one sample can be tested and the results are not as subjective in terms of a data analysis.

Chapter 8: Conclusions

Chapter 2 reviewed relevant literature pertaining to the mechanical behavior of frozen soils as a function of soil cryostructure and testing programs conducted for Fairbanks silt and ice-rich permafrost soils. In chapter 3, a discussion on the geology of the CRREL permafrost was presented. The permafrost mapping was based on a cryofacial approach which assumes that soil cryostructure is related to the depositional and cryogenic genesis. Chapter 4 presented the soils and ice facies used during the course of the testing program. The samples were grouped by soil cryostructure and ice facies with detailed descriptions, macro and micro images, CT scan images, and discussion of unfrozen water. Chapter 5 presented testing equipment and methods used in the course of the program. The two testing techniques consisted of constant stress creep (CSC) tests and relaxation tests. Chapter 6 presented the general deformation patterns for the various soil cryostructures and ice facies as observed from test data and visual observation. Chapter 7 presented the results and discussion of the test program. The focus areas included the interpretations of a minimum strain rate flow law and the long term strength based on CSC and relaxation test data.

The overall goal of this work was to connect the permafrost geology of the soils tested with their creep properties. This was primarily approached through the application of the cryofacies model. In other words, it is assumed that cryostructure is directly related to how a frozen soil was deposited and frozen. The CRREL permafrost tunnel was chosen as it represents a relatively stable environment, a fair amount of previous test data exists for comparison, and a relatively small number of cryostructures are found within a reasonably uniform sediment lithologic zone. Mapping of the tunnel was conducted to understand the geology and cryostructure distribution of the tunnel. Then a testing program was undertaken to explore the creep properties of the tunnel sediments in relation to soil cryostructure and ice facies.

The cryostructure representing the original syngenetic permafrost used in the testing program is micro-lenticular. Secondary reworked sediments occur in the tunnel and either contain reticulate-chaotic or massive cryostructure. Massive ice in the form of wedge ice was also tested. Undisturbed samples included soils with micro-lenticular cryostructure, soils with reticulate-chaotic cryostructure, soils massive cryostructure, and wedge ice. Silt from the tunnel was also used to create remolded samples with massive cryostructure and hence were described as soil with remolded-massive cryostructure. A few samples of glacial and basal glacial ice from the Matanuska Glacier, Alaska, were tested.

Some of the most important findings are summarized below.

1. The volumetric unfrozen water content increases with decreasing ice contents for the silty sediment tested. Conversely, the volumetric unfrozen water content increases with increasing sediment volume. Soils with reticulate-chaotic and remolded-massive cryostructure showed the greatest amount of unfrozen water. Icy soils containing micro-lenticular cryostructure had less unfrozen water at a given temperature than soils with reticulate-chaotic or remolded-massive cryostructure. Most of the unfrozen water changes occurred for temperatures warmer than -2°C. Wedge ice had no unfrozen water at the temperatures tested based on the output of the measurement instrument. Further methods for measuring the unfrozen water content of undisturbed cryostructures need used to verify the results predicted by the Vitel Hydra probes.
2. Minimum strain rate flow laws were compared from literature data and CSC tests. It was found that the minimum strain rate flow laws from the laboratory tests on undisturbed ice-rich Fairbanks silt predict lower strain rates as compared to results from in-situ testing. The creep exponent n equal to 4, was in general agreement with literature sources and CSC testing data for undisturbed frozen Fairbanks silt.
3. Data from CSC creep tests show that the undisturbed soils with vertical micro-lenticular cryostructure creep at a much higher rate than soils with remolded-massive cryostructure for stresses less than 650 kPa at -1°C. This suggests that extrapolation of test data from remolded soils to undisturbed soils is non-conservative. The undisturbed soils and the remolded soils are composed of the same silty sediments. The primary difference is the variation in cryostructure and the associated difference in water content resulting from the variation in cryostructure. Therefore, remolded soils should not be used to represent undisturbed, unconsolidated frozen sediments as the natural soil and ice structures are not duplicated.
4. Stress relaxation behavior is dependent on soil cryostructure. The relaxation behavior of soil with micro-lenticular cryostructure shows a linear regression on a log stress vs. log time plot. This suggests that the creep mechanisms remain the same over the course of the relaxation process. The favorably oriented ice lenses for soil with reticulate-chaotic cryostructure results in a bilinear relaxation process which varies depending on the stress level. At high stresses, creep occurs as planar motion along the oriented ice lenses. At low stress, the stress relaxation rate drops and creep within the frozen silts is assumed to occur. Soils with remolded-massive cryostructure show a similar bilinear stress relaxation pattern. For high stresses, the rate of stress relaxation is high followed by

reduced stress relaxation rates for low stress conditions. The onset of the low stress relaxation rate is interpreted as a long term strength resistance. Wedge ice and glacial ice, show significantly lower rates of stress relaxation than frozen soils. The stress relaxation for wedge ice is independent of temperature for the temperature range tested. The stress relaxation curves for frozen soils show well defined trends with changes in temperature. The rate of the initial stress relaxation increases with warming temperatures which can be related to changes in the unfrozen water content.

5. Long term strengths were estimated from relaxation and CSC tests. Estimates of the long term strengths from relaxation tests are based on strain rate stability criteria and extrapolations of the stress relaxation curves vs. time. Long term strength estimates from CSC tests were based on the time required to achieve a minimum strain rate for a constant stress condition. Using the time to the minimum strain rate, the long term strength estimates were then based on stress vs. time and Vialov's long term strength equation. Vialov's long term strength equation yielded the highest strength estimates and the stress relaxation vs. time from relaxation tests yielded the lowest strength estimates. The difficulty with estimating long term strength from CSC data is the accurate determination of the time to minimum strain rate. Not all soils or ice have a well defined minimum. If a prolonged secondary creep regime dominates, the determination of the time variable is subjective.
6. Soils with micro-lenticular cryostructure showed the lowest long term strengths for the frozen soils. Soils with reticulate-chaotic cryostructure showed long term strengths that were up to 2 times larger than for soils with micro-lenticular cryostructure for temperatures warmer than -2°C. The remolded soils with massive cryostructure showed long term strengths 3 to 4 times greater than the undisturbed frozen soils. It means that extrapolation of remolded soils to the undisturbed soils is non-conservative.
7. The long term strength of wedge ice is greater than undisturbed permafrost soils for temperature conditions warmer than -1.5°C to -2°C. For temperatures colder than -2°C wedge ice shows lower long term strengths. These observation are based on data from relaxation tests using the strain rate criteria condition.
8. The long term strength data for wedge ice is independent of temperature for the temperature range tested (i.e. up to -3°C). The creep response and long term strength for frozen soils is highly sensitive to temperature, especially for temperatures warmer than -2°C, which relates to the unfrozen water content as shown in Chapter 4.
9. Creep data for soils with horizontal micro-lenticular cryostructure and undisturbed soil with massive cryostructure from the tunnel suggest than undisturbed soils with massive

cryostructure show greater creep rates for a given stress than icier soils. This is evidence by well developed creep lobes in soil with horizontal micro-lenticular cryostructure. The creep lobes occur were the soil becomes more "ice poor" to massive.

Overall observations suggest that soil cryostructure influences the time dependent mechanical properties of frozen soils (i.e. creep and long term strength) for uniaxial stress conditions. The mechanical response for frozen soils is influence by temperature. Temperatures warmer than -2°C especially influence the mechanical response. This is attributed to changes in the unfrozen water content. Application of a cryofacial approach to the identification and classification of the mechanical response appears to have validity.

8.1 Recommendations for Improvement

Use of constant stress creep (CSC) tests for undisturbed soils is problematic due to the high degree of data scatter especially at low stresses. In addition to the variable minimum strain rate responses, the time required to determine minimum strain rate flow relationships at low stress is significant. Further research needs to be conducted at low stresses and at high stresses to see if the data trends determined at high stresses can be extrapolated to low stresses. Testing at high stress greatly reduces the amount of time required to determine a minimum strain rate flow relationship.

Volumetric unfrozen water contents were measured using an FDR Vitel Hydra probe. Additional techniques (such as NMR) need to be used to confirm the results of the Vitel Hydra probe for the undisturbed soils. We want to emphasize the point that undisturbed soils should be used as remolded soils are commonly used to estimate the unfrozen water content. In this work, it was found that the volumetric unfrozen content is influenced by soil cryostructure. Based on the apparent importance of the unfrozen water on the mechanical behavior of different soil cryostructures, further research on the affect of cryostructure on the unfrozen water content appears warranted.

In general, laboratory results in this work need to be validated by field measurements. This is generally true for most studies. The goal of every testing program is that the laboratory data can be used for realistic design and evaluation.

In conclusion, a gap generally exists between permafrost science and permafrost engineering. In the field of rock mechanics, it is widely known that the geology of rock mass (including genesis,

rock type, degree of weather, stress and fracture history, water pressure) all combine to determine the engineering parameters. We would like to encourage future researchers and engineers to approach a permafrost site as a system, which includes the permafrost geology and the mechanical properties. All permafrost is not created equal, and therefore should not be treated as equal. Information has been presented in this study on how permafrost soil geology affects the creep and deformation characteristics of frozen soils. However, more work needs to be done to further illustrate this concept.

References

Andersland, O.B. & Ladanyi, B.L. 1994. An Introduction to Frozen Ground Engineering. Chapman & Hall: New York, 352 pp.

Anderson, D.M., and Tice, A.R. 1973. The unfrozen interfacial phase in frozen water systems. In A. Hadar (Editor), Ecological Studies Analysis and Synthesis, 4: 107-124.

Arenson, L.U. and Springman, S.M. 2005a. Triaxial constant stress and constanst strain rate test on ice-rich permafrost samples. Canadian Geotechnical Journal, 42: 412-430.

Arenson, L.U., and Springman, S.M. 2005b. Mathematical descriptions for the behaviour of ice-rich frozen soils at temperatures close to 0°C. Canadian Geotechnical Journal, 42: 431-442.

Barnes, P., Tabor, D., and Walker, J.C.F. 1971. Friction and creep of polycrystalline ice. Proceedign of the Royal Society of London, Series A., 324(1557): 127-155.

Bjella, K.L. 2008. The effect of near-freezing temperatures on the stability of an underground excavation in permafrost. Proceeding of the Ninth International Conference on Permafrost, University of Alaska Fairbanks, Alaska, June 29-July 3, 2008: 120-124.

Bray, M.T. 2003. Field observations of a large diameter chilled pipeline experiment, Fairbanks, Alaska. M.S. Thesis. University of Alaska Fairbanks: 150 pp.

Bray, MT., French, H.M. & Shur, Y. 2006. Further Cryostratigraphic Observations in the CRREL Permafrost Tunnel, Fox, Alaska. Permafrost and Periglacial Processes, 17: 233-243.

French, HM. 1996. The periglacial environment, Second Edition. Addison Wesley Longman: UK: 341 pp.

Gasanov, SS. 1969. Structure and history of formation of permafrost in Eastern Chukotka. Moscow: Nauka; 168 pp (in Russian).

Glen, J.W. 1955. The creep of polycrystalline ice. Proceeding of the Royal Society of London, Series A., 228(1175): 519-538.

Goldsby, D.L., and Kohlstedt, D.L. 2001. Superplastic deformation of ice: experimental observation. Journal of Geophysical Research, 106(B6): 11,017-11,030.

Hamilton, TD, Craig, JL, Sellman, PV. 1988. The Fox permafrost tunnel: a Late- Quaternary geologic record in central Alaska. Geological Society of America Bulletin, 100: 948-969.

Haynes, F.D. 1978. Strength and deformation of frozen silt. Proceeding of the Third International Conference on Permafrost, Edmonton, Alberta, Canada: 656-661.

Haynes, F.D., and Karalius, J.A. 1977. Effect of temperature on the strength of frozen silt. CRREL Report 77-3, CRREL, Hanover, New Hampshire, 27 pp.

Haynes, F.D., Karalius, J.A., and Kalafut, J. 1975. Strain rate effect on the strength of frozen silt. CRREL Research Report 350. CRREL, Hanover, New Hampshire: 27 pp.

Hooke, R.L, Mellor, M., Budd, W.F, Glen, J.W., Higashi, A, Jacka, T.H., Jones, S.J., Lile, R.C., Martin, R.T., Meier, M.F., Russel-Head, D.S., and Weertman, J. 1980. Mechanical properties of polycrystalline ice: an assessment of current knowledge and priorities for research. Cold Regions Science and Technology, 3(4): 263-275.

Huang, S.L., and Speck, R.C. 1989. An investigation into the creep behaviour of CRREL tunnel, Alaska. Proceedings of the International Symposium on Mining in the Arctic, Fairbanks, AK: 65-73.

Huang, S.L, Aughenbaugh, N.B., and Wu, M.C. 1986. Stability study of CRREL permafrost tunnel. ASCE Journal of Geotechnical Engineering, 112: 777-790.

Huang, S.L, Bray, M.T., Akagawa, S., and Fukuda, M. 2004. Field Investigation of soil heave by a large diameter chilled gas pipeline experiment Fairbanks, Alaska. Journal of Cold Regions Engineering, 18(1): 2-34.

Johansen, N.I. and Ryer, J.W. 1982. Permafrost creep measurements in the CRREL tunnel Proceedings of the Third International Sympsoium on ground Freezing, Hanover, New Hampshire. Hanover, New Hampshire: U.S. Army CRREL: 61-63.

Johnston, G.H., and Ladanyi, B. 1972. Field tests of grouted rod anchors in permafrost. Canadian Geotechnical Journal, 9(2): 176-194.

Kamb, B. 1972. Experimental recrystallization of ice under stress. American Geophysical Union, Geophysical Monograph, 16: 211-241.

Katasonov, EM. 1960. Cryogenic textures, ice and earth wedges as genetic indicators of perennially frozen Quaternary deposits. In: Issues of cryology in studies of Quaternary deposits. Moscow, Izd-vo AN SSSR: 86-98 (in Russian).

Kudryavtsev, VA., (editor). 1978. General permafrost science (Geocryology), Second Edition. Moscow University Press: Moscow: 463 pp. (in Russian).

Ladanyi, B. 1981. Mechanical behaviour of frozen soils. In Mechanics of Structured Media, Proceedings of the International Symposium on the Mechanical Behaviour of Structured Media, Ottawa, Ont., 18-21 May 1981. Edited by A.P.S. Selvaduarai. Elsevier, New York,: 205-245.

Ladanyi, B., and Benyamina, M.B. 1995. Triaxial relaxation testing of a frozen sand. Canadian Geotechnical Journal, 32: 496-511.

Ladanyi, B., and Huneault, P.A. 1989. Cone penetrometer tests in permafrost-The Fox tunnel, Alaska. Proceedings of the International Symposium on Mining in the Arctic, Fairbanks, AK: 75-82.

Ladanyi, B., Touileb, B., & Huneault, P. 1991. Pressuremeter stress relaxation testing in a permafrost tunnel. Proceedings of the Geotechnical Engineering Congress, Boulder, CO, 1991, 1-11.

Law, K.H. 1987. Time-dependent bearing capacity of frozen ground. M.S. Thesis, University of Alaska Fairbanks: 129 pp.

Mackay, JR. 1988. Catastrophic lake drainage, Tuktoyaktuk Peninsula area, District of Mackenzie. In Current Research, Part D, Geological Survey of Canada, Paper 88-1D: 83-90.

Mackay, JR. 1997. A full-scale field experiment (1978-1995) on the growth of permafrost by means of lake drainage, western Arctic coast: a discussion of the method and some results. Canadian Journal of Earth Sciences, 34: 17-34.

McRoberts, E.C. 1988. Secondary creep interpretation of ice-rich permafrost. Proceedings of the Fifth International Conference on Permafrost, Trondheim, Norway, August 2-5, 1988: 1137-1142.

McRoberts, E.C., Law, T.C. & Murray, T.K. 1978. Creep tests on undisturbed ice-rich silt. Proceeding of the Third International Conference on Permafrost, Edmonton, Alberta, Canada, 1: 539-545.

Mellor, M. and Cole, D.M. 1982. Deformation and failure of ice under constant stress or constant strain-rate. Cold Regions Science and Technology, 5: 201-219.

Mellor, M., and Testa, R. 1969. Effect of temperature on the creep of ice. Journal of Glaciology, 8(52): 131-145.

Melnikov, VP., and Spesivtsev, VI. 2000. Cryogenic formations in the Earth's lithosphere. Siberian Publishing Center UIGGM, Siberian Branch, Russian Academy of Sciences: Novosibirsk: 343 pp.

Morgenstern, N.R., Roggensack, W.D., and Weaver, J.S. 1980. The behaviour of friction piles in ice and ice-rich soils. Canadian Geotechnical Journal, 17: 405-415.

Murton, JB., and French, HM. 1994. Cryostructures in permafrost, Tuktoyaktuk coastlands, western arctic Canada. Canadian Journal of Earth Sciences, 31: 737-747.

Nixon, J.F. 1978. Foundation design approaches in permafrost. Canadian Geotechnical Journal, 15: 96-112.

Nixon, J.F., and Lem, G. 1984. Creep and strength testing of frozen saline fine-grained soils. Canadian Geotechnical Journal, 21: 518-529.

Nixon. J.F. and McRoberts, E.C. 1976. A design approach for pile foundations in permafrost. Canadian Geotechnical Journal, 13: 40-57.

Pekarskaya, N.K. 1965. Shear strength of frozen ground and its dependence on texture. CRREL, Technical translation AD 715 091. Hanover, NH: 97 pp.

Péwé, TL. 1975. Quaternary geology of Alaska. United States Geological Survey Professional Paper 835: 145 pp.

Rabotnov, Y.N. 1969. Creep problems in structural member. North-Holland Publishing Co., Amsterdam: 822 pp (translated from Russian).

Rein, R.G. 1985. Correspondence of creep data and constant strain-rate data for frozen silt. Cold Regions Science and Technology, 11: 187-194.

Roggensack, W.D. 1977. Geotechnical properties of fine-grained permafrost soils. Ph.D Thesis, Univesity of Alberta, Canada: 449 pp.

Romanovsky, V.E., and Osterkamp, T.E. 2000. Effects of unfrozen water on heat and mass transport processes in the active layer and permafrost. Permafrost and Periglacial Processes, 11: 219-239.

Rosenbaum, GE., Arkhangelov, AA., and Koniakhin, MA., 1978. Thermokarst-cave ice in Yana-Kolyma Lowland. Moscow State University, Problems of Geocryology, 7: 74-92 (in Russian).

Savigny, K.W. and Morgenstern, N.R. 1986a. Creep behaviour of undisturbed clay permafrost. Canadian Geotechnical Journal, 23(4): 515-526

Savigny, K.W. and Morgenstern N.R. 1986b. In situ creep properties in ice-rich permafrost soil. Canadian Geotechnical Journal, 23: 504-514.

Sayles, F.H. 1985. Creep of a strip footing on ice-rich permafrost. Sessions on Foundations in Permafrost and Seasonal Frost, Denver, CO, Apr. 29, 1985: 29-51.

Sayles, F.H & Carbee, D.L. 1981. Strength of frozen silt as a function of ice content and dry unit weight. Engineering Geology, 18: 55-65.

Sego, D.C. and Morgenstern, N.R. 1983. Deformation of ice under low stresses. Canadian Geotechnical Journal, 20: 587-602.

Sellman, PV., 1967. Geology of the USA CRREL permafrost tunnel, Fairbanks, Alaska. US Army Cold Regions Research and Engineering Laboratory, Technical Report 199: 22 pp.

Sellman, PV. 1972. Geology and properties of materials exposed in the USA CRREL permafrost tunnel. US Army Cold Regions Research and Engineering Laboratory, Special Report 177, 15 pp.

Shumskii, PA. 1964. Chapter IX. Ground (subsurface) ice. In: Principles of Geocryology (Permafrost Studies), Academy of Sciences of the USSR, (P.F. Shvetsov and B. N. Dostovalov, editors), 1959, V.A. Obruchev Institute of Permafrost Studies, Moscow, 274-

327 (in Russian). National Research Council of Canada, Ottawa, Technical Translation 1130: 118 pp.

Shur, YL. 1988. Upper horizon of permafrost soils and thermokarst. Novosibirsk 'Nauka', Siberian Branch, 210 pp. (In Russian)

Shur, Y., French, H.M, Bray, M.T. & Anderson, D.A. 2004. Syngenetic permafrost growth: cryostratigraphic observation from the CRREL tunnel near Fairbanks, Alaska. Permafrost and Periglacial Processes 15(4): 339-347.

Shur, Y., Hinkel, K.M., and Nelson, F.F. 2005. The transient layer: implication for geocryology and climate-change science, 16(1): 5-17....

Sinha, N.K. 1982. Constant strain rate and stress-rate compressive strength of columnar-grained ice. Journal of Materials Science, 17(3): 785-802.

Solomatin, VI. 1986. Petrogenesis of ground ice. Novosibirsk, Nauka; 215 pp. (in Russian).

Song, M., Baker, I., and Cole, D.M. 2005. The effect of particle on dynamic recrystallization and fabric development of granular ice during creep. The journal of glaciology, 51(174): 377-382.

Steineman, S. 1958. Experimentelle Untersuchungen zur Plastizitat von Eis. Beitrage zur Geologie der Schweiz No. 10

Thompson, E.G., & Sayles, F.H. 1972. In situ creep analysis of room in frozen soil. Journal of the Soil Mechanics and Foundation Division, 98: 899-915.

Tice, A.R., Black, P.B., and Berg, R.L. 1989. Unfrozen water contents of undisturbed and remolded Alaskan silt. Cold Regions Science and Technology, 17: 103-111.

Tsytovich, N.A. 1975. The Mechanics of Frozen Ground. Scripta Book Company, Washington, D.C.: 426 pp.

Vialov, S.S. 1959. Rheological properties and bearing capacity of frozen soils. CRREL technical translation no. 74, CRREL, Hanover, N.H.: 219 pp.

Vialov, S.S, and Ermakov, V.F. 1967. Simplified method of testing ice for creep and relaxation. Proceedings of the International Conference on Low Temperature Science, Sapporo, Aug. 14-19, 1966, Hokkaido University, Japan, 1(1): 339-347.

Vialov, S.S., Gmoshinskii. V.G., Gorodetskii, S.E., Grigorieva, V.G., Zaretskii, IuK., Perkarskaya, N.K. & Shusherina, E.P. 1962. The strength and creep of frozen soils and calculations for ice-retaining structures. Izd Akademii Nauk SSR Moscow (1962), CRREL Translation 76 (1965), Hanover, NH: 301 pp.

Vyalov, S.S., Gorodetskii, S.E., Ermakov, V.F., Zatsarnaya, A.G., & Pekarskaya, N.K. 1966. Methods of Determining Creep, Long-Term Strength, and Compressibility Characteristics of Frozen Soils. Moscow: Nauka: 109pp. NRC technical translation 1364.

Vyalov, S.S., Dokuckayev, V.V. & Sheynkman, D.R. 1980. Ground-ice and ice-rich ground as structure foundations. CRREL Translation 737. Hanover, NH: 159 pp.

Yoshikawa, K., and Overduin, P.P. 2005. Comparing unfrozen water content measurements of frozen soil using recently developed commercial sensors. Cold Regions Science and Technology, 42: 250-256.

Yuanlin, Z. and Carbee, D.L. 1983. Creep behavior of frozen silt under constant uniaxial stress. Proceedings of the Fourth International Conference on Permafrost, University of Alaska Fairbanks: 1507-1512.

Yuanlin, Z, & Carbee, D.L. 1987a. Creep and Strength behavior of frozen silt in uniaxial compression: CRREL Report 87-10. Hanover, CRREL, 67 pp.

Yuanlin, Z, & Carbee, D.L. 1987b. Tensile strength of frozen silt: CRREL Report 87-15. Hanover, CRREL, 23 pp.

Zhestkova, TN. 1982. Formation of the cryogenic structure of soils. Nauka: Moscow: 209 pp. (in Russian).

Appendix: Relaxation Test Minimum Strain Rate

A.1 Overview and Interpretation

In this appendix the relaxation test data is interpreted in the context of a minimum strain rate flow law. This was not included in the main discussion as the approach is not founded on a solid theoretical base. The method is rather a trial approach for applying relaxation data to minimum strain rate interpretations. The conceptual difficulty is that a transient process typical of a relaxation test is being applied to a non-transient creep process (i.e. minimum strain rates). However, the approach shows good empirical correlations with the literature sources and the CSC data presented in this work.

In Chapter 7, the difficulties associated with determination of minimum strain rates from constant stress creep (CSC) tests were discussed. The two main constraints are the large number of undisturbed samples required and large amount of time required. The advantages to the relaxation test approach are that minimum strain rate creep data can be determined from one sample of undisturbed soil. A second test can be run for confirmation. Typical test times range from 300 to 2000 hrs in contrast to the 6 to 12 month period for which the CSC data in this work was collected.

The results from the relaxation tests allow for qualitative and quantitative comparison between soil cryostructure and ice facies. A large number of tests were run on soils with vertical micro-lenticuar cryostructure, soils with horizontal micro-lenticular cryostructure, soils with reticulate-chaotic cryostructure, and soils with remolded-massive cryostructure. In addition to soils, tests were run on wedge ice, Matanuska basal glacial ice, and Matanuska glacial ice. The results add to the information presented in the main chapters of this thesis. The results also allow for the differences in the creep properties in relation to soil and ice textures to be further explored.

Rabotonov (1969) describes an approach which relates a family of creep curves for a given temperature to stress and time. A generalized form of the ageing theory is expressed in Equation A.1.

$$\varepsilon_p = f_1(\sigma)\, f_2(t) \qquad \text{Eq. A.1}$$

Where ε_p is axial strain of sample, $f_1(\sigma)$ is a stress function relating stress to strain, and $f_2(t)$ is the creep-time function. Equation A.1 indicates that the strain for a given point in time is dependent

on the stress path to that point in time. A variant of Equation A.1 can be expressed in terms of strain rate.

$$\dot{\varepsilon} = g_1(\sigma)g_2(t) \qquad \text{Eq. A.2}$$

Where $\dot{\varepsilon}$ is the axial strain rate, $g_1(\sigma)$ is a stress function, and $g_2(t)$ is a creep time function. Figure A.1 conceptually illustrates Equation A.2. For a given stress condition, the strain rate and hence the total strain follows the path characterized by the given loading conditions. Upon a step in the applied stress, the strain rate will change taking the characteristics of the new stress condition. For each subsequent step in the applied stress, the strain rate will change to the new stress condition. The total strain depends on the total stress history. Figure A.2 (a) represents a primary creep condition and Figure A.2 (b) represents a secondary creep or minimum strain rate condition where the strain rate for a given stress is constant. In Equation A.2, the path of the total strain just takes on the strain rate (thus strain) of the current stress condition without a step change in the total strain. It is assumed that the elastic effects resulting from a step in the loading condition are not significant. Generally, the elastic effects are small for frozen soils in comparison to the creep deformation.

One of the most commonly used relationships for creep is shown in Equation A.3.

$$\varepsilon = A\sigma^n t^b \qquad \text{Eq. A.3}$$

Where ε is the uniaxial strain, σ is applied uniaxial stress, t is time, and A, n, and b are empirical coefficients. The strain rate as determined from Equation A.3 is shown in Equation A.4.

$$d\varepsilon/dt = \dot{\varepsilon} = bA\sigma^n t^{b-1} \qquad \text{Eq. A.4}$$

Applying Equation A.4 to Equation A.2, Equation A.5 is determined.

$$\dot{\varepsilon} = bA\sigma^n(t)t^{b-1} \qquad \text{Eq. A.5}$$

The total strain is determined by taking the integral of Equation A.5. The major assumption in this work, for analysis purposes, is that the stress relaxation process represents a minimum strain rate or secondary creep condition. For this situation the coefficient b is equal to 1. In this case, Equation A.5 reduces to Equation A.6.

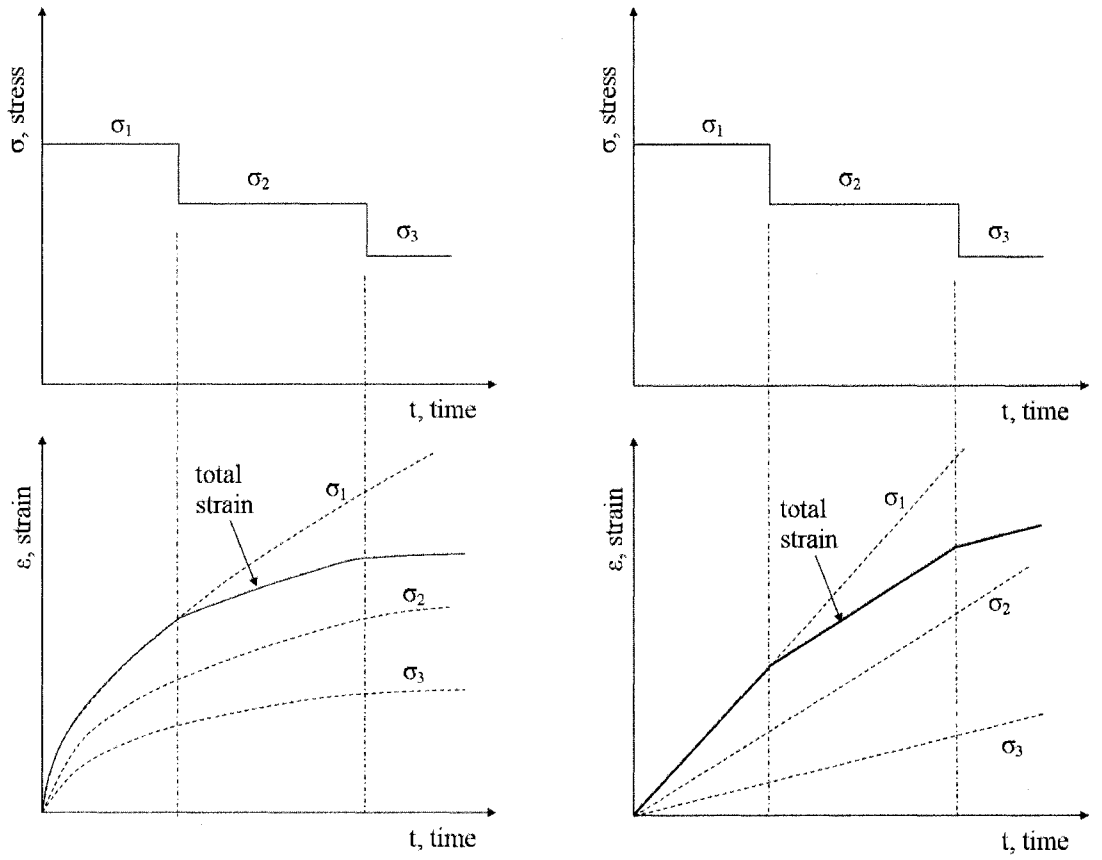

(a) (b)

Figure A.1. Conceptual schematic illustrating the strain rate ageing theory (Equation A.2) for (a) primary creep conditions and (b) secondary creep or minimum strain rate conditions.

$$\dot{\varepsilon} = A\sigma^{n}(t) \qquad \text{Eq. A.6}$$

Where $\dot{\varepsilon}$ is the axial strain rate, σ is the applied stress, A and n are experimentally determined coefficients, and t is time. The condition for Equation A.6 (as applied to Equation A.2) was shown in Figure A.1 (b). The relaxation tests in this work were interpreted directly from Equation A.6.

CSC creep data can supply empirical evidence which partially supports Equation A.2. Figure A.2 shows the strain vs. time and the strain rate vs. time plots for samples no. 5 and no. 17. Sample no. 5 represents a soil with vertical micro-lenticular (vml) cryostructure. As seen in Figure A.2 (a) there are two changes that occur during the course of the test. The first change is a temperature step from -2.11°C to -0.96°C with no change in applied stress of 161.3 kPa. The second change results from a stress step increase from 161.3 kPa to 296.1 kPa with no change in temperature.

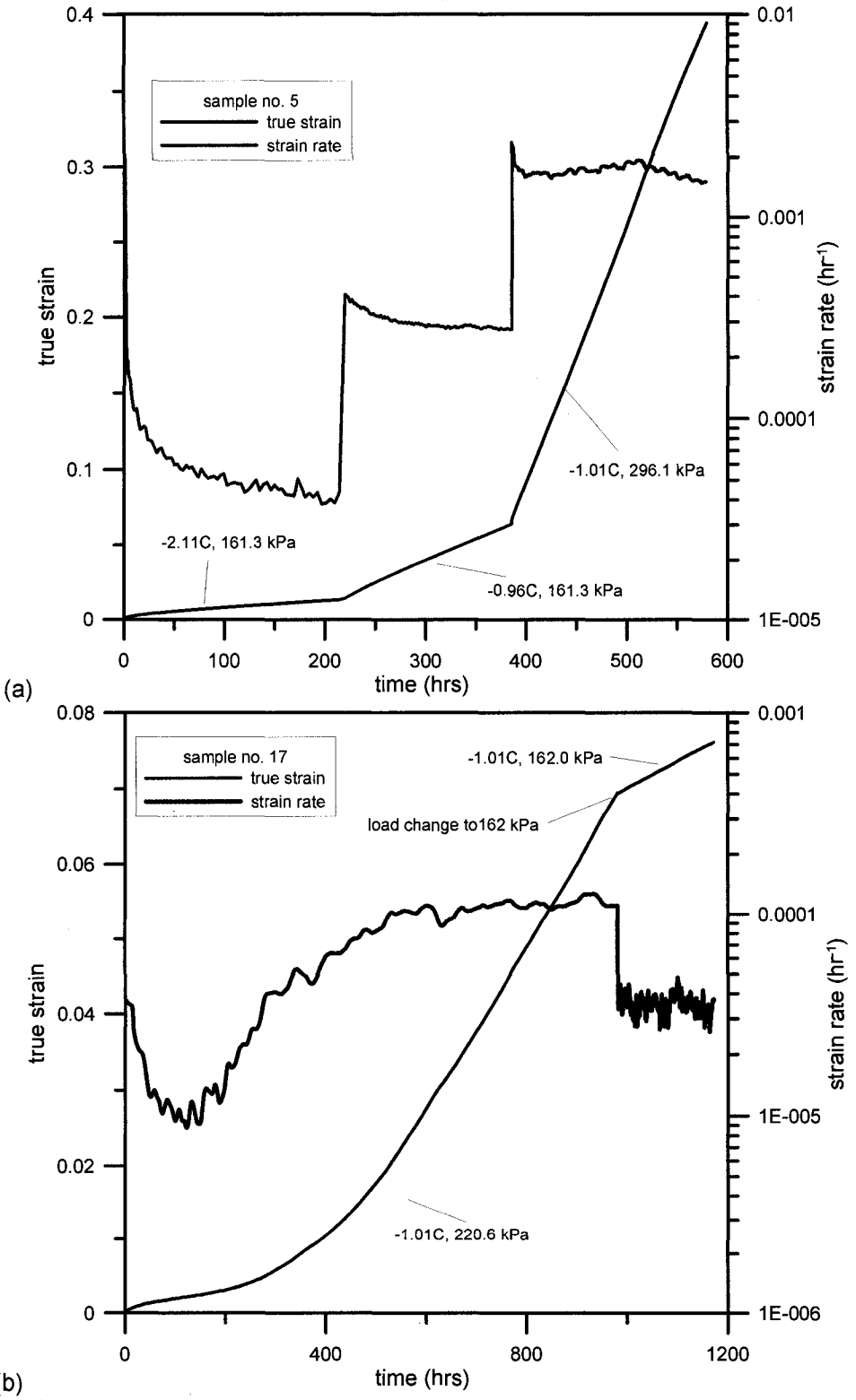

Figure A.2. Strain vs. time and strain rate vs. time for samples no. 5 (soil with vml cryostructure) and no. 17 (Matanuska glacial ice).

For Equation A.2, we are primarily interested in the second step resulting from a step increase in the applied load. With the increase in load, the strain rate jumps rapidly to a new value. The value of the new strain rate remains nearly constant in contrast to a prolonged strain rate reduction with time. The true strain vs. time curve also shows a rapid increase in slope corresponding with the load change. Figure A.2 (b) shows sample no. 17 which is a Matanuska glacial ice sample. As discussed in Chapter 7, the first minimum strain rate, followed by an increase in the strain rate to a second "plateau" is attributed to recrystallization of the ice. At a time close to 1000 hours, the stress level was abruptly lowered. As with sample no. 5, the strain rate rapidly decreases and then remains nearly constant with time. The strain vs. time curve also shows a rapid change in slope at the time of the load change. Figure A.2 supports the validity of applying Equation A.2 and subsequently Equation A.6 for a varying stress condition. A relaxation test performed in this study can be considered as a creep test with a smooth and continuous step change in the applied stress. Also seen in Figure A.2 (or subsequent CSC creep tests) is that the initial reaction to an applied stress is a primary creep condition were the strain rate decreases with time. The validity of applying Equation A.2 to a minimum strain rate or secondary creep condition appears to develop with time and strain. The amount of time required depends on the soil cryostructure and ice facies. This concept holds true for the relaxation test, where the initial portions of the relaxation curve do not correspond to a minimum strain rate condition.

Figure A.3 supplies additional experimental evidence to suggest the validity of the minimum creep rate assumption and thus the applicability of Equation A.6. Figure A.3 compares a relaxation test and a constant strain rate test for Nordale silt. Nordale silt was not described earlier as the data was not presented in this work. The Nordale silt permafrost is organic rich and lies on a raised floodplain of the Chena River, Alaska. The formation of the permafrost layer can be generally described as quasi-syngenetic in cryogenic genesis and is a component of the intermediate layer (Shur et al., 2005). The cryostructure ranges from thick well developed micro-lenticular cryostructure to ataxitic cryostructure (soil blocks suspended in ice). In the North American literature, ataxitic is commonly called suspended. The test temperature was approximately -5.8°C. The samples were obtained from a depth of 50 to 93 cm below the ground surface. A relaxation test was first conducted. Approximately 550 hours into the relaxation test, a linear approximation of the deformation rate was conducted based on the deformation vs. time curve. The deformation rate was approximately 0.00043 mm/hr. A dashed line in Figure A.3 shows the load level from which the deformation rate was determined. A companion sample from the same core was then tested at a deformation rate close to the deformation rate determined for the 550 hour time period of the relaxation test. The constant deformation rate was conducted at a rate of

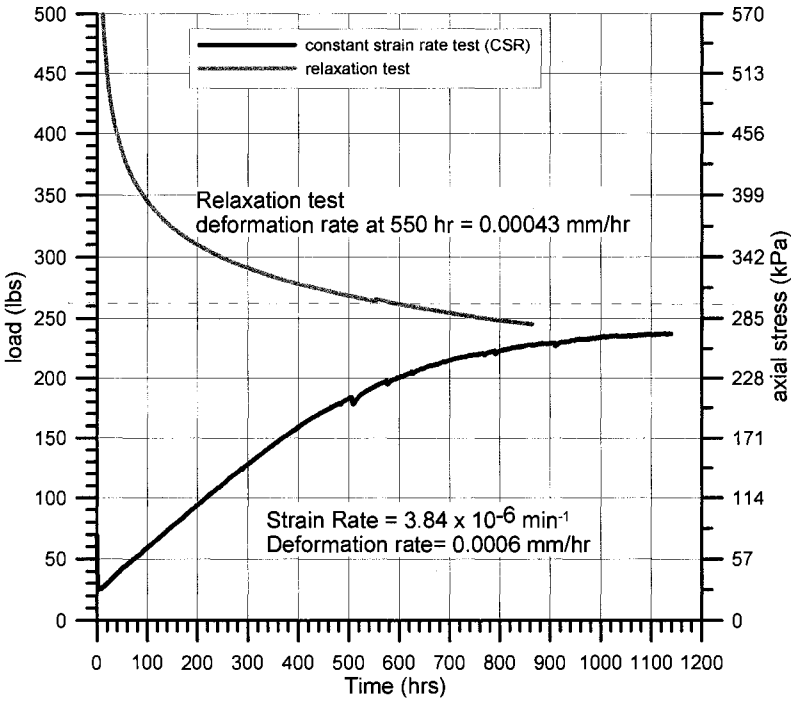

Figure A.3. Comparison between relaxation and constant strain rate (CSR) tests for soils containing Nordale silt with micro-lenticular to ataxitic (soil suspended in ice) cryostructure tested at a temperature of -5.8°C.

0.0006 mm/hr. As seen in Figure A.3, the stress or load is slowly approaching the dashed line. Numerous studies have shown than that the peak stress from constant strain rate tests corresponds to the minimum strain rate for constant stress tests (Ladanyi, 1981;, Hooke et al., 1980, Sego and Morgenstern, 1983, Arenson and Springman, 2005b). Therefore, if the relaxation test is used to approximate a minimum strain rate condition, the peak stress from the CSR test should correspond to the stress value for the 550 hour time period of the relaxation test.

Since the relaxation tests represent a condition where axial strain and stress vary with time, strain rates for a given stress condition can be determined. Figure A.4 shows how the axial strain rate and stress conditions are determined. For a given time, t, the strain rate can be determined from the tangent of the strain vs. time plot. For the same time, t, the stress can be determined from the stress relaxation vs. time plot. The strain rate and stress are then plotted to conform to equation A.6. Figure A.5 shows the axial strain rate vs. stress plotted on a log-log plot for sample no.24. For Equation A.6 to be valid, a linear line is expected. As can be seen in Figure A.5 the resulting data plots as a straight line on the log-log plot. This supplies further evidence for the validity of Equation A.6 as applied to relaxation tests. The coefficients A and n from Equation A.6

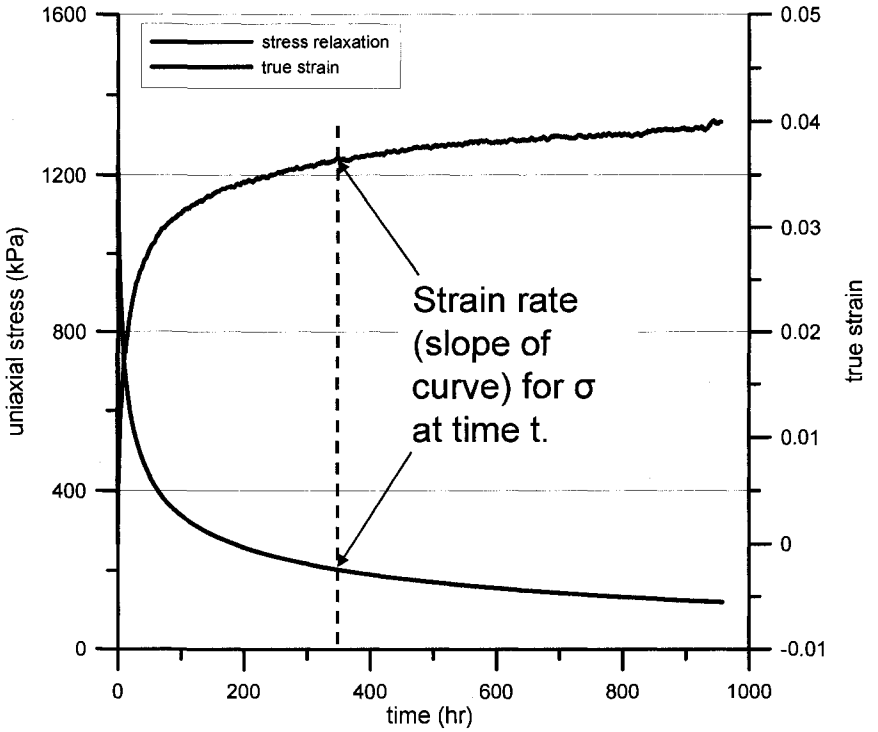

Figure A.4. True strain vs. time and stress relaxation vs. time curves for sample No. 36 (IW, -0.98°C). From these two curves, the strain rate vs. stress relationships are established

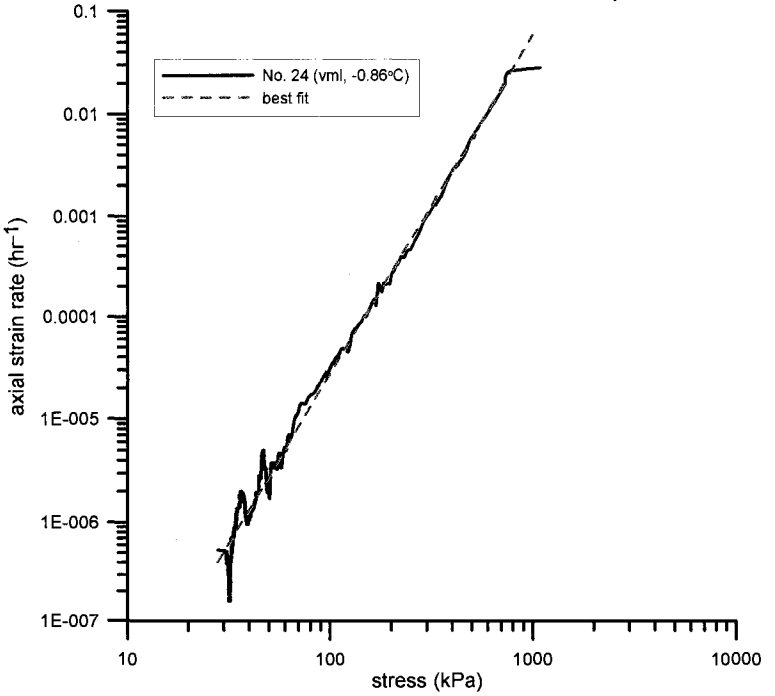

Figure A.5. Log-log plot of axial strain rate vs. axial stress from the relaxation test for sample no. 24 with vml cryostructure.

are determined from the log-log plot. The slope gives the n coefficient and the intercept at log 1 gives the A coefficient. Also shown on the plot is a small deviation from the straight line from approximately 800-1100 kPa. This is commonly seen for the relaxation tests where a straight line power regression may not be seen for the high stresses and initial relaxation interval. However, at lower stresses, the minimum strain rate approximation for Equation A.6 appears valid for most of the samples tested. The creep coefficients A and n are generally not derived from the larger stress intervals unless the data conforms to equation A.6. From an engineering standpoint, using a steady state approximation to interpret the creep coefficients from the relaxation tests should yield conservative results if the relaxation process truly does not represent minimum strain rate conditions. For the lower stress range in Figure A.5, small fluctuations are seen for the data curve. This is common at low strain rates for data presented in this work and work by others (ex. Yuanlin and Carbee, 1987a; McRoberts, 1988). The fluctuations are interpreted as noise.

Tables A.1 and A.2 list the basic gravimetric and volumetric properties for the samples used during the relaxation phase of the testing program (these tables were also shown in Chapter 7). The sample number, sampling description, type of cryostructure or ice facies, and physical properties are indicated in the tables. The samples listed in Tables A.1 and A.2 will be references during the presentation of the results for the minimum strain rate flow laws

A.2 Minimum Strain Rate Flow Law

Utilizing the concepts discussed above, minimum creep rate approximations were applied to the various soils and ice samples that were tested. Tables A.3 to A.5 list the creep coefficients A and n as outlined by Equation A.6. In the tables, the creep coefficients A and n are defined for the stress range cited. Also included is the full stress range experienced by the sample for comparison purposes. This corresponds with the concept described earlier in which the minimum creep rate approximation may not be valid during the initial relaxation period. In addition, nearly all power law empirical fits showed high correlation coefficients. Strain rate vs. stress on log-log plots will be presented for soils with vertical and horizontal micro-lenticulare cryostructure, soils with reticulate-chaotic cryostructure, soils with remolded-massive cryostructure, wedge ice, and Matanuska basal glacial ice, and glacial ice. Samples for a given soil cryostructure and ice facies will be presented for the temperature range tested.

Table A.1. Summary of soil properties for undisturbed permafrost samples tested under relaxation conditions.

No.	Sample	cryostructure	γ_{bf} (lb/ft^3)	γ_{bf} (g/cm^3)	γ_{dry} (g/cm^3)	w_{grav} (%)	$w_{vol,ice}$ (%)
23	PF tunnel 032506 0+98c RWH 3-17 cm	vml	79.7	1.28	0.57	123.1	76.6
24	PF tunnel 032506 0+98c RWH 34-50 cm	vml	80.7	1.29	0.59	118.9	76.4
25	PF tunnel 032506 0+98b RWH	vml	78.2	1.25	0.51	144.8	80.6
26	PF tunnel 032506 ml block CORE 3	hml	82.2	1.32	0.62	111.3	75.4
27	PF tunnel 032506 ml block CORE 4	hml	83.9	1.34	0.65	108.0	75.8
28	PF tunnel 032506 ml block CORE 5	hml	83.3	1.33	0.66	100.8	72.8
29	PF tunnel 032506 ml block CORE 6	hml	81.6	1.31	0.61	115.5	76.1
30	PF tunnel 032506 1+00a RWH	vml	84.0	1.35	0.66	102.8	74.2
31	PF tunnel 121906 2+35 RWH Core a	RC	91.8	1.47	0.84	74.0	68.0
32	PF tunnel 121906 2+35 RWH Core b	RC	93.5	1.50	0.87	71.4	67.8
33	PF tunnel 121906 2+35 RWH Core c	RC	88.4	1.42	0.76	86.2	71.2
34	PF tunnel 121906 2+35 RWH Core e	RC	83.3	1.33	0.62	115.7	77.8
35	PF tunnel IW CORE a	IW	55.8	0.89	0.00	41936	96.9
36	PF tunnel 020207 IW CORE 4	IW	55.9	0.90	0.00	29160	97.0
37	PF tunnel 020207 IW CORE 5	IW	54.8	0.88	0.00	48294	95.2
38	PF tunnel 020207 IW CORE 6	IW	57.2	0.92	0.03	2643	95.9
39	PF tunnel 020207 IW CORE 9	IW	55.4	0.89	0.01	14061	95.8
40	PF tunnel 020207 IW CORE 10	IW	55.9	0.89	0.02	3971	94.9
41	PF tunnel 020207 IW CORE 11	IW	55.9	0.90	0.00	45783	97.2
42	Matanuska Basal ICE CORE 1	BI	69.1	1.11	0.31	259	86.8
43	Matanuska Basal ICE CORE 2	BI	59.1	0.95	0.02	3715	100.2
44	Matanuska Basal ICE CORE 3	BI-micro-lenticular	87.3	1.40	0.76	83.1	69.0
45	Matanuska Glacial Ice CORE 3	GI	57.5	0.92	--	--	--
46	Matanuska Glacial Ice CORE 5	GI	58.2	0.93	--	--	--
47	PF tunnel ml block CORE SM1-conv. relax	vml	75.0	1.20	0.47	157.4	79.9
48	PF tunnel ml block CORE SM2-conv. relax	vml	77.5	1.24	0.50	150.1	81.0

γ_{bf} is frozen bulk density, γ_{dry} is dry density, w_{grav} is gravimetric water content, $w_{vol,ice}$ is the volumetric ice content

Table A.2. Summary of soil properties for remolded samples tested under relaxation conditions.

No.	Sample	cryostructure	γ_{bf} (g/cm^3)	γ_{bf} (g/cm^3)	γ_{dry} (g/cm^3	w_{grav} (%)	$w_{vol,ice}$ (%)
49	PF RM CORE 1	RM	99.5	1.59	1.05	52.5	59.7
50	PF RM CORE 5	RM	97.7	1.57	1.04	50.6	57.2
51	PF RM CORE 6	RM	99.6	1.59	1.06	50.2	58.0
52	PF RM CORE 8	RM	95.9	1.54	1.01	51.5	56.8
53	PF RM CORE 9	RM	95.5	1.53	1.03	48.2	54.1
54	PF RM CORE 10	RM	95.7	1.53	0.98	55.9	59.8
55	PF RM CORE 11	RM	96.5	1.55	1.01	52.4	57.8
56	PF RM CORE 12	RM	96.7	1.55	1.01	52.7	58.1
57	PF RM CORE 13	RM	97.4	1.56	0.99	57.0	61.6
58	PF RM CORE 14	RM	97.3	1.56	1.00	55.5	60.5
59	PF RM CORE 15	RM	95.5	1.53	0.98	55.7	59.5
60	PF RM CORE 17	RM	94.4	1.51	0.96	57.1	59.8
61	PF RM CORE 18	RM	95.2	1.52	0.96	58.6	61.3
62	PF RM CORE 19	RM	96.0	1.54	1.01	51.9	57.1
63	PF RM CORE 20	RM	96.9	1.55	1.00	55.1	59.9
64	PF RM CORE 23-conv. relax	RM	96.5	1.54	0.98	57.9	61.6
65	PF RM CORE 24-conv. relax	RM	100.7	1.61	1.07	50.4	58.8

γ_{bf} is frozen bulk density, γ_{dry} is dry density, w_{grav} is gravimetric water content, $w_{vol,ice}$ is the volumetric ice content

Table A.3. Minimum creep rate coefficients for soils with vertical and horizontal micro-lenticular cryostructure derived from relaxation tests.

No.		T (°C)	σ_{range} (kPa)	n	A ($hr^{-1} \cdot kPa^{-n}$)	r^2	$\sigma_{full\ range}$ (kPa)
23	vml	-0.77	31.6-1000	4.1768	4.302E-14	0.955	31.6-1658
24	vml	-0.86	28-800	3.351	5.922E-12	0.986	28.1-1140.8
25	vml	-2.78	247.7-1000	5.6464	1.807E-19	0.998	247.7-2176.8
26	hml	-0.77	58.2-800	4.3764	5.037E-14	0.956	58.2-1239.3
27	hml	-0.82	58.4-1000	3.9846	4.001E-13	0.977	58.4-1356.3
28	hml	-1.81	151-1000	6.3843	1.614E-20	0.971	151.8-1604.6
	hml	-2.81	198-1000	6.3746	5.720E-21	0.976	198-1750
29	hml	-1.86	150-1000	4.5331	1.395E-15	0.997	150-1650.5
	hml	-2.81	176-1000	4.3882	2.187E-15	0.989	176.3-1869.5
30	vml	-1.82	151-1000	4.7809	2.731E-16	0.992	151.9-1832.1
31	RC	-0.88	70-943	5.4610	7.164E-17	0.983	70.3-1441.7
			200-943	4.1975	1.297E-13	0.994	--
			70-150	7.4608	8.683E-21	0.918	--
31	RC	-2.08	170-1000	7.2740	1.845E-22	0.962	169-1689.6
			500-1000	5.4244	1.097E-17	0.929	--
			170-400	8.1536	7.357E-25	0.662	--
32	RC	-1.85	165-1400	5.5111	4.299E-18	0.974	165-1951.7
			500-1624	3.5824	1.507E-12	0.999	--
			165-300	8.5160	4.722E-25	0.906	--
33	RC	-2.79	230-1500	5.5482	3.674E-19	0.983	230.2-1761.5
			600-1500	4.0359	1.331E-14	0.997	--
			230-500	6.6970	5.310E-22	0.903	--
34	RC	-1.85	127.7-1049	6.0137	3.003E-19	0.959	127.7-1103.8
			400-900	4.2183	3.167E-14	0.996	--
			128-230	9.5550	6.500E-27	0.679	--

note: Eq. A.6, $\dot{\varepsilon}=A\sigma^n$. T is temperature in degrees C, σ_{range} is the stress range from which n and A where determined from relaxation test, n and A are empirical coefficients, and $\sigma_{full\ range}$ is the total range of applied stress experience by the sample over the course of the relaxation test.

Table A.4. Minimum creep rate coefficient for syngenetic wedge ice and Matanuska basal ice and glacial ice derived from relaxation tests.

No.		T (°C)	σ_{range} (kPa)	n	A ($hr^{-1} \cdot kPa^{-n}$)	r^2	$\sigma_{full\ range}$ (kPa)
35	IW	-0.96	128-1300	3.1455	4.563E-13	0.965	127.8-1566.2
36	IW	-0.98	122-1100	3.2103	4.052E-13	0.924	122.6-1226.7
37	IW	-1.86	209-1100	2.6515	1.003E-11	0.993	209.2-1412.1
38	IW	-1.86	201-700	3.0460	1.142E-12	0.972	200.8-1283.2
39	IW	-3.1	160-800	3.3029	3.014E-13	0.994	160.6-1442.2
40	IW	-3.1	129.3-1000	3.5219	1.211E-13	0.977	129.3-1456.2
41	IW	-0.44	207-700	2.5836	1.586E-11	0.996	207.4-936.2
	IW		**AVERAGE**	**3.066**	**4.044E-12**		
43	BI	-1.86	500-900	3.9358	4.230E-13	0.996	88.3-1784.3
			87.1-400	6.7502	2.317E-20	0.968	
			125-700	5.864	2.527E-18	0.991	
44	BI-ml	-1.02	300-1381	3.4195	4.744E-12	0.996	105.8-1642.8
			105-150	12.394	7.600E-32	0.811	
			105-1381	5.1081	8.816E-17	0.956	
45	GI	-1.02	400-887	2.0296	7.055E-08	0.935	56.3-916.9
			56.3-250	5.3753	2.467E-16	0.932	
			56.3-887	4.5567	9.215E-15	0.977	
46	GI	-1.00	300-460	2.8067	1.483E-11	0.995	141.7-518.2
			141.7-300	4.0312	1.278E-14	0.958	
			141.7-500	3.3194	5.907E-13	0.962	

note: Eq. A.6, $\dot{\varepsilon}=A\sigma^n$. T is temperature in degrees C, σ_{range} is the stress range from which n and A where determined from relaxation test, n and A are empirical coefficients, and $\sigma_{full\ range}$ is the total range of applied stress experience by the sample over the course of the relaxation test.

Table A.5. Minimum creep rate coefficients for remolded soils with remolded-massive cryostructure derived from relaxation tests.

No.		T (°C)	σ_{range} (kPa)	n	A ($hr^{-1} \cdot kPa^{-n}$)	r^2	$\sigma_{full\ range}$ (kPa)
49	RM	-1.05	400-1196	5.1533	8.557E-17	0.96	275.9-1423
50	RM	-0.99	350-965	5.3381	3.682E-17	0.997	253.3-1335.4
51	RM	-1.00	400-983	5.4330	2.208E-17	0.995	204-1327.2
52	RM	-1.98	700-1613	7.1053	2.546E-23	0.992	526.7-1613.6
53	RM	-1.99	700-1648	7.1931	1.609E-23	-0.969	505.7-1647.8
54	RM	-3.01	950-1903	7.7974	3.754E-26	0.975	969.2-1903.3
55	RM	-2.99	900-1700	8.3914	5.265E-28	0.958	714.8-1909.3
56	RM	-0.50	200-750	4.2462	1.868E-13	0.992	141.6-1044.8
57	RM	-0.50	225-980.6	4.4396	3.758E-14	0.998	131.5-1049.9
58	RM	-0.30	150-822	3.8380	4.377E-12	0.994	72.7-953.9
59	RM	-0.16	80-700	3.7863	1.094E-11	0.997	14-989.5
60	RM	-4.02	1100-2153	9.0313	8.868E-31	0.982	917.3-2381
61	RM	-4.01	1100-2371	8.2672	2.184E-28	0.982	888.5-2371.2
62	RM	-5.01	1400-2588	8.6396	3.161E-30	0.991	1146.8-2749.8
63	RM	-5.01	1500-2778	7.2155	3.038E-25	0.965	993.6-2520.4

note: Eq. A.6, $\dot{\varepsilon}=A\sigma^n$. T is temperature in degrees C, σ_{range} is the stress range from which n and A where determined from relaxation test, n and A are empirical coefficients, and $\sigma_{full\ range}$ is the total range of applied stress experience by the sample over the course of the relaxation test.

Figure A.6 shows the strain rate vs. stress plots for soils with vertical micro-lenticular (vml) cryostructure. Figure A.6 (a) shows all the relaxation tests for soils with vml cryostructure. As test temperatures decrease, the curves shift to the right which partially correlates to a decrease of the A coefficient. Also seen is a slight increase in the steepness of the slope and thus an increase in the n coefficient with decreasing test temperatures. The curves for samples no. 23 and no. 24, which were conducted under similar temperatures, show some of the inherent variability of testing undisturbed soils. Samples no. 23 and no. 24 were tested for a 2067 hour relaxation period. The stress at the end of the relaxation period was 32 kPa and 28.5 kPa for samples no. 23 and 24 respectively. Figure A.6 (b) shows the individual power law curve and regression for sample no. 24 (test temperature -0.86°C). For the soils with vml cryostructure, a single power law regression fit is typical. High correlation coefficients are common with a high degree of linearity over a large range of stresses

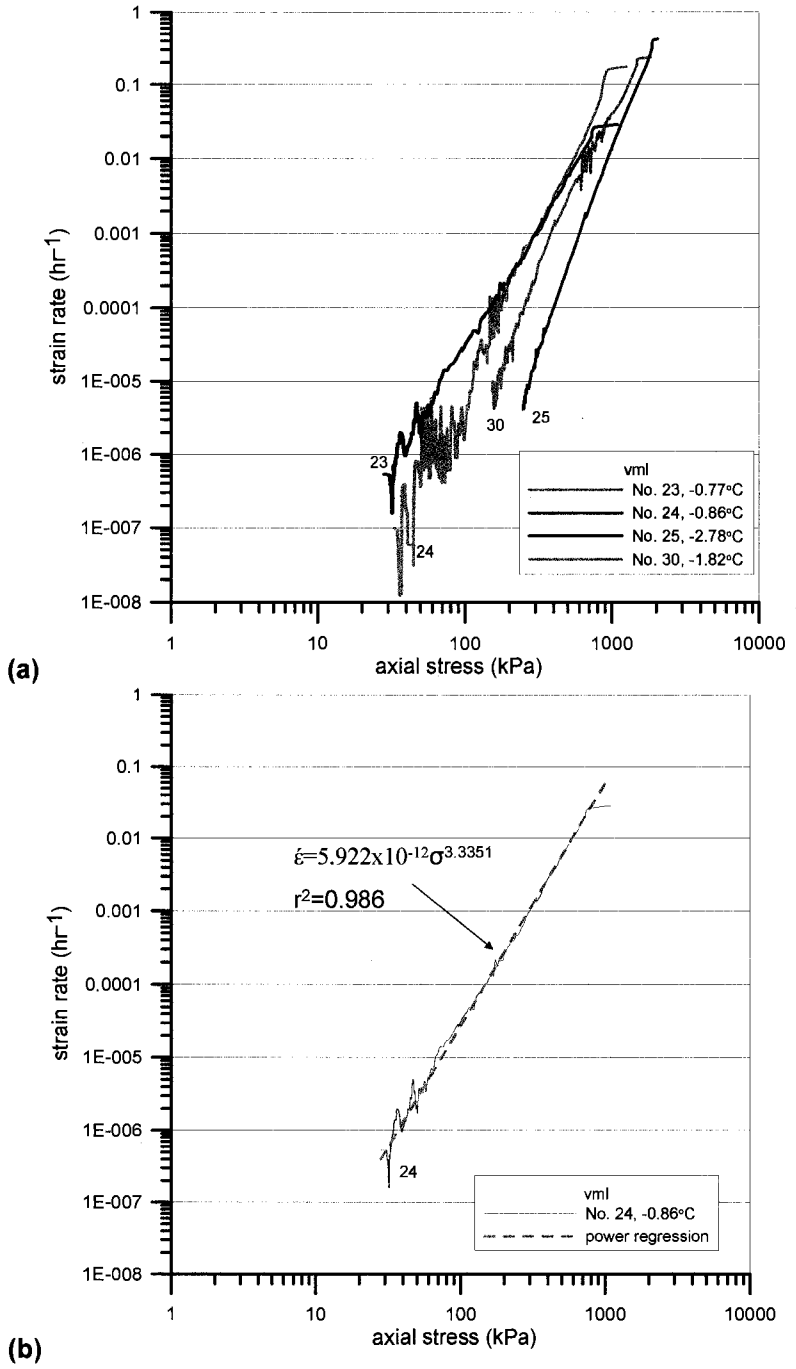

Figure A.6. Minimum strain rate approximation (Eq. A.6) shown for soils with vertical micro-lenticular cryostructure shown on a log-log plot of strain rate vs. stress. Image (a) shows all the vml cryostructures. Image (b) shows a single power fit regression typical for vml soils.

Figure A.7 shows the strain rate vs. stress plots for soil with horizontal micro-lenticular (hml) cryostructure. Table A.3 gives the power law regression coefficients for soils with hml cyrostructure. Figure A.7 (a) shows a select number of data curves for the relaxation tests. As for soils with vml cryostructure, a shift of the curves to the right is seen for decreasing test temperatures. The result of this shift partially relates to the decrease of the A parameter with decreasing test temperatures. There appears to be an increase of the n coefficient (slope of curve) with decreasing temperature. However, sample no. 29 (for both -1.86°C and -2.81°C) has n values close to sample no. 26. Sample no. 28 was tested at the same temperatures as sample no. 29, but higher n values are seen for sample no. 28. Figure A.7 (b) shows a best fit power law regression for sample no. 29 at -1.86°C. The power law regression fits are similar to those for soils with vml cryostructure in that a single regression and high linearity dominates.

Figure A.8 shows the strain rate vs. stress plots for soils with reticulate-chaotic (RC) cryostructure. Table A.3 gives the power law regression coefficients for the soils with RC cryostructure. Figure A.8 (a) shows a select number of strain rate vs. stress relationships. When compared to soils with vml and hml cryostructure (Figures A.6 and A.7), the curves for soils with RC cryostructure show a difference in the relaxation process. The curves for soils with RC cryostructure show a high degree of similarity and a well defined shift to the right with decreasing test temperatures. The curves for soil with RC cryostructure show two approximately linear portions with a small transition between the two segments. The first portion occurs at the higher stresses and the second portion at the lower stresses. Figure A.8 (b) shows the individual data curve and power law regression fits for sample no. 32 (-1.85°C). Comparing the first portion of the relaxation curve (i.e. higher stresses) for all RC samples, the n values range from 3.6 to 4.2 for all temperatures. The exception is sample no. 31 (-2.08°C) which consisted of two loading cycles. The other samples only experienced one loading stage. For the second linear portion, the n values show more variability and range 6.7 to 9.6 for all temperatures. Also included in Figure A.8 (b) is a full stress range best fit power regression. The bilinear nature of the data curves is interpreted to be directly related to the nature and orientation of the ice lenses in the sample.

This bilinear nature was discussed in Chapters 6 and 7. However, a brief discussion will be included here. Soils with RC cryostructure are characterized by well developed ice lenses running at an angle through the samples as shown in Figure 4.12. The axial stress was applied in the vertical direction in relation to Figure 4.12. As a result, the ice lenses are orientated in approximately the same direction as the shear planes which develop under uniaxial stress

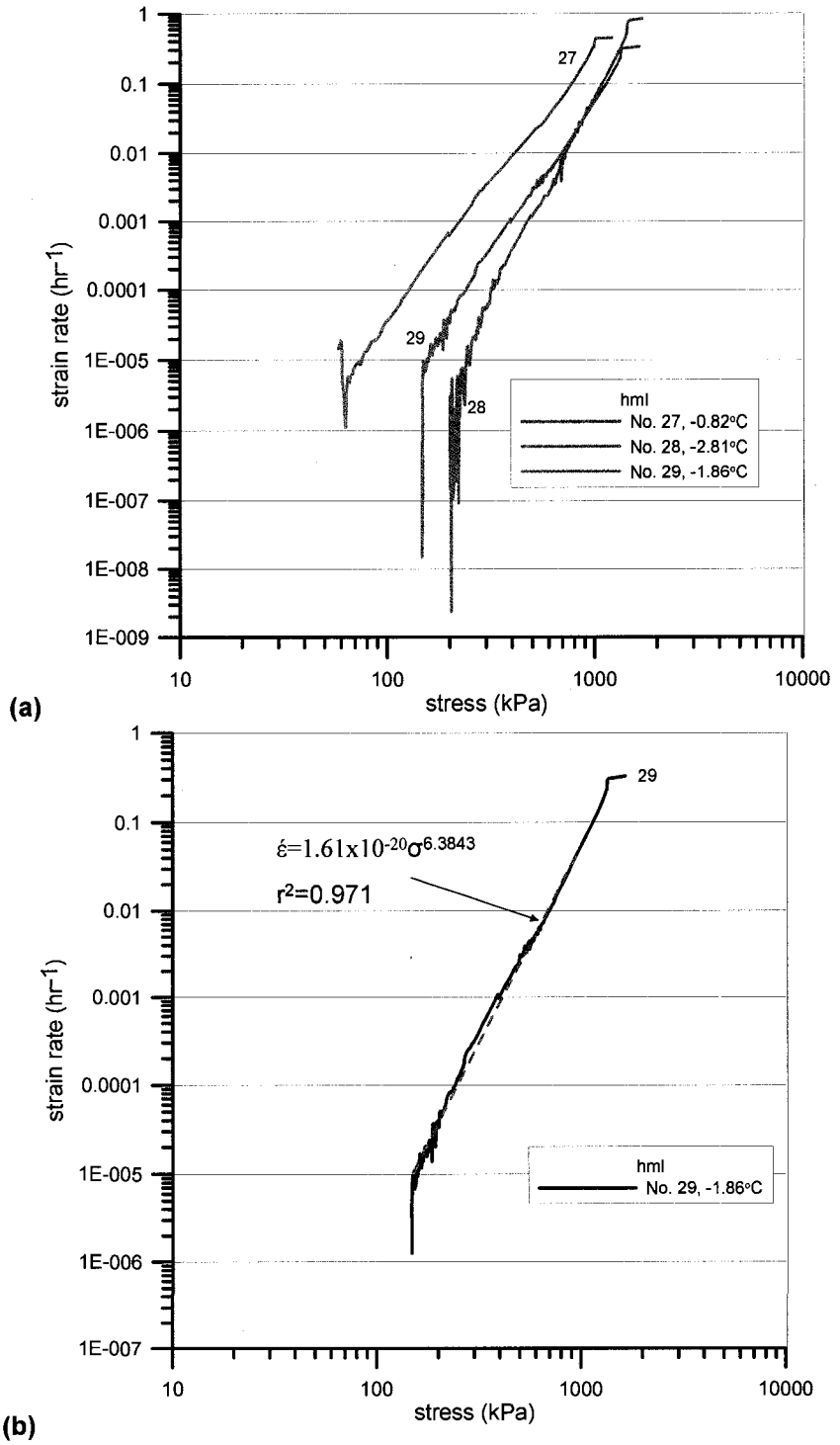

Figure A.7. Minimum strain rate approximation (Eq. A.6) shown for soils with horizontal micro-lenticular (hml) cryostructure shown on a log-log plot of strain rate vs. stress. Image (a) shows a select number vml cryostructures samples. Image (b) shows a single power fit regression typical for hml soils.

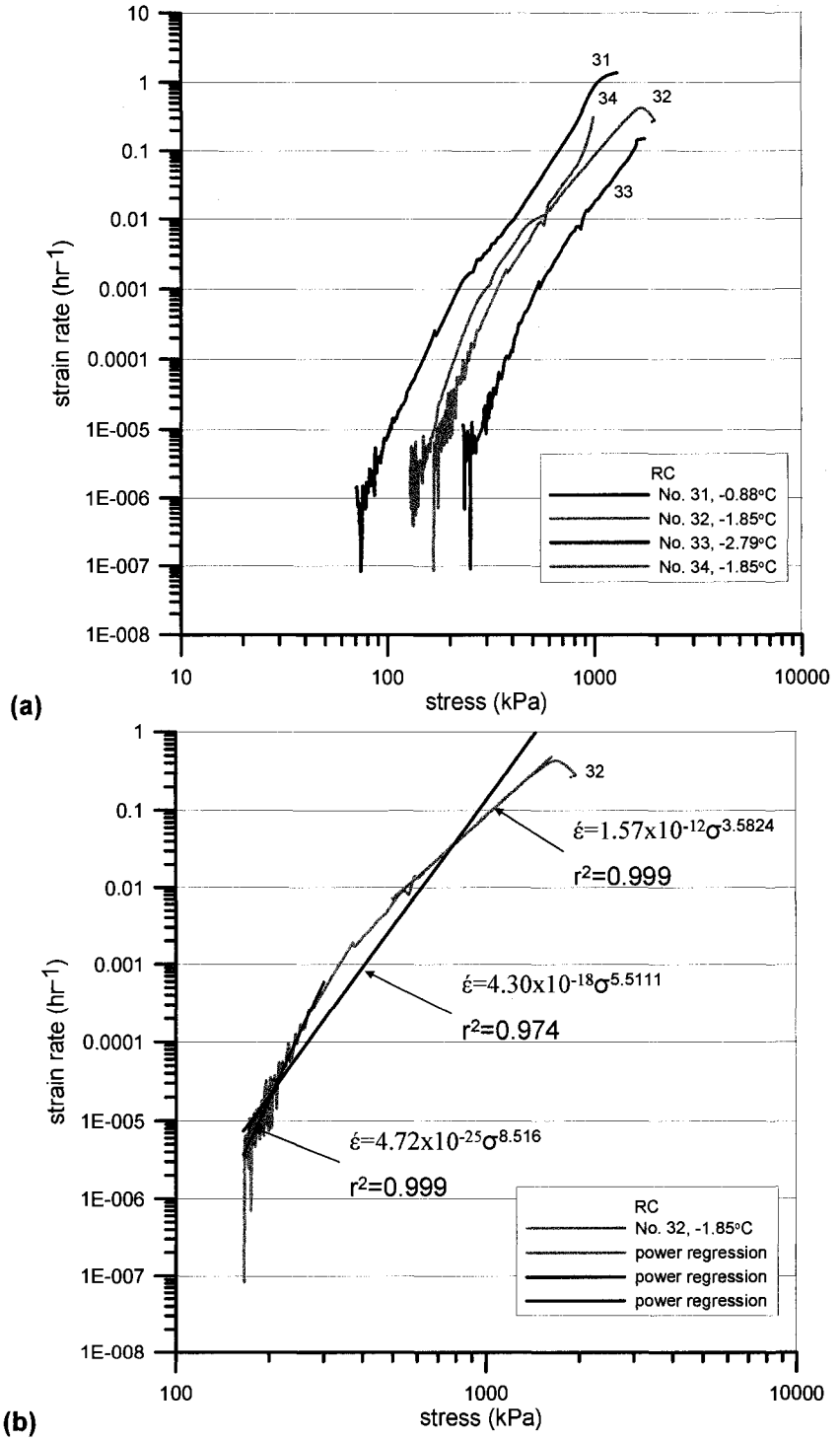

Figure A.8. Minimum strain rate approximation (Eq. A.6) shown for soils with reticulate-chaotic (RC) cryostructure shown on a log-log plot of strain rate vs. stress. Image (a) shows a select number RC cryostructure samples. Image (b) a bilinear power regression fit in addition to a full stress range average fit.

conditions. The first linear portion of the data curves are therefore interpreted as creep along the orientated ice lenses. The values of the n and A coefficients compare favorably to those for ice tested in this study and thus suggest that creep of ice is the dominating mechanism. The soil between ice lenses tends to be relatively ice poor in comparison to the other silt cryostructures such as micro-lenticular cryostructure. The n values for the second linear portion of the data curve tends to correlate more closely with the values for remolded-massive (RM) cryostructure tested in this study and for remolded massive silts tested by Yuanlin and Carbee (1987a). Therefore, the mechanism for the second linear portion is interpreted to be dominated by creep in the massive silts located between ice lenses.

Figure A.9 shows the strain rate vs. stress curves for select samples of soil with remolded-massive cryostructure. Table A.4 gives the power law regression coefficients A and n (Eq. A.6). As seen in Figure A.9 (a), an obvious shift to the right occurs for decreasing test temperatures. The largest shifts occur for test temperatures ranging between -0.3°C to -2°C. A smaller shift occurs from -2°C to -3°C. From -3°C to -5°C, the shift occurs at approximately equal increments. The n coefficient increases with decreasing temperature to about -3°C. Further decrease in temperatures to -4°C and -5°C did not result in further decrease of n coefficient. The n coefficient referred to was determined from the first linear portion of the data curve as shown in Figure A.9 (b). In chapter 4 (Figure 4.22 and Table 4.4) it was shown that the most significant changes in unfrozen water content occur between 0°C and -3°C. Therefore, the nature or quantity of unfrozen water appears to influence the creep behavior. In Figure A.9 (b), the data curve and power regression are shown for sample No. 51 (-1.00°C). As seen for soils with RC cryostructure, the data curves show a linear segment at higher stresses which then transitions into a pseudo linear segment for the lower stress section of the curve. The best fit power regressions were not shown for the bottom portions of the curves in Table A.4. However, the bottom linear regression is shown in Figure A.9 (b) to demonstrate the magnitude of the power equation. The resulting coefficients for the lower section are A is equal to 7.10×10^{-203} and n is equal to 79.9386. The n values for the second linear segment decrease for warmer temperatures and increase for colder temperatures. The A coefficients for the second linear segment increase for warmer temperature and decrease for cold temperatures. However, from a practical standpoint, the value of A and n are sufficiently large that the strain rate for a given stress, drops so rapidly it can be assumed that further deformation is essentially zero. Based on this concept, the transition into the steep section of the curve is can be interpreted as the activation of a long term strength resistance within the soil. Therefore, this portion is not interpreted as a minimum strain rate condition, but rather represents a damped creep regime. In Chapter 6, it was shown

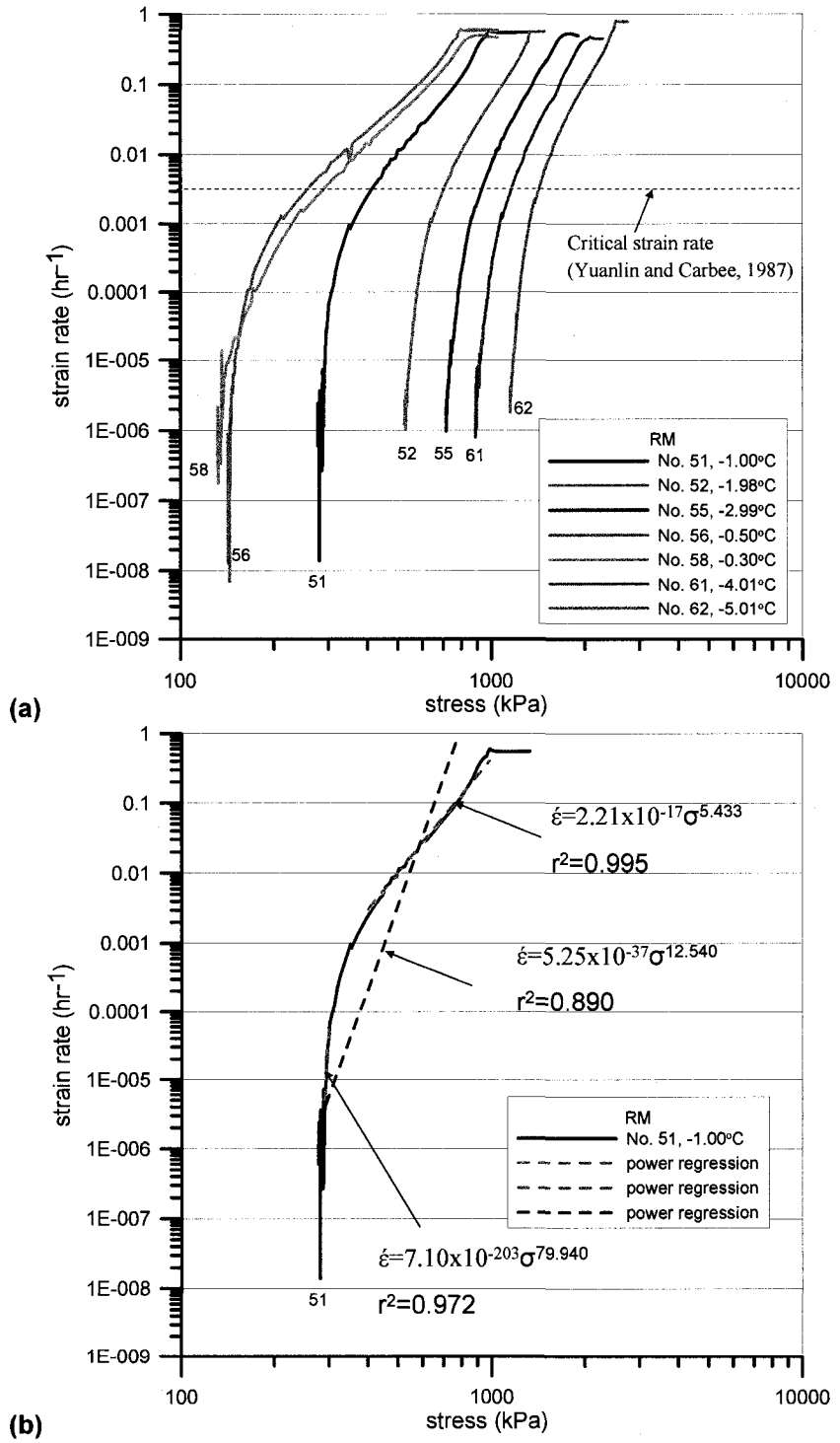

Figure A.9. Minimum strain rate approximation (Eq. A.6) shown for soils with remolded-massive (RM) cryostructure shown on a log-log plot of strain rate vs. stress. Image (a) shows a select number RM cryostructure samples. Image (b) a bilinear power regression fit in addition to a full stress range average fit.

that the long term strength of soil with remolded-massive cryostructure is considerably higher than the undisturbed permafrost soils.

Yuanlin and Carbee (1987a) reported a change in slope on log-log plots of strain rate vs. stress for remolded Fairbanks silt at what they defined as a critical strain rate equal to $1x10^{-6}$ s^{-1}. This corresponds to a strain rate of 0.0036 hr^{-1}. In Figure A.9 (a), a dashed line was inserted which corresponds to this critical strain rate. Interestingly, the data curves in this work also appear to change slope at strain rates close to that identified by Yuanlin and Carbee (1987a). Also evident in their work is a gradually lessening of the critical strain rate for temperature of -1°C or warmer.

Figure A.10 shows the strain rate vs. stress curve for select samples of syngenetic wedge ice. Table A.5 gives the power law regression coefficients A and n (Eq. A.6). Figure A.10 (a) shows the data curves for a range of test temperatures. As compared to the frozen soils tested, the data curves tend to group together rather than shift with decreasing test temperatures. The initial applied stress varied about 500 kPa between the lowest and highest applied stress. Despite the initial load, the same trend is seen for nearly all samples. The A and n coefficients are similar for the temperature range tested. For the temperature range tested (-0.44°C to -3.10°C) the value of n ranged from 2.6 to 3.5. The value of A ranged from $1.56x10^{-11}$ to $4.563x10^{-13}$ ($kPa^{-n}\cdot hr^{-1}$). Since the data is grouped, the mean n and A value can be determined to be 3.066 and $4.044x10^{-12}$ ($kPa^{-n}\cdot hr^{-1}$). Generally for polycrystalline ice, n is assumed to be equal to 3 (Glen, 1955; Morgenstern et al, 1980; Sego and Morgenstern, 1983, Sinha, 1982). Morgenstern et al. (1980) reports an A value of $2.283x10^{-12}$ ($kPa^{-n}\cdot hr^{-1}$) for polycrystalline ice. The mean values for wedge ice determined in this study agree well with the reported values for polycrystalline ice. Figure A.10 (b) shows the data curve and power fit regression for sample no. 38 (-1.86°C). Minimum creep rate power law approximations do not conform to the wedge ice relaxation process for the higher stresses, as seen during the initial relaxation. As the relaxation process continues, a single power law regression fit can be applied to the data curve.

Figure A.11 shows the strain rate vs. stress curve for Matanuska basal ice (BI) and Matanuska glacial ice (GI). Table A.5 gives the power law regression coefficients A and n (Eq. A.6). Figure A.11 (a) presents the Matanuska BI and GI data curves. Samples no. 44, 45, and 46 are concentrated around -1°C. Sample no. 43 was tested at -1.86°C. A range of responses were seen. Sample no.43 has a suspended/dispersed cryostructure which consists of particles suspended in ice. The volume of ice was nearly 100%. For a stress range of 500-900 kPa, the sample had an n value equal to 3.94 and an A value of $4.23x10^{-13}$ ($kPa^{-n}\cdot hr^{-1}$). One would expect

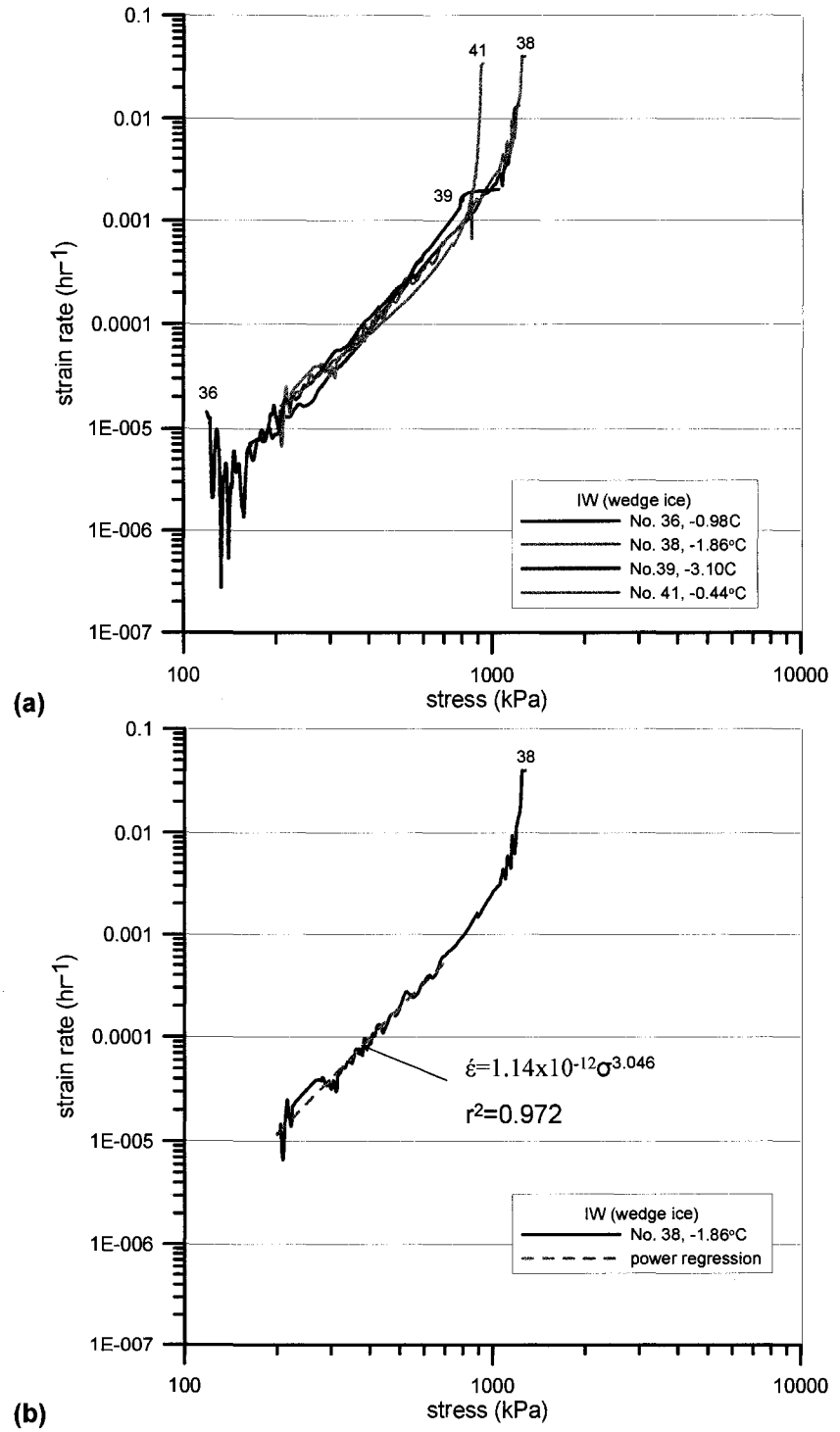

Figure A.10. Minimum strain rate approximation (Eq. A.6) shown for syngenetic wedge ice (IW) shown on a log-log plot of strain rate vs. stress. Image (a) shows a select number IW samples. Image (b) a single power regression typical for wedge ice.

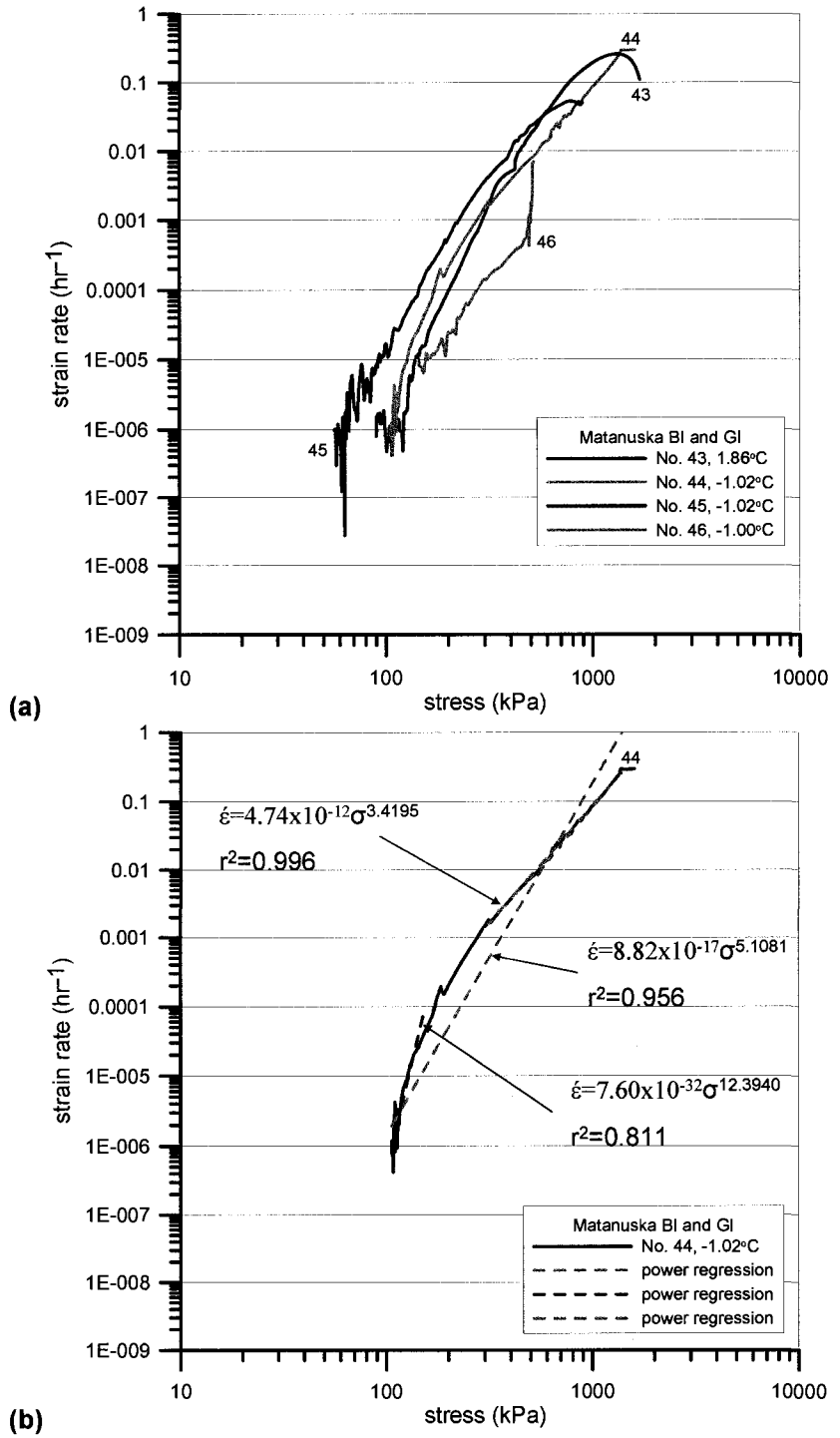

Figure A.11. Minimum strain rate approximation (Eq. A.6) shown for soils with Matanuska basal ice (Mat. BI) cryostructure and Matanuska glacial ice (Mat. GI) shown on a log-log plot of strain rate vs. stress. Image (a) shows a select number Mat. BI and GI samples. Image (b) shows a bilinear power regression fit in addition to a full stress range average fit for sample no. 44.

slightly lower value for such high ice contents but they are within range. However, at lower stresses, the value of n and A increase noticeably and correspond to an increase of the curve slope. Post analysis of the sample shows fracture cracks as evidenced by wing cracks on the outer surface and internal cracks concentrated along the interior central region. It is assumed that the resulting fracture raised the n and A values. Sample no. 44 has a well developed, slightly inclined micro-lenticular cryostructure. The micro-lenticular ice lenses range up to 0.5 mm in thickness to 1 to 2 cm in length. Sediment fabric runs at an angle close to 45° to the long axis of the core. Figure A.11 (b) shows the data curve and associated best fit power regressions for sample no. 44. From approximately 300-1400 kPa, the data curve can be approximated by a linear regression. The resulting n and A coefficients are similar to the those found for wedge ice and soils with micro-lenticular cryostructure for similar test temperatures. However, the lower portion of the curve (i.e. lower stresses) appears similar to those seen for soils with remolded-massive cryostructure in which the slope continues to increase, thus the values of n and A increase with decreasing stress. Visual observation shows a slight sand fraction within the core. As with the soils containing remolded-massive cryostructure, this affect is interpreted as activation of a long term strength mechanisms. Sample no. 45 is a glacial ice core. The resulting curve is similar to sample no. 43. Post analysis reveals a similar internal fracture pattern. Sample no. 46 is a Matanuska glacial ice sample. In response to sample no. 45, the initial load was reduced. The resulting data curve is similar to the trend seen for wedge ice. The n and A coefficients are closer to the expected values for a stress range of 142-500 kPa.

Summarizing the results, some general observation can be made. For certain soils and wedge ice, a single power law regression could be applied over a given stress range after the initial stress reduction. For soils with reticulate-chaotic cryostructure, the log-log plot of strain rate vs. stress generally yields two linear portions which can describe a bilinear power law. A small transition exists between the two linear portions. A full range power fit is also supplied for comparison purposes. Soils with remolded-massive cryostructure generally contain a linear portion (on the log-log plot of strain rate vs. stress) during relaxation at higher stresses. At a certain threshold, the slope starts to increase noticeably which is interpreted as the activation of a long term strength mechanism. The creep coefficients for Equation A.6 for the various soil cryostructures and ice facies are listed in Tables A.3 to A.5.

A.2.1 Minimum Strain Rate Cryostructure Comparison

In the previous section, interpretation of the relaxation based on a minimum strain rate relationship in the form of a power law of the Glen type was explored. In this section, a brief comparison of the minimum strain rate relaxation curves for various soil cryostructures, wedge

ice, and Matanuska ice will be made by grouping samples with temperatures near -1°C, -2°C, and -3°C.

Figure A.12 shows the relaxation data plotted as the strain rate vs. stress for select samples near -1°C. The curves suggest that the frozen soil tested creeps at a faster rate for given stress than ice samples, which in this case includes wedge ice (no. 36) and glacial ice (no. 46). Above 300 kPa, a similar creep rate response is seen for the undisturbed soils. Extrapolating the strain rate-stress relationship for ice samples (no. 36 and 46) to stresses lower than 100 kPa, the creep rates appear higher than for soils with RC cryostructure (no 31) and basal ice with micro-lenticular cryostructure (no. 44). The data suggests that for silty soils with micro-lenticular cryostructure, the creep rates remain higher than for the ice samples when extrapolated to stresses below 100 kPa. Figure A.13 shows the relaxation data plotted as the strain rate vs. stress for select samples near -2°C. The same basic trend is seen where the undisturbed frozen soils show greater creep rates of a given stress than wedge ice. However, at approximately 200 kPa, the strain rates for wedge ice are of the same magnitude for a given stress as the undisturbed soils. Extrapolating to stresses lower than 200 kPa, the data suggest that wedge ice shows greater creep rates than the frozen soils. The strain rate response for soils with vml, hml, and RC cryostructures appears similar. As the test temperatures approach -3°C, the difference between the undisturbed soils and wedge ice diminishes as shown in Figure A.14. Between 200 and 400 kPa, the strain rate for ice is greater than or equal to the strain rate for the undisturbed frozen soils. Below 200 kPa, wedge ice shows higher creep rates for a given stresses than the frozen soils. Soils with hml cryostructure (no. 28 and 29) show higher strain rates than soils with vml cryostructure for a given stress (no. 25).

Figures A.12 through A.14 suggest that as the soil temperature increases or warms, the creep response (or creep rates) for a given stress increases as compared to wedge ice or ice. As the stress lowers, the creep rates for wedge ice and undisturbed permafrost soils more closely correlates. It is anticipated that, for colder temperatures, the creep rates for ice would be greater than for undisturbed ice-rich soils. The data also suggest that at lower stresses (less than 100-200 kPa), the creep rates for wedge ice are equivalent or greater than the undisturbed soils for all temperature ranges tested. This same trend was seen by Pekarskaya (1965), where ground ice showed lower creep rates for higher stresses. At lower stresses, ground ice showed higher creep rates. Pekarskaya (1965) showed that this transition occurred approximately between 200-240 kPa for ground ice and frozen clay at -1°C. For undisturbed frozen soils (vml, hml, and RC), the creep rates for soils with hml and RC cryostructure were equivalent or greater than for soils with

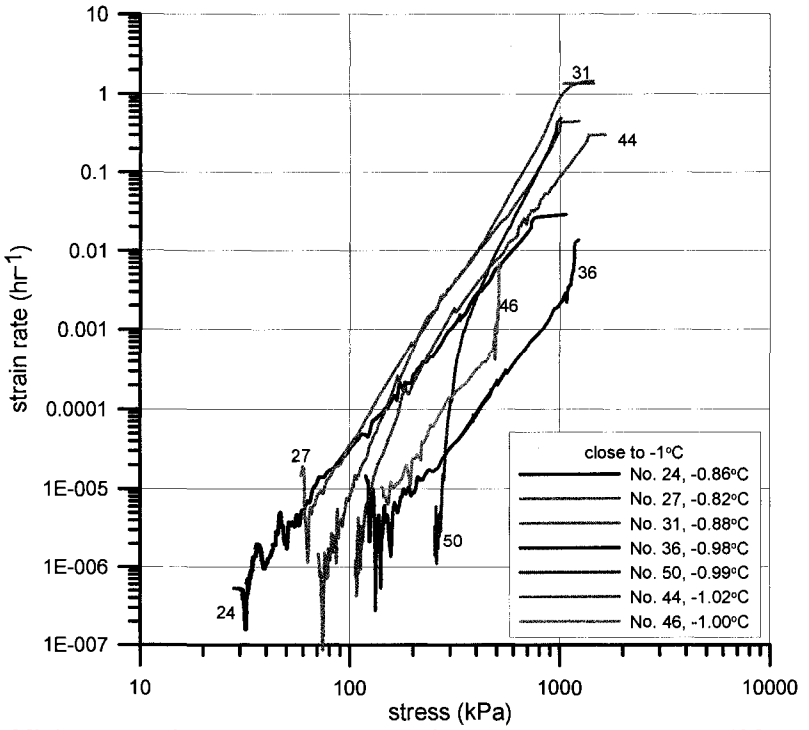

Figure A.12. Minimum strain rate approximation for tested samples near -1˚C.

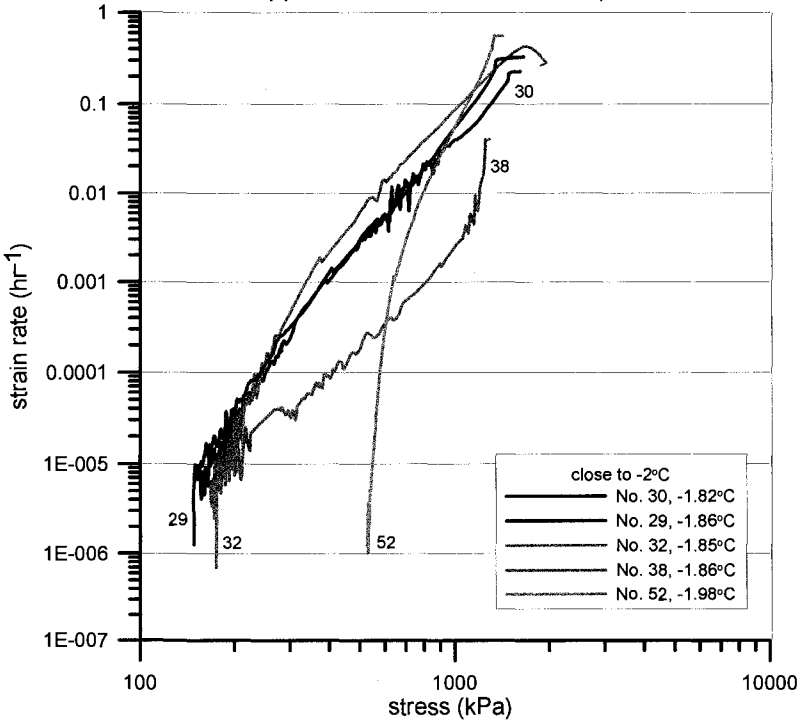

Figure A.13. Minimum strain rate approximation for tested samples near -2˚C.

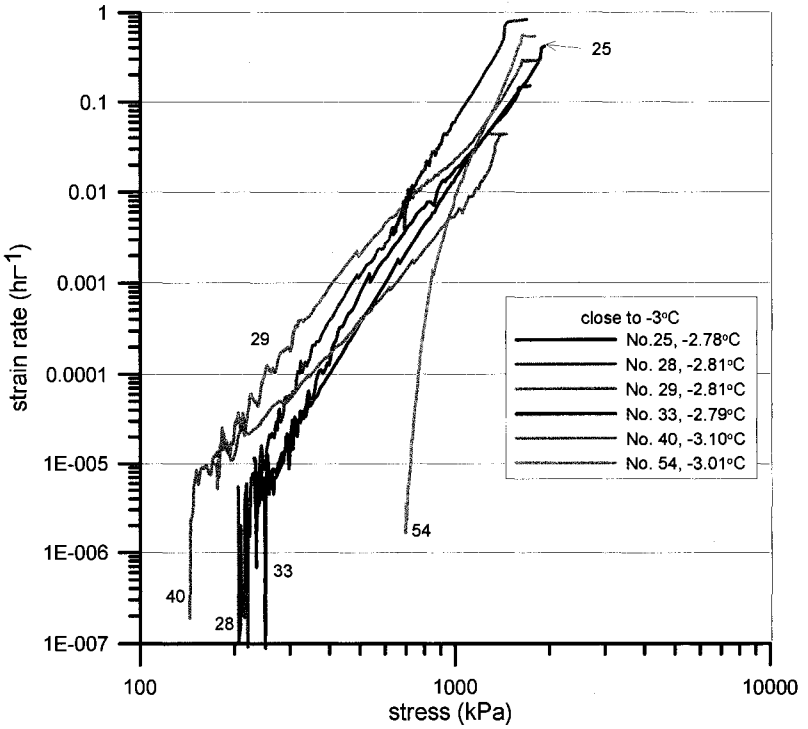

Figure A.14. Minimum strain rate approximation for tested samples near -3˚C.

vml cryostructure at stresses greater than approximately 200 kPa. Pekarskaya (1965) showed that clay with massive cryostructure exhibited higher creep rates for a given stress condition than icier soil cryostructures (i.e. cellular and stratified cryostructure). McRoberts (1988) suggests that at temperatures warmer than -1.5˚C, permafrost soils can creep at a faster rate than for ice. At temperatures colder than -2˚C, the flow law for ice offers an upper bound for soil creep. The apparent tendency for frozen soils to creep at a faster rate than ice for warm temperatures is likely linked to the quantity of unfrozen water.

A.2.2 Temperature and Ice Influence

The power law relationship for strain rate as function of stress was expressed in Equation A.6. Nixon and McRoberts (1976) reported that the empirical coefficients A and n (Eq. A.6) are a function of temperature for polycrystalline ice. Arenson and Springman (2005b) reported for CSC and CSR tests on rock glacier specimens that A is function of temperature and ice content and n is a function of ice content. The most common method for relating the creep coefficients to temperature is through the empirical (T+1) relationship (Vialov, 1959; Nixon and McRoberts, 1976). Nixon and McRoberts (1976) report that both A and n can be related to temperature by a simple power law where

$A, n = f(T+1)$ Eq. A.7

The relationship can be determined by plotting log A vs. log (T+1) and log n vs. log (T+1). T is the absolute value of the number of degrees below °C. Figures A.15 and A.16 show the relationships between coefficients A and n as function of (T+1). The data shows apparent trends with temperature. The value of A decreases with colder temperatures and n increases with colder temperatures. However, the data also shows considerable scatter making interpretation difficult. In addition to the temperature trends, the effects of cryostructure (and massive ice) can be seen by the grouping of data based on soil cryostructure. The empirical relationships for A and n as a function of temperature are presented in Table A.6. Caution should be exercised when applying these equation as the correlation coefficient are low for soils with hml and RC cryostructure and IW due to the high data scatter. Good correlations are found for soils with vml and RM cryostructures.

The minimum strain rate is correlated to temperature by utilizing the (T+1) empirical relationship (McRoberts, 1988; McRoberts et al., 1978) and is presented in Equation A.8.

$$\dot{\varepsilon} = \frac{A \cdot \sigma^n}{(T+1)^m} \qquad \text{Eq. A.8}$$

Where T is the absolute value of the number of degrees below 0°C and m is an experimental coefficient. Equation A.8 implies that n is not a function of temperature. A is considered a function of temperature. By plotting log A vs. log (T+1), the parameter m is determined by the slope of the curve. The power exponents from the empirical expressions for the creep coefficient A in Table A.6, supply the m exponent in Equation A.8. Nixon and McRoberts (1976) suggest an m value ranging from 1.9 to 2.4 for polycrystalline ice. McRoberts (1978) used an m value (assumed for ice) of 1.8, which was applied to CSC creep data for ice-rich Norman Wells silt. McRoberts (1988) used an m value of 2.0 for temperatures warmer than -1.5°C and an m value of 1 for temperatures colder than -2°C. It was assumed that the m value of frozen silt (or frozen ice-rich soils) would conform to the values determined for ice. In this work, wedge ice is the closest representative to polycrystalline ice. The m value for wedge ice is 2.6, which is realistic as compared to the available literature. The m values for the frozen soils in this work are considerably higher than suggested in the literature. The m values for the various cryostructures

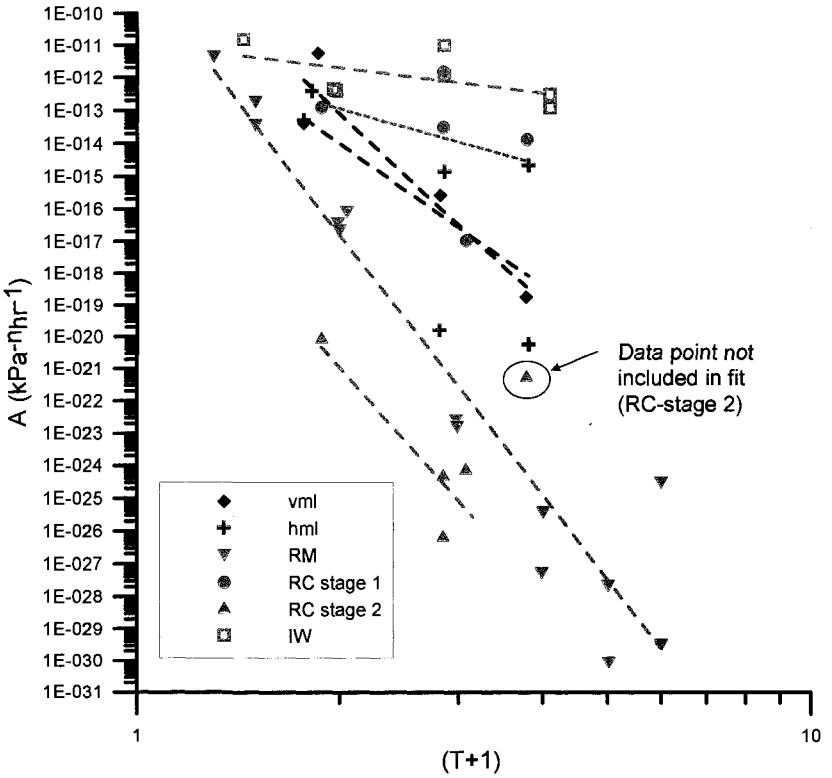

Figure A.15. Temperature relationship for A coefficient (Eq. A.6).

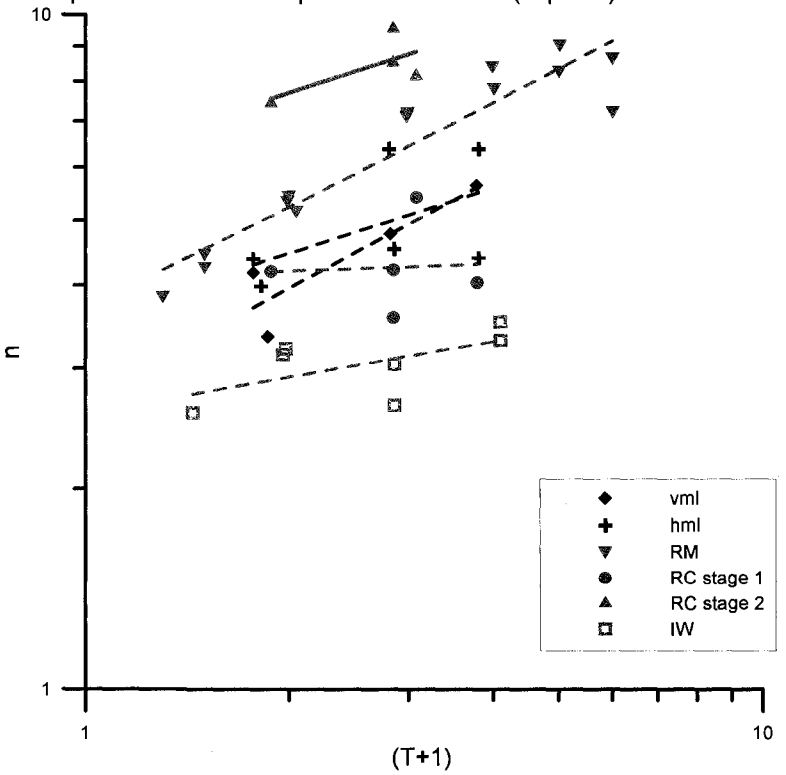

Figure A.16. Temperature relationship for n coefficient (Eq. A.6).

Table A.6. Empirical power regression fits for coefficients A and n from Eq. A.6 and Figures A.15 and A.16.

cryostructure/sample	A ($kPa^{-n} \cdot hr^{-1}$)	r^2	n	r^2
vml	$5.4613x10^{-8} \cdot (T+1)^{-19.317}$	0.886	$2.7170 \cdot (T+1)^{0.544}$	0.790
hml	$2.3861x10^{-10} \cdot (T+1)^{-14.568}$	0.414	$3.5600 \cdot (T+1)^{0.327}$	0.289
RM	$1.8596x10^{-9} \cdot (T+1)^{-26.851}$	0.922	$3.6882 \cdot (T+1)^{0.5070}$	0.889
RC - stage 1	$5.9405x10^{-12} \cdot (T+1)^{-5.736}$	0.109	$4.0950 \cdot (T+1)^{0.036}$	0.003
RC –stage 2*	$1.4894x10^{-14} \cdot (T+1)^{-23.559}$	0.787	$7.7270 \cdot (T+1)^{0.179}$	0.472
IW	$1.2215x10^{-11} \cdot (T+1)^{-2.606}$	0.313	$2.5828 \cdot (T+1)^{0.175}$	0.368

A and n are empirical coefficients in Eq. A.6- (i.e. $\dot{\varepsilon}=A\sigma^n$). T is the temperature in °C of absolute value of the number of degrees below 0°C.
*One data point not included in regression (RC stage 2).

are 19.3 for vml, 14.6 for hml, 26.9 for RM, 5.7 for RC stage 1, and 23.6 for RC stage 2. The validity of the m values presented is unknown. Using CSC power law data for soils with vml cryostructure (Chapter 7), the results agree with values derived from relaxation tests for estimation of the m value. The values from CSC data used for comparison were derived from minimum or steady state relationships from Figure 7.5 (-1°C) and the relationship from Figure 7.6 (-2°C). This does lend credibility to the results. The significant scatter for some of the data sets makes interpretation difficult. Modification of a few data points can bring the slope of the A vs. (1+T) plots in line with wedge ice. A larger data set would help to clarify the results. Therefore caution should be used when exercising the supplied relationships. Using an m value for ice (or wedge ice) should act as a conservative estimate for temperatures colder than -1°C.

In their work on remolded Fairbanks silt, Yuanlin and Carbee (1987a) used a temperature factor to express the creep exponent n as a function of temperature. The temperature factor is simply the test temperature (θ) divided by -1°C (θ_{-1}). By plotting the log of n vs. log of (θ/θ_{-1}), a simple power law expression for n can be determined. For the soils with RM cryostructure used in this program, n as a function of the temperature factor is shown in Equation A.9.

$$n=5.4516\left(\frac{\theta}{\theta_{-1}}\right)^{0.3001} ; r^2 = 0.930 \qquad \text{Eq. A.9}$$

Yuanlin and Carbee (1987a) for short term creep defined the n exponent with Equation A.10.

$$n=5.59\left(\frac{\theta}{\theta_{-1}}\right)^{0.223};r^2=0.943 \qquad \text{Eq. A.10}$$

The similarity of the two relationships is quite good. The second stage relationships for soils with RM cryostructure were not compared as a large degree of variability exists in regard to n and A values. No relationship is included for A vs. the temperature factor as A is already defined for (T+1) in Table A.11. The similarity of the n relationships, combined with the transition at a similar critical strain rate (Figure A.9), lend support to the validity of the minimum creep relationships for the remolded silts with massive cryostructure (RM).

Figures A.17 and A.18 show the relationships between the creep coefficients A and n as a function of volumetric ice content and temperature. As can be seen, there is a good relationship with volumetric ice content. Included in the plots are soils with vml, hml, and RM cryostructure along with wedge ice. These soils types and ice types represent the greatest degree of homogeneity. Soils with RC cryostructure were not included as the ice lenses highly influence the deformation behavior. The relationship with volumetric ice content is presented here with some hesitance. One of the main foci of this work was to bring into focus the potential role of cyrostructure and thus ice patterns. By grouping the ice patterns simply into volumetric ice contents, it is possible to lose sight of the ice structure. However, for frozen soils that contain a uniformly distributed ice matrix it may be possible to simply use a volumetric ice relationship as shown.

The affect of temperature was discussed previously, but is well illustrated as temperature isotherms for volumetric ice content relationships (Figures A.17 and A.18). The creep coefficient A is plotted as log A vs. volumetric ice content in Figure A.17. A distinct difference is seen for the -1°C isotherm as compared to the -2°C and -3°C isotherms. As the temperature proceeds from -2°C to -3°C, the magnitude of change reduces. The creep coefficient n is plotted as n vs. volumetric ice content and linear relationships are determined in Figure A.18. The trend for n is an increase with colder temperature and a decrease in ice content. The -2°C and -3°C curves are similar in slope. The differences seen between -1°C and the colder temperatures is most likely the result increasing unfrozen water at temperatures greater than -2°C (see Chapter 4.4) Wedge ice shows little influence with respect to temperature. As the volume of ice decreases, the influence of temperature appears to increase for temperatures between -1°C to -3°C.

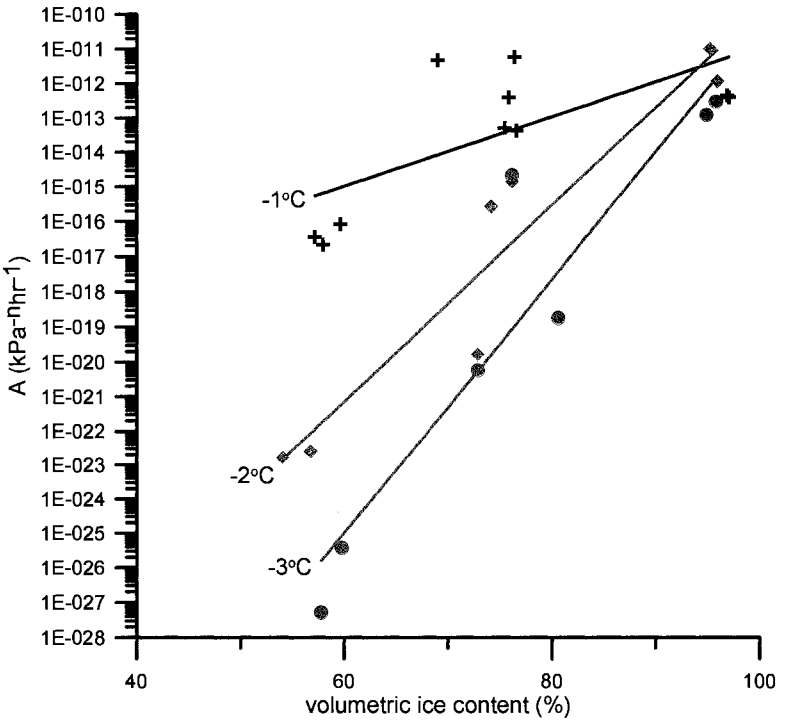

Figure A.17. Creep coefficient A as a function of volumetric ice content and temperature.

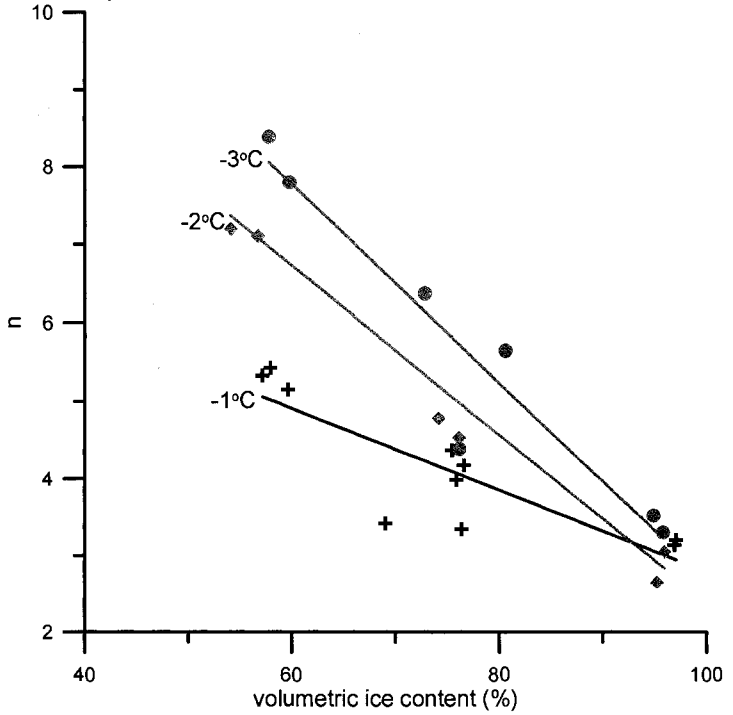

Figure A.18. Creep coefficient n as a function of volumetric ice content and temperature.

Equation A.6 can be rewritten as a function of temperature and volumetric ice content and is shown in Equation A.11.

$$\dot{\varepsilon} = A(T, W_{ice}) \cdot \sigma^{n(T,\, W_{ice})} \qquad \text{Eq. A.11}$$

Where T is temperature and W_{ice} is volumetric ice content. Table A.7 presents the creep coefficients A and n as a function of volumetric ice content and temperature. Table A.7 should only be considered if the soil contains uniformly distributed ice. Interestingly, Arenson and Springman (2005b) show that the creep exponent n decreases with decreasing volumetric ice content for coarse grained rock glacier material. The data for fine grained frozen silt, suggests the opposite trend.

Table A.7. Creep coefficients A and n as function of volumetric ice content based on Figures A.17 and A.18 for Fairbanks silt.

Temperature (°C)	A ($kPa^{-n}hr^{-1}$)	r^2	n	r^2
-1°C	$9.054 \times 10^{-22} e^{0.233 \cdot Wice}$	0.484	$8.094 - 0.053 \cdot W_{ice}$	0.720
-2°C	$8.106 \times 10^{-39} e^{0.649 \cdot Wice}$	0.916	$13.236 - 0.108 \cdot W_{ice}$	0.922
-3°C	$9.505 \times 10^{-48} e^{0.845 \cdot Wice}$	0.883	$15.376 - 0.127 \cdot W_{ice}$	0.908

note: $\dot{\varepsilon} = A\sigma^n$. W_{ice} is volumetric ice content is in %.

A.3 Minimum Creep Rate Comparison: Relaxation, CSC and Literature

Determination of minimum creep rate relationships based on a Glen type power law (Glen, 1955) was presented for CSC (constant stress creep) tests in Chapter 7.1. The purpose of this section is to compare the results from CSC tests and literature for ice-rich frozen soils. The comparison is primarily based on soils with vertical micro-lenticular (vml) cryostructure at -1°C and -2°C and soil with remolded-massive (RM) cryostructure at -1°C.

The minimum strain rate relationships determined from CSC and relaxation data are presented in Figures A.19 and A.20 for soils with vml cryostructure at test temperatures near -1°C. Figure A.19 includes all of the minimum creep rate relationships for CSC data along with relaxation data. Figure A.20 only includes a select number of minimum creep rates relationships from the CSC data. Included in both plots is the minimum strain rate data points determined from CSC tests for soils with vml cryostructure at -1°C. In Figure A.19, the upper bound relationship (curve d) from Figure 6.4 gives the most conservative prediction for low stresses. At high stresses, the lower

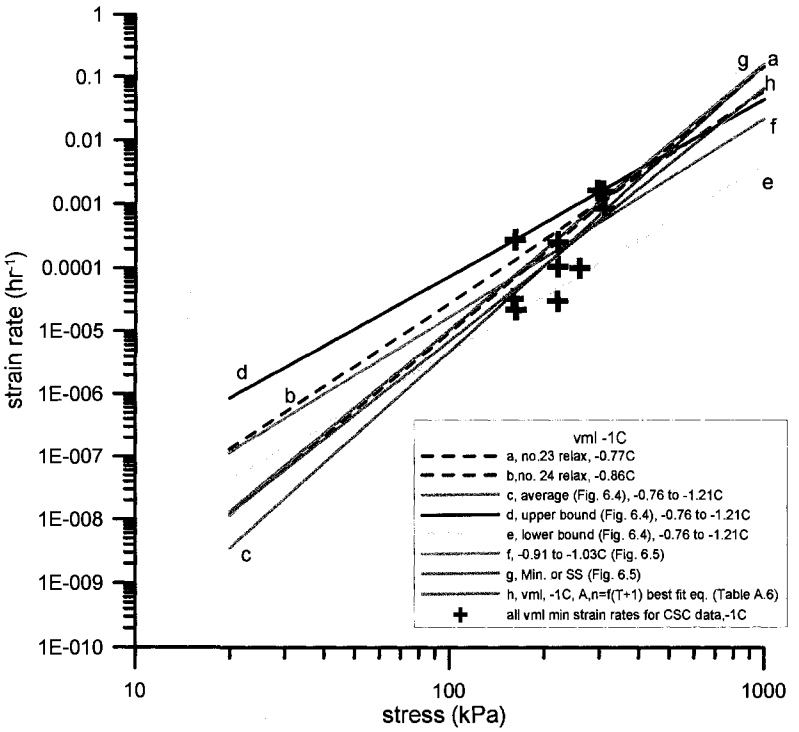

Figure A.19. Minimum strain rate power law relationships for vml cryostructure at -1°C based on CSC and relaxation tests.

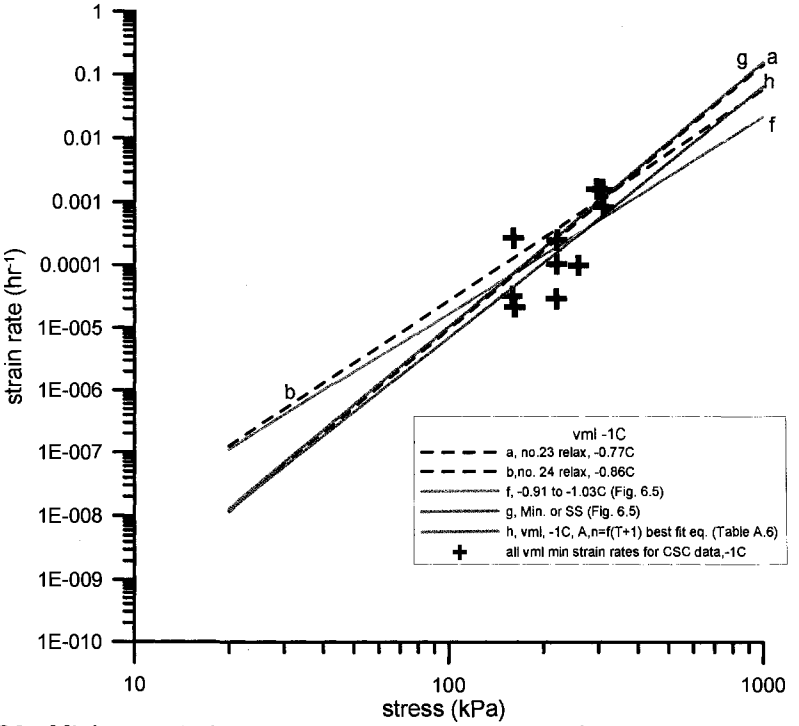

Figure A.20. Minimum strain rate power law relationships for vml cryostructure at -1°C based on select CSC and relaxation tests.

bound relationship (curve e) from Figure 6.4 is the least conservative. The minimum creep rate expressions derived from the relaxation tests are represented by curves a (black) and b (blue). Curve h is based on the temperature relationships for (T+1) for creep coefficients A and n (Table A.6, Figures A.15 and A.16). Figure A.20 presents the relationships developed from relaxation tests (samples no. 23 and 24), the relationships as a function of (T+1), the CSC relationships developed for minimum or steady state data points (Fig. 6.5) and all CSC data points close to -1°C. All five relationships provide a good representation of the data. The relaxation relationships (curves a and b) and the minimum or steady state relationship (curve g) include most of the CSC minimum strain rates. In other words, the three relationships are slightly more conservative. The minimum creep rate relationship developed for temperature (T+1), predicts strain rates that are slightly slower than the three previous relationships. However, the predictions are reasonable. Based on the CSC minimum strain rates, the expression derived from relaxation test approximations of minimum strain rate agree well. One limitation is that the stress range for CSC data is rather narrow, ranging from 160 to 290 kPa. Therefore comparison of CSC data to relaxation data over a larger stress range is not possible.

The CSC flow law, relaxation flow law, and CSC minimum strain rate data points are compared in Figure A.21 for soils with vml cryostructure tested at temperatures near -2°C. The correlation between the minimum strain rate power relationships derived from CSC data (curve a) and relaxation data (curve b) is high. When compared to the actual data (from which the CSC relationship was derived), the relaxation data predicts the minimum strain rates well. Also included in Figure A.21 is the minimum strain rate relationships developed from the creep parameter A and n as a function to temperature, (T+1) (i.e. Table A.6 and Figures A.15 and A.16). The (T+1) relationship slightly under predicts the strain rates for a given stress. Minimum strain rate data from CSC tests was not determined for stresses less than 100 kPa. Therefore, the validity of the relationships to low stresses is still unknown.

The data for soil with remolded-massive (RM) cryostructure provides the largest data set and therefore, special significance. Figure A.22 present the minimum strain rate power law relationships for CSC and relaxation data along with the CSC minimum strain rate point data. The relaxation relationship presented is derived from sample no. 50 (-0.99°C). The two segments of the curve are presented which represent the first segment (curve a, creep exponent n=5.34) and the second steeper segment (curve b, creep exponent n=25.40). See section A.2 for description of the two curve segment. Also included is a full stress range power regression for sample no. 50 which takes into account all sections of the curve (curve c). Curve f shows the

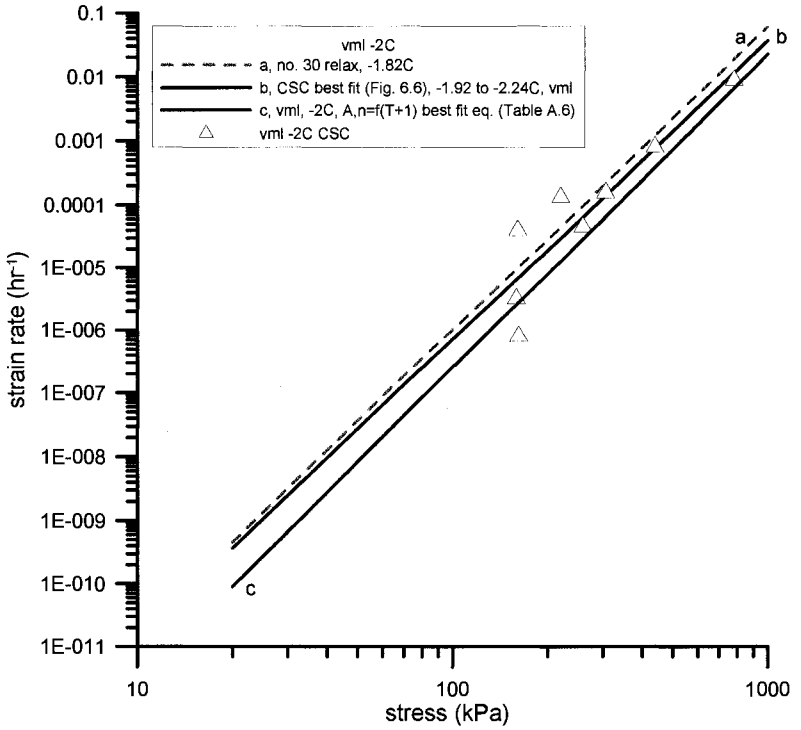

Figure A.21. Minimum strain rate power law relationships for vml cryostructure at -2°C based on CSC and relaxation tests.

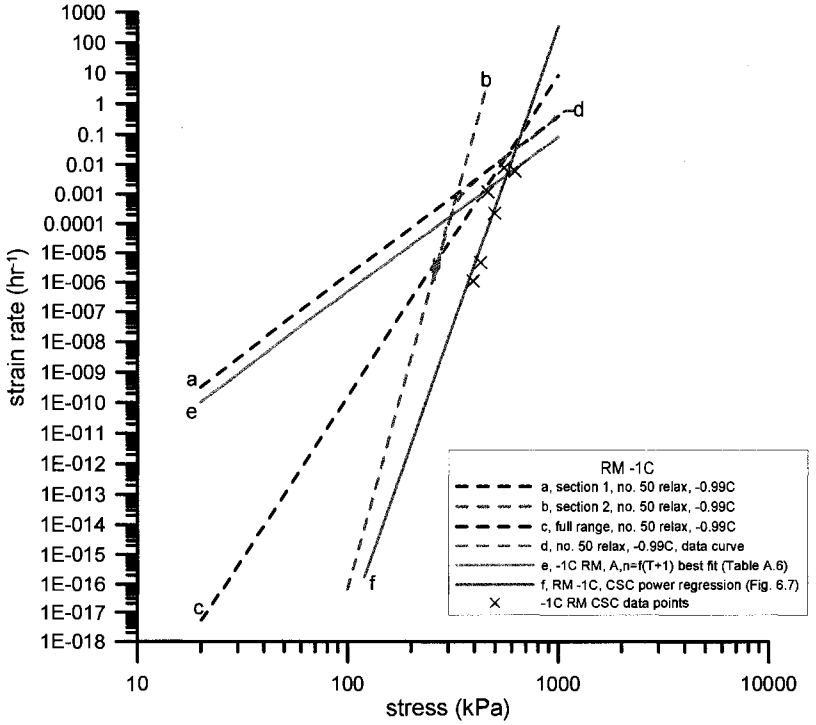

Figure A.22. Minimum creep rate power law relationships for RM cryostructure at -1°C based on CSC and relaxation tests.

minimum strain rate relationship derived from CSC data. The (T+1) relationship from Table A.6 is shown by curve e. The raw data for sample no. 50 is plotted as strain rate vs. stress and is shown by curve d (red) which is essentially the bilinear relationship for segments 1 and 2 (curves a and b). Curves a and e, which were derived from segment 1 of the relaxation curves, predict the peak values and would serve as very conservative estimates at low stresses. The minimum strain rate relationship derived from segment 2 of the relaxation curve, provide more realistic estimates at low stresses, however, as the stresses increase the creep rate estimates would be excessively large. The raw relaxation data curve for sample no. 50 (as does all RM relaxation data) suggest that at higher stresses, the increase in strain rate for an increase of stress does not rise as rapidly as would be predicted by the CSC relationship (curve f) and segment 2 of the relaxation relationship (curve b). Instead, a "plateau" like step is predicted for further increases of the strain rate with increasing stress. The two highest stress data points for the CSC minimum strain rates show only a slight increase in the strain rate with a stress increase of 70 kPa. This may lend support to the predicted decrease in the creep exponent n at higher stresses. However, more data points are needed to establish this. Yuanlin and Carbee (1987a) show a step change in slope for medium density remolded silts, which is similar to the slope change seen from the raw relaxation data. A full stress range minimum creep rate approximation (curve c) for sample no. 50 (-0.99°C) was included, which is a best fit regression over the entire stress range seen during the relaxation test. This trend has the most similarity to the power relationship derived from CSC data.

A.4 Relaxation Test Minimum Creep Rate Summary

CSC tests were conducted in order to compare minimum strain rates with minimum strain rate estimates derived from relaxation tests. It was found that the minimum strain rate approximations supply reasonable estimates of minimum strain rate conditions derived from CSC tests. The RM CSC data was derived over a period of 4 to 5 months. The relaxation tests were conducted for approximately 300 to 400 hours. The determination of CSC data for vertical micro-lenticular tests took up to 12 months at -1°C. A typical relaxation test was conducted for a period between 300 to 700 hours for soils with vertical micro-lenticular cryostructure. The longest was conducted for 3 months with no apparent change in the trend. If minimum strain rate data can be approximated from relaxation tests, the time savings are obvious. In addition, trying to test similar undisturbed samples is extremely difficult. Attempts were made to find minimum creep estimates as a function of temperature and volumetric ice content. The minimum strain rate relationships as a function of temperature tend to under predict the strain rates as compared to relaxation or CSC

data. The volumetric ice content relationships were not compared directly. A summary of minimum strain rates for different cryostructures will be included below.

1. Soils with vertical micro-lenticular (vml) cryostructure were one of the two primary cryostructures used to compare minimum strain rate flow laws determined from relaxation and CSC tests. The prevalent data scatter near -1°C made interpretation of CSC data difficult. The data scatter is attributed to increased unfrozen water contents. The relaxation tests carried out to 2067 hours (samples no. 23 and 24) showed a consistent power relationship between strain rate vs. stress even to very low stresses (approx. 30 kPa). The average minimum strain rate flow law for -1°C is an average of samples no 23 and 24. The strain rate expression for -2°C agrees well for relaxation and CSC data.

   $\dot{\varepsilon}=3.86432\text{x}10^{-13}\sigma^{3.80}$, (valid for vml near -1°C) Eq. A.12

   $\dot{\varepsilon}=2.73106\text{x}10^{-16}\sigma^{4.78}$, (valid for vml near -2°C) Eq. A.13

   with units of $\dot{\varepsilon}$ (hr^{-1}), A=($kPa^{-n}\cdot hr^{-1}$), and σ (kPa).
2. Soils with horizontal micro-lenticular (hml) cryostructure showed trends similar to soils with vertical micro-lenticular cryostructure. However, soils with horizontal micro-lenticular cryostructure appear to have slightly higher creep rates for given stress as compared to soils with vertical micro-lenticular cryostructure. This may be the influence of massive cryostructure zones in the soil as discussed in Chapter 6.
3. Soils with reticulate-chaotic (RC) cryostructure generally exhibit two segments on the log strain rate vs. log stress plot. The first segment maintains higher creep rates resulting from smaller n values. At some point, the slope increases, resulting in a quicker drop in strain rate. For the first segment of the relaxation curves (higher stresses), the n values generally ranged from 3.6 to 4.2 for all temperatures tested. For the second linear segment, the n values show more variability and ranges from 6.7 to 9.6. Comparing select data, the first segment is similar to wedge ice and soils with micro-lenticular cryostructure and the second segment is similar to soils with remolded-massive cryostructure. Therefore, it is interpreted that initial deformation occurs along the ice lenses oriented in the shear zones and secondary deformation occurs in the massive soils between ice lenses.

4. Soils with remolded-massive cryostructure show creep behavior which is significantly different than the undisturbed soils. As with soils with RC cryostructure, a bilinear log strain rate vs. log stress curve is seen. At higher stresses, a first linear segment is seen. The first

linear segment begins to transition into a steep segment (higher n value) at a strain rate of approximately 0.0036 hr^{-1} ($1x10^{-6}$ s^{-1}). This agrees well with observations made by Yuanlin and Carbee (1987a) for remolded Fairbanks silt. The transition is interpreted as a transition into a damped creep stage and an activation of a long term strength "resistance threshold."

5. The wedge ice used in this study represents syngenetic ice wedges. The average volumetric ice content ranged from 95-98%. The relaxation data suggest that the creep coefficients A and n are not heavily influenced by temperature (over the range tested -0.44°C to -3.10°C). The resulting minimum strain rate flow law relationship is similar to that proposed for ice. Using an average value, the flow law for wedge ice can be identified as:

$$\dot{\varepsilon}=4.044x10^{-12}\sigma^{3.07} \qquad \text{Eq. A.14}$$

where strain rate $\dot{\varepsilon}$ has units of hr^{-1} and stress σ has units of kPa. Equation A.14 assumes no temperature dependence. In reality there appears to be a small dependence. For temperatures ranging from -1°C to -3°C, wedge ice shows slower creep rates than undisturbed frozen soils for stresses above approximately 200 kPa. At stresses lower than 100 kPa, extrapolations suggest that wedge ice shows higher creep rates than undisturbed frozen soils.

6. Matanuska basal glacier ice and glacier ice showed variable signals. Samples no. 43 and 45 showed internal fracture patterns. Sample no. 44, which was a Matanuska basal ice sample containing well developed micro-lenticular cryostructure, showed creep behavior similar to the tunnel soils with micro-lenticular cryostructure for a stress range from 300-1400 kPa. At lower stresses the n value rapidly increases. The overall affect is similar to the remolded soils. The sample visually contained some fine sand. Sample no. 46 was a core of Matanuska glacial ice. The overall trend is similar to that for wedge ice.
7. Using relaxation data for the interpretation of minimum strain rates agrees fairly well with the results for constant stress creep (CSC) tests conducted in this study. More results are needed, but the relaxation testing technique in this study could potentially offer an alternative and viable approach for determination of minimum strain rate flow law parameters. However, the relaxation tests in this work initially subjected the sample to a high initial stress. More work needs to be conducted to verify if the results represent a failure condition or not.